FY08

Engineering Research & Technology Report

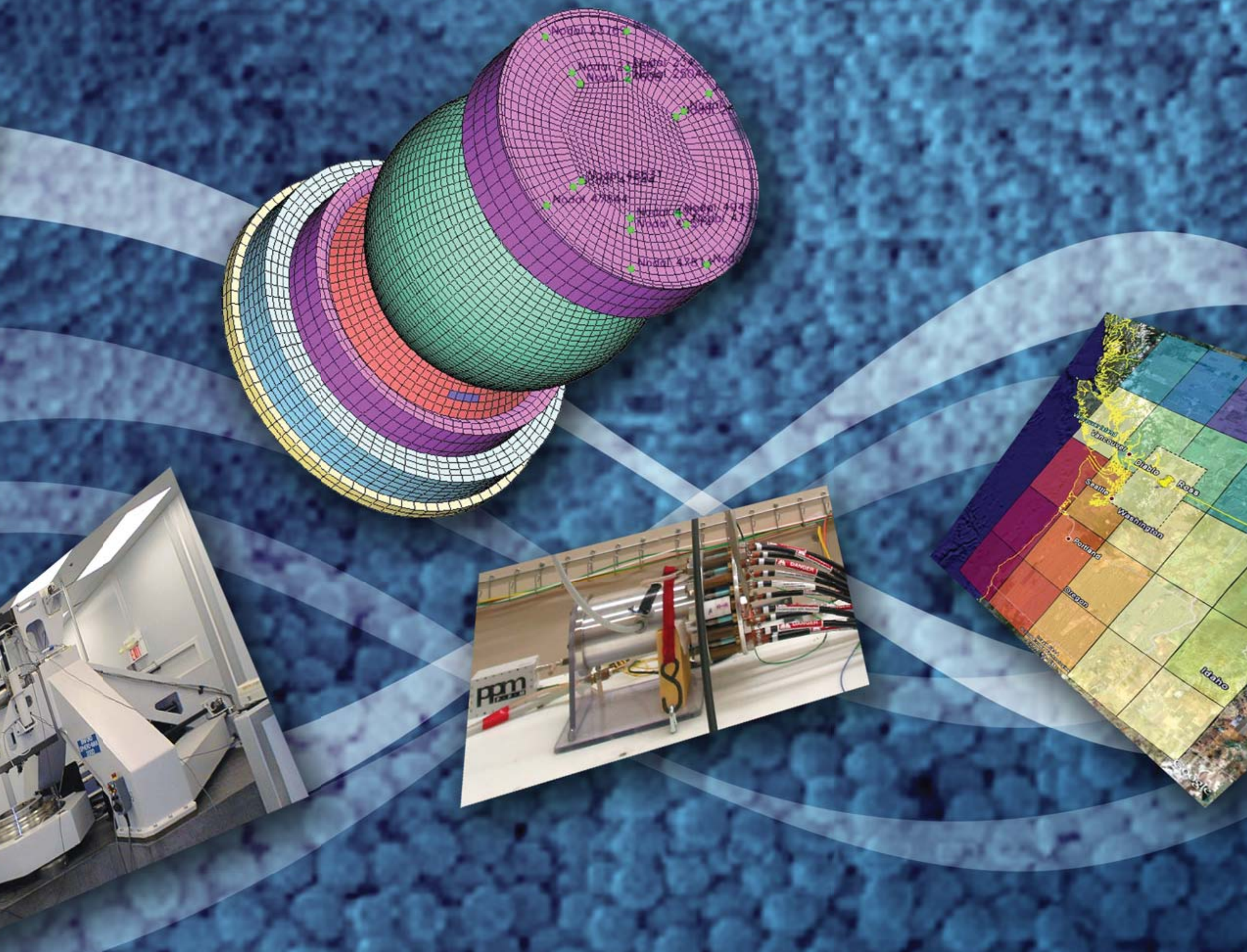

April 2009

Lawrence Livermore National Laboratory

LLNL-TR-414026

Acknowledgments

Scientific Editors
Camille Minichino
Don McNichols

Graphic Designers
Jeffrey Bonivert
Lucy C. Dobson
Kathy J. McCullough
Debbie A. Ortega

Project Manager
Debbie A. Ortega

Cover:
Graphics representing projects from Engineering's research and technology areas.

FY08
Engineering Research & Technology Report

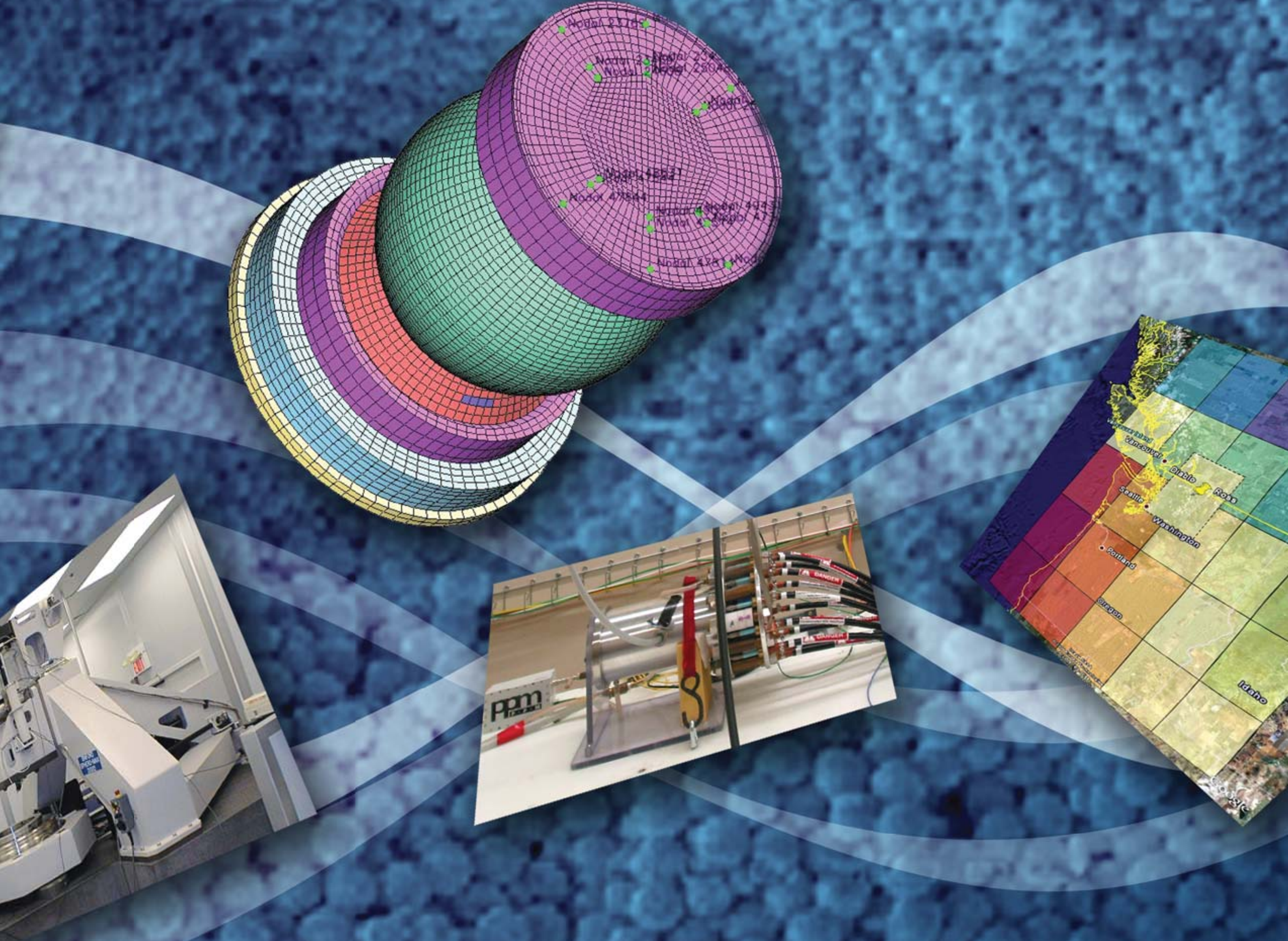

April 2009

Lawrence Livermore National Laboratory

LLNL-TR-414026

A Message From

Monya A. Lane

Associate Director for Engineering (Acting)

This report summarizes the core research, development, and technology accomplishments in Lawrence Livermore National Laboratory's Engineering Directorate for FY2008. These efforts exemplify Engineering's more than 50-year history of developing and applying the technologies needed to support the Laboratory's national security missions. A partner in every major program and project at the Laboratory throughout its existence, Engineering has prepared for this role with a skilled workforce and technical resources developed through both internal and external venues. These accomplishments embody Engineering's mission: "Enable program success today and ensure the Laboratory's vitality tomorrow."

Engineering's mission is carried out through basic research and technology development. Research is the vehicle for creating competencies that are cutting-edge, or require discovery-class groundwork to be fully understood. Our technology efforts are discipline-oriented, preparing research breakthroughs for broader application to a variety of Laboratory needs. The term commonly used for technology-based projects is "reduction to practice." As we pursue this two-pronged approach, an enormous range of technological capabilities result.

This report combines our work in research and technology into one volume, organized into thematic technical areas: Engineering Modeling and Simulation; Measurement Technologies; Micro/Nano-Devices and Structures; Engineering Systems for Knowledge and Inference; and Energy Manipulation. Our investments in these areas serve not only known programmatic requirements of today and tomorrow, but also anticipate the breakthrough engineering innovations that will be needed in the future.

Engineering Modeling and Simulation efforts focus on the research, development, and deployment of computational technologies that provide the foundational capabilities to address most facets of Engineering's mission. Current activities range from fundamental advances to enable accurate modeling of full-scale DOE and DoD systems performing at their limits, to advances for treating photonic and microfluidic systems.

FY2008 research projects encompassed material studies and models for low symmetry materials and materials under extreme pressures; and multiphysics coupling of electromagnetics with structural mechanics to simulate systems such as electromagnetic railguns. Technology projects included enhancements, verification, and validation of engineering simulation tools and capabilities; progress in visualization and data management tools; and extensions of our competence in structural damage analysis.

Measurement Technologies comprise activities in nondestructive characterization, metrology, sensor systems, and ultrafast technologies for advanced diagnostics. The advances in this area are essential for the future experimental needs in Inertial Confinement Fusion, High-Energy-Density Physics, Weapons, and Department of Homeland Security programs.

FY2008 research featured probes for micrometer-scale metrology and advanced algorithms for illicit radionuclide detection. Technology projects included new error budgeting tools for nondestructive evaluation systems and component implementation for prompt diagnostics of key single-shot experiments.

Micro/Nano-Devices and Structures encompass technology efforts that fuel the commercial growth of microelectronics and sensors, while simultaneously customizing these technologies for unique, noncommercial applications that are mission-specific to the Laboratory and DOE. The Laboratory's R&D talent and unique fabrication facilities have enabled highly innovative and custom solutions to technology needs in Stockpile Monitoring and Stewardship, Homeland Security, and Intelligence.

FY2008 research projects included systems for defense against biothreats and for the manipulation of biomolecules and viruses; studies of transport behavior and crystal-driven neutron sources; and the exploration of advanced detectors for identifying nuclear material. Technology projects included validation of acoustic modeling for microfluidic systems; applications of lasers and optical sensors; and new capabilities for micro- and nano-fabrication.

Engineering Systems for Knowledge and Inference, an emerging focus area for Engineering as well as for the country at large, encompasses a wide variety of technologies. The goal is to generate new understanding or knowledge of situations, thereby allowing anticipation or prediction of possible outcomes. With this knowledge, a more comprehensive solution may be possible for problems as complex as the prediction of disease outbreaks or advance warning of terrorist threats.

FY2008 research efforts were centered on the extraction of information from unstructured text and advancing classification methods for a variety of applications. Technology efforts included adversarial modeling and improving the ability to track in a low-resolution large-scale scene scenario.

Energy Manipulation, a long time focus that is receiving increased emphasis due to newly emerging applications, encompasses the fundamental understanding and technology deployment for many modern pulsed-power applications. This area has broad applications for magnetic flux compression generators and components for modern accelerators.

FY2008 research focused on an ultra-high velocity railgun. Technology efforts focused on railgun pulse power systems and diagnostics; UV-induced flashover; diagnostics for electrical breakdown in vacuum; and fiber optic current measurements.

Contents

Introduction

A Message from Monya A. Lane ...iii

Engineering Modeling and Simulation

Deformation of Low Symmetry and Multiphase Materials
Nathan R. Barton ...2

Integrated Analysis and Simulation Software Tools for Calibration and Validation of Crystal Scale Material Models
Joel V. Bernier ...4

Model-Based Flaw Localization from Perturbations in the Dynamic Response of Complex Mechanical Structures
David H. Chambers ...6

Plasticity at High Pressures and Strain Rates using Oblique-Impact Isentropic-Compression Experiments
Jeffrey N. Florando ...8

Advanced Composite Modeling Capabilities for ALE3D
Michael J. King ...10

Fast Running Tools for Explosions in Urban Environments
Chad R. Noble ...12

Arc Initiation Modeling for High Explosives
James F. McCarrick ...14

Applying MESA Epidemiological Model to Human Diseases
Matthew J. Dombroski ...16

Mitigation of Electromagnetic Pulse Effects from Short-Pulse Lasers and Fusion Neutrons
Charles G. Brown, Jr. ...18

Finite Element Analysis Visualization and Data Management
Bob Corey ...20

New Algorithm for Stiffness-Proportional Damping and Other Improvements in DYNA3D
Jerry I. Lin ...22

NIKE3D Code Maintenance and Enhancement
Michael A. Puso ...24

Electromagnetics Code Maintenance
Daniel A. White ...26

Measurement Technologies

Detection, Classification, and Estimation of Radioactive Contraband from Uncertain, Low-Count Measurements
James V. Candy 30

Error Mapping and Automated Calibration of PrISMM
Jeremy J. Kroll 32

Standing Wave Probes for Micrometer-Scale Metrology
Richard M. Seugling 34

Prompt Experimental Diagnostics
John E. Heebner 36

Serrated Light Illumination for Deflection Encoded Recording (SLIDER)
John E. Heebner 38

Recirculating Optical Probe for Encoding Radiation (ROPER)
Stephen P. Vernon 40

Automated PID Tuning Using Extremum Seeking
Nicholas J. Killingsworth 42

Micro/Nano-Devices and Structures

Hybridization, Regeneration, and Selective Release on DNA Microarrays
N. Reginald Beer 46

Thermal-Fluidic System for Manipulating Biomolecules and Viruses
Klint A. Rose 48

Fluidic Platform for DNA Microarrays
John M. Dzenitis 50

A Mesoscale Approach to Characterize Material Properties of Polymeric Media
Todd H. Weisgraber 52

Tunable Optical Cavities for Absorption Spectroscopy
Tiziana Bond 54

A Micro-Opto-Mechanical Photoacoustic Spectrometer
Jack Kotovsky 56

Cadmium-Zinc-Telluride Sandwich Detectors for Gamma Radiation
Rebecca J. Nikolić 58

Fabrication of High Resolution CZT Detectors
Rebecca J. Nikolić 60

Flow Programmed Mesoscale Assembly of Nanoengineered Materials and Net Shape Components
Klint A. Rose 62

High-Resolution Projection Micro-Stereolithography (PμSL) for Advanced Target Fabrication
Christopher M. Spadaccini 64

Microfabricated Technologies for Target Fabrication
Robin Miles 66

Compact High-Intensity Neutron Source Driven by Pyroelectric Crystals
Vincent Tang 68

Study of Transport Behavior and Conversion Efficiency in Pillar Structured Neutron Detectors
Rebecca J. Nikolić 70

Validation of 3-D Commercial Codes for Microfluidic Systems
Klint A. Rose 72

Engineering Systems for Knowledge and Inference

Ultra-Scale Tracking in Low-Resolution Image Sequences
Carmen Carrano 76

Automatic Learning of Probabilistic Causal Models
Brenda M. Ng 78

Enhanced Event Extraction from Text via Error-Driven Aggregation Methodologies
Tracy D. Lemmond 80

Robust Ensemble Classifier Methods for Detection Problems with Unequal and Evolving Error Costs
Barry Y. Chen 82

Evaluating Deterrence Measures in Adversary Modeling
Carol A. Meyers 84

Insider Threat Scenarios and Signatures
Deborah W. May 86

Proliferation Resistance and Physical Protection of Current Nuclear Fuel Cycles
Thomas A. Edmunds 88

Software Module for Statistical Analysis in Climate-Related Impact
Gardar Johannesson 90

Energy Manipulation

Ultrahigh-Velocity Railgun
Jerome M. Solberg 94

Pulse Power Systems and Diagnostics for the Fixed Hybrid Armature Railgun
Todd J. Clancy 96

ALE3D/EM Validation Experiments
Laura K. Tully 98

Magnetic Insulation in a Sulfur Hexaflouride (SF_6) Filled Power Flow Channel
Timothy L. Houck 100

Evaluation of Spark Gap Technologies for High Current, High Charge Transfer Switches
Brent McHale 102

Pulsed Magnetic Field Measurements Using Faraday Rotation Diagnostics
Brent McHale 104

UV-Induced Insulator Flashover
Jay B. Javedani 106

Author Index 108

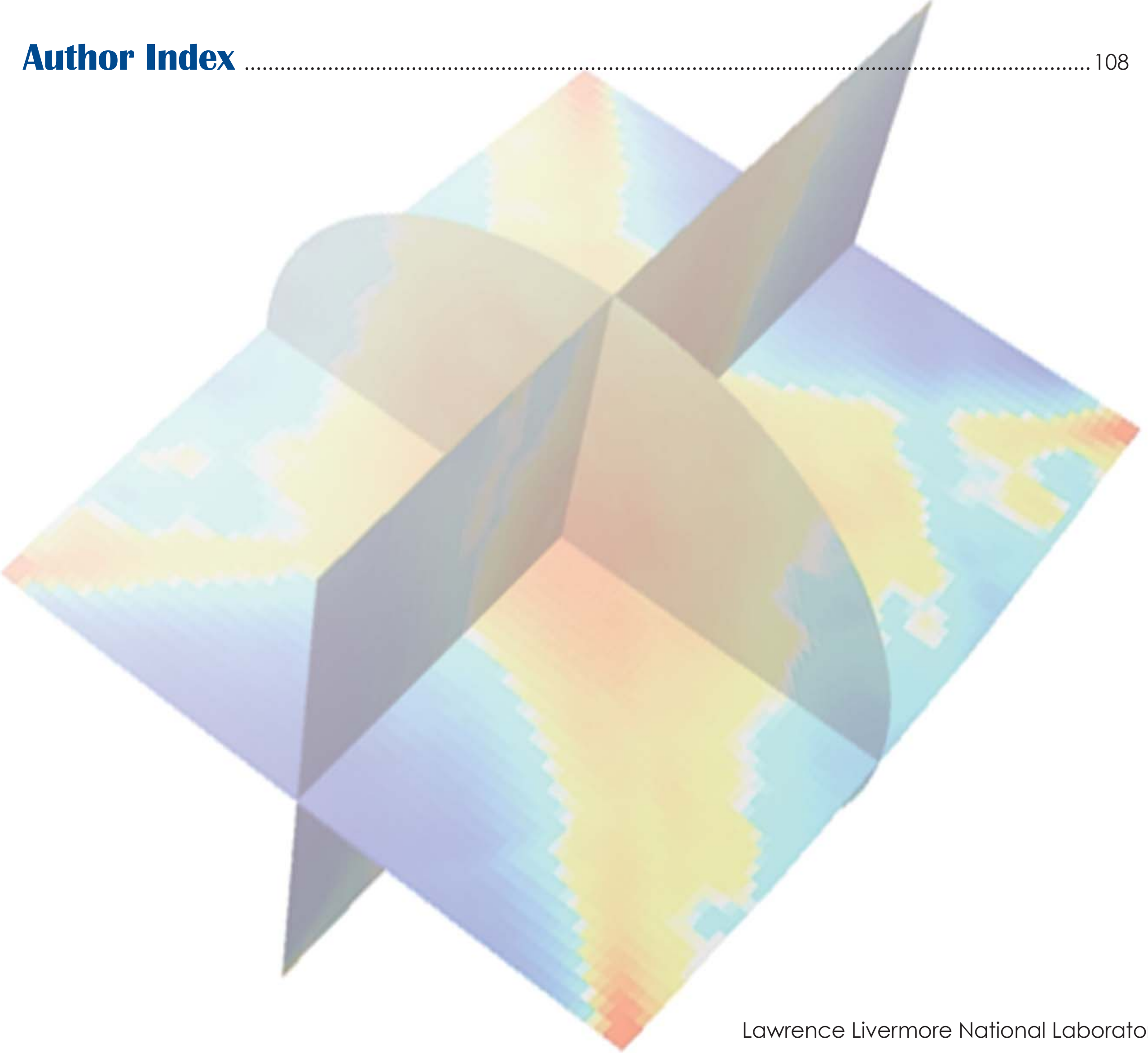

Engineering Modeling & Simulation

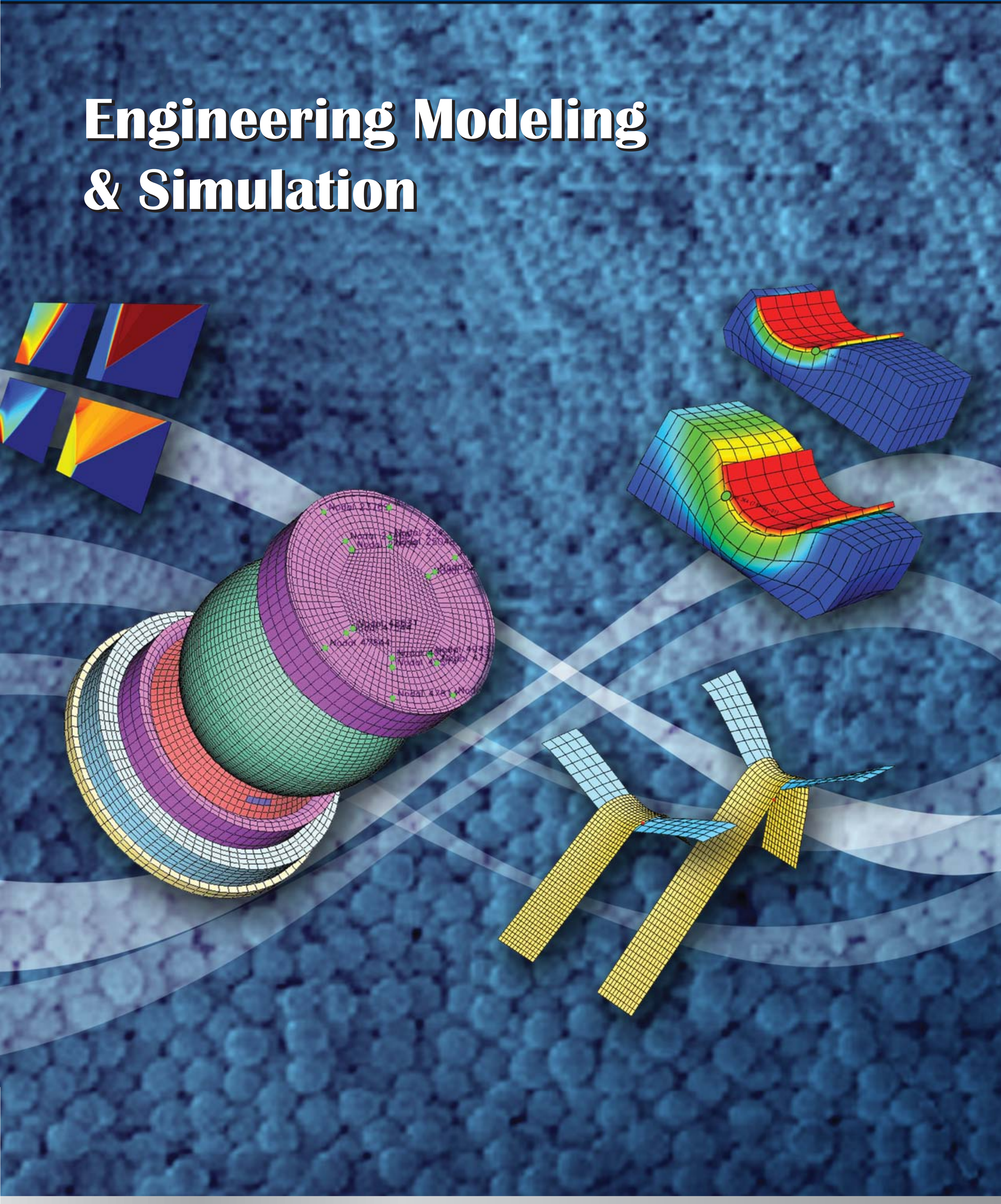

Deformation of Low Symmetry and Multiphase Materials

Nathan R. Barton
(925) 422-9426
barton22@llnl.gov

Materials composed of low symmetry crystals or of multiple solid phases exhibit heterogeneous deformation at the microstructural scale, presenting significant challenges to efforts to construct macroscale constitutive models. This deformation heterogeneity at the microstructural scale also produces stress concentration that can lead to fracture or influence the onset and progress of phase transformations. We are developing an approach that explicitly incorporates effects of microstructure and deformation heterogeneity in a framework suited to analysis of engineering scale components.

Applications involving fully developed plastic flow are targeted. We explicitly represent the microstructure and we build on emerging technologies for effectively combining microscale plasticity simulations with macroscale models. The goal is to obtain effective macroscale models for materials whose behavior is difficult to predict using conventional approaches. New capabilities capture the impact of microstructure and thus material processing on the performance of engineering scale components.

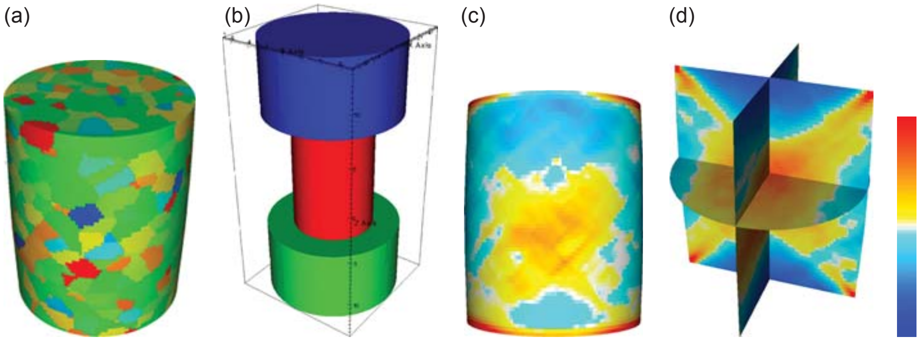

Figure 1. Results from a simulated Ti-6Al-4V compression test: (a) long range ordering of the microstructure associated with prior beta grain structure at elevated temperature; (b) full simulation geometry including hardened steel compression platens. Strain localization patterns are shown in plots of the plastic strain rate on (c) the surface of the sample, and (d) slices through the sample. Both short- and long-range localization patterns are observed, with the stress concentrations associated with frictional contact influencing the long-range localization patterning. The fine-scale polycrystal effectively embedded within each coarse scale finite element is composed of 1302 α orientations and 600 β orientations with weights determined from x-ray diffraction measurements conducted at the Advanced Photon Source at Argonne National Laboratory.

Project Goals

Our overarching goal is to produce effective macroscale models through novel homogenization methods for materials for which conventional methods fail. The immediate application space includes a broad class of engineering simulations, ranging from forming operations to dynamic loading scenarios. Figures 1 and 2 show example applications, with computations informed by experimental data including measured microstructural information for the multi-phase Ti-6%Al-4%V (Ti-6Al-4V) alloy (Fig. 3). Initial development is focused on Ti-6Al-4V alloy given its widespread use and the availability of relevant experimental data. Preliminary results have also been generated for application to $CaIrO_3$ post-perovskite, a low symmetry mineral of interest in the geophysics community. Software is developed in a component-oriented fashion, making use of tools that enhance parallel load balancing through task parallelism.

Relevance to LLNL Mission

The project aligns directly with the processing for performance and fracture components of the Engineering Simulation Roadmap. Upon completion, the project will deliver a capability focused on closing the microstructure-properties relationship capability gap described in the roadmap. Through the advancement

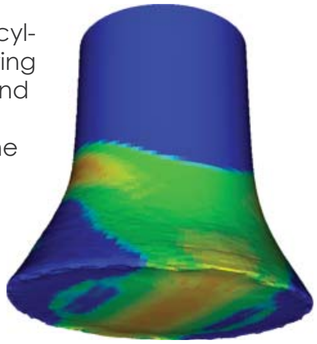

Figure 2. Simulation of a Taylor cylinder impact experiment, showing plastic strain rate localization and the influence of plastic anisotropy, with coarse scale and fine scale state descriptors distributed as in Fig.1. The majority of c-axes of the α phase crystals are aligned with the impact direction. The hardened steel anvil is not shown.

FY2009 Proposed Work

The focus in FY2009 will be on including more detailed evolution of polycrystal scale state, specifically the probability density function for lattice orientations. This will increase model fidelity and will allow us to treat deformation by deformation twinning. In this context, polycrystal scale calculations will be based on a viscoplastic self-consistent formulation. Initial development and testing will be performed on magnesium, given the availability of experimental data. A preliminary model for α-uranium will be developed.

of high-fidelity simulations and novel computational methods, the effort also aligns with the discovery class science and engineering component of the LLNL Science and Technology Plan. We will provide a more predictive modeling framework for a programmatically important class of materials.

FY2008 Accomplishments and Results

Finite element calculations at the polycrystalline aggregate scale have been performed for both Ti-6Al-4V and $CaIrO_3$ post-perovskite using ALE3D, with the calculations resolving sub-grain heterogeneities as shown in Fig. 4. Parallel finite element calculations have been successfully performed as part of remote method invocations suitable for use in multiple-program multiple-data parallelism strategies. Development of coarse scale material models has continued, working toward numerical robustness and computational efficiency of the overall simulation. Due to numerical challenges associated with the coarse scale material model that can embed the finite element based polycrystal calculations, production simulations to date have used a lower fidelity polycrystal model. Simulations do however still capture strain localization events at the coarse scale (Figs. 1 and 2). As the result of collaboration with researchers at LANL, we have identified an alternative to the finite element based polycrystal calculations that would render comparable model fidelity, a potentially more robust numerical implementation, and substantially lower computational cost.

Related References

1. Barton, N. R., J. Knap, A. Arsenlis, R. Becker, R. D. Horning, and D. R. Jefferson, “Embedded Polycrystal Plasticity and Adaptive Sampling,” *International Journal of Plasticity*, **24**, pp. 242–266, 2008.
2. Barton, N. R., and H.-R. Wenk, “Dauphiné Twinning in Polycrystalline Quartz,” *Modeling and Simulation in Materials Science and Engineering*, **15**, pp. 369–394, 2007.
3. Barton, N. R., “Novel Algorithms in Computational Materials Science: Enabling Adaptive Sampling,” *ASCR PI Meeting, US DOE Office of Science HPCSW*, 2008,
4. Bernier, J. V., N. R. Barton, and J. Knap, “Polycrystal Plasticity Based Predictions of Strain Localization In Metal Forming,” *Journal of Engineering Materials and Technology*, **130**, 2008.

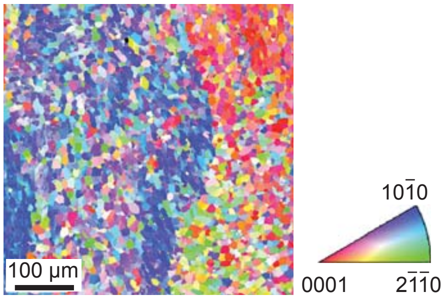

Figure 3. Electron backscatter diffraction data, showing lattice orientation in the α phase of a Ti-6Al-4V sample. The plot is colored according to the crystal plane normal to the sample surface.

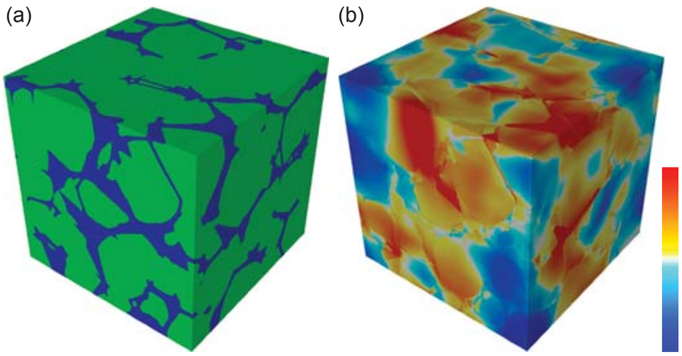

Figure 4. Finite element calculation performed using ALE3D, showing (a) phase distribution and (b) strain localization with the average plastic strain rate seen in the white/gray areas.

Integrated Analysis and Simulation Software Tools for Calibration and Validation of Crystal Scale Material Models

Joel V. Bernier
(925) 423-3708
bernier2@llnl.gov

Recent advances in diffraction-based experimental mechanics have provided unprecedented levels of detail in the co-evolution of microstructure and micromechanical state in (poly) crystalline materials, such as structural metals, loaded *in situ*. Simultaneously, LLNL engineers have created constitutive models with increasing levels of physical detail, advancing the state of computational mechanics. There is, however, a dearth of fundamental software tools suitable for integration of experimental and simulated data. Existing tools were typically generated on an *ad hoc* basis and lack the robustness and modularity necessary to make them more generally applicable. This hampers critical validation and verification procedures for advanced material models, as well as collaborations seeking to leverage such models implemented in major LLNL simulation codes, such as ALE3D. The goal of this project is to bridge this gap by producing an open-source software toolkit for reducing and analyzing data from both experiments and simulations.

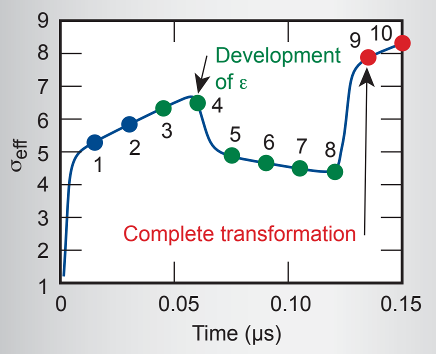

Figure 1. Simulation results, showing the deviatoric stress response of an iron polycrystal subject to 1-D compression. Blue dots are time-steps prior to transformation (100% α); green dots indicate the onset of transformation from α→ε; and red dots indicate the complete transformation of the original α phase.

Project Goals

Our goals for FY2008 include building a comprehensive open-source library of Python modules that provide the following functionalities:

1. Experimental diffraction data reduction:
   (a) lattice strain extraction;
   (b) pole figure inversion (quantitative texture analysis); and
   (c) strain pole figure inversion (quantitative strain/stress analysis).
2. Simulation data reduction:
   (a) data extraction from ALE3D;
   (b) discrete orientation distributions (quantitative texture analysis); and
   (c) lattice strain/stress distributions (strain partitioning, phase transformations, strain localization).
3. Material Point Simulator (MPS): lightweight material model evaluation using mean field theories.
4. Model parameter optimization: general harness for running the MPS or ALE3D within a nonlinear optimization framework.

Relevance to LLNL Mission

This contribution supports ongoing work under LLNL's Engineering Simulation and Measurement Technology Roadmaps. Specifically, this software toolkit will supplement simulation efforts toward understanding the fracture and strength of metals,

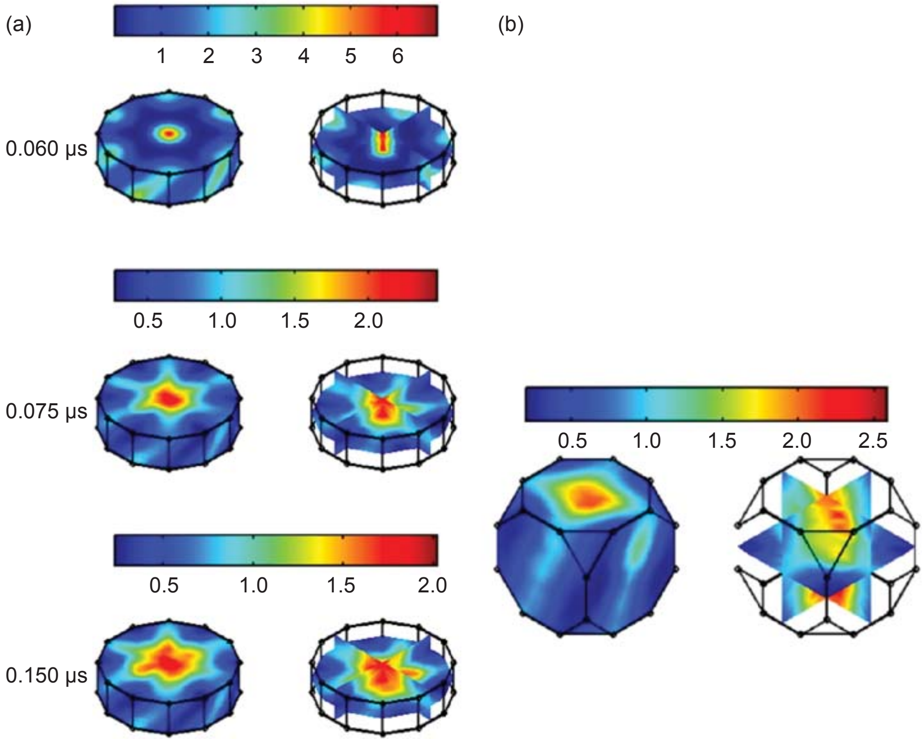

Figure 2. (a) ALE3D simulated evolution of the orientation distribution for the ε iron at several times from initiation of shock, shown as contours over the hexagonal orientation space (Rodrigues' parameterization). The apparent texture is due to both variant selection and plasticity. (b) The orientation distribution in the α iron prior to complete exhaustion (~ 0.120 µs) plotted over the cubic orientation space. Such data may be compared directly to experimentally measured distributions.

as well as experimental characterization of relevant microstructural features such as orientation distributions and intergranular stresses. In addition, the software will benefit users of materials science beamlines at diffraction facilities throughout the DOE complex, such as the Los Alamos Neutron Science Center at Los Alamos National Laboratory, the Advanced Light Source at Lawrence Berkeley National Laboratory, and the Advanced Photon Source at Argonne National Laboratory.

FY2008 Accomplishments and Results

We are able to exercise material models using the MPS as well as ALE3D, extract the relevant history variables, and create data metrics such as orientation distributions, which are readily compared to experimental results. For example, Fig.1 shows the deviatoric stress response of an initially texture-free iron polycrystal subject to simulated shock loading. The constitutive model is elasto-viscoplastic, and includes kinetics for the α↔ε phase transformation. As deformation proceeds, the body-centered cubic (BCC) phase both deforms plastically and transforms to the hexagonal close-packed (HCP) phase. Orientation distributions can be calculated at selected points to examine variant selection (Fig. 2). Similar distributions can be constructed from experimental data, which may in turn be used to verify the model performance. A framework for parameter optimization using the MPS is provided as well.

Related References

1. Bernier, J. V., M. P. Miller, J. –S. Park, and U. Lienert, "Quantitative Stress Analysis of Recrystallized OFHC Copper Subject to Deformation *In Situ*," *J. Eng. Mater. Technol.*, **130**, 2, pp. 021021-1–11, 2008.
2. Margulies, L, T. Lorentzen, H. F. Poulsen, and T. Leffers, "Strain Tensor Development in a Single Grain in the Bulk of a Polycrystal Under Loading," *Acta Mater.*, **50**, pp. 1771–1779, 2002.
3. Barton, N. R., D. J. Benson, and R. Becker, "Crystal Level Continuum Modelling of Phase Transformations: the α↔ε Transformation in Iron," *Modell. Simul. Mater. Sci. Eng.*, **13**, pp. 707–731, 2005.
4. Bernier, J. V., N. R. Barton, and J. Knap, "Polycrystal Plasticity Predictions of Strain Localization in Metal Forming," *J. Eng. Mater. Technol.*, **130**, 2, pp. 021020-1–5, 2008.

Project Summary

The software toolkit produced under this project comprises a library of core routines that facilitate several fundamental data analysis tasks. Future efforts will focus on enhancing the user interface and adding new functionality, such as virtual microstructure generation from statistical data.

Model-Based Flaw Localization from Perturbations in the Dynamic Response of Complex Mechanical Structures

David H. Chambers
(925) 423-8893
chambers2@llnl.gov

The response of a mechanical structure to vibration is determined by the geometry and mechanical properties of the components that make up the structure. Structural damage in a component can cause observable changes in the overall dynamic response. As a result, vibration measurements are often used in machine health monitoring and for detecting damage in bridges and buildings. In this project, we evaluate the performance of a new model-based approach to locate structural damage in complex mechanical assemblies using measurements of the vibrational response. This model-based method uses a numerical model of the assembly to process the measurements and estimate damage locations. The approach was previously demonstrated on simple objects.

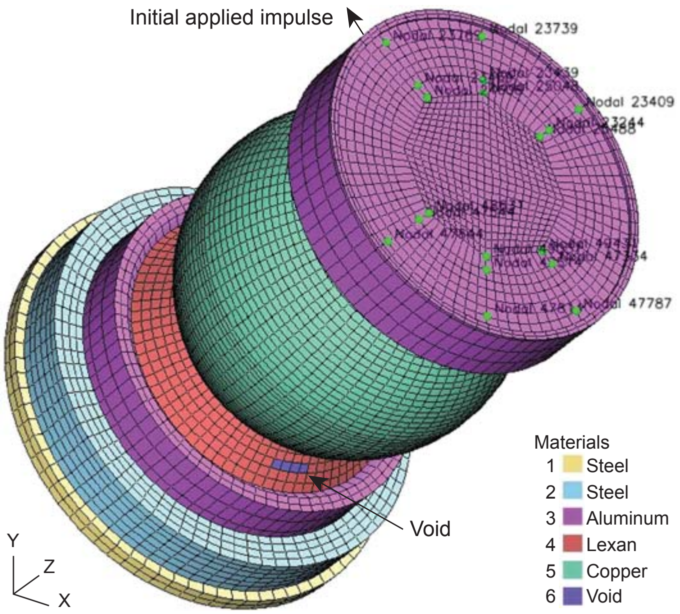

Figure 1. Interior subassembly used for initial test. Green dots are the 18 sample points used for analyzing the vibrational response.

Project Goals

The single goal of this project was to demonstrate the feasibility of the model-based method for localizing structural damage on a complex mechanical structure.

Relevance to LLNL Mission

Present methods for inspection of weapon systems are based on disassembly. Though successful, this method is expensive, time-consuming, and requires removing weapon units from service and transporting them to a central disassembly point.

With DOE's ongoing emphasis on finding more cost-effective ways to maintain the nation's stockpile, alternative methods of inspecting weapons without disassembly will likely play a significant role in future approaches to stockpile inspection. Currently, industry uses vibration monitoring to determine the health of production machinery. Other groups are investigating vibration monitoring for detecting damage in buildings and bridges. LLNL development of this technology will enable the design of internal and external sensor systems for measuring critical structural parameters for surveillance and long-term monitoring.

FY2008 Accomplishments and Results

To determine the relevance of the model-based approach to localizing damage in a complex mechanical structure,

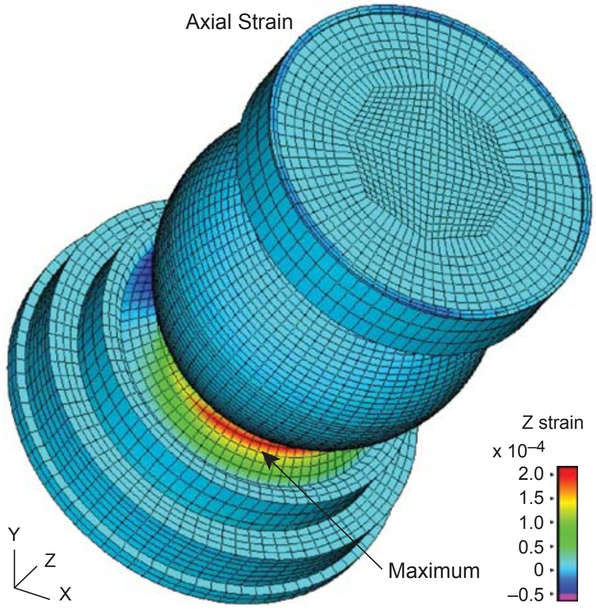

Figure 2. Axial strain field computed from the differences in the vibrational response at the sample points, showing a maximum at the position of the void.

we used the LLNL developed code NIKE3D to calculate the vibrational response of a numerical test structure to a force applied at one point. We first calculated the response to the intact structure, then created a small void in the structure and recalculated the vibrational response. The differences between the vibration patterns at a set of sample points are converted to applied forces in a third simulation of the vibrational response. The location of the damage is estimated from the location of the maximum vibration in this last calculation.

We applied this technique to a numerical model used previously for vibration analysis, changing the materials for several components in order to increase the complexity. The first test was on the interior subassembly (Fig. 1). An impulsive force was applied at one end and the vibration calculated on 18 sample points on one surface. We then created a small void by removing a few elements from a component near the lower surface, and repeated the vibration calculation. The differences between the original and the void cases at the sample points were converted to forces applied at the sample points in the last simulation. The resulting strain field showed a peak at the position of the void (Fig. 2). Next we repeated the procedure for the full model. The resulting strain field again showed a maximum at the position of the void, validating the method for a complex structure.

Project Summary

We demonstrated that the model-based method for localizing structural damage by analyzing vibration data worked for a complex object. This allows one to localize interior structural damage using measurements made on the exterior of a complex structure and a numerical model of the original structure. This is one of a number of possible approaches to damage detection that could significantly reduce the need for disassembly for stockpile inspection. We expect the relevant programs will support further development of this approach.

Plasticity at High Pressures and Strain Rates using Oblique-Impact Isentropic-Compression Experiments

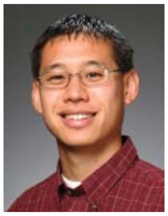

Jeffrey N. Florando
(925) 422-0698
florando1@llnl.gov

Various aspects of LLNL's national security mission depend on accurate computer code simulations of materials in high strain-rate plastic flow (*i.e.*, nonreversible deformation) under conditions of high hydrostatic pressures. While progress has been made in recent years, especially at the extreme ranges of pressure and strain-rate, there is still an uncertainty in understanding the strength of materials under conditions of combined high strain-rate (10^4 to 10^6 s^{-1}) and high pressure (1 to 100 GPa).

Current strength models used in simulations include some physically based models such as the Mechanical Threshold Stress formulation, which has over 20 parameters. The uncertainty in the values for these parameters as well as values for the parameters in other physically based models is under question due to the inherent difficulties in conducting and extracting high-quality experimental data in the high-pressure and high-strain-rate regimes. The experimental studies of material strength at these pressure and strain rate regimes will further the understanding of the underlying physical strength mechanisms needed for accurate material strength models.

Project Goals

The goals of this project are to develop an oblique-impact isentropic-compression experiment (Fig. 1), to measure the strength of materials under a condition of combined high strain-rate (10^4 to 10^6 s^{-1}) and high pressure (1 to 100 GPa). The isentropic compression allows for high pressures to be achieved over relatively long time frames (microseconds), and the oblique impact allows for a measurement of the strength properties under pressure. The strength data will then be used to refine and enhance the current strength models. When completed, this work will increase the Laboratory's ability to develop predictive strength models for use in computer code simulations.

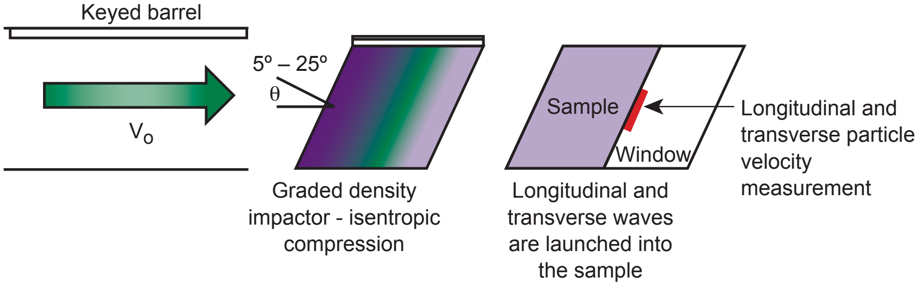

Figure 1. Oblique-impact isentropic-compression experiment using keyed barrel to maintain impactor orientation.

Relevance to LLNL Mission

This experiment, including understanding and simulating the strength of materials under dynamic loading conditions, is closely tied to the Weapons Science theme area under the Laboratory's Science and Technology Plan. More specifically, this project falls under the thrust areas of advanced experiments and improved understanding of materials properties for weapons. In addition, this work is closely aligned with the Engineering Simulation focus area.

FY2008 Accomplishments and Results

Building upon the results from last year, the focus this year was on designing experiments that have a longer measurement interval, which is essential in understanding how the transverse wave is related to the strength of the material under the dynamic loading conditions. In addition we have performed a number of simulations to compare to the data and to help aid in the experimental design.

Experimental results. We have performed a number of experiments on Cu samples backed by a sapphire window on a 2-in. keyed barrel gas gun at Brown University. The result from an experiment with a 1.5-mm-thick Cu sample backed by a 10-mm sapphire window is shown in Fig. 2. The sample was impacted at 150 m/s with a Ta-10%W target. Comparing the results with the simulations, also shown in Fig. 2, indicates that there is fairly good agreement when the flow stress of the Cu is set to 180 MPa. The magnitude of the transverse wave is on the cusp of the experimental resolution of the system, and the drops seen in transverse velocity data are most likely due to the "noise" in the system. Materials with higher strength, and therefore higher velocities, should produce a smoother signal.

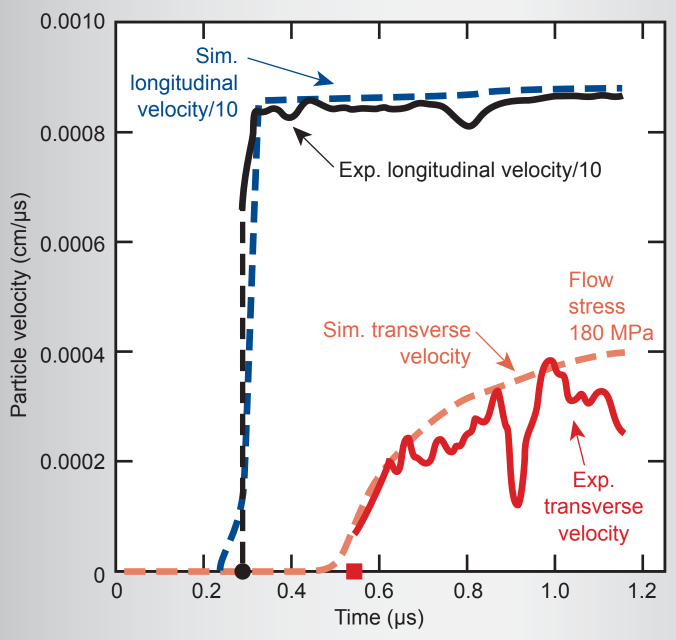

Figure 2. Experimental data showing the measured longitudinal and transverse waves. There is good agreement between the simulation and experiment in both the longitudinal wave and transverse waves when the flow stress in the simulation is set to 180 MPa.

Simulations. A number of simulations have been performed using ALE3D not only to compare the results with the experiment, but also to investigate the sensitivity of the results to experimental factors such as friction of the interfaces. While the results show that the measured waves have some sensitivity to the friction, the effect is small for the range of frictional values encountered during the experiment. In addition, simulations have been performed to aid in the experimental design, and show that future experiments on vanadium should increase the velocity of the transverse wave by nearly an order of magnitude, which will allow for a more accurate measurement.

Related References

1. Remington, *et al., Mat. Sci. and Tech.*, **22**, p. 474, 2006.
2. Follansbee, P. S., and U. F. Kocks, *Acta Metall.*, **36**, p. 81, 1988.
3. Nguyen, J. H., D. Orlikowski, F. H. Streitz, N. C. Holmes, and J. A. Moriarty, *AIP Proceedings*, **706**, p. 1225, 2004.
4. Clifton, R. J., and R. W. Klopp, *ASM Handbook 9th ed.*, **8**, p. 230, 1985.

FY2009 Proposed Work

In FY2009 we plan to continue experiments on vanadium, which will give us a higher velocity signal, at both low and moderate pressures. In addition we will continue to develop high strength graded density impactors for use with these higher strength materials. We also plan on using the strength data to begin refining and developing strength models.

Advanced Composite Modeling Capabilities for ALE3D

Michael J. King
(925) 422-0627
king74@llnl.gov

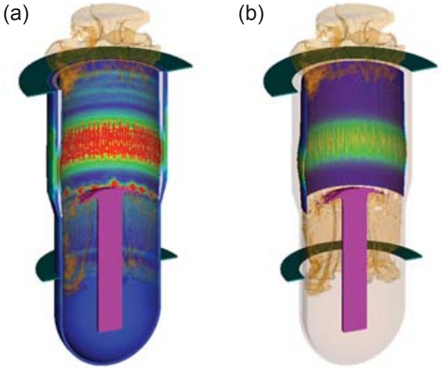

Figure 1. Simulation of explosive detonation inside conceptual magazine with alternating layers of composite and steel: (a) damage and failure of inner composite lining; (b) plastic strain in steel.

Composite structures are increasingly being used in both advanced weapon and armor systems. We had previously implemented several composite material models in ALE3D (a 3-D arbitrary Lagrangain-Eulerian multi-physics code created at LLNL) by porting existing constitutive models from DYNA3D (an explicit 3-D structural dynamics code also created at LLNL). This year, we extended our composite modeling capabilities by adding more realistic failure responses to the models, implementing strain-driven progressive damage, and creating tools for estimating homogenized composite material properties and optimizing pressure vessel design. Experiments were used to characterize composite material properties and to validate the new model capabilities.

Project Goals

Our goal is to be able to efficiently model composite materials under a wide variety of loading conditions, including large and/or high-velocity deformations. Specific goals include:

1. capturing the failure modes specific to different types of composites with different layups, such as fiber breakage, fiber buckling, and through-thickness crush;
2. modeling states of partial damage, and allowing damage to occur progressively within an ALE framework;
3. capturing the damage to individual plys;
4. capturing the layup-dependent response to local bending; and
5. incorporating thermally-driven or thermally-assisted damage.

In addition, we require experimental characterization of composite material properties, tools for rapidly estimating appropriate properties when they cannot be measured, and experimental validation of our models.

Relevance to LLNL Mission

Modeling composite structures before and after failure is necessary in many LLNL programs. Applications include composite munitions; magazines, damage containment, and insensitive

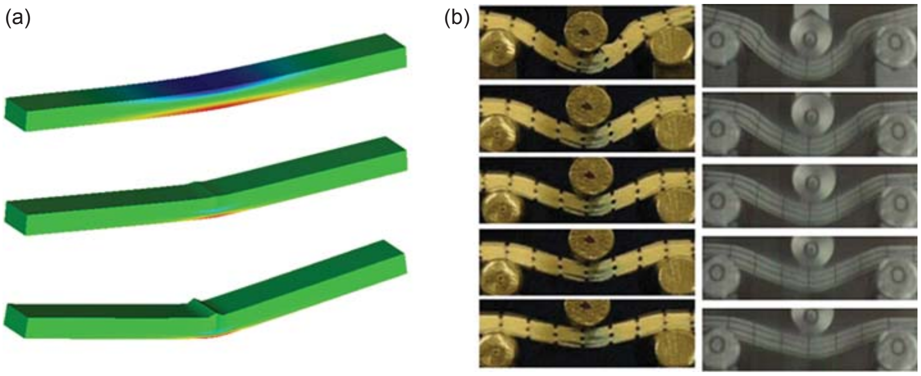

Figure 2. Three-point bend tests to measure the out-of-plane response of Dyneema armor panels: (a) in-plane stress contours predicted by simulations with fiber buckling failure mode enabled; (b) time sequence photographs of experiments at different speeds.

munitions; pressure vessels; rocket motors; and armors. The work done to date has directly supported various efforts within the DoD Joint Munitions Program (including the Focused Lethality Munition and Blast-Induced Traumatic Brain Injury Programs), TraVuls (HOPS) work for DHS, and work for others such as armor for ARL and magazines for Northrop-Grumman. By extending our modeling capabilities to composites, we have enhanced LLNL's core competency in simulation of engineering structures under extreme loading conditions.

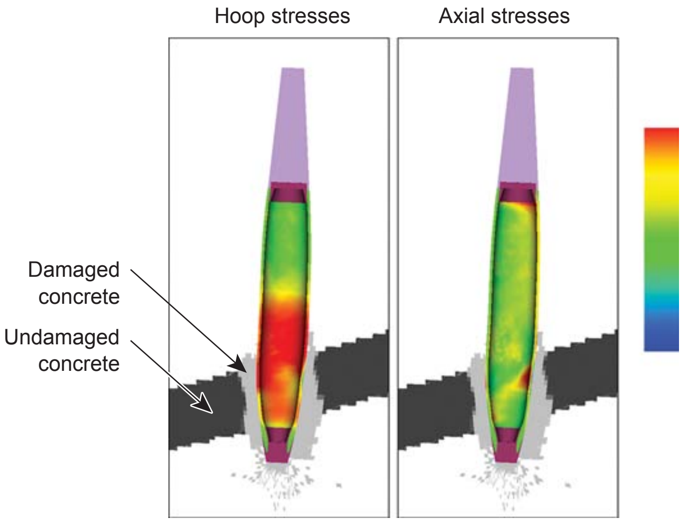

Figure 3. Simulations of a composite-cased focused lethality version of the Mk82 bomb impacting a concrete wall. Damage to both the concrete and the bomb casing is predicted.

FY2008 Accomplishments and Results

At the start of FY2008, only basic composite models with specialized failure formulations were available. These models were not applicable to a wide enough range of materials, and were not robust enough to give accurate results when the advection capabilities of ALE3D were used. We implemented several alternative damage formulations to better represent the response of bidirectional composites and composites with a wide range of ply orientations. Implementing a progressive damage model improved accuracy and made the models more robust in the presence of advection, especially in high loading rate scenarios such as armor impacts. We also created a model that can account for progressive damage to specific plies of a multiply layup.

In conjunction with these new capabilities, we conducted a wide range of experiments on various composite materials, including carbon fiber-epoxy composites and high molecular weight polymer composites. We also leveraged experimental data from other programs and from outside partners. Some experiments were used to characterize the material behavior and create material property sets that can be used in future analyses. Other experiments were used to validate the models and identify aspects that required improvement.

Finally, we supported the creation of other tools for composite study, including composite pressure vessel tools using the commercial code ANSYS, and a composite homogenization tool for quickly estimating homogenized properties given the composite's layup and the properties of its component materials.

Figures 1 through 4 illustrate some of our results.

Related References

1. Chang, F., and K. Chang, "A Progressive Damage Model for Laminated Composites Containing Stress Concentrations," *Journal of Composite Materials*, **21**, pp. 831–855, 1987.
2. Christensen, R., and E. Zywicz, "A Three-Dimensional Constitutive Theory for Fiber Composite Laminates," *Journal of Applied Mechanics*, **57**, pp. 948–955, 1990.
3. Christensen, R., "The Numbers of Elastic Properties and Failure Parameters for Fiber Composites," *Transactions of the ASME: Journal of Engineering Materials and Technology*, **120**, pp. 110–113, 1998.
4. Hashin, Z., "Failure Criteria for Unidirectional Fiber Composites," *Journal of Applied Mechanics*, **47**, pp. 239–334, 1980.
5. Holzapfel, G. A., Nonlinear Solid Mechanics: A Continuum Approach for Engineering, John Wiley & Sons, Chichester, England, 2001.

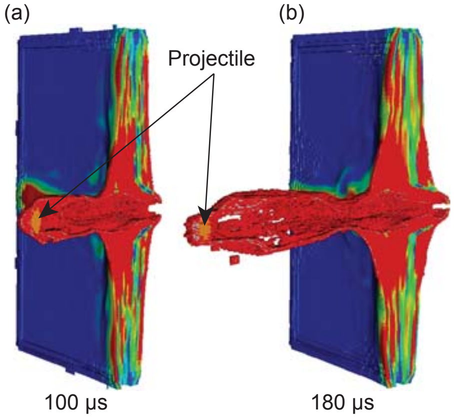

Figure 4. Simulation of hypervelocity projectile penetrating a Dyneema armor panel at (a) 100 and (b) 180 μs after impact. Colors show the degree of delamination.

FY2009 Proposed Work

Our proposed work for FY2009 will focus on three areas. First, we plan to generalize the formulation to account for finite strains. Second, we plan to acquire the capability to accurately capture the ply-specific local bending response of the composite, which would enable more efficient models with larger elements. Third, we plan to implement thermally driven and thermally assisted damage mechanisms, to account for cases when the composite is damaged by a thermo-mechanical load.

Fast Running Tools for Explosions in Urban Environments

Chad R. Noble
(925) 422-3057
noble9@llnl.gov

Many of the "fast-running" blast effects tools available to date are computational algorithms with lookup table techniques to use the vast array of empirical data in the open literature on blast effects of structures and their individual components. For example, ConWep or TM5-1300, are DoD manuals that exist for obtaining peak overpressures at various standoffs and explosive amounts. These overpressures can then be cross-referenced against other empirical datasets to determine the damage to various structural components, such as columns or windows. The goal of this project is to investigate the utility of "fast-running" hydrocode and structural models and how these may be developed and used to augment or improve existing tools.

Project Goals

Our objective is to determine the feasibility of a rapid blast-structure analysis approach using blast pressures obtained from ALE3D or blast manuals (ConWep/TM5-1300), simplified engineering building models to determine the effects of those pressures on that building or structural component, and empirical data for structural damage. We then determine the probability of damage using advanced statistical learning techniques such as mixture modeling and/or sequential importance sampling.

Relevance to LLNL Mission

Blast effects engineers are attempting to develop their own fast-running tools for the purpose of selling them to government and private industry. The proposed LLNL-developed fast-running tool has the potential to be much better because of the state-of-the-art finite element tools (such as ALE3D and DYNA3D), advanced stochastic techniques that reduce the number of realizations necessary for a convergent lookup table, and the powerful computers at our disposal for lookup table population. Federal entities within DoD, DHS, TSA, and FEMA have need of such tools.

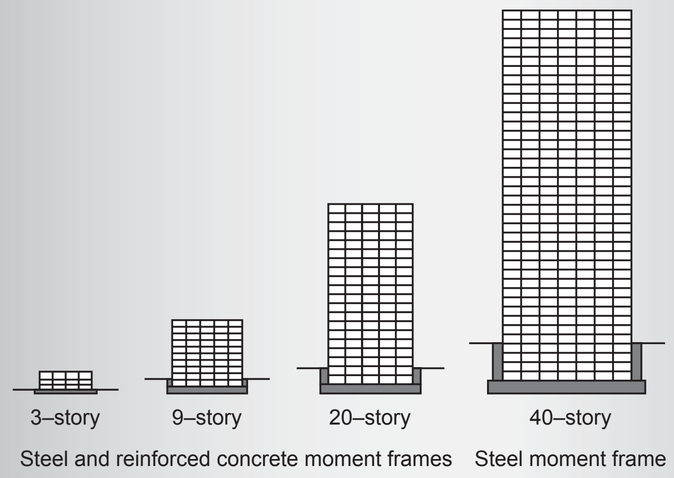

Figure 1. Schematic views of structures used in the study.

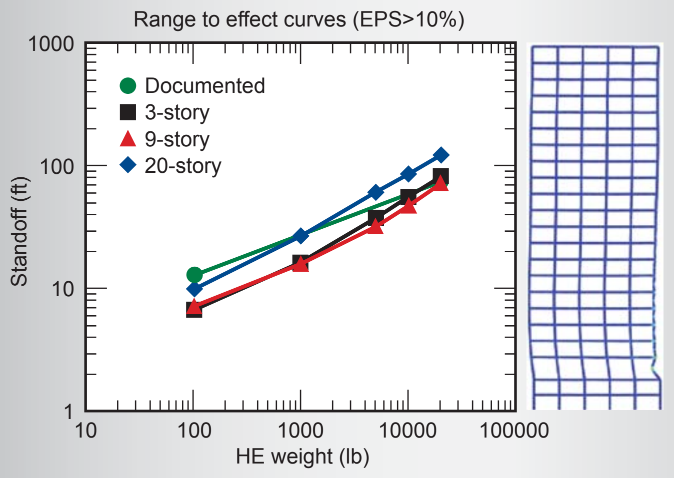

Figure 2. Range to effect curves for 3-, 9-, and 20-story steel moment frame building designs compared to documented empirical data. On the right is an example blast analysis of the 2-D 20-story structural model.

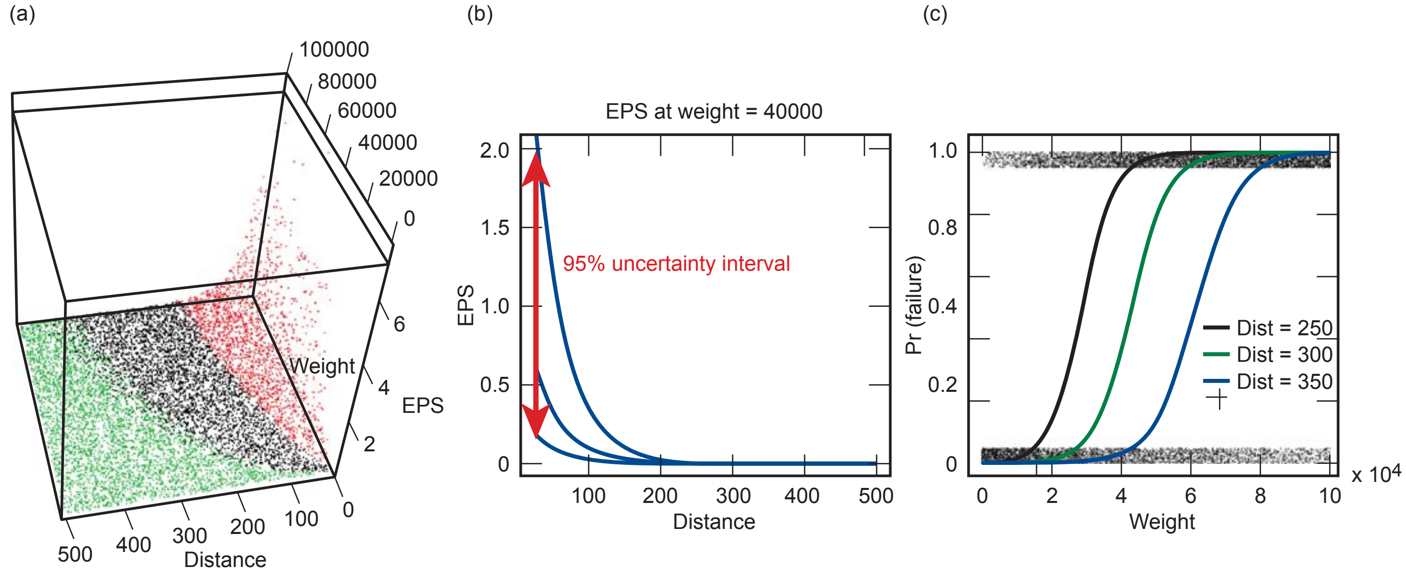

Figure 3. (a) Graph of 10,000 simulation results with green, black, and red points representing no damage, moderate damage, and severe damage, respectively; (b) EPS as a function of weight showing 95% uncertainty interval; (c) logistic curves showing probability of experiencing yielding or worse (EPS_{MAX}>0.1%) as functions of charge weight for specific values of distance.

FY2008 Accomplishments and Results

The canonical building models used for this effort were initially developed and designed at UC Berkeley for the Southern Nevada Ground Motion and Infrastructure Response Project at LLNL. The buildings had 3, 9, 20, and 40 stories representing low, medium, and high-rise office and residential buildings.

The linear elastic 2-D steel moment frame building models developed for the Southern Nevada Project were improved upon for this effort. The improvements included: developing the models for use in DYNA3D and NIKE3D; adding material nonlinearities; and adding the capability for the models to use Kingery and Bulmash equations to determine the blast loads on the structure.

In addition to modifying the 3-, 9-, 20-, and 40-story steel moment frame models (Fig. 1), a 3-D version of the 3-story building was developed for comparison with the 2-D model. The wall time to perform a blast analysis using these simplified beam element models is approximately 30 s for the 3-story structure to 3 min for the 20-story structure.

Multiple methods for applying the 3-D blast pressures to the 2-D models were studied. The results from the various methods were compared against empirical and historical data to determine the best method. Figure 2 shows the range to effect (charge weight versus standoff) comparison between the 3-, 9-, and 20-story building models and the empirical data.

After the building model validation, a stochastic analysis of the 3-story building model was performed. Our primary goal was to study the effects of charge weight and standoff on the resulting effective plastic strain (EPS) experienced by the structural elements. We generated 10,000 simulations varying the charge weight, standoff, yield stress, tangent modulus, and damping factor. Of primary interest were the variation and uncertainty of maximum EPS with the given sets of parameters. Maximum EPS was mapped (Fig. 3) into three categories of damage defined as follows: *no damage* (EPS_{max} < 0.1%); *minor to moderate damage* (0. 1% < EPS_{max} < 10%); and *severe damage* (EPS_{max} > 10%).

We used a logistic regression model to obtain probabilities of types of damage as functions of weight and standoff. Figure 3c shows a 1-D plot of the probability of "yield or worse" (EPS_{max} >0.1%) as a function of weight for three different values of standoff. Since a large fraction of EPS values are exactly zero we use a mixture model combining logistic regression for all data points and ordinary regression model for only positive EPS. The mixture model provides levels of confidence in the results, *e.g.*, in Figure 3b the 95% uncertainty interval on EPS_{max} decreases with distance for a particular charge weight.

As expected, other parameters (yield stress, tangent modulus, and damping factor) proved to have statistically insignificant effects on results compared to weight and standoff. It should be noted that Sequential Importance Sampling (SIS) can and should be used to reduce the number of realizations necessary to produce such response curves. For this, a user-defined "rare event" criterion will be needed, *e.g.*, search for onset of yield, EPS_{max} of 10% +/– d.

Related References

1. Gelman, A., J. B. Carlin, H. S. Stern, and D. B. Rubin, Bayesian Data Analysis, CRC Press, New York, New York, 2000.

2. James, J. W., T. M. Wood, E. M. Kruse, and J. D. Veatch, "Vehicle Bomb Blast Effects and Countermeasures," *35th Annual IEEE International Carnahan Conference on Security Technology*, October 16–19, 2001.

Arc Initiation Modeling for High Explosives

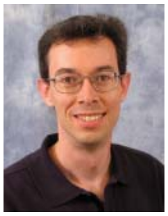

James F. McCarrick
(925) 423-8182
mccarrick1@llnl.gov

Initiation of high explosives (HE) by an electrical arc is a phenomenon with significant impact on the safety of both existing and future nuclear and conventional munitions. Previous work has shown that existing models of HE initiation do not apply to arc initiation and that existing safety-oriented testing of as-built components is insufficient to gain basic understanding. An experimental and modeling infrastructure has been successfully constructed to support a variety of existing and future programmatic efforts.

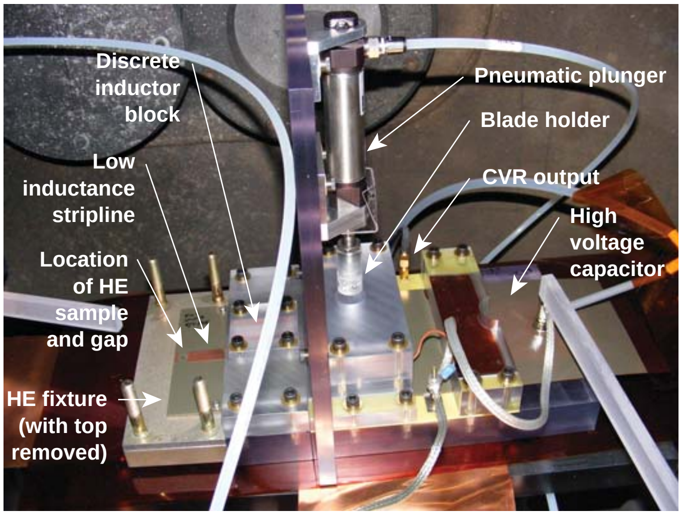

Figure 1. An assembled fireset, shown inside a shot tank. Features visible in this view, from left to right, include the gap in the stripline where the arc is created, the drop-in inductor block, the air-driven blade switch, and the high-voltage capacitor.

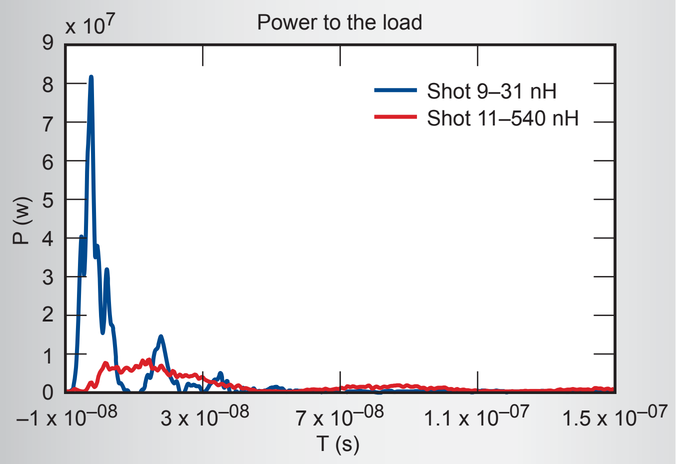

Figure 2. Measured power delivered to the load in high- and low-inductance configurations, at fixed source energy (720 pF and 32 kV).

Project Goals

The goals of this effort are first to construct an arc initiation testing infrastructure with a much broader set of controllable parameters, such as arc path length, air gap, and independently varied power and energy, and with time-resolved diagnostics integrated into the apparatus. A secondary goal is to create a simple modeling tool which allows rapid, flexible exploration of appropriate physics models for high-temperature HE kinetics, arc-to-HE energy transport, and equations of state (EOS), including coupling to output from the Cheetah chemical code.

Relevance to LLNL Mission

Arc initiation appears in multiple LLNL programs in the context of the safety of the existing stockpile, the configuration of future systems as part of the weapons transformation efforts, joint studies of HEs used in DoD munitions, and basic science supporting LLNL's role as an NNSA Center of Excellence for HE.

FY2008 Accomplishments and Results

On the experimental side, our major accomplishment is the creation of a fireset and associated testing protocol specifically for testing the response of HEs to electrical arcs. An assembled

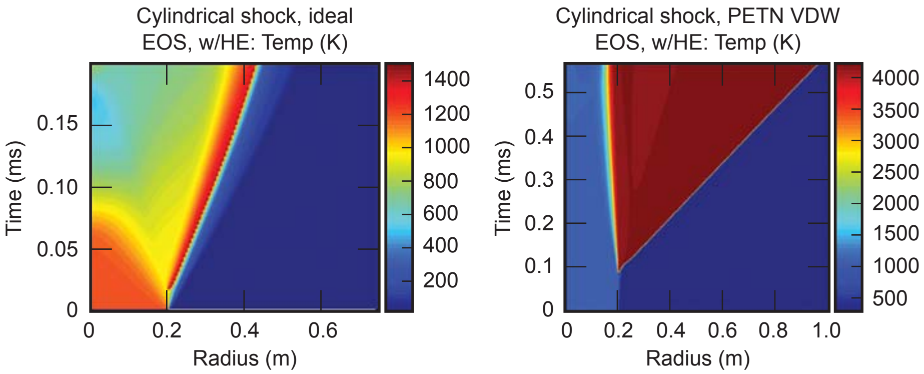

Figure 3. Temperature evolution from a simple MATLAB tool to study various combinations of HE kinetics, transport, and EOS models.

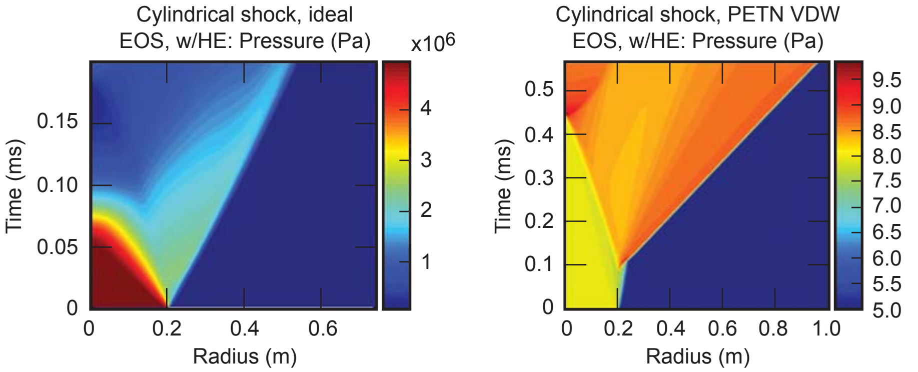

Figure 4. Pressure evolution for the same two cases depicted in Fig. 3.

fireset (with the HE fixture removed to show the gap) is shown in Fig. 1. The major characteristics include:

1. a set of easily swappable high-voltage capacitors, successfully operated at up to 35 kV;
2. a set of discrete drop-in inductors that allow independent variation of power and energy delivered to the load;
3. a knife switch and stripline coupling to the load, achieving a source impedance as low as 250 mΩ and 31 nH;
4. integrated diagnostics, including a foil-based current viewing resistor and a capacitive voltage probe that measure the current through and voltage across the arc.

Figure 2 shows how the power to the load is easily varied by an order of magnitude while keeping the total energy fixed. Operation in a fixed-power, variable-energy mode is also possible. This is key in characterizing arc initiation response thresholds, which are expected to show energy and power asymptotes analogous to the James criterion used for shock initiation thresholds. We have also successfully demonstrated batch testing in a single shot-tank purge cycle, allowing a significant increase in shot rate and project efficiency.

On the modeling side, we have created a MATLAB-based simulation tool with "plug and play" elements for the HE kinetics, energy transport models, and EOS. The tool is one-dimensional and easily switched between cylindrical and spherical limits. Prior work has established that the most unique aspect of arc initiation is the extremely high temperature, of order several eV, which is well beyond the range of validity for existing HE kinetics models. There have been promising recent advances in EOS for energetic materials. Therefore, the architecture of the tool was specifically chosen to allow these two aspects to be modified as ongoing studies produce new results; a particularly useful option for the EOS is incorporation of data produced by the Cheetah code.

Figures 3 and 4 show simulated pressure and temperatures for a cylindrical arc in an inert material (representing a surface track on a detonator header) surrounded by a PETN-like HE. The initial conditions are identical but the results change dramatically from subthreshold to detonation depending on choice of EOS.

Related References

1. James, H. R., "An Extension to the Critical Energy Criterion Used to Predict Shock Initiation Thresholds," *Propellants, Explosives, and Pyrotechnics*, **21**, pp. 8–13, 1996.
2. Glaesemann, K. R., and L. E. Fried, "Recent Advances in Modeling Hugoniots with Cheetah," *AIP Conference Proceedings*, **845**, 1, pp. 515–518, 2006.

Project Summary

We have successfully constructed, and tested a flexible fireset configuration with integrated diagnostics and the capability of delivering very high powers to the load. These firesets form a standardized testing infrastructure to study arc initiation of HE in various programmatic contexts. We have also created a simple modeling tool that will be used to explore the basic phenomena of arc initiation as new data and physical insight are obtained. These experimental and modeling tools have been transferred to ongoing and newly started programmatic efforts.

Applying MESA Epidemiological Model to Human Diseases

Matthew J. Dombroski
(925) 424-2433
dombroski2@llnl.gov

Although existing human epidemiological models are highly sophisticated and useful, they do not have the capability to assess the full distribution of epidemiological impacts from diseases since many of them are fixed point estimate input/output models. This study applies the Multi-Scale Epidemiologic Simulation and Analysis (MESA) system used for foreign animal diseases to assess consequences from a human disease outbreak in the United States.

The advantageous computational capabilities of the MESA system enable a broad array of extensive stochastic analyses of model runs. The methodology applied here divides census tract level data into different demographics. Analysis of a baseline influenza scenario indicated that one of the following outcomes will result: 1) the outbreak burns itself out before it has a chance to spread regionally; 2) the outbreak spreads regionally and lasts a relatively long time; or 3) the outbreak spreads through air travel and lasts a long time with unconstrained geography becoming a nationwide pandemic. These results are similar to historical trends in real-world influenza outbreaks.

Project Goals

The goal of this project was to apply the existing MESA model to human influenza and evaluate its capability to provide stochastic analysis output for a fixed set of input parameters. Relevant modeling literature was reviewed and components necessary for a nationwide epidemiological model were identified. Next, the MESA modeling approach was assessed and relevant databases on population, mixing behavior, and disease spread needed to instantiate the model were identified and gathered. Finally, the MESA model was applied by loading the relevant databases and assessing output.

Relevance to LLNL Mission

There is a need for an accurate and computationally efficient human epidemiological simulation model that incorporates detection events and countermeasures in a meaningful way. The model created in this study improves LLNL's competency in human epidemiology, which will help identify requirements for biological detection and countermeasure strategies to address this

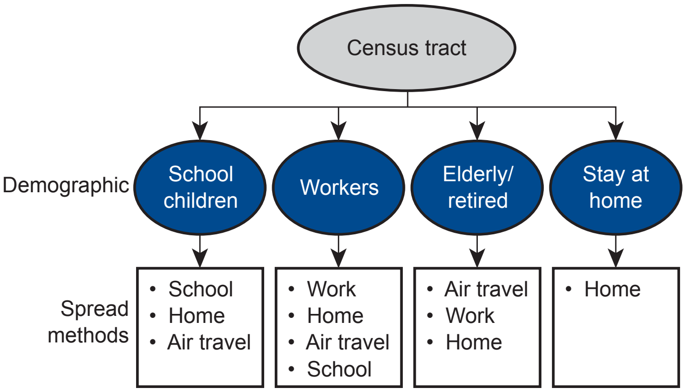

Figure 1. Breakdown of census tracts into four demographic variables and associated spread methods used for modeling human populations and disease spread using the MESA model.

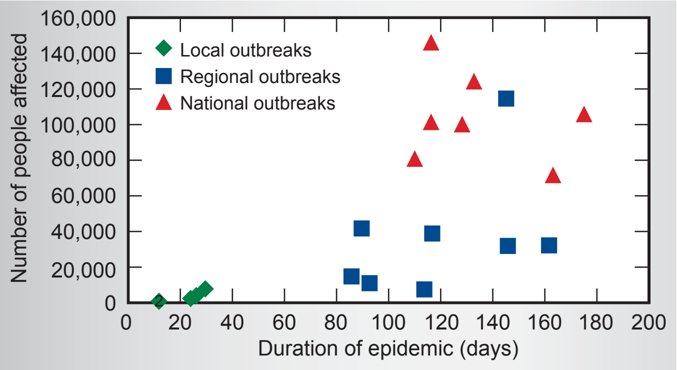

Figure 2. Number of people affected by the duration of the outbreak for 20 baseline scenario model runs.

threat. This capability will improve the Laboratory's planning and response capabilities for biological threats through improved inference and prediction.

FY2008 Accomplishments and Results

Different demographics in human populations are comparable to different herd types in the animal model. Therefore, US Census data at the census tract level were broken down into four overarching demographics (Fig. 1), including school aged children, work-force adults, retired/elderly persons, and stay-at-home individuals.

There are two spread models in MESA. The intra-facility model contains a basic SEIR model populated with influenza parameters used to simulate spread within a census tract and a specific demographic group. The inter-facility spread model is an agent-based model, which contains four different spread methods: schools, workplaces, households, and air travel. The air travel spread method was populated with airport boarding statistics for major airports, which enabled a gravitational model to probabilistically assign air traveler destinations.

To simulate a baseline scenario, an index case of an infected school child was placed in Queens, New York, and simple social distancing control measures were implemented after disease detection occurs. These control measures restricted school- and work-related contacts after disease confirmation and ultimately restricted air travel of infected persons. Twenty instances of the baseline scenario are shown in Fig. 2.

Outbreaks fell into one of three categories: those that spread locally, those that spread regionally, and those that spread nationally. Figure 3 displays the geographic extent of spread for each type of outbreak. Among local outbreaks, the disease burned itself out on its own. Among regional outbreaks, the disease adversely affected school children near the index case, but eventually control measures contained disease spread. Among national outbreaks, airline passengers enabled the disease to spread unnoticed far beyond the state of introduction.

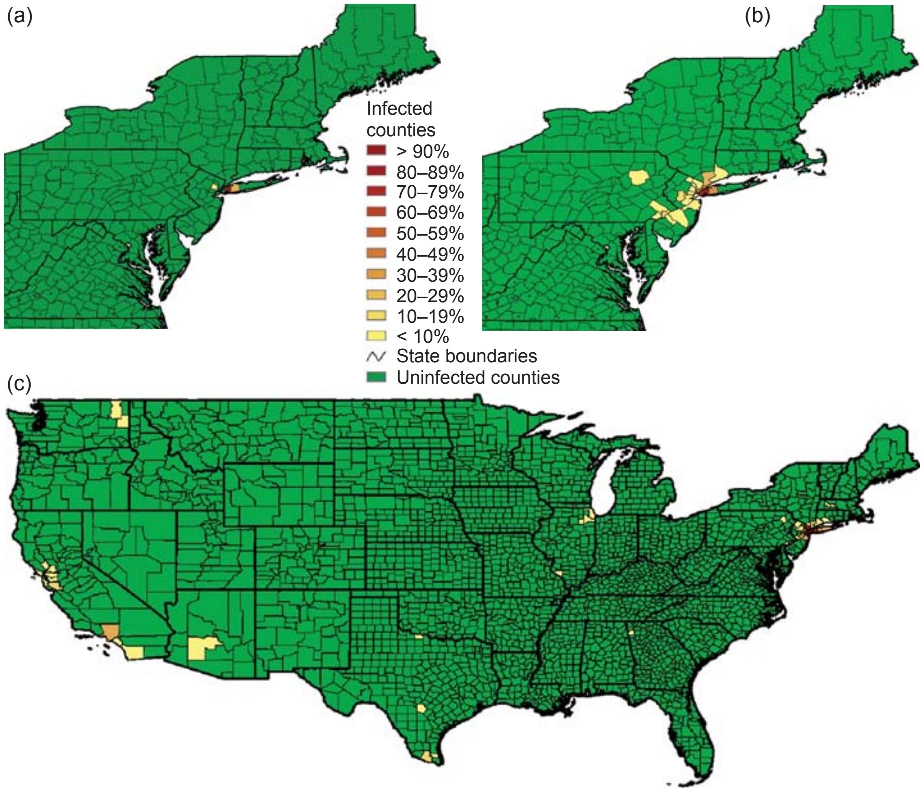

Figure 3. Geographic spread of each class of simulated outbreaks from the MESA model for (a) local outbreaks, (b) regional outbreaks, and (c) national outbreaks.

These results conform to CDC historical influenza data which show that the majority of influenza outbreaks are limited to local or regional outbreaks, but periodically a pandemic occurs if it spreads further and faster than control measures can monitor and contain it. The study has shown that scaling up regional models is not effective because of a wide range of complex variables that must be accounted for in a nationwide epidemic.

Related References

1. Germann, T. C., K. Kadau, I. M. Longini, and C. A. Macken, "Mitigation Strategies for Pandemic Influenza in the United States," *Proceedings of the National Academy of Sciences*, **103**, 15, pp. 5935–5940, 2006.
2. Melius, C., T. Bates, S. Hazlett, *et al.*, "MESA: Multi-Scale Epidemiologic Simulation and Analysis Decision Support System," *STEP Infectious Disease Modeling Conference*, March 23–24, 2006.
3. National Institute of General Medicine Sciences, Models of Infectious Disease Agent Study (MIDAS): http://www.nigms.nih.gov/Initiatives/MIDAS/, 2008.
4. Potter, C. W., "A History of Influenza," *Journal of Applied Microbiology*, **19**, pp. 572–579, 2001.

Mitigation of Electromagnetic Pulse Effects from Short-Pulse Lasers and Fusion Neutrons

Charles G. Brown, Jr.
(925) 423-4435
brown207@llnl.gov

Electromagnetic pulse (EMP) is a known issue for LLNL short-pulse laser facilities such as Vulcan, Titan, and Omega EP; therefore, EMP will be an issue with NIF/Advanced Radiographic Capability (ARC). ARC uses up to four of NIF's 192 beams in a short picosecond pulse mode to provide short-pulse, high-energy, x-ray backlighting. The NIF program has a research effort to better understand short-pulse laser EMP issues using experiments in Titan. This effort seeks to improve the fundamental EMP theory and analysis.

During FY2008, this project focused on improving simulation capabilities of EM fields due to electrons from laser/target interactions; providing post-processing algorithms and software; and analyzing measurements from dedicated shots on Titan.

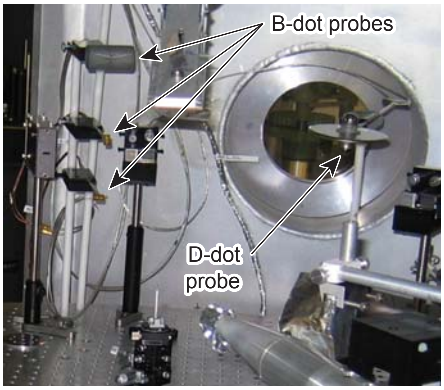

Figure 1. Interior of Titan showing some B- and D-dot probes for the 2008 dedicated shot series.

Project Goals

The overarching goal of this project is to simulate EMP in the Titan short-pulse laser due to electrons from laser/target interactions and to validate the simulation results with measurements. For simulations we use EMSolve, an LLNL EM solver. Unlike most available codes, EMSolve's architecture allows seamless integration of user-created sources and boundary conditions, and the developers have augmented EMSolve with electron beam sources. Validation of simulations is best accomplished by assisting the NIF team in the measurement process and by working with signal processing experts to calibrate and analyze the data.

Relevance to LLNL Mission

The National Ignition Campaign (NIC) will use NIF to demonstrate fusion in the laboratory. The ARC diagnostic is critical to the success of NIC and it is essential that the magnitude and the frequency dependence of EMP during ARC operation be understood so that appropriate mitigation techniques can be applied. An understanding of the EMP in Titan, through simulation and analysis in this project, can be extended to NIF and other short-pulse lasers around the world to better mitigate EMP effects.

FY2008 Accomplishments and Results

During FY2008, we assisted in dedicated shot measurements; continued

Figure 2. Zoomed view of EMSolve simulation of an electron beam pulse at 0.825 ns from leaving the target post. The pulse is Gaussian shaped with a 100-ps (full width at half maximum) duration and cosine-shaped transverse profile, with a 10˚ maximum axial angle from the direction of motion. The electron pulse is to the right of the target positioner, which is near the center of the image. The colored vectors represent the electric field, and the streamline tubes depict the magnetic field.

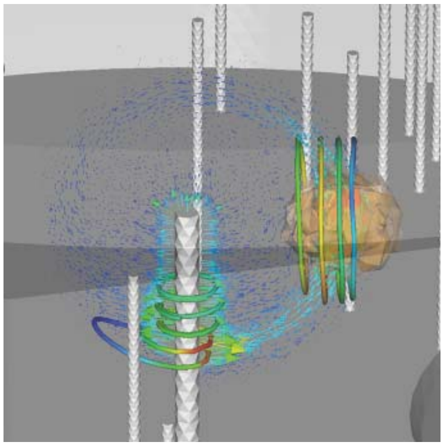

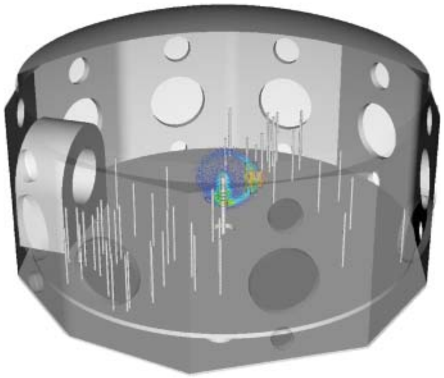

Figure 3. Figure 2 in context of a full view of the Titan laser chamber.

work in post-processing algorithms and software; began ongoing analyses of the dedicated shot measurements; further augmented EMSolve; and performed additional EMSolve simulations.

In particular:

1. We assisted the NIF team in documenting the 2007 dedicated shot series and aided in planning, execution, and documentation of the EM measurement portion of the 2008 dedicated shot series (Fig. 1) and helped analyze the resulting data.
2. We developed and implemented an adaptive filtering technique to reduce noise in measurements due to direct interaction of electrons and gamma rays with the probes, and also implemented automated processing to determine trends in the measurements.
3. We provided guidance in measurement planning and signal processing.
4. Our continued efforts to further augment EMSolve have resulted in development of a method for simulating late-time EM fields in lossy cavities using an eigenmode expansion. We have also implemented a particle-in-cell method for more faithfully simulating stiff electron beams (the electron motion is predetermined and not affected by the EM fields) in EMSolve (Figs. 2 through 5).

Earlier EMSolve simulations of Titan using a previous, less accurate method of simulating stiff electron beams and post-processed using VisIt, an LLNL code for visualizing simulation data, have received much attention.

Related References

1. Mead, M. J., *et al.*, “Electromagnetic Pulse Generation within a Petawatt Laser Target Chamber,” *Rev. Sci. Instr.*, **75**, pp. 4225–4227, 2004.

2. Brown, Jr., C. G., *et al.*, “Electromagnetic Pulses at Short-Pulse Laser Facilities,” *Journal of Physics: Conference Series*, **112**, 032025.

FY2009 Proposed Work

Our analysis, application to Titan and NIF, and the publication of our results will continue in FY2009.

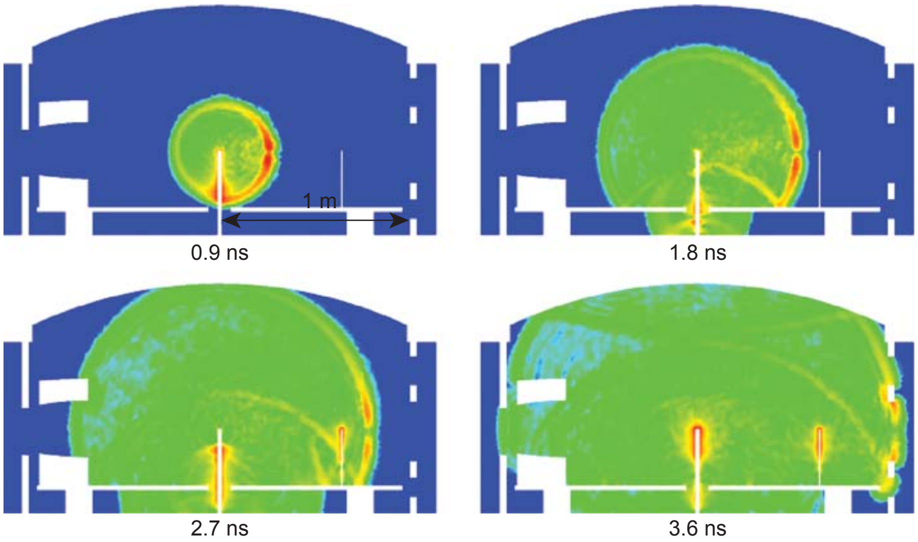

0.9 ns 1.8 ns

2.7 ns 3.6 ns

Figure 4. Vertical cross section through simulation in Figs. 2 and 3 for different time steps.

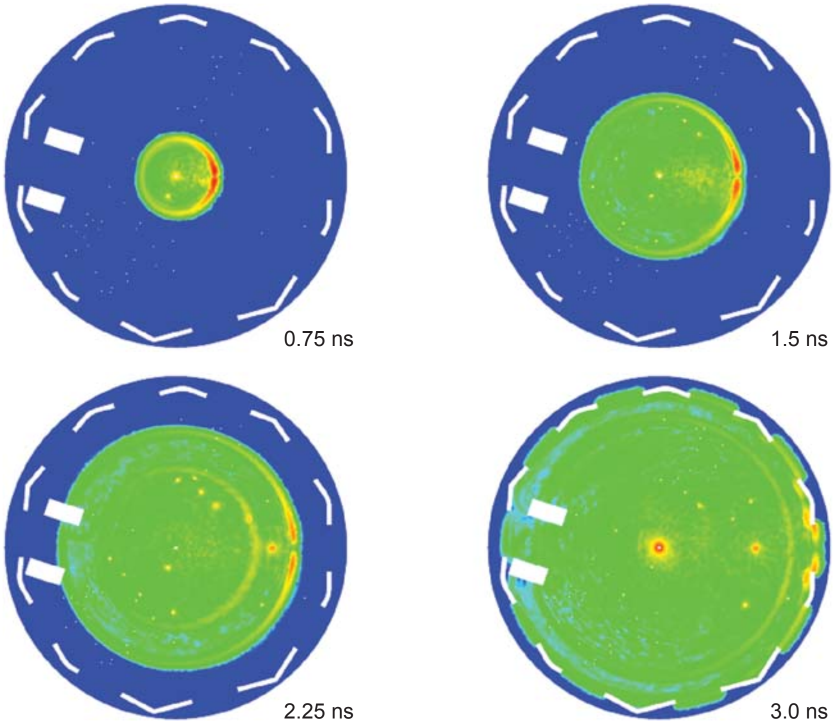
0.75 ns 1.5 ns

2.25 ns 3.0 ns

Figure 5. Horizontal cross section through simulation in Figs. 2 and 3 for different time steps.

Finite Element Analysis Visualization and Data Management

Bob Corey
(925) 423-3271
ircorey@llnl.gov

Support for and enhancement of several visualization and post processing tools are key components of our project. These tools include the Griz finite element visualization postprocessor, the Mili data management library, and a data file manipulation tool called Xmilics. These tools are used by analysts and engineers across LLNL to interpret data from a variety of simulation codes such as DYNA3D, ParaDyn, NIKE3D and Diablo. We also provide support in the area of data translation tools and processes for performing intra-code calculations.

Griz provides advanced 3-D visualization techniques and is our primary tool for visualizing finite element analysis results on 2- and 3-D unstructured grids. Mili is a high-level mesh I/O library intended to support computational analysis and postprocessing on unstructured meshes. It provides the primary data path between other LLNL analysis codes and Griz. Mili databases are also viewable with the LLNL VisIt postprocessor. Xmilics is a utility used to combine results from multiple processors that are generated by our large parallel computing platforms.

Project Goals

User support continues to be a high priority goal. The project provides on-going support for LLNL's visualization and postprocessing tools and

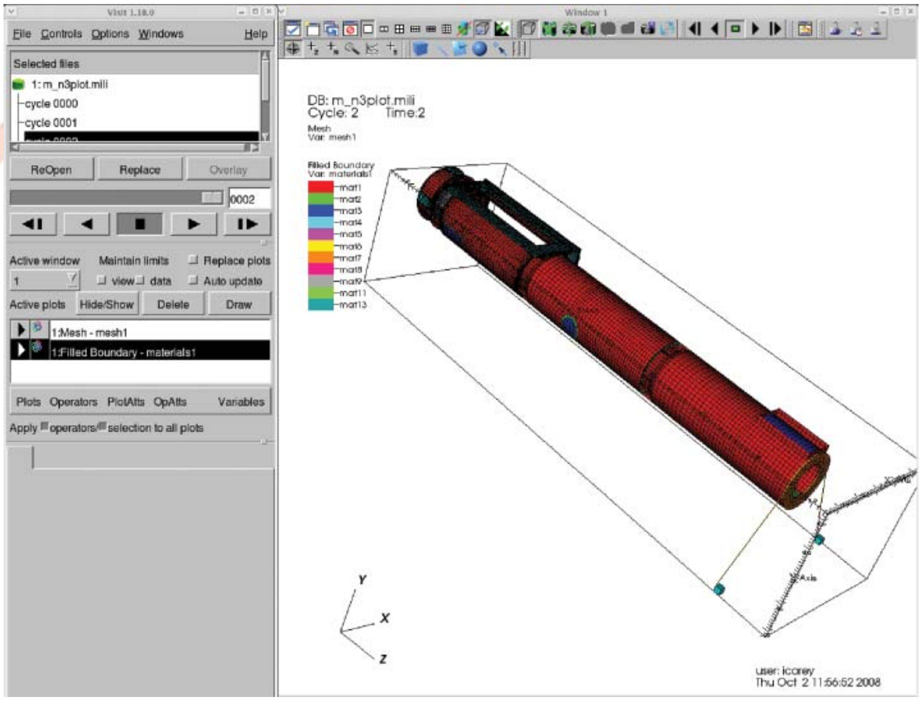

Figure 1. Engineering simulation results stored in a Mili database format as viewed in VisIt.

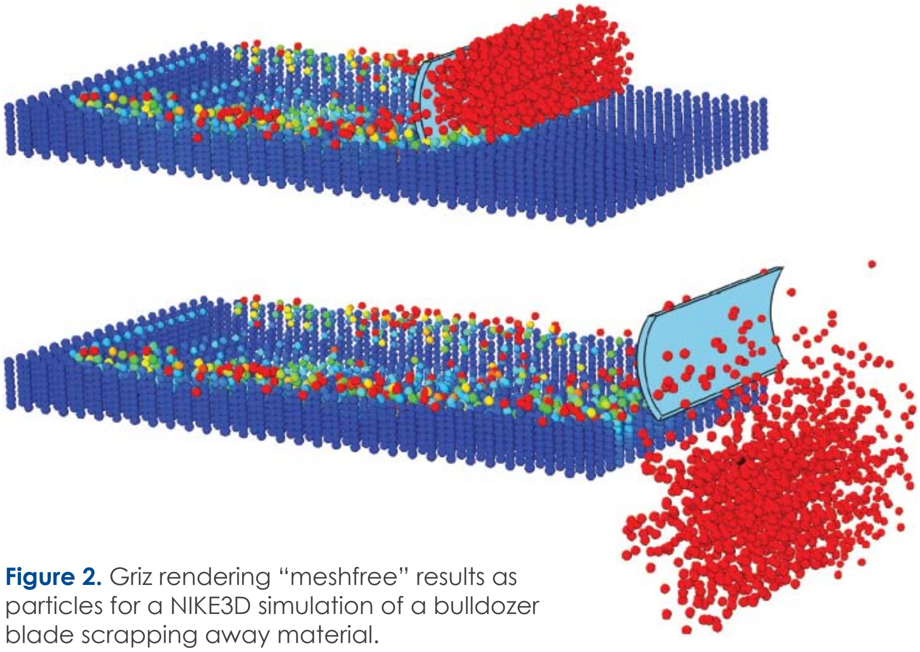

Figure 2. Griz rendering "meshfree" results as particles for a NIKE3D simulation of a bulldozer blade scrapping away material.

adds new capabilities to these tools to support evolving, multi-programmatic requirements.

Relevance to LLNL Mission

These postprocessing tools provide important user interfaces for our simulation capabilities and are critical elements in our tool suite. Without these, analysts would be severely limited in their ability to interpret the vast amounts of data generated by simulation and to synthesize key results.

FY2008 Accomplishments and Results

We are currently supporting approximately 30 to 40 active users on a variety of platforms across LLNL and some off-site users including Los Alamos National Laboratory and the Naval Surface Warfare Center, Indian Head Division. This year we saw a high level of usage and special requests from users supporting projects in LLNL's Weapons & Complex Integration, NIF, and Global Security.

We continued progress in migrating Mili to a modern file structure, namely Silo/HDF. The architecture is hierarchical with a separation between the Mili and Silo layers. Both new and legacy interfaces are maintained in one library to provide backward compatibility and reduce the migration impacts to our simulation codes. We completed the Silo I/O library and added a capability to read and write Overlink files. This is one example of ongoing efforts to integrate Mili database support directly into LLNL's parallel visualizer VisIt (Fig. 1).

We added a variety of new visualization features to Griz, with the most significant being: 1) enhanced strain rotation calculations for shell elements; 2) added support for computing rotations for beam elements; 3) batch support for most Livermore Computing platforms; 4) support for arbitrary labels across the entire postprocessing tool suite; and 5) additional improvements to support "meshfree" techniques (Fig. 2).

In response to an analyst request, we incorporated a generic error indicator metric into Griz. This leveraged past work in the Diablo code on adaptive mesh refinement. The algorithm, a basic Zienkiewicz-Zhu error estimator, identifies areas of the model where the solution field is changing rapidly across neighboring elements. When plotted on the screen, it provides feedback to the analyst as to where they may need to further refine their mesh.

Software quality engineering efforts continued to include the use of a commercial tool to create a baseline assessment of potential defects. We completed three baselines for Griz and identified/resolved over 300 issues using the latest version of *KlockWorks*. We performed a similar analysis for Mili and identified approximately 50 issues.

FY2009 Proposed Work

We will continue to provide support for our user base. Efforts targeted for next year include: 1) migration from Mili native format to Silo/HDF for our analysis codes; 2) delivery of an initial version of a Griz command interpreter for VisIt; and 3) deployment of end-to-end regression testing for code suites including Griz and Mili.

New Algorithm for Stiffness-Proportional Damping and Other Improvements in DYNA3D

Jerry I. Lin
(925) 423-0907
lin5@llnl.gov

DYNA3D is one of our main computational tools for the simulation and analysis of transient response of solids and structures to short-duration, impulsive loadings. This explicit finite element code was originally created to support defense programs, but over the years has evolved into a versatile tool for many other applications such as infrastructure vulnerability and protection, and vehicle structure assessment. DYNA3D is also the foundational mechanics code for the highly parallel ParaDyn simulation tool. This project funds the ongoing implementation of user-requested features, general technical support, documentation updates, and Software Quality Assurance (SQA) compliance for DYNA3D.

This project also supports the broader interagency DYNA3D activities through LLNL's Collaborator Program. The Collaborator Program grants selected users licensed access to LLNL's computational mechanics/thermal codes in exchange for their results and acknowledgement. These collaborative members include our sister laboratories, U.S. government agencies, and other institutions.

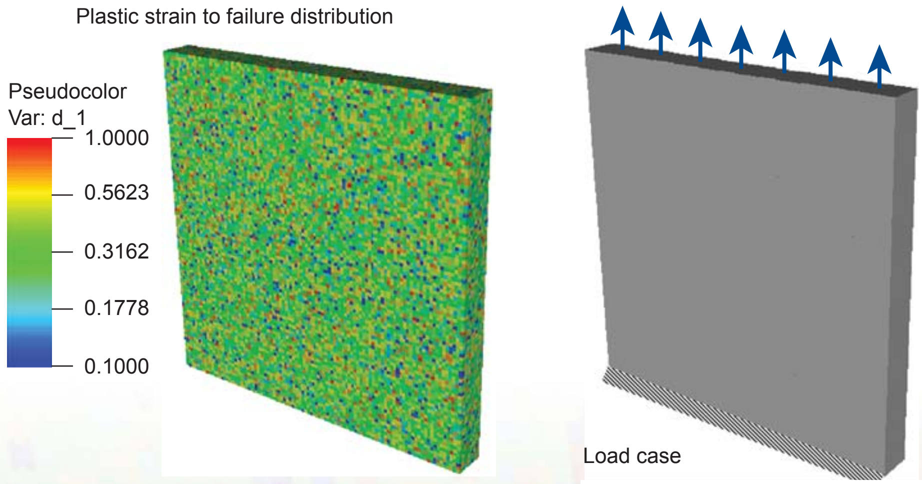

Figure 1. Plate of Johnson-Cook elastic-plastic material under uniform tension. The picture at left shows a material failure parameter with the Weibull Statistical Distribution.

Project Goals

The planned tasks include user support and code maintenance, implementation of new functionalities for program needs, enhancement of existing features, and continued compliance work on SQA and the Fortran 95 standard.

Relevance to LLNL Mission

The national security projects undertaken by Engineering on behalf of LLNL programs require robust simulation tools, expert technical support, and new functionalities. Other programs and projects involve the Laboratory's collaboration with other institutions and federal agencies, such as Los Alamos National Laboratory, the Naval Surface Warfare Center, Department of Homeland Security, Missile Defense Agency, US Army Corps of Engineers, Boeing, and selected universities.

FY2008 Accomplishments and Results

Many materials display significant variations in their properties and resulting response. Capturing such effects requires the introduction of random statistical distributions of material properties, but to be tractable, the analyst must have simple means of specifying a material characterization. A failure definition based upon a Weibull distribution is added to DYNA3D's Johnson-Cook elastic-plastic material model. Instead

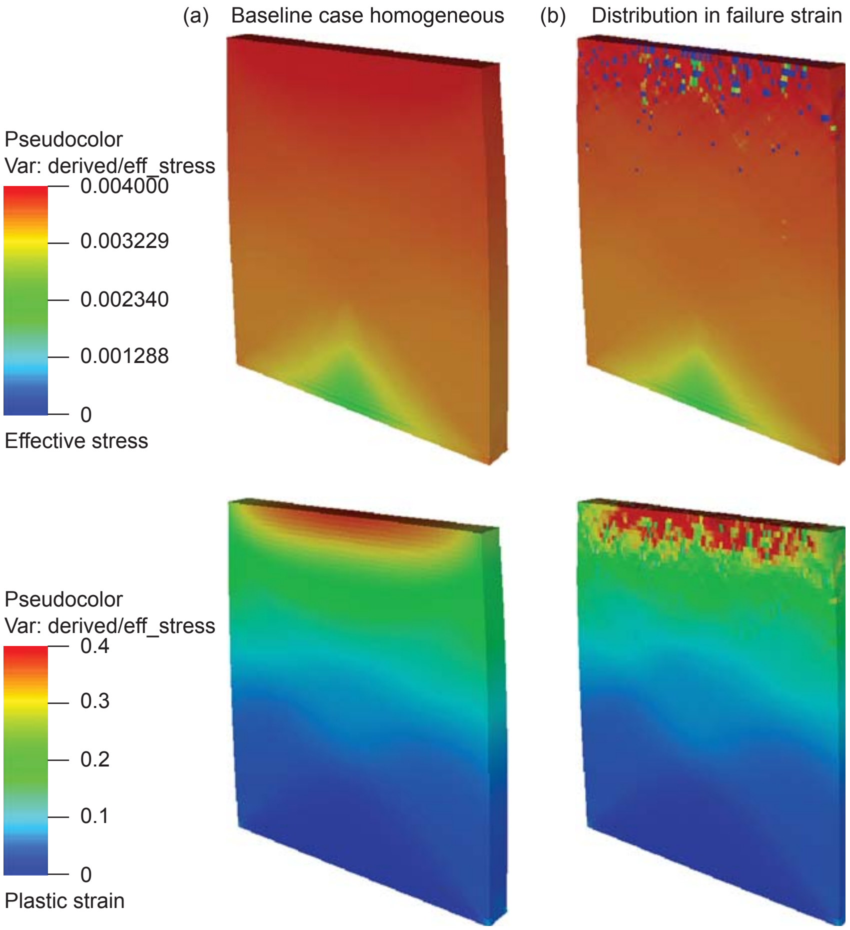

Figure 2. Stress and strain fields for (a) plate using a uniform material failure parameter, and (b) plate with a Weibull statistical distribution.

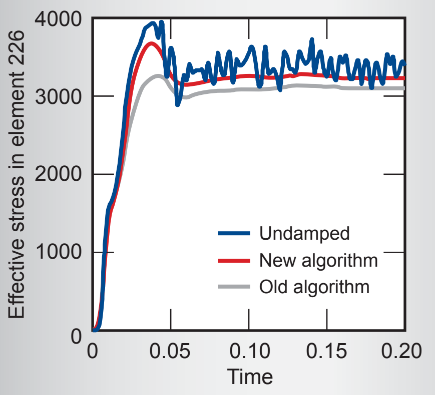

Figure 3. Comparison of the effective stress time history for one element in a block of elastic-plastic material subjected to a rapidly applied loading. The revised algorithm accounts for the yielding of the material, avoiding the excessive dissipation of the baseline method.

of a uniform failure criterion dictated by assumed material homogeneity, a more realistic failure pattern is realized with the new feature. The simple plate depicted in Fig. 1 shows a distribution of the failure parameter and its loading and boundary conditions. The more realistic spatial variation of material failure due to the distribution is compared to a homogeneous baseline in Fig. 2.

The Stiffness-Proportional Rayleigh Damping feature in DYNA3D has been an effective tool for filtering out under-resolved high-frequency responses and numerical “noise.” The baseline algorithm for this feature assumes an isotropic, linear material. The damping force is then derived from the largest of the material elastic moduli at a node, often leading to excessive damping once the material locally softens due to yielding. (Large directional variations of moduli in anisotropic materials can have similar effects.)

A new algorithm based on the material’s instantaneous stiffness is now implemented as an alternative. This algorithm yields a higher fidelity response for a user-specified fraction of critical damping at a given frequency. Figure 3 compares the response for a simple verification problem using old and new algorithms. As can be observed, the two algorithms yield virtually the same response in early time when the material is elastic, whereas the old algorithm creates excessive dissipation once the material yields.

FY2009 Proposed Work

User support for Laboratory projects, the addition of user-requested capabilities, the ongoing modernization toward Fortran 95 compatibility, and SQA-compliance work will continue. Functionality enhancements will include 1) the algorithmic implementation of a bi-phase foam model with gas transport and internal friction for the simulation of some elastomeric materials; and 2) the application of special numerical treatments, such as enhanced hourglass control and contact smoothing, to elements with faces that are part of a body’s external surface.

NIKE3D Code Maintenance and Enhancement

Michael A. Puso
(925) 422-8198
puso1@llnl.gov

The objective of this work is to enhance, maintain and support the implicit structural mechanics finite element code NIKE3D. New features are added to accommodate engineering analysis needs. Maintenance includes bug fixes and code porting to the various platforms available to engineering analysts. User support includes assisting analysts in model debugging and general analysis recommendations.

Project Goals

Code enhancement requires continuous interactions with users as well as new features to meet our evolving needs. Each year some activities are preplanned, *e.g.*, adding mortar contact/tying capabilities for shell elements. Other efforts arise in response to evolving needs. Such ‘just in time’ enhancements included adding a mid-step running restart capability as well as redundant running restart files to accommodate larger problems within the constraints of batch production job submittal.

Relevance to LLNL Mission

Assessment of structural integrity is one of the most important functions of LLNL’s Engineering and the in-house maintenance, support, and code enhancement are crucial for meeting analysis needs. NIKE3D, in particular, is a premier code for handling difficult nonlinear static structural analysis problems. It has the most diverse and robust contact algorithms at LLNL to capture the complex interactions of unbonded material interfaces.

FY2008 Accomplishments and Results

The mortar contact/tying algorithms added to NIKE3D in previous years have proven highly successful in solving many difficult production analyses. Most of these analysis models were composed solely of solid (*e.g.*, brick) finite elements and the original mortar contact implementation was capable of handling only such continuum elements. Often analysts wish to also use shell finite elements; the mortar contact algorithms were extended to accommodate these. This required small modifications to the contact search algorithm and calculation of contact penalties. The main work involved the modification of the gap calculation to handle shell thickness. For shell-on-shell contact, the contact gap at slave node A is now calculated in the following way:

$$g_A = \frac{\int_S N_A\left(x^s - x^m - 1/2\left(t^s + t^m\right)\right) dS}{\int_S N_A dS}$$

where S is the contacting surface, N_A is the slave node shape function, x^s and x^m are, respectively, the coordinates of the slave and master shell mid-surfaces, and t^s and t^m are, respectively, the thicknesses of the slave and master shells. The new mortar shell contact is much more robust compared to the node-on-segment shell contact, as demonstrated in Figs. 1 and 2.

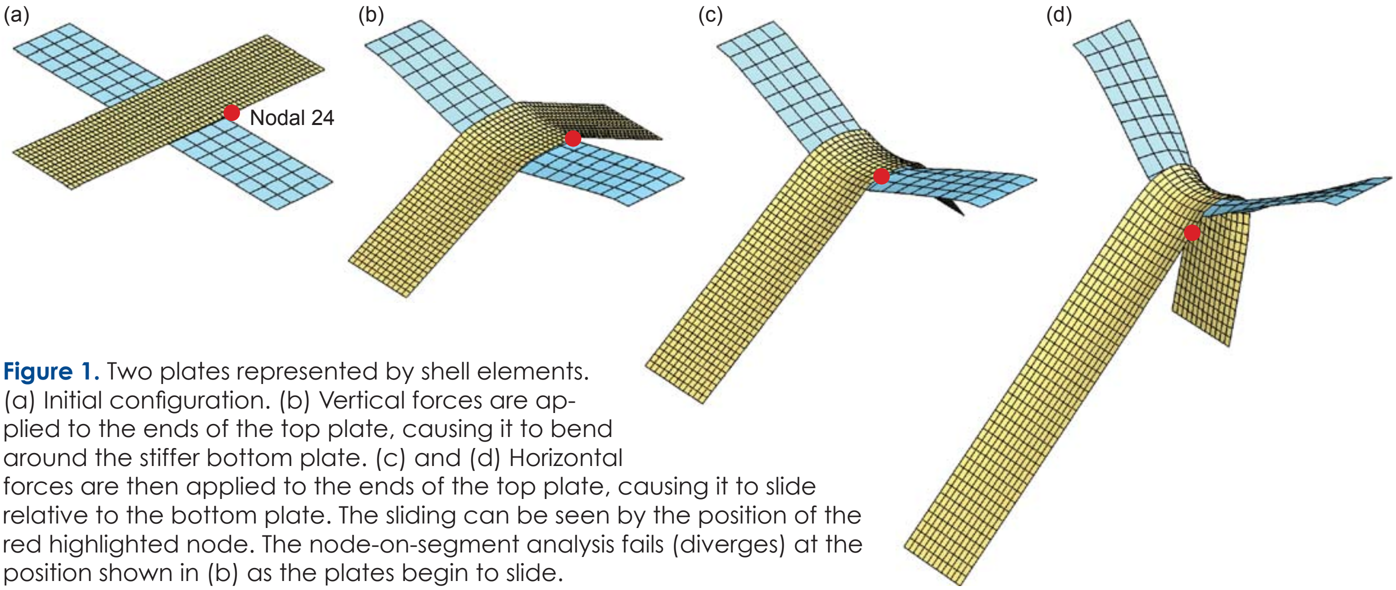

Figure 1. Two plates represented by shell elements. (a) Initial configuration. (b) Vertical forces are applied to the ends of the top plate, causing it to bend around the stiffer bottom plate. (c) and (d) Horizontal forces are then applied to the ends of the top plate, causing it to slide relative to the bottom plate. The sliding can be seen by the position of the red highlighted node. The node-on-segment analysis fails (diverges) at the position shown in (b) as the plates begin to slide.

The mortar contact algorithm in NIKE3D was ported into our new parallel thermo-mechanics code, Diablo, enhancing its contact capabilities. In addition, the primary set of NIKE3D nonlinear solver features were ported to Diablo. This included revisions to the BFGS quasi-Newton solver algorithm with linesearch, and the addition of a Broyden quasi-Newton solver algorithm. The new Diablo implementation was tested on a difficult set of the NIKE3D mortar contact verification problems. One of these problems was extended to a thermo-mechanical contact test problem. Figures 3 and 4, demonstrate the robustness of the new Diablo contact implementation, and the new behaviors to be captured through coupled thermal-mechanical simulation.

Related Reference

Amestoy, P. R., I. S. Duff, and C. Vomel, "Task Scheduling in an Asynchronous Distributed Memory Multifrontal Solver," *SIAM J. Matrix Anal. Appl.*, **25**, pp. 544–565, 2005.

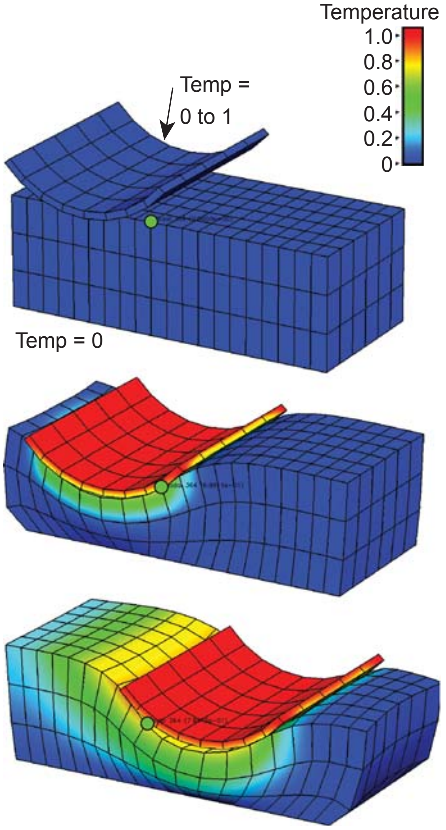

Figure 3. A coupled thermo-mechanical contact problem. The curved plate has an upper boundary condition where temperature T goes from 0 to 1 as it is displaced vertically. The upper plate temperature is held at T=1 as the plate is slid across. The thermal expansion of the block as it heats causes it to expand underneath the warmer plate. This in turn causes the highlighted green node to displace laterally from under the plate and then cool, as illustrated in the plot of Fig. 4. Expansion of nodes outside the contact surface causes the standard node-on-segment contact algorithms to fail for this problem, but is treated smoothly with the mortar contact algorithm, leading to its robustness.

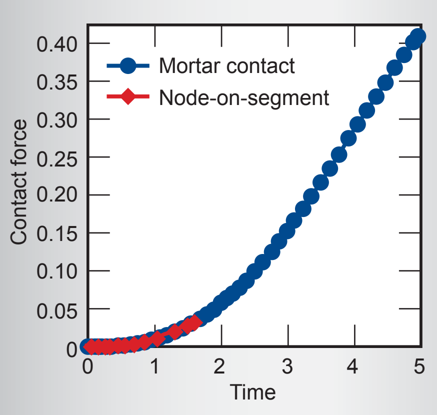

Figure 2. Contact force versus time (non-dimensional) between upper and lower plates in Fig 1. The node-on-segment results fail to converge early in the analysis.

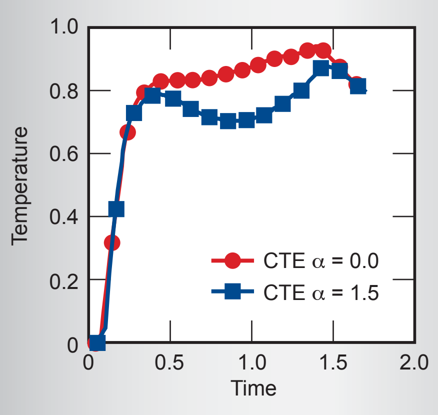

Figure 4. Temperature of the edge node highlighted in Fig. 3. With a nonzero coefficient of thermal expansion (CTE), the node displaces laterally from under the curved plate and then cools. With a CTE of zero, the block does not expand and remains under the curved plate where the temperature increases due to the transient thermal loading. The temperature curves merge at late time, corresponding to the plate sliding completely past the node.

FY2009 Proposed Work

Current mortar contact implementation uses the N^2 search algorithm. Better and faster search algorithms, *e.g.*, bucket sort, will be implemented in FY2009.

We will also undertake implementation of interior point method within a quasi-Newton framework for the solution of unilateral contact problems.

Electromagnetics Code Maintenance

Daniel A. White
(925) 422-9870
white37@llnl.gov

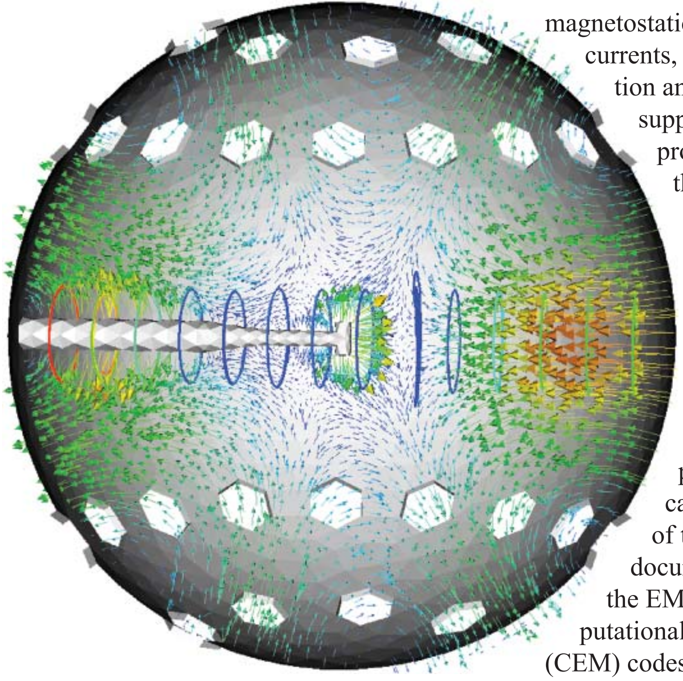

Figure 1. NIF target chamber electromagnetic eigenmode computed using EMSolve. The arrows denote the electric field; the contours denote the magnetic field.

LLNL Engineering's EMSolve code is a 3-D, parallel, finite element code for solving Maxwell's equations. EMSolve has modules for electrostatics, magnetostatics, eigenvalues, eddy currents, and wave propagation and has been used to support many LLNL programs, including the National Ignition Facility (NIF), Reliable Replacement Warhead (RRW), and Global Security. In addition, EMSolve results have appeared in approximately 30 peer-reviewed publications. The purpose of this effort is to verify, document, and maintain the EMSolve suite of computational electromagnetics (CEM) codes.

Project Goals

The goals for FY2008 were to:

1. Improve the configuration management, build process, and documentation of EMSolve. This will reduce the future costs of maintaining EMSolve and will enable deployment of EMSolve to DoD facilities.
2. Incorporate the latest available direct solvers and eigenvalue solvers into EMSolve.
3. Collaborate with Ohio State University (OSU) on fast domain-decomposition-based solvers for the frequency-domain Helmholtz equation. For linear narrow-band EM problems, analysis in the frequency-domain is the most accurate approach, but this results in a complex-valued Helmholtz equation that is computationally expensive to solve. Efficient algorithms for solution of the finite element Helmholtz equation is still an area of active study. Our goal is to incorporate the latest algorithms from OSU into EMSolve.

Relevance to LLNL Mission

EMSolve can perform EM analyses that cannot be performed by commercial codes. This allows LLNL to better support its programs. Having this advanced CEM capability allows LLNL to have a unique role when assisting with DOE and work-for-others projects. Increasing the accuracy and efficiency of our CEM codes will benefit all customers.

FY2008 Accomplishments and Results

Configuration management and documentation. EMSolve is a massively parallel, higher-order finite element code for CEM. The EMSolve code suite consists of 7971 separate files and over two million lines of code, not including external libraries. EMSolve uses 11 external libraries consisting of 20,361 files and over seven million lines of code in total. Hence, organizing the software and creating an easy-to-understand build process is essential to porting the code to new computers. We ported the code to the Mac OSX system for use by the Defense Threat Reduction Agency (DTRA).

In addition to improving the configuration management and build process we created documentation for new users. We also began documenting the plug-ins for material properties, sources, and boundary conditions using the Doxygen tool.

Eigenvalue solver. The EMSolve code suite has a module for computing EM eigenvalues (resonant frequencies) and eigenmodes of resonant cavity-like

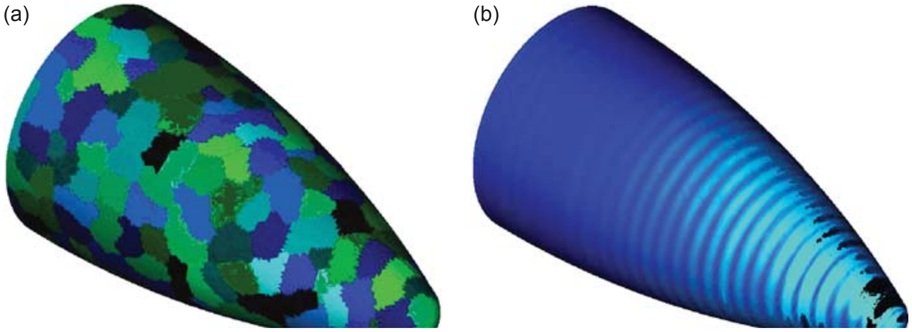

Figure 2. Example of a frequency-domain finite element analysis of a generic aircraft antenna system. The solution was computed using an Ohio State University non-overlapping domain decomposition preconditioner and represents a state-of-the-art calculation. Shown are (a) domain decomposition, and (b) computed electric field.

structures. We completed two enhancements to the eigenvalue solver this year. The first enhancement was to allow for complex eigenvalues, required for analysis of imperfect cavities with low Q-factors. As an example, Fig. 1 shows the twelfth lowest eigenmode of the NIF target chamber with open portholes. The second enhancement is a novel approach for combining a transient calculation with an eigenvalue calculation in order to accurately compute EM spectra.

Fast frequency domain solver. We continued to collaborate with OSU on the application of fast iterative solvers for the finite element frequency-domain Helmholtz equation. The resulting linear system is sparse, complex, non-Hermitian, and indefinite, hence standard fast methods such as multigrid cannot be applied.

Domain decomposition preconditioners are particularly well suited for large-scale parallel computing, the different domains being distributed amongst the processors with communication between domain boundaries. The key step in the domain decomposition preconditioner is in the transmission conditions that are enforced across domains. These conditions mimic the propagation of EM waves in free space. We performed numerous computational experiments to evaluate the approach.

As an application example, consider the generic aircraft antenna and radome system shown in Fig. 2. The antenna consists of 137 quarter-wave dipoles arranged in a disc; the radome consists of a conical body of revolution with dielectric of $\varepsilon = 3.0$. The computational mesh consisted of 1,993,853 tetrahedra, resulting in a linear system dimension of $n = 14{,}370{,}776$. The problem was partitioned into 500 domains. This problem required 125 iterations and 138 min for a tolerance of 10^{-2}.

As a second example, Fig. 3 shows a horn antenna array fed by a Rotman lens. The lens had a width of 12 λ and a length of 10.4 λ at the operating frequency. Sixteen input ports and 32 output ports are connected to micro-strip transmission lines, as shown in Fig. 3. The 32 outputs are then connected via coaxial cables of equal length to 32 horn antenna elements. The resulting geometry is quite complex, resulting in a computational mesh consisting of 2,847,778 tetrahedral elements. The resulting linear system size was $n = 17{,}153{,}388$. Using the domain decomposition preconditioner with 500 domains, the iterative solver required 150 iterations and 195 min for a tolerance of 10^{-2}.

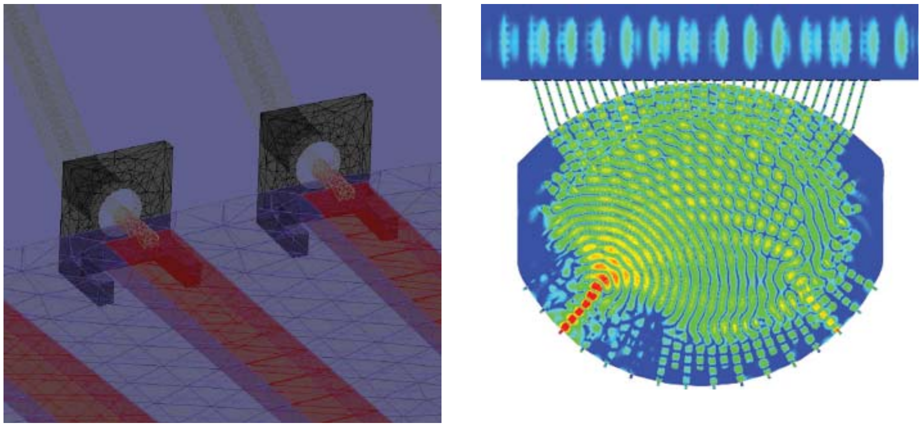

Figure 3. Finite element analysis of a Rotman lens phased array antenna. A zoom-in view of the geometry is shown in the left image. An example electric field pattern is shown in the right image. This calculation, with a linear system size of over 17 million, is well beyond what can be achieved with commercial or publicly available software.

Measurement Technologies

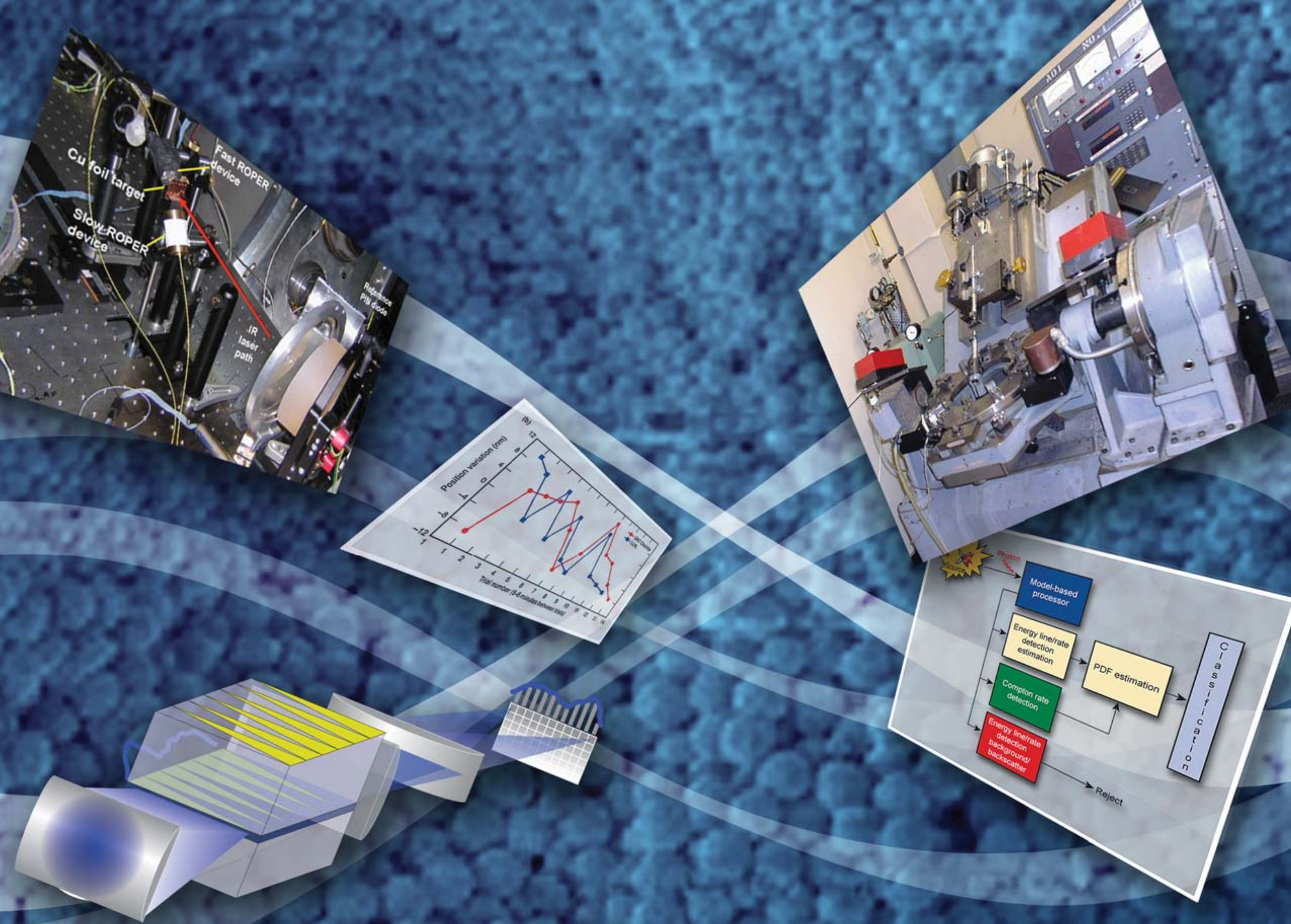

Detection, Classification, and Estimation of Radioactive Contraband from Uncertain, Low-Count Measurements

James V. Candy
(925) 422-8675
candy1@llnl.gov

The timely and accurate detection of nuclear contraband, whether it is located in a vehicle at a border crossing, a cargo container entering a port, or simply in luggage at an airport scanner is an extremely important problem of national security, especially in this era of constant terrorist activities. Radionuclide emissions from threat materials challenge both detection and measurement technologies to capture and record each event. The development of a Bayesian sequential processor that incorporates both the underlying physics of gamma-ray emissions and the measurement of photon energies offers a signal-processing and physics-based approach to attack this challenging problem. The inclusion of a basic radionuclide physics representation is used to extract the information available from the uncertain measurements. This approach leads to a "physics-based" structure that can be used to develop an effective detection technique and can be implemented using advanced signal processing methodologies such as sequential Monte Carlo processors or, equivalently, particle filters to enhance and extract the required information.

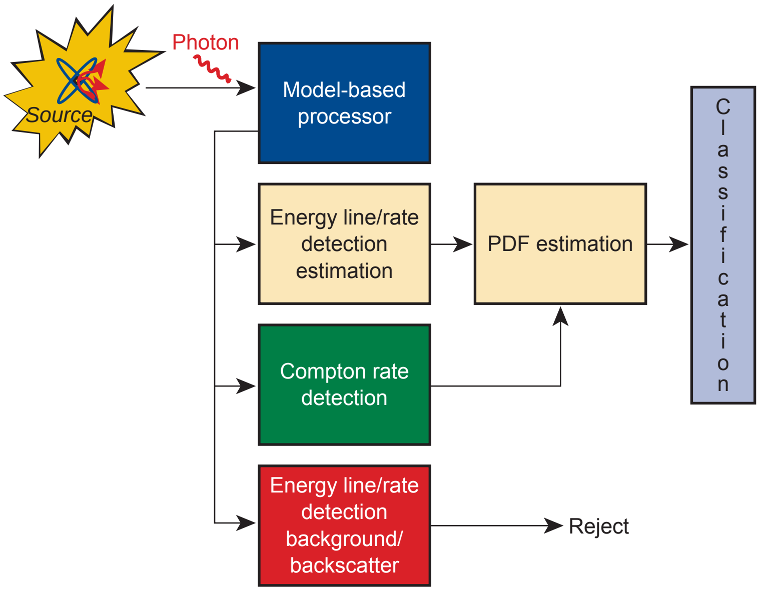

Figure 1. The Bayesian design shown (simply) as a photon-by-photon processor. We initially used a model-based (physics-based) processor to enhance the raw detector measurement while rejecting instrumentation noise and estimating the photopeaks through energy/rate discrimination, providing input to the probability density function (pdf) estimates. Compton photons are identified and extracted using a Bayesian processor to also provide information to the pdf estimator. Finally, background and backscatter photons are rejected. The estimated radionuclide pdfs are then used in a distributed physics-based classification scheme to detect and classify the threats.

Here we are focused on the detection, classification and estimation of illicit radioactive contraband from highly uncertain, low-count radionuclide measurements using a statistical approach based on Bayesian inference and physics-based signal processing.

Project Goals

We expect to develop the techniques to provide fast, reliable radiation detection methods capable of making a more rapid decision with higher confidence along with the ability to quantify performance as well as develop solutions for the detection, classification, and estimation of a moving radionuclide source and/or detector. Our goal is reliable detection (on the order of kilograms) of shielded Pu with a 95% detection probability at a 5% false alarm rate in less than a minute.

Relevance to LLNL Mission

The detection of illicit radionuclides is a top priority in furthering the national security mission of the Laboratory. Radionuclide detection, classification, and estimation are critical for detecting the

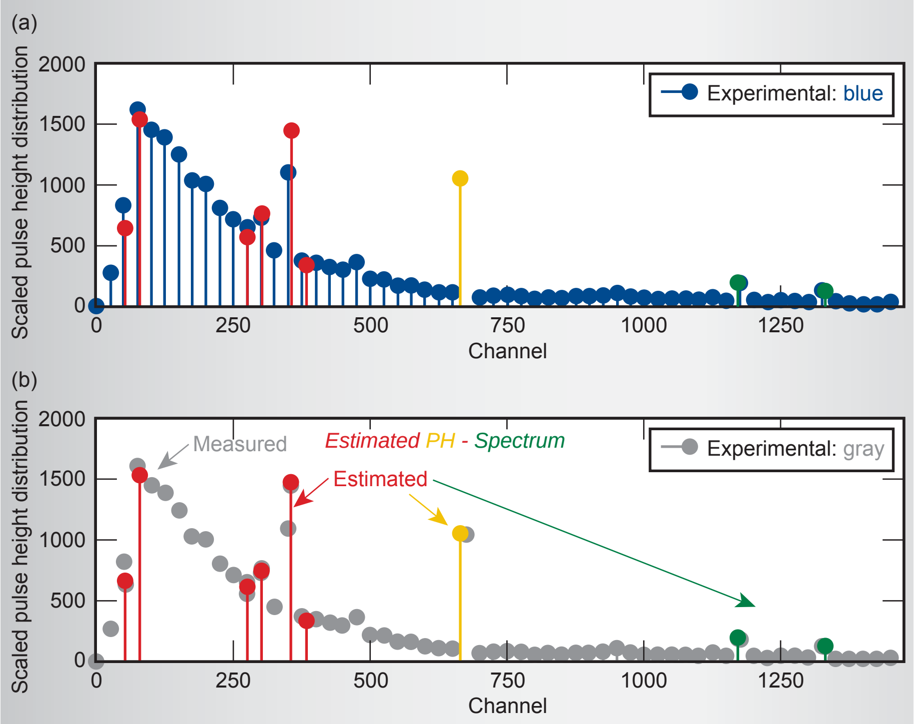

Figure 2. (a) Results of pulse height (PH) spectral estimation using a standard processing scheme (blue), compared to that of the Bayesian model-based processor (BMBP) (red). The detection is limited to photo-peak processing using the energy/rate discrimination described in Fig. 1. (b) The experimental data consists of three radionuclides: ^{133}Ba (6 energy lines, in red), ^{137}Cs (1 energy line, in yellow) and ^{60}Co (2 energy lines, in green). In (a) we see the standard PH processor output (blue) with the BMBP (red/yellow/green) along with the extraneous background noise. In (b) we see the same information simplified with the data as gray circles and the BMBP in red/yellow/green. Note the simple PH spectrum provided by the BMBP design.

transportation of radiological materials by terrorists, an important goal in both national and international security.

FY2008 Accomplishments and Results

Our FY2008 accomplishments included:

1. development of the full-physics simulation and validation on controlled experimental data;
2. development of a novel “point-to-point” signal processing model capable of being incorporated into a Bayesian processor to identify Compton scattered photons;
3. development and patenting of a distributed/parallel solution to the radionuclide “detection problem” (Fig. 1) capable of extension to moving sources;
4. development of a solid design for classification;
5. demonstration of feasibility of the approach by applying it to both simulated and controlled experimental data (Fig. 2);
6. completion of experimental runs for both germanium and sodium iodide detector materials; and
7. discussion of collaboration/licensing with potential industrial partners for implementation.

These results are quite promising and demonstrate the potential capability of the Bayesian model-based approach to solving a variety of radiation detection problems.

FY2009 Proposed Work

Our proposed work for FY2009 consists of incorporating more and more of the transport physics into the point-to-point Bayesian processor, enabling the “unraveling” of the Compton photons and providing more useful and timely information. We will apply the LLNL transport physics code COG to validate and refine our initial design concepts. We plan to execute a set of demonstration experiments towards the later part of the year.

Error Mapping and Automated Calibration of PrISMM

Jeremy J. Kroll
(925) 422-6437
kroll4@llnl.gov

LLNL can and should be the premier facility for hydrodynamic material fabrication and precision manufacturing/metrology of defense-related components, such as machining, part metrology, pin-dome assembly, and hydro assembly. Significant investments from various LLNL program sources have already been made. The future success of LLNL requires it to stand out above the other sites. The Precision Inspection Spherical Measuring Machine (PrISMM), shown in Fig. 1, will replace the current instrument used for part metrology, shown in Fig. 2, which is not only 40 years old, but is showing reproducibility error that is worse than tolerances needed for future defense-related work.

In this project, we will prepare PrISMM to be the primary shell-measuring machine at LLNL and potentially serve as a model for the entire nuclear weapons complex. This involves increasing its current accuracy through a modeling and compensation methodology, and automating measurement and mastering algorithms for operation by inspectors within LLNL's inspection shop. In its current state, PrISMM is degraded in accuracy due to incomplete error mapping and compensation. Also, the complexity of setting up and operating PrISMM precludes its use as a shop tool by members of the inspection shop. An important goal is to transition its operating procedure and control software for convenient use by shop personnel.

Project Goals

The goal is to produce a reliable and accurate shell-measuring tool for use by the inspection shop. A software compensation capability will be demonstrated as well as automated routines for probe

Figure 1. Precision Inspection Spherical Measuring Machine (PrISMM).

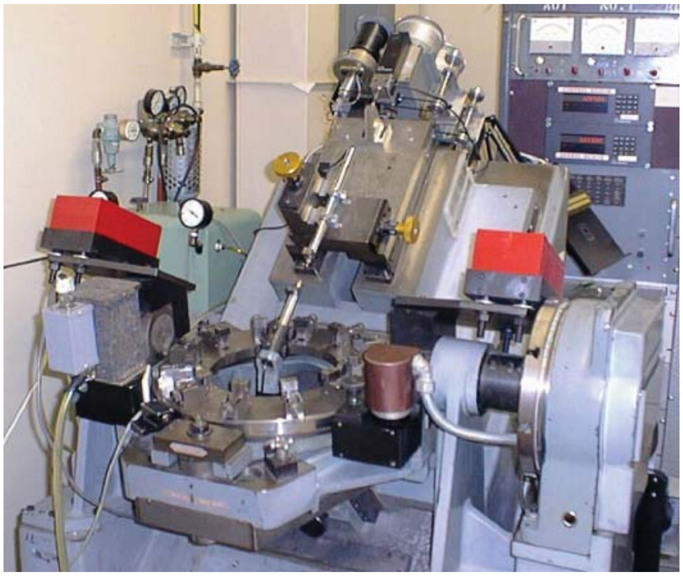

Figure 2. Rotary Contour Gage, the current spherical measuring machine.

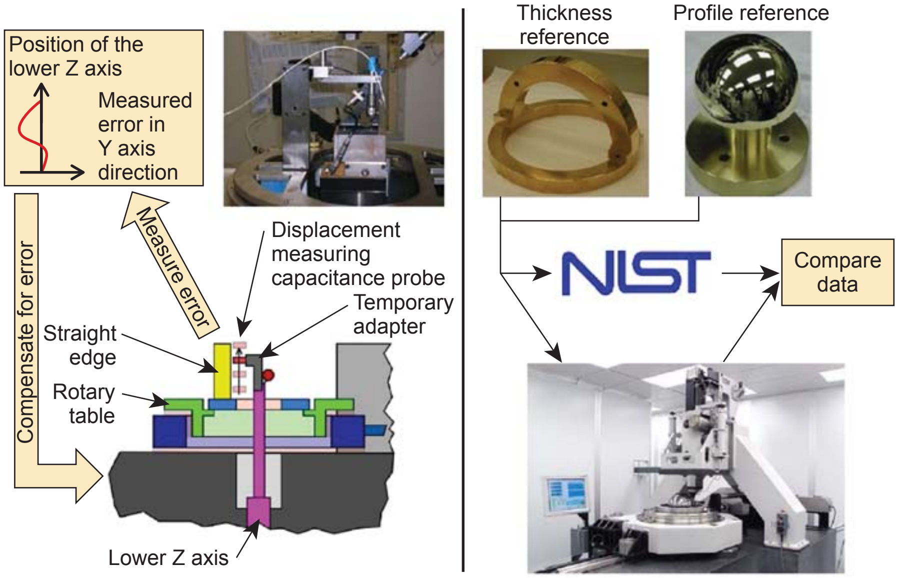

Figure 3. Software error compensation and validation using calibrated reference parts on PrISMM.

calibration. The final goal of this project is to transition the operation of PrISMM to the inspection shop staff. In this effort, a precision engineer will improve the accuracy and usability of PrISMM.

Relevance to LLNL Mission

The shell-measuring capability is a critical capability for support of defense-related work both at the Laboratory and nationally. This project aligns with LLNL's Measurement Technology focus area.

FY2008 Accomplishments and Results

Through a series of recent upgrades, including an upgrade of the laser position feedback system, PrISMM is now a reliable measuring machine. We did not have down time due to problems with the machine throughout FY2008. Figure 3 shows the error compensation methodology as well as methods for validation of this compensation. A procedure and software have been created for measurement and generation of compensation tables for the positioning, straightness, and squareness errors of the four axes. These procedures and software have been demonstrated and have shown that individual errors can be compensated down to the repeatability of the machine. PrISMM has successfully measured a standard spherical part, which was measured at the National Institute of Standards and Technology (NIST), to an accuracy of 1 µm.

Automated mastering routines have been created which will decrease the complexity and increase repeatability of machine setup. PrISMM mastering involves geometrically relating the upper Z probe to the lower Z probe. The calibrated test fixture, shown in Fig. 4, contains a precision sphere used for the mastering routine. The calibrated test sphere allows the determination of the spatial relation between the upper and lower probes, and facilitates measurements of probe radii and profile. An automated routine for finding the pole of the test sphere has been created and tested.

Related References

1. Blaedel, K. L., "Error Reduction in Technology of Machine Tools," *Technology of Machine Tools – Machine Tool Accuracy*, pp. 61–71, 1980.
2. PMAC Users Manual, Delta Tau Data Systems, Inc., Northridge, California.

Project Summary

An error compensation methodology has been created that can compensate axis errors to the repeatability of the machine. This process has been demonstrated and a standard part has been measured to an accuracy of 1 µm. Automated mastering routines have been created and have been partially implemented to decrease the complexity of machine setup. PrISMM is now a reliable and accurate metrology instrument for the measurement shells for current and future defense-related work.

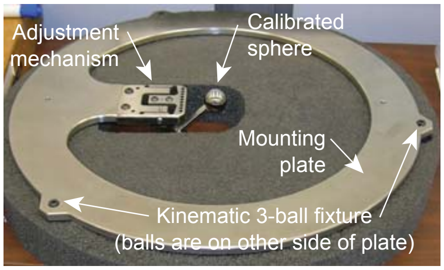

Figure 4. Master ball fixture used to calibrate the two measurement probes on PrISMM.

Standing Wave Probes for Micrometer-Scale Metrology

Richard M. Seugling
(925) 423-8525
seugling2@llnl.gov

In this project we are developing a low force, high-aspect-ratio, mechanical probe for the nondestructive characterization of manufactured components and assemblies. The key concept for the probe is the correlation between the dynamic response of an oscillating cantilever rod (probe) and the interaction of its tip with a surface. The applications for this probe begin with surface location, but may encompass the characterization of the material properties of the surface, and perhaps branch into the modification of the surface. This project is a collaborative effort between LLNL, the University of North Carolina at Charlotte (UNC-Charlotte) and an industrial partner, InsituTec Inc.

Project Goals

We plan to provide the scientific understanding of a low-force contact probe capable of being applied on a number of machine tools and metrology platforms with a characterized uncertainty based on the fundamental understanding of the probing process. The exit strategy includes continued collaboration with the UNC-Charlotte team, rigorous calibration efforts with the National Institute of Standards and Technology (NIST), engaging a commercial source of probing instruments, and the probe's practical application at LLNL and its vendors for target fabrication. A prototype instrument developed during this project will provide an exceptional platform for continual reduction-to-practice efforts.

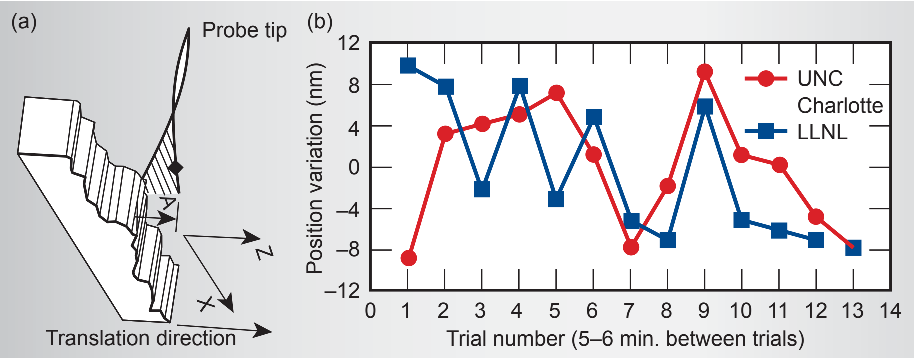

Figure 1. (a) Sample surface, stepped into contact with the probe tip using a precision motion stage (<1.0 nm resolution); (b) sensitivity/repeatability of contact location of probe systems at the ± 10 nm level.

Relevance to LLNL Mission

Currently, Inertial Confinement Fusion (ICF) and high-energy-density science (HEDS) targets comprise components with dimensions in the millimeter range, while having micrometer-scale, high-aspect-ratio functional features, including fill-tube holes and counterbores, hohlraum starburst patterns, and step-joint geometry on hemispherical targets. Future target designs will likely have additional challenging features. Variations in geometry from part to part can lead to functional limitations, such as limited flow rates during target filling, unpredictable instabilities during an ICF experiment, and the inability to assemble a target from poorly matched subcomponents. Adding to the complexity are the large number and variety of materials, components, and shapes that render any single metrology technique difficult to use with low uncertainty.

The near-term impact of this project is the expansion of LLNL's ability to accurately perform dimensional measurements of micrometer-scale features using a low-force, high-aspect-ratio probe system. The final goal of this work is to enhance LLNL's precision engineering capabilities, which encompass key core technologies supporting NIF, DNT, and nanofabrication.

FY2008 Accomplishments and Results

A prototype probe system, including upgraded electronics for increased

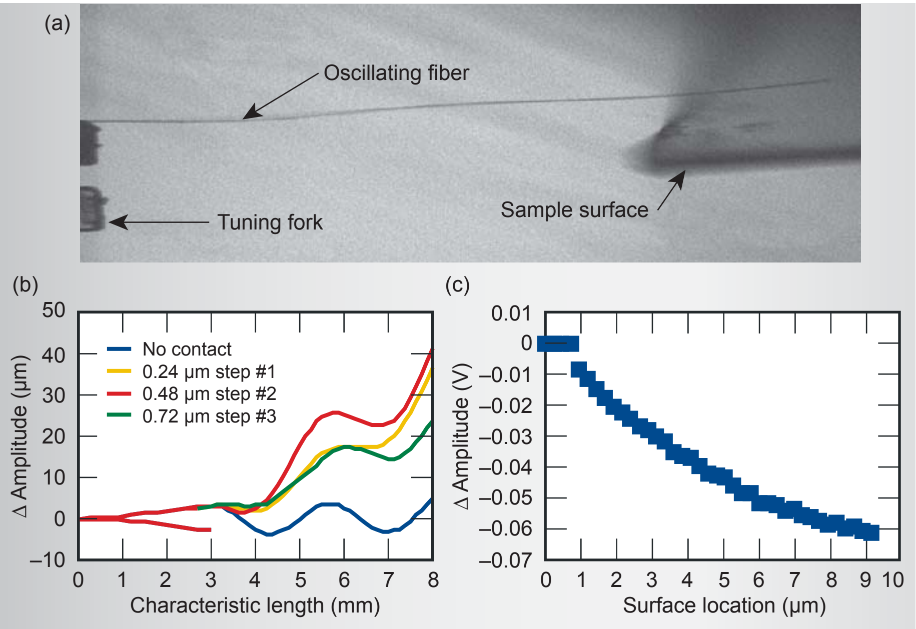

Figure 2. (a) Photograph of oscillating fiber contacting a sample surface during a sensitivity experiment; (b) snapshot in time of the probe fiber model output contacting an elastic surface as it is stepped in at .24 mm steps; (c) output of probe model as the surface is contacted with the probe tip.

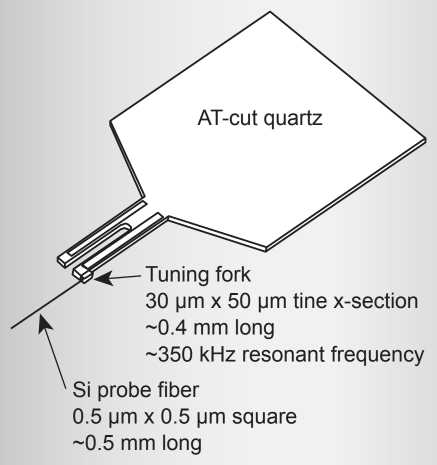

Figure 3. Scaled probe design incorporating high-frequency quartz tuning fork (~350 kHz) and a 0.5-mm-long Si fiber probe with 0.5-µm-x-0.5-µm cross-section. The oscillation amplitude is ± 1 µm at ± 10 V input.

sensitivity, has been built and is operational at LLNL. The system has been integrated with a precision motion stage station with subnanometer-level positioning and data acquisition capability. Experimental evaluation of probe performance is shown in Fig. 1. Probe sensitivity and repeatability to contact have been measured on a hardened steel gage block and have been shown to be at the ± 10 nm level for experimental systems at both UNC-Charlotte and LLNL.

A model of the probe dynamics including contact has been derived as a stand-alone model in Fortran. Figure 2 shows an image of the experimental probe fiber contacting a surface. The model output of the fiber as an elastic surface is brought into contact with the fiber tip. The current scale system has a restoring force due to the strain energy in the distorted beam during oscillation of ~ 100 mN, while the theoretical and experimentally measured combined contact force is less than 10 mN.

Scaling the system by an order of magnitude and using the same analysis, the restoring force in the oscillating beam is approximately 2 mN while the combined surface forces are nearly 0.5 mN. The influences of the surface forces are much more dominant at the smaller scale, as expected. By using our modeling techniques, we have designed a system that can overcome the surface effects by either increasing the drive frequency at constant amplitude and/or shortening the fiber length to produce a larger restoring force.

The second year of the effort uses the theoretical models and experiments derived in the first year to design a scaled probe system applicable to the micrometer-sized features found in target parts. A prototype scaled system is currently being built as a collaborative effort between LLNL, UNC-Charlotte and InsituTec and is illustrated in Fig. 3. We have also designed a 2-D oscillator being adapted to allow sensitivity of the probe in two directions.

Related References

1. Bauza, M. B., R. J. Hocken, S. T. Smith, and S. C. Woody, "Development of a Virtual Probe Tip with an Application to High Aspect Ratio Microscale Features," *Rev. Sci. Instrum.*, **76**, p. 095112, 2005.
2. Arnau, A., Piezoelectric Transducers and Applications, Springer, New York, 2004.
3. Yang, J., Analysis of Piezoelectric Devices, World Scientific, Hackensack, New Jersey, 2006.
4. Yang, F., "Adhesive Contact of Axisymmetric Suspended Miniature Structure," *Sensors and Actuators A*, **104**, pp. 44–52, 2003.
5. Israelachvili, J. N., Intermolecular and Surface Forces, 2nd Ed., Academic Press, London, 1992.

FY2009 Proposed Work

We are currently building a scaled version of the probe system and prototyping a 2-D oscillator with the intention of expanding this technology to operate with sensitivity in two dimensions. We are also continuing analytical assessment of the probe system to incorporate the feasibility of using the probe geometry for determination of material properties and/or surface modification.

Prompt Experimental Diagnostics

John E. Heebner
(925) 422-5474
heebner1@llnl.gov

We are creating a high-fidelity, transient x-ray recording diagnostic for High Energy Density Physics (HEDP). The system architecture, depicted in Fig. 1, consists of a front-end x-ray sensor, optical link, and back-end optical recorder. The front-end sensor promptly transcodes x-ray transients onto an optical carrier through refractive index changes arising from excited charge carriers in a III-V semiconductor resonant cavity. The optical link transmits the encoded signal out of the target chamber, while preserving its bandwidth, and avoiding spurious electromagnetic pulse (EMP) transients. At a suitable standoff distance, an advanced ultrafast optical recorder processes and digitizes the signal with near picosecond resolution and high dynamic range.

Project Goals

The overall goal of this project is to build an HEDP diagnostic capable of recording fusion burn on NIF with high fidelity. This project leverages prior efforts in 1) resonant-cavity-based x-ray-to-optical transcoding, and 2) ultrafast, high-dynamic-range optical recording based on time-magnified optical preprocessing and ultrafast optical deflection. Near term goals are focused on mating existing subsystems (transcoders and recorders) into a robust, packaged, field-ready instrument. Long term goals are focused on demonstrating the new capability on a laser-driven HEDP system. Targeted performance metrics for the system include near picosecond temporal resolution and dynamic range in excess of 8 bits.

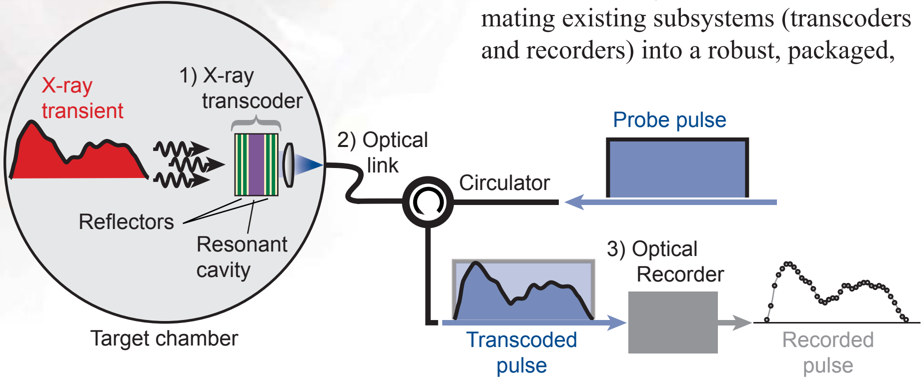

Figure 1. Schematic of system architecture.

Relevance to LLNL Mission

The experimental validation of codes used to model fusion burn is critical to stockpile stewardship at LLNL. Radiation signatures exhibit important features that span many orders of magnitude. As a result, upcoming weapons-related and NIF experiments will require high-dynamic-range characterization of these signatures. The system being created in this project will deliver a unique, high-performance recording capability for upcoming NIF experiments.

FY2008 Accomplishments and Results

A primary deliverable for FY2008 was the demonstration of the single transient response of the sensor to short-pulse x-ray irradiation. Instrument-limited transcoded response was demonstrated in single-shot x-ray experiments at the COMET laser at the Jupiter Laser Facility (JLF). Figure 2 shows the experimental setup. Short duration x rays were generated from a 10-µm-thick copper-foil target illuminated by picosecond-laser pulses at 1064 nm, with 5 J of energy. Radiation from the laser-produced plasma was detected with a sensor preconditioned for ultrafast recovery. Conditioning was accomplished by the introduction of defect states through proton bombardment to speed up the recovery of excited charge carriers from the nanosecond scale to the picosecond scale. Optical probe radiation, reflected

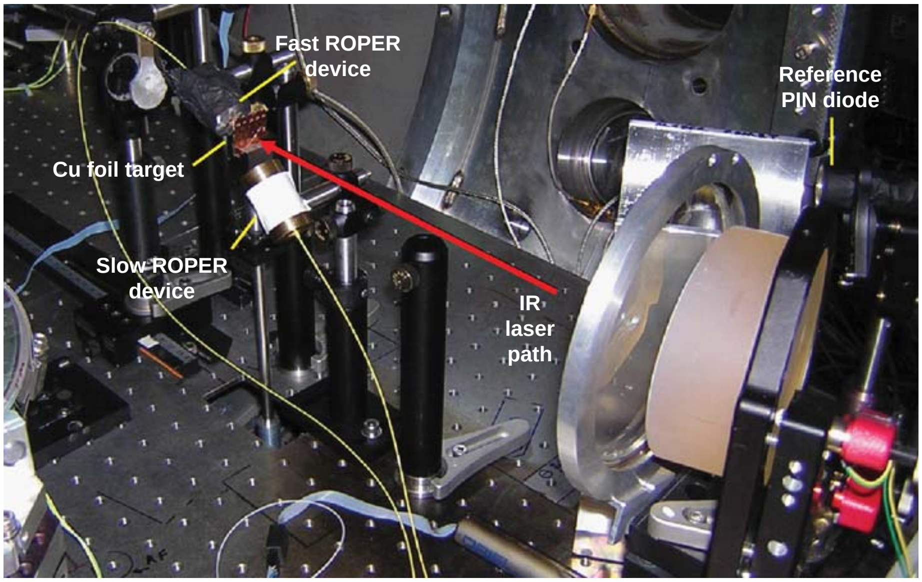

Figure 2. Experimental setup using the Recirculating Optical Probe for Encoding Radiation (ROPER) for validating ultrafast x-ray transient transcoding to an optical carrier.

from the sensor was detected with a fast amplified photodiode and recorded with a 20-GHz real-time oscilloscope. Figure 3 shows the signal recorded on the oscilloscope at 50 GS/s (20 ps per data point).

Secondary deliverables consisted of integrating GaAs- and InGaAsP-based transcoders with two advanced back-end recorders in offline test beds.

The first of the recorders is a guided-wave parametric temporal-imaging system at 1550 nm configured for 100-ps record length, 33-x time magnification, and 500-fs resolution when used in conjunction with a 30-GHz streak camera. This system implemented a new mode multiplexing/demultiplexing Y-branch aperiodically-poled lithium niobate (APPLN) time-lens mixing crystal to remove unwanted pump second harmonic noise, and improve the dynamic range and signal strength. Recording of a ring down test pattern showed the expected signal decay with a peak signal of 3000:1 over the noise floor of the instrument.

The second of the recorders is the Serrated Light Illumination for Deflection Encoded Recording (SLIDER) all-optical streak camera. This ultrafast optical beam deflector at 940 nm has demonstrated near picosecond resolution with 3000:1 dynamic range, extendable beyond 10,000:1 when later mated with a 16-bit camera. Integration of a GaAs transcoder with SLIDER was performed in an offline test bed where an x-ray surrogate 800-nm pulse was transcoded to 940 nm, deflected by SLIDER, and recorded on a 12-bit camera. The test demonstrated transcoder-limited resolution.

Related References

1. Lowry, M. E., *et al.*, “X-Ray Detection By Direct Modulation of an Optical Probe Beam-Radsensor: Progress On Development For Imaging Applications,” *Rev. Sci. Instrum.*, **75**, p. 3995, 2004.
2. Bennett, C. V., B. D. Moran, C. Langrock, M. M. Fejer, and M. Ibsen, “640 GHz Real-Time Recording Using Temporal Imaging,” *OSA Conference on Lasers and Electro-Optics*, San Jose, California, May 6, 2008.
3. Bennett, C. V., B. D. Moran, C. Langrock, M. M. Fejer, and M. Ibsen, “Guided-Wave Temporal Imaging Based Ultrafast Recorders,” *OSA Conference on Lasers and Electro-Optics*, Baltimore, Maryland, May 11, 2007.
4. Heebner, J. E., and C. H. Sarantos, “All Optical Streak Camera,” *Conference on Lasers and Electro-Optics*, 2008.
5. Heebner, J. E., and C. H. Sarantos, “Ultrafast Optical Beam Deflection in a GaAs Planar Waveguide by a Transient, Optically-Induced Prism Array,” *Integrated Photonics and Nanophotonics Research and Applications*, 2008.

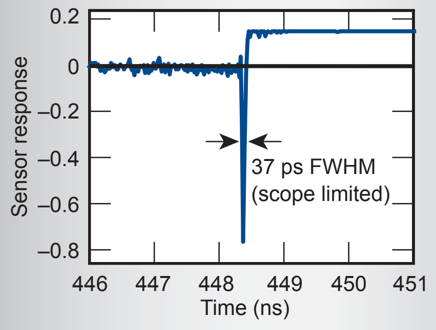

Figure 3. Single transient ROPER sensor response to x rays generated by short-pulse laser ablation of a Cu foil. The recorded trace is instrument limited to ~20 GHz by the detection system electronics.

FY2009 Proposed Work

For FY2009 we will continue the refinement of integrated system demonstrations in the laboratory using a Ti:Sapphire laser as a surrogate for x rays. Work in parallel will proceed towards a packaged, robust, field-ready instrument capable of recording fusion burn on NIF.

Serrated Light Illumination for Deflection Encoded Recording (SLIDER)

John E. Heebner
(925) 422-5474
heebner1@llnl.gov

Deflection of *optical* beams at picosecond timescales enables a novel approach to the ultrafast measurement of transient optical signals. In the first year of this project, we demonstrated a novel, ultrafast, optical beam deflection technique based on an array of transient, optically-induced prisms within a GaAs/AlGaAs planar waveguide. The deflection enables the direct mapping of time-to-space, allowing a conventional, high-fidelity camera to record temporal waveforms in parallel with high dynamic range. In the past year we have identified and mitigated several performance limitations and demonstrated that the technique is capable of serving as a high-fidelity diagnostic for recording fusion reaction history on NIF.

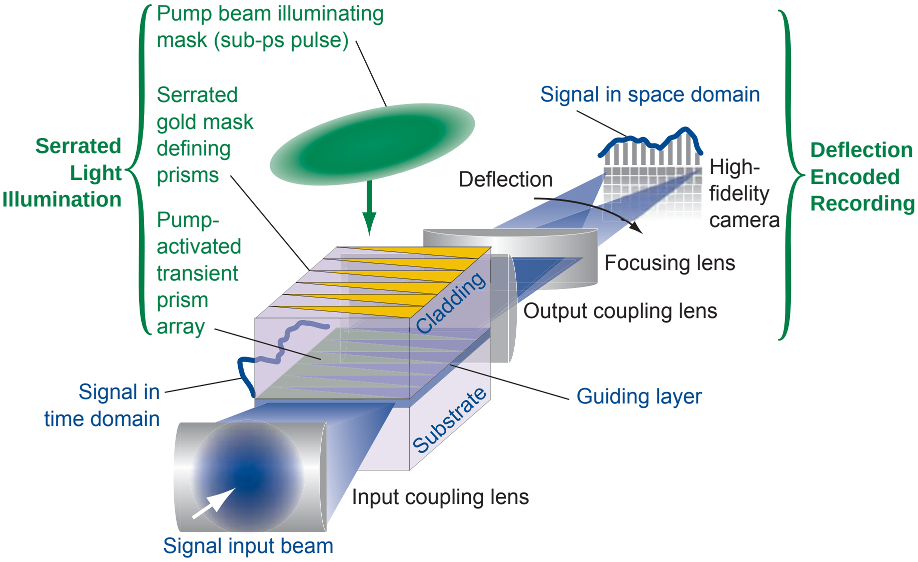

Figure 1. The SLIDER concept. SLIDER is based on the optically-induced deflection of an optical signal propagating in a planar slab waveguide. The deflection is caused by a sequential array of transient prisms that are simultaneously created by a pump beam through charge-carrier-based nonlinear optical mechanisms. The pump beam passes first through a serrated gold mask deposited atop the cladding to acquire the pattern of prisms and then imprints the pattern into the guiding layer. Due to the latching nature of the excited carriers, the prisms remain active for the duration of the beam sweep. Signal time of flight through the device then ensures a linear mapping of time to angle. A cylindrical focusing lens maps angle to space, where a conventional camera records the energy in each time slot with high dynamic range.

Project Goals

Serrated Light Illumination for Deflection Encoded Recording (SLIDER, Fig. 1) is already the fastest optical beam deflector reported to date. Implementing this technique in the past year, we demonstrated the operation of an all-optical streak camera with 2.5-ps temporal resolution and dynamic range in excess of 3000:1. With further improvements identified this year and scheduled to be tested in FY2009, we now believe that near-picosecond resolution in excess of 10,000:1 dynamic range is achievable. When later mated with x-ray-to-optical transcoding devices under development, we aim to deliver a means of recording fusion reaction histories with resolution and fidelity required for code validation.

Relevance to LLNL Mission

The experimental validation of codes used to model fusion burn is critical to stockpile stewardship at LLNL. Fusion burn on NIF will be a transient event less than 100 ps in duration with details spanning many orders of magnitude. A diagnostic that can faithfully record this reaction is crucial to this Laboratory mission.

FY2008 Accomplishments and Results

In FY2008, we identified several limitations present in the FY2007 rudimentary demonstration of the SLIDER optical deflector. These largely resulted from sub-optimal formatting of the pump beam illumination and the probe beam bandwidth. Illumination of the prisms with a non-uniform pump beam resulted in dynamic wavefront aberrations that increasingly blurred the deflecting spot on the camera. The quadratic nature of a Gaussian beam illuminating a linear wavefront-inducing prism array resulted in a cubic wavefront error similar to coma in a 2-D imaging system. By using a refractive shaper to change the illuminating beam from a Gaussian profile to a flat-top profile, we were able to mitigate the dynamic aberration.

The test signal derived from a Ti:Sapphire-pumped optical parametric amplifier. The signal pulse bandwidth, if left untreated, led to large group velocity dispersion in the waveguide, blurring the signal waveform. To lessen this, we constructed a tunable, grating-based filter to limit the bandwidth to 1.4 nm, where a compromise between dispersion and transform-limited pulse duration preserved 1-ps features for testing. After successfully mitigating these issues we observed deflected impulses with 2.5 ps resolution.

The optimized setup enabled us to record both the magnitude and attenuation of a deflecting impulse as a function of carrier density (inferred from the pump fluence). This in turn provided a means of validating models that predict the induced refractive and absorptive changes resulting from excited electron-hole pairs. Optically excited free carriers induce index changes through the plasma effect (Drude model); bandfilling (Pauli exclusion, Burstein-Moss effect); and bandgap shrinkage (charge screening).

As can be seen in Fig. 2, the data is in close agreement with the sum total of models adapted from the literature. The number of resolvable spots within a 1/e decay record in time is proportional to the refractive index to free carrier absorption ratio. This ratio is in turn governed by the carrier mobility. The highest mobilities are found in GaAs where we compute that 50 resolvable spots should be attainable. Further enhancement can be achieved in a Multiple Quantum Well (MQW) engineered guiding layer.

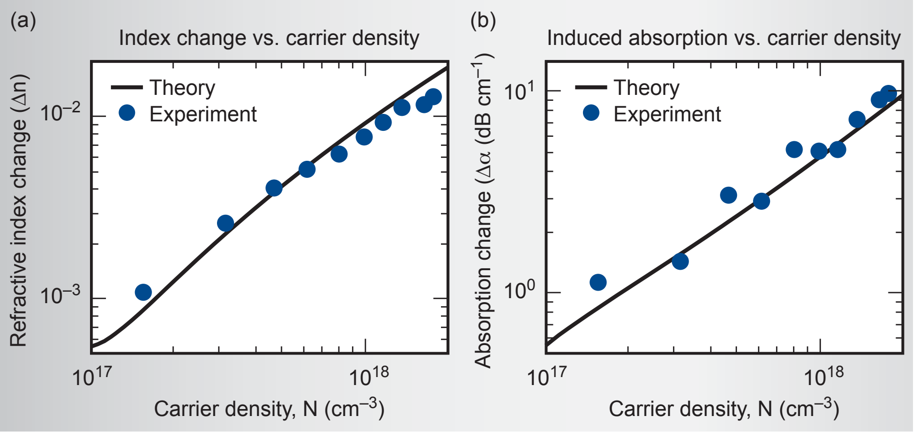

Figure 2. Experimental (points) and theoretical (solid line) data for (a) refraction and (b) free-carrier absorption for carrier densities varying from 10^{17} to 10^{18} cm^{-3} (maximum corresponds to a peak fluence of 65 μJ/cm^2). The material is bulk GaAs and the wavelength is 950 nm. As expected, the bandfilling and plasma effects dominate to produce a negative refractive index change with sufficient magnitude (~0.01) to achieve picosecond response.

We also studied the feasibility of mating a SLIDER and x-ray-to-optical converter as an integrated, fieldable, x-ray transient recording instrument. Plans toward this goal include designs for integrating a Ti:Sapphire pump laser and a 950-nm probe pulser in a rack-mounted geometry.

Related References

1. Heebner, J. E., and C. H. Sarantos, “All Optical Streak Camera,” *Conference on Lasers and Electro-Optics*, 2008.
2. Heebner, J. E., and C. H. Sarantos, “Ultrafast Optical Beam Deflection in a GaAs Planar Waveguide by a Transient, Optically-Induced Prism Array,” *Integrated Photonics and Nanophotonics Research and Applications*, 2008.
3. Lowry, M. E., *et al.*, “X-Ray Detection by Direct Modulation of an Optical Probe Beam-Radsensor: Progress on Development for Imaging Applications,” *Rev. Sci. Instrum.*, **75**, p. 3995, 2004.
4. Li, Y. D., Y. Chen, L. Yang, and R. R. Alfano, “Ultrafast All-Optical Deflection Based on an Induced Area Modulation,” *Optics Letters*, **16**, p. 438, 1991.
5. Hubner, S., *et al.*, “Ultrafast Deflection of Spatial Solitons in Algaas Slab Waveguides,” *Optics Letters*, **30**, p. 3168, 2005.

FY2009 Proposed Work

For the third year of the project, we intend to further drive the resolution, record, and dynamic range of the SLIDER device toward fundamental limits. Our models predict that further enhancement of the number of resolvable spots by a factor of three may be possible with a MQW engineered guiding layer. We will also attempt to extend the record length to several hundred picoseconds in order to add margin for trigger jitter in a recording instrument. Finally, every effort will be made to ensure that SLIDER complements ongoing efforts towards an x-ray-to-optical transcoder.

Recirculating Optical Probe for Encoding Radiation (ROPER)

Stephen P. Vernon
(925) 423-7826
vernon1@llnl.gov

LLNL is performing physics experiments on the NIF, OMEGA and Phoenix platforms, including those addressing DT burn physics, equations of state, and dynamic material properties. The dynamic range, spatial resolution, bandwidth and noise robustness required in these experiments are extremely challenging and surpass present capabilities. This project is undertaking engineering reduction-to-practice of a picosecond response time, radiation to optical down-converting detector that can address these requirements. The concept can be optimized for the detection of x rays, γ rays and neutrons.

The Recirculating Optical Probe for Encoding Radiation (ROPER) sensor is a resonant optical cavity consisting of high-reflectance mirrors that surround a direct band-gap semiconductor detection medium (Fig. 1). Radiation absorption within the detection medium induces a change in its optical refractive index. The index change produces phase modulation of an optical probe beam that transits the sensor medium. Interferometry is used to convert the phase modulation to amplitude modulation. In effect, the sensor down-converts the radiation signature to amplitude modulation of the optical probe beam.

Ultrafast, approximately picosecond response is achieved using a H^+ ion implant of the sensor medium to tailor the sensor temporal response. The H^+ implant produces a high volumetric density of recombination centers in the medium that increases the carrier recombination rate and, therefore, reduces the temporal duration of the transient index perturbation.

Project Goals

The ROPER project was re-scoped in FY2008. The new plan focused on incorporating the H^+ ion implant process in our engineering of the ROPER sensors to produce detectors with approximately picosecond response times. Sensors were built for integration and testing with prototype, next-generation, all-optical recording systems at LLNL. The recorders operate at 900 and 1535 nm, respectively; GaAs technology was used for the 900-nm sensors, and

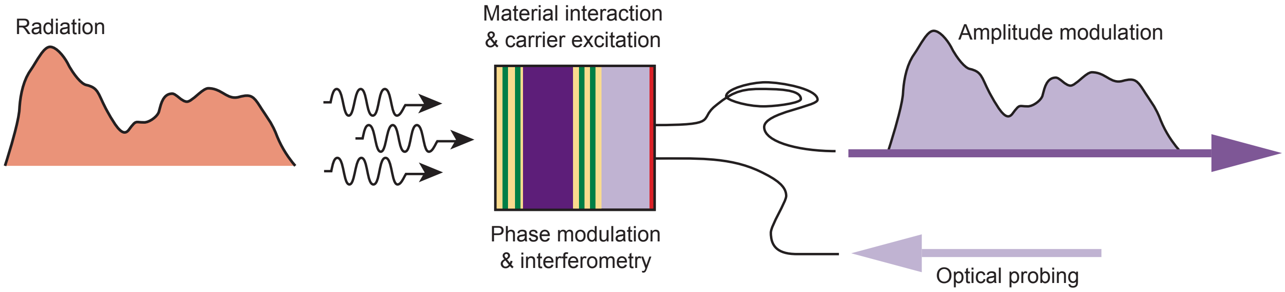

Figure 1. The ROPER system. Radiation absorption within the ROPER sensor modifies the sensor optical refractive index. Interferometric detection of the phase-modulated probe beam converts the radiation signature to an amplitude modulated optical signal.

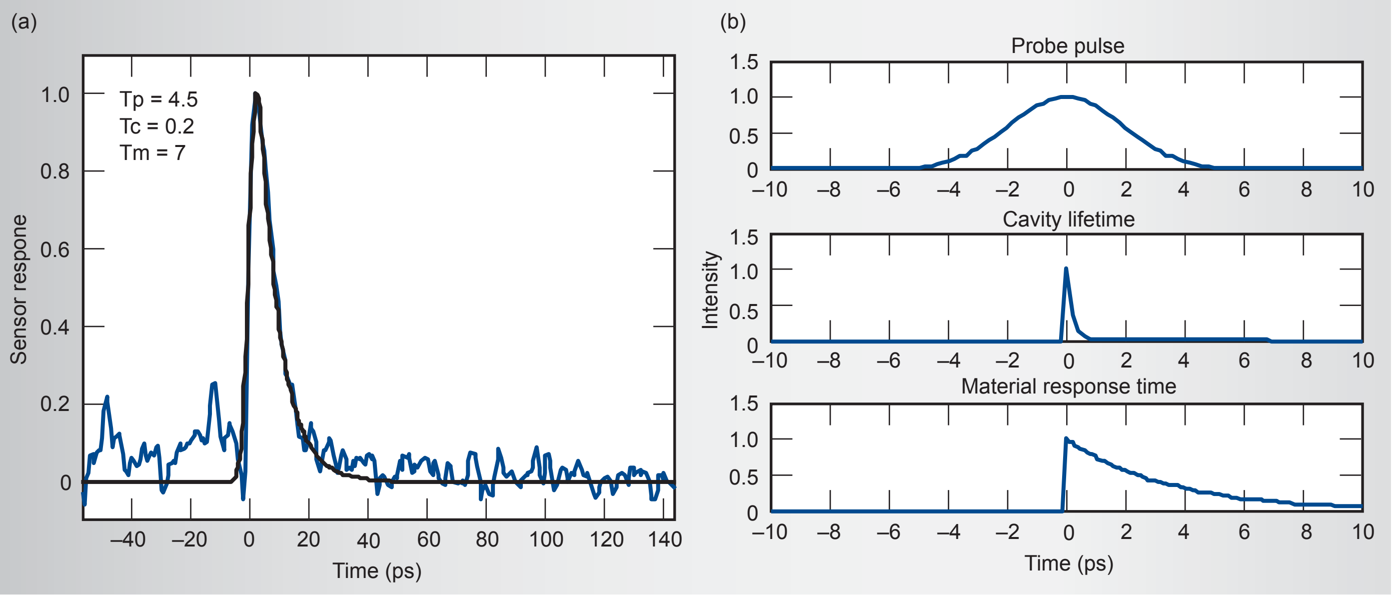

Figure 2. (a) Measured ROPER sensor response using pump-probe techniques and above-bandgap optical excitation of the sensor. The signal is the convolution of the probe pulse, cavity temporal response, and material temporal response (b). The analysis indicates a material response time of ~7 ps.

InGaAsP technology was used for the 1535-nm application.

Relevance to LLNL Mission

This project specifically addresses the instrumentation requirements of Weapons and Complex Integration (WCI). It is well aligned with institutional Science and Technology Plan thrust areas in Weapons Science ("Advanced Experimental Platforms Including Diagnostics") and Discovery Class Science ("Beyond-State-of-Art Instrumentation and Measurement Capabilities"). The project enhances LLNL's core competency in measurement science at extreme dimensions. In addition, we anticipate that, when available, ICF and HEDP experimental programs will identify applications for these detectors.

FY2008 Accomplishments and Results

In FY2008 we successfully combined the radoptic and ion-implant technologies in a reduction-to-practice effort yielding ROPER sensors with approximately picosecond temporal response. This was demonstrated experimentally in pump-probe measurements using above band-gap optical excitation of the sensor medium. The excitation pulse was ~200 fs from a mode-locked Ti:sapphire laser and regenerative amplifier operated at 780 nm. The probe pulse was generated using an optical parametric amplifier pumped by the same Ti sapphire oscillator. Figure 2a illustrates the measured sensor response of ~7ps. This is a convolution of the probe pulse, the material response time, and the sensor cavity lifetime, illustrated in Fig. 2b.

Related References

1. Lowry, M. E., C. V. Bennett, S. P. Vernon, R. Stewart, R. J. Welty, J. Heebner, O. L. Landen, and P. M. Bell, *Rev. Sci. Inst.*, **75**, pp. 3995–3997, 2004.
2. Bennett, C. V., and B. H. Kolner, *IEEE J. Quant. Electr.*, **36**, pp. 430–437, 2000.
3. Lambsdorff, M., J. Kuhl, J. Rosenzweig, A. Axmann, and J. Schneider, *Appl. Phys. Lett.*, **58**, 1881, 1991.

Project Summary

H^+ ion implant techniques were used to fabricate radoptic ROPER radiation sensors with approximately picosecond temporal response. This represents a five-order-of-magnitude improvement in sensor response time. (ROPER sensors using undamaged material exhibit response times ~ 200 ns.) The spatial distribution and intensity of the ion dose can be selected to tune and optimize both the temporal response and the detection sensitivity of the ROPER sensor for specific radiation detection applications.

Automatic PID Tuning Using Extremum Seeking

Nicholas J. Killingsworth
(925) 422-8489
killingsworth2@llnl.gov

About ninety percent of all control loops use proportional integral derivative (PID) controllers. These controllers are typically tuned manually, often with poor results. A large increase in system performance can be achieved using a more systematic approach to controller tuning, leading to a more efficient and robust system. However, available tuning methods are overly complex, are valid only for linear systems, or require a model of the system. There is considerable need for straightforward non-model-based methods that are easy to implement and applicable to nonlinear systems.

We have created a non-model-based method of tuning PID controllers that can be applied to nonlinear systems online. This method uses extremum seeking (ES), which is a non-model-based real-time optimization algorithm (Fig. 1). The ES PID controller tuning tool has the potential to optimize system performance while minimizing engineers' time dedicated to controller tuning.

Project Goals

The main goal of this project is to create a set of rules to automate the selection of the parameters of the extremum seeking algorithm. A block diagram of the ES algorithm is presented in Fig. 2. To effectively use the ES algorithm, the adaptation gain, γ_i, and the perturbation amplitude, α_i, must be selected for each input to the system because they depend on the system's being optimized. Automating this selection procedure will allow non-experts to use the ES algorithm for optimization

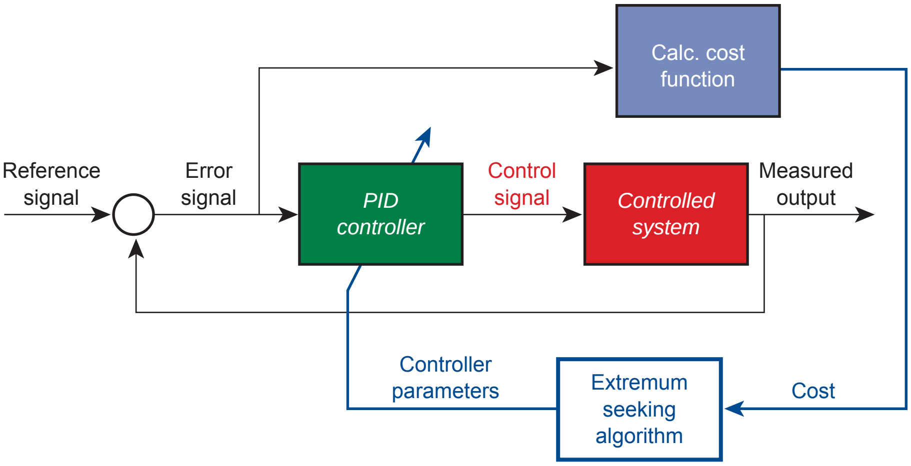

Figure 1. The overall ES PID tuning scheme. The ES algorithm updates the PID controller parameters to minimize a cost function that quantifies the performance of the PID controller on the controlled system.

of their system. This automated tuning procedure will be implemented in a user-friendly software package, permitting inexperienced users to optimally tune a PID controller for any application.

After testing the automated procedure on simulated systems we are planning to demonstrate the capabilities of the methodology by applying it to the control system for advanced internal combustion engines. Additionally, we plan on applying the method to the sulfur hexafluoride (SF_6) gas pressure control system of the flash x-ray (FXR) radiographic facility at LLNL. FXR constitutes the ideal test bed for this application due to its great complexity (currently with 27 PID controllers, expandable up to 66), which makes it extremely time-consuming to tune with other available procedures.

Relevance to LLNL Mission

Our automated tuning procedure has great potential for improving operational control due to the widespread use of PID controllers. The market potential within and outside LLNL is enormous, leading to improved operation and external funding. This project has application to many LLNL programs using feedback control. We will be applying this tuning method to the FXR experiment. We also anticipate applicability of this technology to energy security topics of interest to LLNL, such as control of hybrid vehicles and internal combustion engines.

FY2008 Accomplishments and Results

We have produced a methodology to automate the selection of ES parameters. This methodology has been successfully implemented in software and applied to find the extrema of various nonlinear maps. This automated software package was then adapted to optimally tune PID controllers. The tuning method has been demonstrated on a variety of *simulated* systems, including systems that are difficult to control, such as those presenting non-minimum phase behavior and nonlinearities. Fig. 3 shows an initial PID controller tuned using the industry standard Ziegler-Nichols tuning rules (ultimate sensitivity method) and acting on a system with non-minimum phase behavior. A controller tuned using the automated ES algorithm greatly improves the performance, reducing the system's overshoot and settling time.

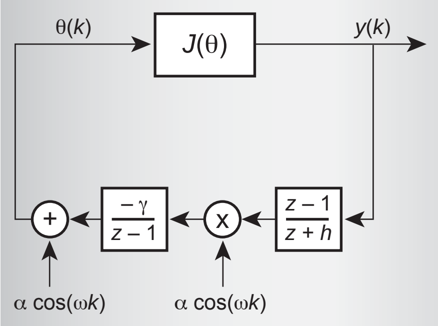

Figure 2. Block diagram of ES algorithm. The input parameters θ (*k*) are perturbed by the signal $\alpha_i, \cos, (\omega_i, k)$. The output of the cost function *J* (θ (*k*)) is then high-pass filtered, demodulated, and finally low-pass filtered to yield new output parameters.

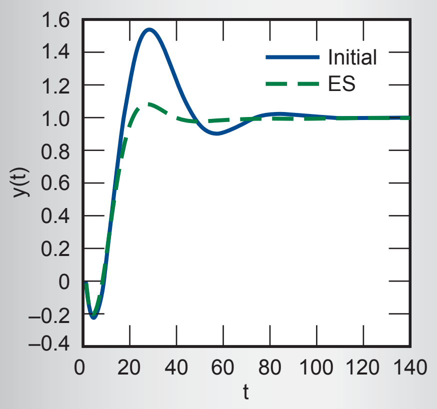

Figure 3. Step response of initial PID controller tuned using the Ziegler-Nichols tuning rules and the PID controller tuned using the automated ES methodology both applied to a non-minimum phase system. The automated ES tuning method decreases the system's overshoot and settling time versus the initial controller when a step function is applied at time zero.

Related References

1. Killingsworth, N. J., and M. Krstic, "PID Tuning Using Extremum Seeking," *Control Systems Magazine*, **26**, pp. 70–79, 2006.
2. Killingsworth, N. J., S. M. Aceves, D. L. Flowers, F. Espinosa-Loza, and M. Krstic, "HCCI Engine Combustion Timing Control: Optimizing Gains and Fuel Consumption Via Extremum Seeking," *IEEE Transactions On Control Systems Technology*, 2008.
3. Ariyur, K. B., and M. Krstic, Real-Time Optimization by Extremum Seeking Feedback, Wiley-Interscience, Hoboken, New Jersey, 2003.
4. Astrom, K. J., and T. Hagglund, PID Controllers: Theory, Design and Tuning, Instrument Society of America, Research Triangle Park, North Carolina, 2nd Ed., 1995.

FY2009 Proposed Work

After successful testing of the tool in simulations, the tuning method will be demonstrated on experimental systems, including a high-pressure gas system for an internal combustion engine at UC Berkeley and the FXR SF_6 gas pressure control system. We will work with experienced engineers on both systems to create an implementation plan and desired outcomes. We will apply the PID tuning tool to each system and compare the performance to the PID controllers currently in use.

Micro/Nano-Devices & Structures

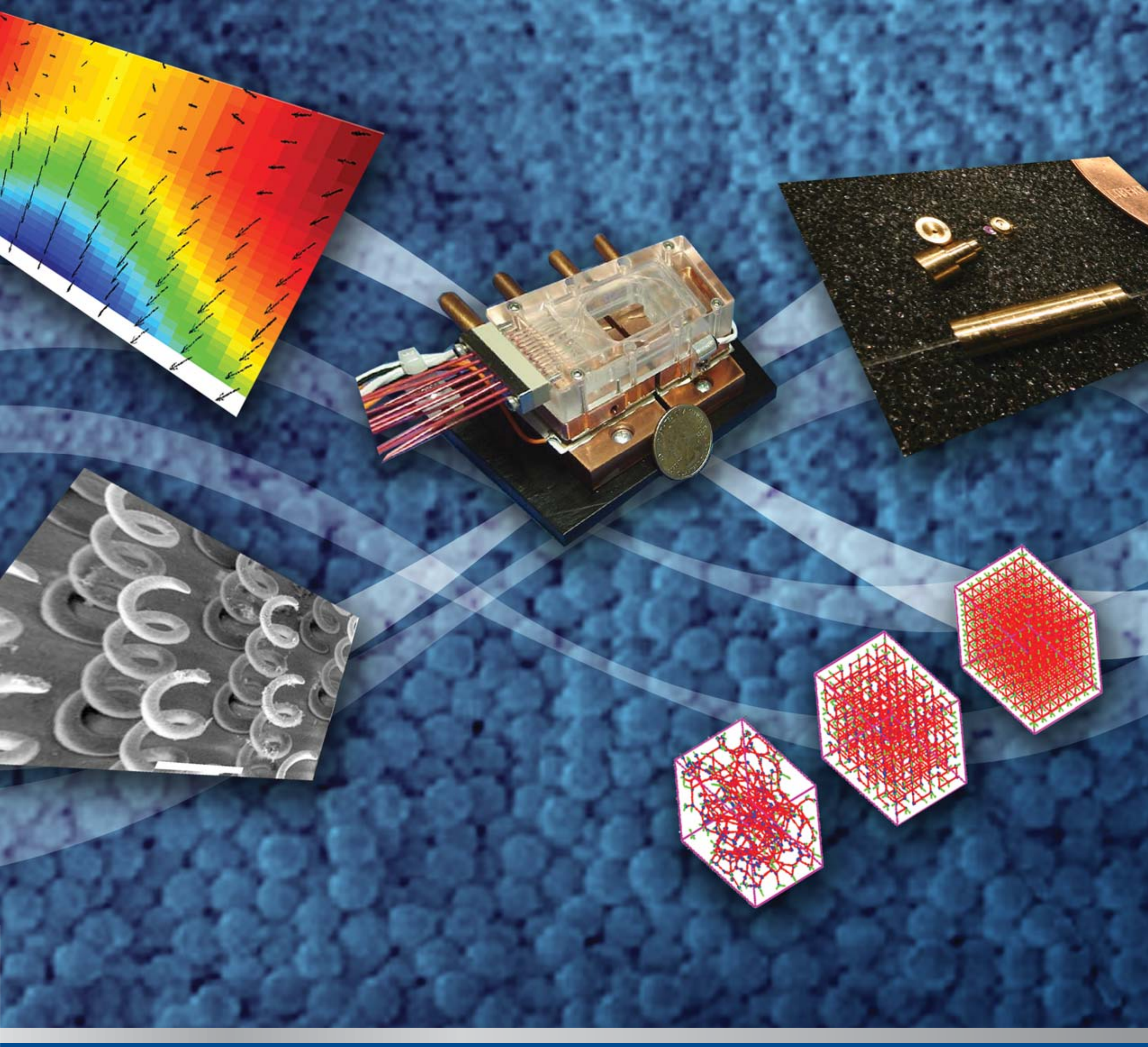

Hybridization, Regeneration, and Selective Release on DNA Microarrays

N. Reginald Beer
(925) 424-2232
beer2@llnl.gov

DNA microarrays can contain a large number of distinct, agent-specific probes that can be spotted onto their surface, making them ideal for environmental background sampling, broad-spectrum clinical monitoring, and continuous bio-threat detection. Microarrays are also excellent filtering tools for target enrichment of complex mixtures for subsequent sequencing. Microarrays easily generate hybridization patterns and signatures, but there still is a critical and unmet need for methodologies enabling rapid and selective analysis of these patterns and signatures. Detailed analysis of individual spots by subsequent sequencing could potentially yield significant information for rapidly mutating and emerging (or deliberately engineered) pathogens. This is a significant challenge especially in large, high-density microarrays where it is extremely difficult to implement single spot control. The ability to analyze individual spots eliminates the complex background signal, a confusing factor in the current bioinformatics data analysis.

Optical energy deposition with coherent light will be explored to quickly provide the thermal energy to heat the aqueous solution at the hybridization site to 94 ºC. This will denature the desired DNA from the surface probes without damaging the probes themselves, and allow for capture of the released DNA. The author has previously studied the same optical energy deposition method for ultrafast aqueous sample heating, which has led to the identification of several promising wavelengths in the IR spectrum for optimal energy transmission through the glass slide and absorption into the aqueous solution at the hybridization site. These wavelengths correspond to O-H bond modes in the H_2O molecule, and can be selected with respect to the absorption spectra of the

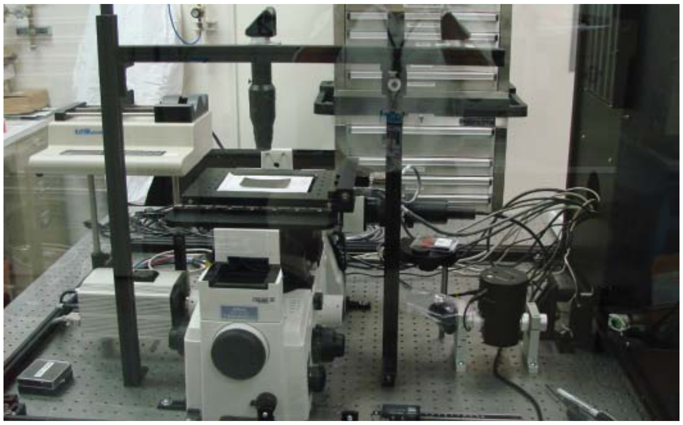

Figure 1. The DRACULA system.

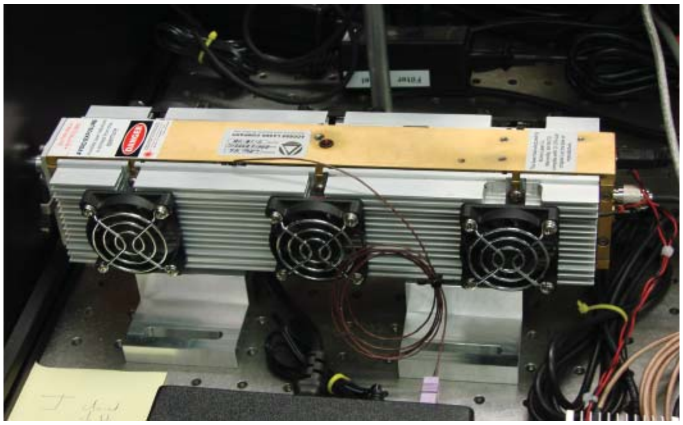

Figure 2. The 10.6-μm CO_2 CW laser powering DRACULA.

type of glass slide used, such as fused silica and borosilicate, to minimize the amount of energy absorbed by the slide.

Laser sources typically have beam widths on the order of several millimeters, so a focusing optic with the proper focal length and magnification should successfully reduce the beam spot to less than 100 µm. Once released, the oligos will need to be collected. A flow cell that can reliably process µL amounts of liquid over the array will be sufficient for the collection.

Project Goals

The goal for this one-year project has been to research the optical methods capable of denaturing double-stranded DNA (dsDNA) on the surface of a microarray slide. The method must cause the single-stranded target to dehybridize from the surface-bound, spot-specific probe molecule. To support this goal, the following tasks were proposed:

1. optical source investigated and selected for optimal transmission and absorption by the aqueous surface layer;
2. optical system designed for single spot addressability and resolution; and
3. optical system experimentation to confirm appropriate energy deposition.

Relevance to LLNL Mission

LLNL made a strategic commitment to pursue microarrays using *in-situ* synthesis technology developed by NimbleGen Systems, Inc. This technology is unique in its ability to produce high-density (400,000 spots) arrays with long (up to 90 bases) probes. The ability to use all the capabilities of these arrays and perform spot selection and sequencing will become an almost immediate component of our life sciences and national security work, supporting our DOE, DoD, and DHS missions.

FY2008 Accomplishments and Results

The optical source investigation led to the prototyping of a 10.6-µm CO_2 laser excitation continuous wave (CW) source to be adequately absorbed in the microarray's aqueous surface layer. To adequately position, align, focus, and attenuate this source, the DNA Release and Capture Laser (DRACULA) system was designed, and is shown in Figs. 1 and 2. This system reaches an estimated single spot addressability and resolution of approximately 50 µm. Finally, experiments on the DRACULA system were conducted to confirm appropriate energy deposition. The "burn" spots in Fig. 3 show where the beam has been directed to different locations to confirm time and power/energy deposition.

Related References

1. Chan, V., D. J. Graves, and S. E. McKenzie, "The Biophysics of DNA Hybridization with Immobilized Oligonucleotide Probes," *Biophys. J.*, **69**, pp. 2243–2255, 1995.

2. Pease, A. C., D. Solas, E. J. Sullivan, M. T. Cronin, C. P. Holmes, and S. P. Fodor, "Light-Generated Oligonucleotide Arrays for Rapid DNA Sequence Analysis," *Proc. Natl. Acad. Sci.*, **91**, 11, pp. 5022–5026, 1994.

3. Singh-Gasson, S., R. D. Green, Y. J. Yue, C. Nelson, F. Blattner, M. R. Sussman, and F. Cerrina, "Maskless Fabrication of Light-Directed Oligonucleotide Microarrays Using a Digital Micromirror Array," *Nat. Biotech.*, **17**, pp. 974–978, 1999.

4. Wang, D., A. Urisman, Y. Liu, M. Springer, M., *et al.*, "Viral Discovery and Sequence Recovery Using DNA Microarrays," *PLOS Bio.*, **1**, pp. 257–260, 2003.

5. West, J., K. Hukari, T. Shepodd, and G. Hux, "A High Density Microfluidic Microarray Platform for Rapid Genomic Profiling," *Eighth International Conference on Miniaturized Systems for Chemistry and Life Sciences*, pp. 26–30, Malmo, Sweden, September 2004.

Figure 3. IR "burn" spots showing desired beam deposition energy profiles.

FY2009 Proposed Work

The insight developed through this project applies to our efforts in detection and characterization of novel biological threats and emerging infectious diseases. Follow-on work is proposed for FY2009 and FY2010 to test this method on microarrays populated with surface bound oligonucleotide probes to hybridized target nucleic acids from viral or bacterial genomes, in support of detecting and characterizing next-generation biological threats.

Thermal-Fluidic System for Manipulating Biomolecules and Viruses

Klint A. Rose
(925) 423-1926
rose38@llnl.gov

We are developing a reconfigurable fluidic system that demonstrates the ability to *simultaneously* perform separations, concentrations, and purifications of biomolecules and viruses. This microfluidic technology is an equilibrium gradient version of capillary electrophoresis (CE) that allows for the stationary fractionation and concentration (up to 10,000 x) of target analytes on the dimension of bulk or free solution electrophoretic mobility. In this technique, a delicate balance is achieved in a microchannel between a net fluid flow and an opposing electrophoretic velocity gradient to capture charged analytes at a specific location (see Fig. 1). The analytes are then separated based on their free solution electrophoretic mobility, which is related to the analyte's surface charge (zeta potential) and hydrodynamic drag (shape and size).

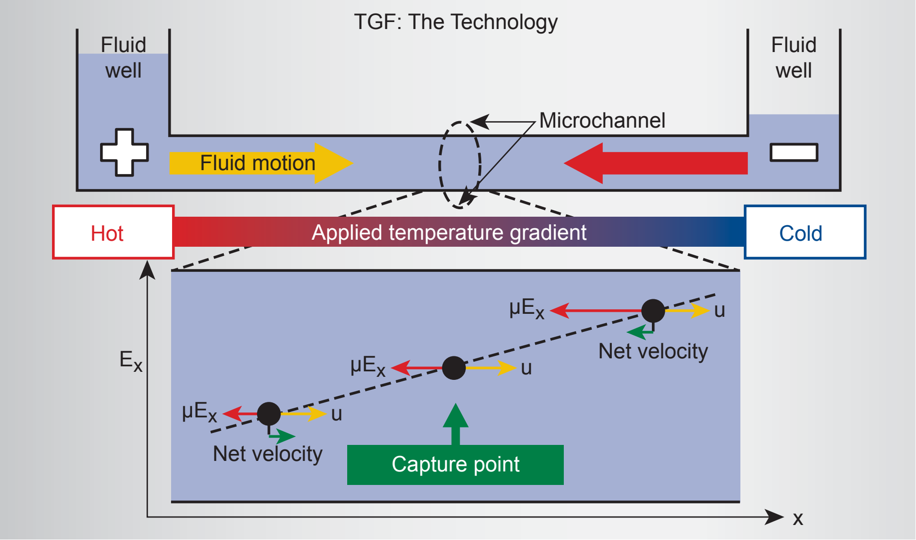

Figure 1. Schematic of temperature gradient focusing. Bulk fluid motion (yellow arrow) is balanced by an opposing electrophoretic velocity (red arrow) to capture analytes at a unique spatial location within a specific electrophoretic mobility range.

Project Goals

The project goal is to develop an automated temperature gradient focusing (TGF) instrument to improve the separation resolution and throughput when applied to front-end sample processing of biological samples. Two specific application areas are identified to demonstrate the novel sample manipulation capabilities inherent to TGF: 1) the purification and separation of different virus strains in complex samples; and 2) protein concentration and separations for *in vitro* transcription/translation (IVT) protein expressions.

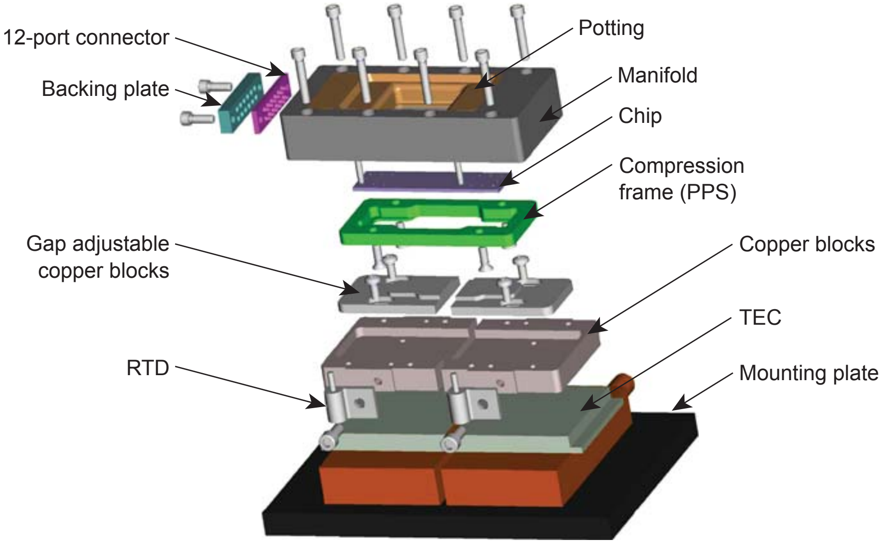

Figure 2. Exploded view of microfluidic package. The microfluidic package is composed of a fluidic manifold, a compression frame, and two independently controlled thermal regulation surfaces.

Relevance to LLNL Mission

TGF specifically addresses needs of the bio-security program at LLNL, for the detection of biomolecules, viruses, or cells at low concentrations through

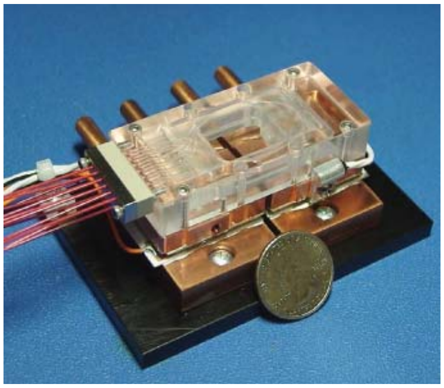

Figure 3. Photograph of the assembled package. The microfluidic package once assembled is compact and very robust. The chip can be loaded directly into the fluidic manifold and does not require the thermal module to form a fluidic seal.

enhanced collection, separation, and purification strategies. This is facilitated by performing the necessary front-end sample preparation through concentration procedures and removing noisy background signals/contaminants. This project supplies LLNL with a novel capability to perform biomolecular, viral, and cellular control in a flexible format to address a wide range of programmatic assay conditions.

FY2008 Accomplishments and Results

A thermal-fluidic package was developed and successfully tested to reproducibly control fluid flow, temperature gradients, and electric fields in microfabricated glass chips. The packaging allows for fluorescent optical access with an adjustable mounting surface to modify the temperature gradient length. Figure 2 shows an expanded view of the package and fluidic manifold for a 12-port chip with a 1/32-in. quick connect and a compression frame for repeatable leak-free fluidic connections. Once assembled, the package was very stable and required no further maintenance or monitoring. Figure 3 shows a camera image of an assembled package.

Previous analysis determined the need for thicker walled glass chips, a more robust thermal mounting to the heat source, and improved pressure stability. We were able to successfully demonstrate the capture and concentration of a small fluorescent dye molecule in the newly constructed package (Fig. 3). The package demonstrated a significant improvement in robustness over previous packaging by reducing common failure modes such as liquid leaks, air bubbles, clogging, temperature profile linearity, and overall pressure stability.

To help guide the experimental testing, a 2-D numerical modeling effort was developed that captures the relevant physics during the electrokinetic capture process. For the initial modeling of the relevant field variables (temperature, velocity, and voltage) we used a commercially available finite element modeling (FEM) package (COMSOL Multiphysics). To solve for the important analyte concentration profiles in the system, these known field variables (from FEM) were fed into a Monte Carlo simulation. Figure 4 shows good agreement between the experimental data (Fig. 4a) and simulation results (Fig. 4b), which validates the numerical modeling approach.

From here specific metrics, such as peak height, peak width, throughput, and limit of detection, can be extracted to determine the efficiency and resolving power for a particular set of capture conditions. Design guidelines and rules (geometric and operating conditions) were constructed for specific applications to aid in the design and testing of devices.

FY2009 Proposed Work

Starting from the manually controlled proof-of-principle TGF system, we propose to develop a more robust system to perform the following: 1) concentrate and separate different virus strains directly; and 2) perform protein purification and separation for IVT protein expressions. Although seemingly very different, both applications are possible because the assays themselves are used as a test platform to characterize and optimize the system performance.

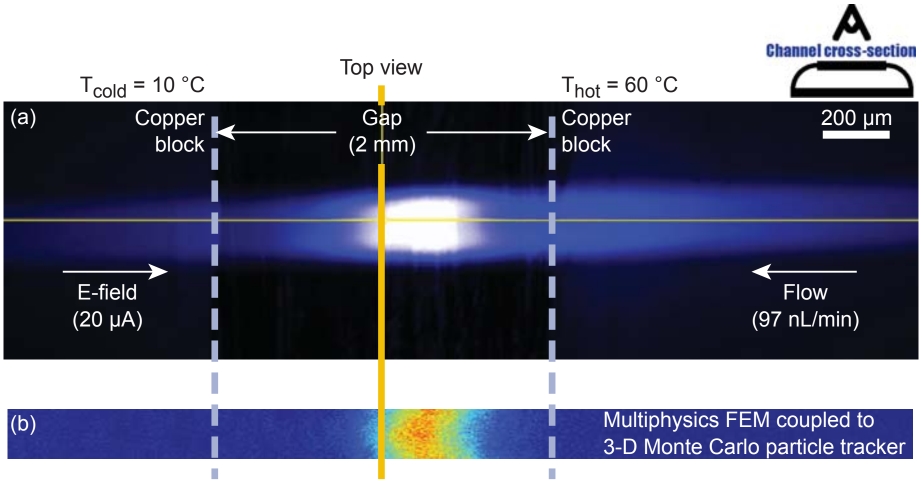

Figure 4. Numerical modeling validation: (a) experimental capture and concentration of a fluorescent dye using a rectangular channel (20 μm x 200 μm) as observed with fluorescent microscopy; (b) Monte Carlo simulations, showing good agreement with experimental data. Curvature in the focused analyte band is observed and predicted due to the high-aspect-ratio rectangular channel used.

Fluidic Platform for DNA Microarrays

John M. Dzenitis
(925) 422-6695
dzenitis2@llnl.gov

This project demonstrates a combined fluidic and imaging platform for DNA microarray experiments. This will be a new tool for biological countermeasures and sciences. The fluidic platform will enable new studies of microarray reuse directed at reducing the cost of the technique and new studies of kinetics to reduce the processing time. These are major steps on the way to new microarray applications in assays, environmental detection, and medical diagnostics. In addition, the platform itself could be a component of proposals to external sponsors for instrumentation work. The system will include the microarray flow cell (MFC), modified laser scanner, thin-film heater, and data acquisition capabilities.

Current detection approaches using DNA methods have good utility in predictive value, but the number of sequence signatures or probes that can be evaluated in practice is very limited. This is due to the fact that the material and labor costs per test are high, and the number of probes evaluated per test is low. For example, real-time PCR using TaqMan can assess up to four probes in a test; this approach is limited to testing for a specific agent. In an improvement, new suspension arrays can use 100 to 500 probes per test; this approach enables testing for a panel of known, fixed threat agent signatures. This approach is used on LLNL's Autonomous Pathogen Detection System.

The next stage of molecular diagnostics for biological threats is to look much more broadly for emerging threat biosignatures, such as virulence elements or natural and engineered mutations.

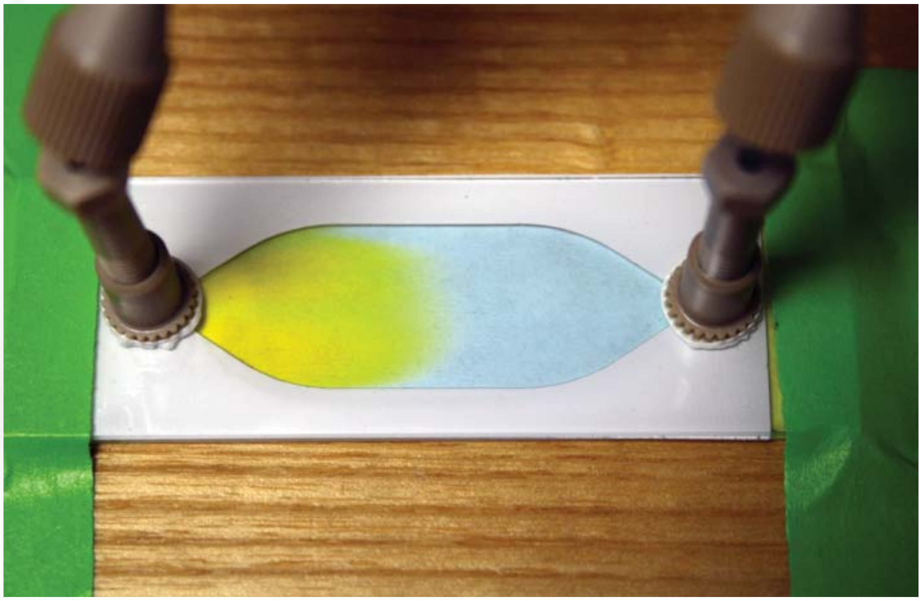

Figure 1. Dye visualization experiment testing liquid exchanges in the MFC.

This capability is targeted against new natural pandemics and engineered biological warfare agents to enable prompt countermeasures. High-density DNA microarrays have the capability to provide this broad type of search, using on the order of over 100,000 to 1,000,000 probes, depending on the platform. A group at the Naval Research Laboratory used high-density, short-probe microarrays to identify genetic variations of influenza viruses in clinical samples. A group at LLNL used high-density, long-probe microarrays to identify virulence elements in spiked environmental samples.

Project Goals

The goal of this effort is to demonstrate a combined fluidic and imaging platform for DNA microarray experiments.

Relevance to LLNL Mission

This project will be of great use to LLNL in its global security mission and ongoing efforts in detection methods against biological terrorism by providing the micro-fluidic "backbone" for these efforts.

FY2008 Accomplishments and Results

The implementation of the MFC, thin-film heater, and modified scanning platform was completed. The next step is to characterize the system and use it for experiments directed at reducing the cost and processing time of the technique.

Our results, illustrated in Figs. 1 and 2, include the following:

1. fabrication and assembly of a MFC;
2. modification of commercial (GenePix) microarray reader optics, stage, and housing to accommodate the MFC;
3. assembly, programming, and validation of fluidics test bed;
4. demonstration of fluidic control with fully assembled MFC system;
5. fabrication and characterization of a flexible polyimide heater with integrated heat spreader; and
6. performance of initial visualization experiments of a typical test microarray in the MFC.

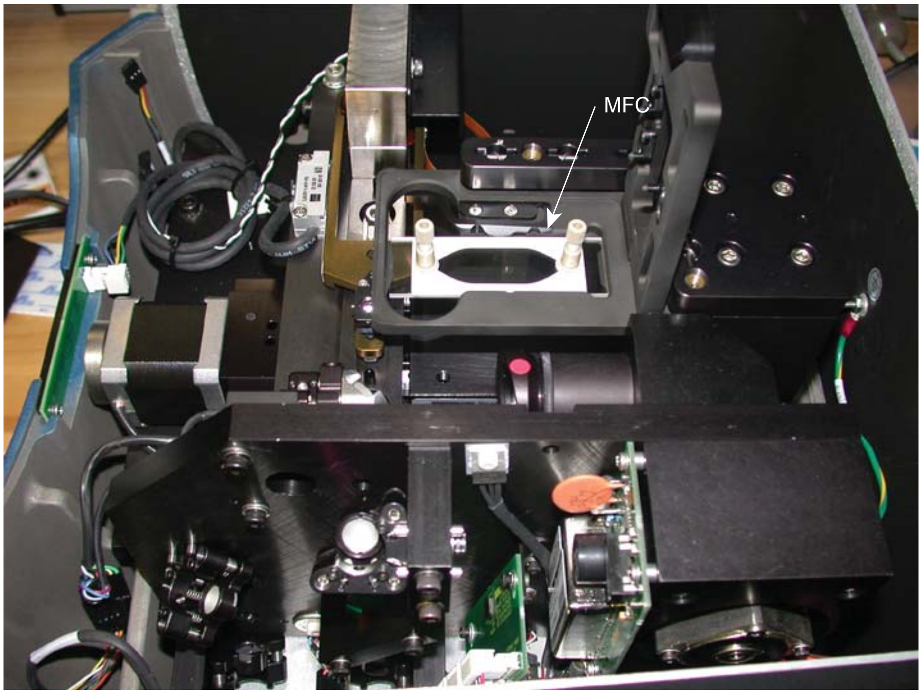

Figure 2. MFC integrated into a modified microarray laser scanner during a fit check.

Related References

1. Jaing, C., S. Gardner, K. McLoughlin, N. Mulakken, M. Alegria-Hartman, P. Banda, P. Williams, P. Gu, M. Wagner, C. Manohar, and T. Slezak, "A Functional Gene Array for Detection of Bacterial Virulence Elements," *PLoS ONE*, **3**, 5, p. 2163, 2008.
2. Wang, Z., L. T. Daum, G. J. Vora, D. Metzgar, E. A. Walter, L. C. Canas, A. P. Malanoski, B. Lin, and D. A. Stenger, "Identifying Influenza Viruses with Resequencing Microarrays," *Emerging Infectious Diseases*, **12**, 4, pp. 638–646, 2008.
3. Regan, J. F., A. J. Makarewicz, B. J. Hindson, T. R. Metz, D. M. Gutierrez, T. H. Corzett, D. R. Hadley, R. C. Mahnke, B. D. Henderer, J. W. Breneman, IV, T. H. Weisgraber, and J. M. Dzenitis, "Environmental Monitoring for Biological Threat Agents Using the Autonomous Pathogen Detection System with Multiplexed Polymerase Chain Reaction," *Anal. Chem.*, **80**, 19, pp. 7422–7429, 2008.

A Mesoscale Approach to Characterize Material Properties of Polymeric Media

Todd H. Weisgraber
(925) 423-6349
weisgraber2@llnl.gov

Over time, changes in the network microstructure of filled or reinforced elastomers due to chemical bond scission and crosslinking can alter the physical properties of these materials. In particular, chemical aging can strongly affect the elastic properties of the network through modifications to the network as well as changes in the interactions between the polymer and filler particles. Furthermore, changes in the mechanical properties can depend on the strain history. For example, an elastomer that undergoes additional crosslinking in a state of strain can acquire a permanent set or deformation when the stress is removed. The ability to accurately predict the mechanical behavior of these materials through robust models to predict lifetime performance in different environments is essential. We have adopted a mesoscale network model that retains information about the microstructure and is not limited by some of the assumptions found in constitutive descriptions.

Project Goals

The goals of this project were to 1) add the capability to extract material elastic properties from the network model; 2) conduct parametric studies to determine how these properties depend on crosslink density and interaction potentials; and 3) validate the capability of the model to predict material aging effects by comparison with experiments.

Relevance to LLNL Mission

This effort has enabled LLNL to play a key role in the multiscale modeling of mission critical materials through the linkage of scales. Specifically, we examine the relationship between a coarse-grained representation of the microstructure and the mechanical properties and lifetime performance of these materials. A variety of ongoing programs will benefit from these capabilities. A specific early adopter of this technology will be the Enhanced Surveillance Campaign (ESC).

FY2008 Accomplishments and Results

The mesoscopic network model consists of a set of nodes with selected node pairs linked by a single “bond,” which represent a crosslink in the network. Initially the connectivity is arranged on a simple cubic lattice with periodic boundary conditions (Fig. 1). The bond interactions are described by a FENE spring potential and the standard Lennard-Jones potential. Bonds within the initial cubic lattice are randomly selected and deleted from the lattice to obtain the desired crosslink density. The ensemble of bonded nodes is then relaxed via energy minimization to obtain the initial structure.

For the evaluation of the model we limited our tests to uniaxial extensions. We deformed the system in a static manner by first stretching the domain along the x-axis from L_x to λL_x at a constant volume. In the strained state, crosslinks were removed and added to simulate changes in the microstructure

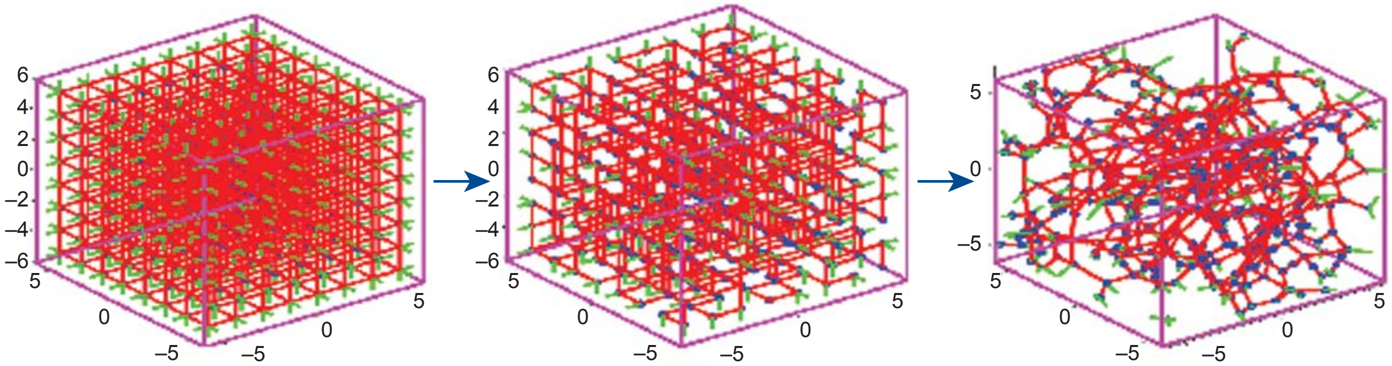

Start with a periodic cubic lattice

Randomly delete bonds to desired crosslink density

Relax to equilibrium

Figure 1. Initializing the microstructure in the mesoscopic model. Initially the crosslink bonds are arranged in a cubic lattice. After randomly depleting a fraction of crosslinks, the network is relaxed to an equilibrium state.

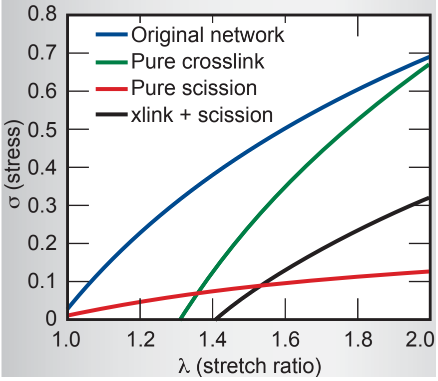

Figure 2. Modifying the crosslink network in a state of strain ($\lambda = 2$). The blue curve is the response of the original network, the green curve is the response after adding additional crosslinks, the red curve is the response after scissioning a fraction of the original network, and the black curve is the response after a combination of crosslinking and scissioning.

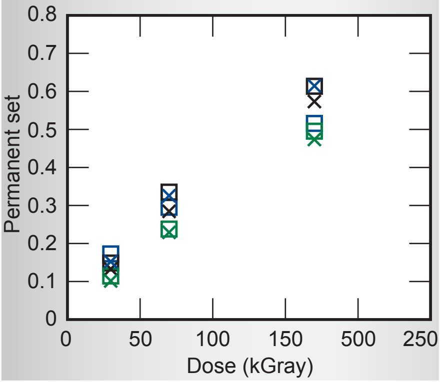

Figure 3. Permanent set experimental data (Chinn *et al.*) (squares) and model predictions (x's) for a range of radiation dosages applied at strained states of $\lambda_1 = 1.2$ (blue), $\lambda_1 = 1.4$ (black), and $\lambda_1 = 1.9$ (green).

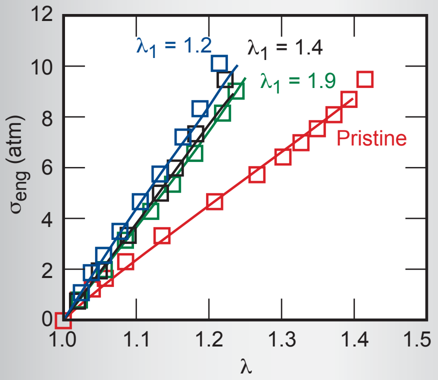

Figure 4. Stress response of experimental siloxane composite samples (Chinn *et al.*) (squares) after irradiating at 170 kGray at different stretch ratios, λ_1, and response of the mesoscopic model (lines).

due to aging phenomena. Bonds were randomly selected for scissioning and the new network was generated by selecting node pairs within a specified range from one another. An example of the model's response to modifying the bond structure at an extension ratio of $\lambda=2$ is depicted in Fig. 2. The blue curve represents the original network. If only crosslinks are added, the stress at $\lambda=2$ remains unchanged, which is consistent with the independent network hypothesis. However, when the model is compressed the additional crosslinks modify the elastic modulus and produce a permanent set in the system. The permanent set is defined as

$$P_s = \frac{\lambda_s - 1}{\lambda_1 - 1},$$

where λ_s is the extension ratio at which the stress returns to zero, and λ_1 is the applied deformation. If a fraction of the original network is scissioned without any additional crosslinking the strength of the network is reduced, resulting in a smaller modulus, but no permanent set results and the state of zero stress coincides with the original length. When both crosslinking and scissioning occur the network experiences both a reduction in stress and permanent set. The mesoscopic model reproduces the expected behavior for both crosslinking and scissioning.

To evaluate the predictability of the model, we compared our results to experiments that exposed samples of DC-745 under uniaxial strain to controlled dosages of γ-radiation from a Co-60 source. After removing the applied strain, the permanent set and stress response of the aged samples were measured. Figure 3 compares the permanent set predictions from the mesoscopic numerical model and the corresponding experimental values. Considering the simplicity of the model, the agreement is excellent, with the largest difference of 10% occurring at the 170-kGray dosage.

Finally, we further extended the networks irradiated at 170 kGray to compare the predicted material responses with the experimental samples. As shown in Fig. 4, the agreement at small stretch ratios is excellent and the increasing elastic modulus with decreasing λ_1 is reproduced.

Related References

1. Andrews, R. D., A. V. Tobolsky, and E. E. Hanson, "The Theory of Permanent Set at Elevated Temperatures in Natural and Synthetic Rubber," *J. Appl. Phys. Chem.*, **17**, pp. 352–36, 1946.
2. Rottach, D. R., J. G. Curro, G. S. Grest, and A. P. Thompson, "Effect of Strain History on Stress and Permanent Set in Cross-Linking Networks: A Molecular Dynamics Study," *Macromolecules*, **37**, 14, pp. 5468–5473, 2004.
3. Kremer, K., and G. S. Grest, "Dynamics of Entangled Linear Polymer Melts – A Molecular-Dynamics Simulation," *Journal of Chemical Physics*, **92**, 8, pp. 5057–5086, 1990.
4. Grimson, M. J., "Structure and Elasticity of Model Gel Networks," *Molecular Physics*, **74**, 5, pp. 1097–1114, 1991.
5. Chinn, S., S. DeTeresa, A. Sawvel, A. Shields, B. Balazs, and R. S. Maxwell, "Chemical Origins of Permanent Set in a Peroxide Cured Filled Silicone Elastomer – Tensile and H-1 NMR Analysis," *Polymer Degradation and Stability*, **91**, 3, pp. 555–564, 2006.

FY2009 Proposed Work

In the next fiscal year we have proposed to evaluate the mesoscopic model for other materials of programmatic interest (filled elastomers and foams) and compare its performance with established constitutive models.

Tunable Optical Cavities for Absorption Spectroscopy

Tiziana Bond
(925) 423-2205
bond7@llnl.gov

Frequency stability, low power consumption, and the compact nature of Vertical Cavity Surface Emitting Lasers (VCSELs) lead to a number of advantages over existing semiconductor laser technologies for use in tunable diode-laser-based absorption spectroscopy (TDLAS). VCSELs enable selective and sensitive trace-gas analysis, instrumental in environmental monitoring; and combustion research.

With MEMS-tunable VCSELs, the required wavelength tuning to sweep the gas absorption fingerprints is realized through the actuation of a suspended Bragg reflector, leading to physical variation of the optical path length. This results in the ability to tune emitted wavelengths on the order of tens of nanometers. Given the short axial length of a typical VCSEL, displacement of the suspended mirror results in the continuous tuning of a single lasing mode. These MEMS-tunable VCSEL devices have recently shown promise as a high-performance alternative to standard VCSELs for optical gas sensing, with demonstrations of the detection of carbon monoxide and carbon dioxide, as well as ammonia, at the telecom-relevant wavelength range near 1550 nm. We demonstrated the first MEMS-tunable VCSELs that operate within the 760 to 780 nm range, a relevant wavelength range for the detection of O_2.

Project Goals

Our goal has been to establish complex fabrication procedures to reliably reproduce electrostatically tunable MEMS-tunable VCSELs (Fig. 1a) for future miniaturized absorption spectroscopy sensors. In these devices, rapid and wide wavelength tuning is realized through the use of an electrostatically actuated micromechanical Bragg reflector (Fig. 1b). A novel fabrication method based on gas-phase etching of a room-temperature deposited amorphous-germanium (α-Ge) sacrificial layer to generate the suspended mirror was used.

The fabrication procedure for the short-wavelength MEMS-tunable VCSELs is a relatively complex process involving up to 12 lithographic levels for wire-bond enabled devices (Fig. 2). Fortunately, wafer scale processing is possible, which enables higher throughput in the fabrication of arrays of devices. It is also worth noting the strong potential of this platform for the simultaneous detection of various gases, since the critical central emission wavelengths, from visible to near-infrared to shortwave-infrared, depend on the selection and engineering of the epi-material.

Relevance to LLNL Mission

Our project supports several applications at the core of LLNL's national security missions, from Stockpile Stewardship to Homeland Security. It will sustain the development of a new class of compact, fiber compatible optical gas sensors for real-time detection of chemicals. This will facilitate minimally invasive trace-gas analysis for next-generation sensors. The 2-D nature of the technology enables other interesting applications such as multiplexed smart detection systems, adaptive imaging, beam forming, optical computing, and high-power lasers.

FY2008 Accomplishments and Results

In this second year, we have completed the creation and the characterization of the first MEMS-tunable VCSELs

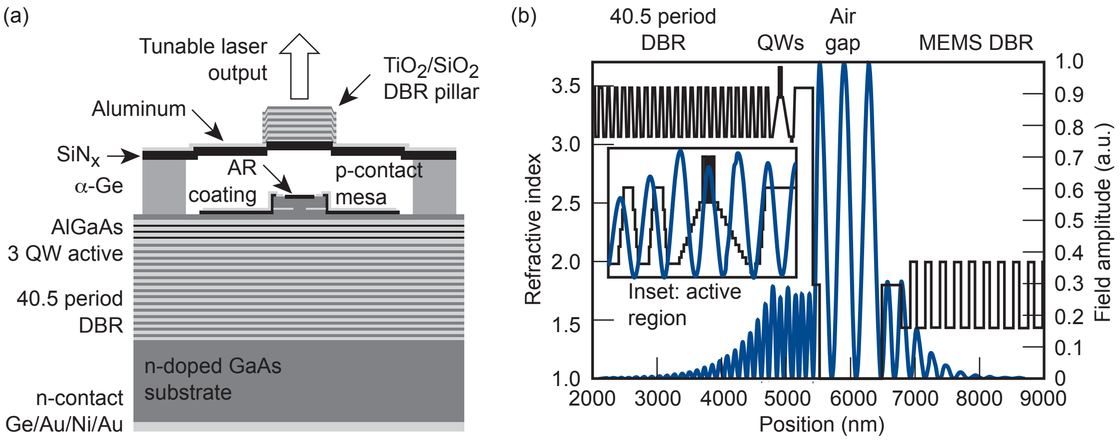

Figure 1. Short-wavelength MEMS-tunable VCSELs. (a) Schematic cross-section of the full materials structure; (b) refractive index profile and electric field intensity generated with a transmission matrix model.

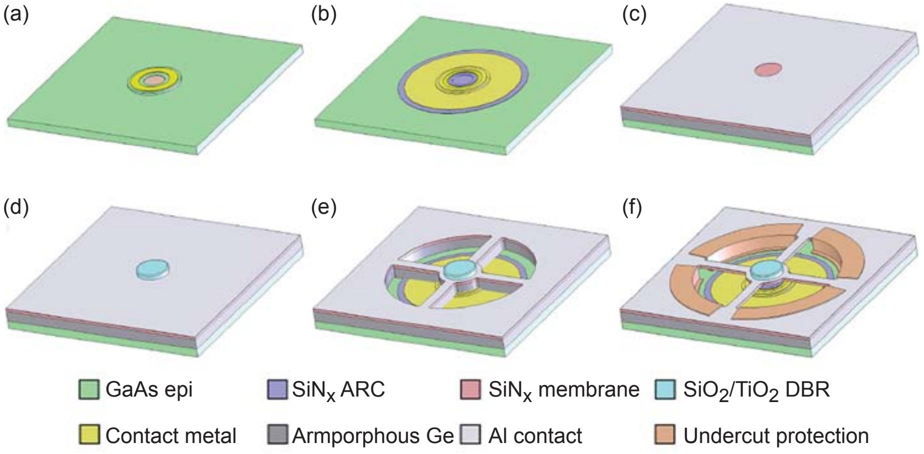

Figure 2. Schematic of the short-wavelength MEMS-tunable VCSEL process flow. (a) Mesa etch, AlGaAs oxidation, p-contact metallization, and contact window etch; (b) definition of the SiN$_x$ AR coating and Ti/Au pad; (c) deposition of the α-Ge sacrificial layer, SiN$_x$ membrane, and Al top contact, followed by patterning of the emission window; (d) blanket SiO$_2$/TiO$_2$ DBR evaporation and etch back; (e) ECR etch of actuator geometry; (f) liftoff of SiO$_2$ undercut protection and release by sacrificial Ge etching in XeF$_2$.

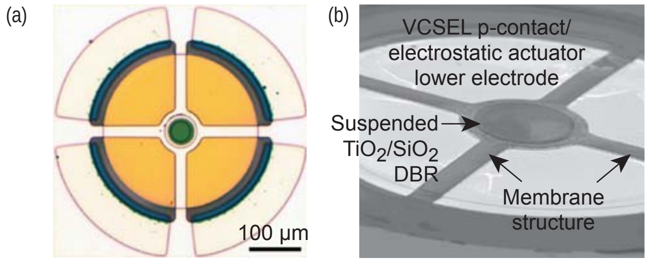

Figure 3. (a) Optical micrograph and (b) SEM photograph of an individual tunable VCSEL.

at emission wavelength below 800 nm with potential for a wavelength tuning range of +/– 30 nm, with scan rates up to 1 MHz (Figs. 3 and 4 show preliminary results). Currently, these devices exhibit multimode lasing operation between 767 and 737 nm. With an improved output power and single-mode emission, short-wavelength MEMS-tunable VCSELs should be extremely attractive as widely-tunable swept sources for unambiguous O_2 sensing.

Related References

1. Hovde, D. C., and C. A. Parsons, "Wavelength Modulation Detection of Water Vapor with a Vertical-Cavity Surface-Emitting Laser," *Appl. Opt.*, **36**, pp. 1135–1138, 1997.

2. Kögel, B., H. Halbritter, S. Jatta, M. Maute, G. Böhm, M.-C. Amann, M. Lackner, M. Schwarzott, F. Winter, and P. Meissner, "Simultaneous Spectroscopy of NH3 and CO Using a > 50 nm Continuously Tunable MEMS-VCSEL," *IEEE Sens. J.*, **7**, pp. 1483–1489, 2007.

3. Zappe, H. P., M. Hess, M. Moser, R. Hövel, K. Gulden, H.-P. Gauggel, and F. Monti di Sopra, "Narrow-Linewidth Vertical-Cavity Surface-Emitting Lasers for Oxygen Detection," *Appl. Opt.*, **39**, pp. 2475–2479, 2000.

4. Cole, G. D., E. Behymer, L. L. Goddard, and T. C. Bond, "Fabrication of Suspended Dielectric Mirror Structures Via Xenon Difluoride Etching of an Amorphous Germanium Sacrificial Layer," *J. Vac. Sci. Technol., B* **26**, pp. 593–597, 2008.

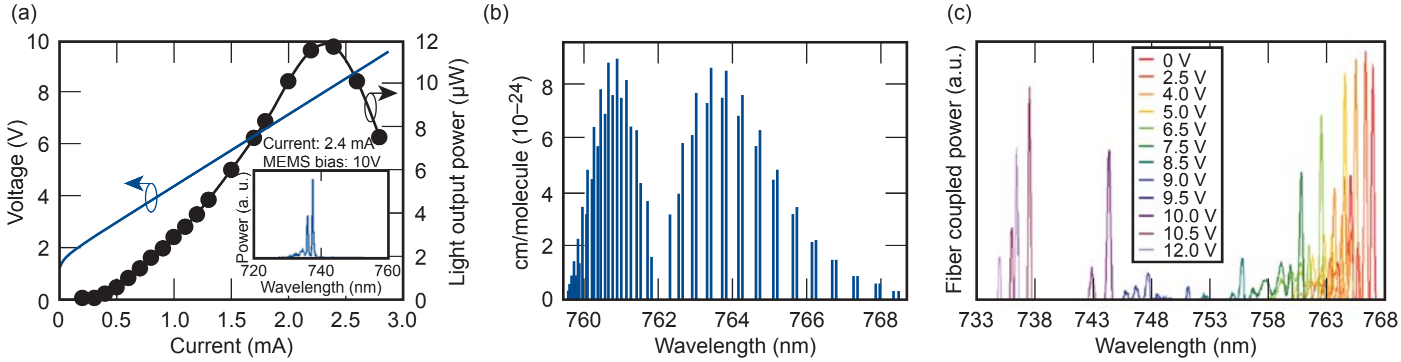

Figure 4. (a) Voltage and light output as a function of drive current for a MEMS-tunable VCSEL with a 13.5 period suspended mirror structure. Inset: tuning response for a constant laser drive current of 2.4 mA over a range of 30 nm. (b) HTRAN O_2 absorption spectrum. (c) Wavelength tuning range as a function of applied voltage.

A Micro-Opto-Mechanical Photoacoustic Spectrometer

Jack Kotovsky
(925) 424-3298
kotovsky1@llnl.gov

This report describes progress achieved in a one-year feasibility study of a photoacoustic spectrometer (PAS). Specifically, this team sought to create an all-optical and miniaturized photoacoustic spectrometer sensing (PASS) system. The PASS system includes all the hardware needed within a gas environment to analyze the presence of a large variety of molecules. The all-optical PASS system requires only two optical fibers to communicate with the optoelectronic power and readout systems that exist outside of the gas environment. These systems can be at any distance from the PASS system since signal loss through the optical fibers is very small.

The PASS system is intended to be placed in a small space where gases need to be measured. The size and all-optical constraints placed on the PASS system demand a new design. The PASS system design includes a novel acoustic chamber, optical sensor, power fiber coupling and sensing fiber coupling.

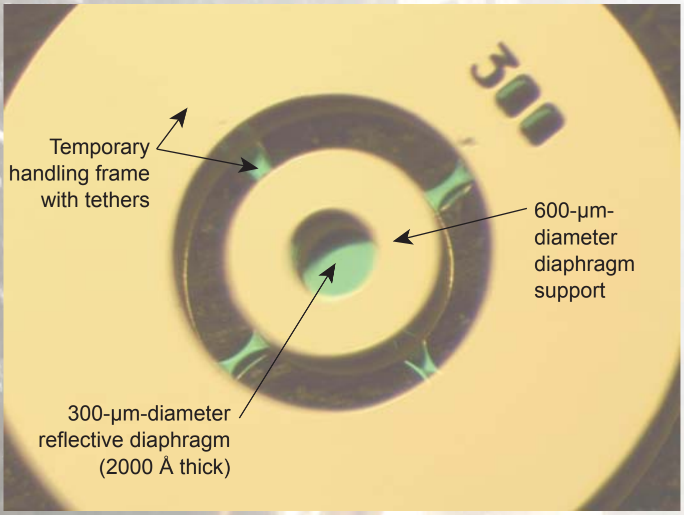

Figure 1. Backside view of the micro-opto-mechanical (MOMS) diaphragm sensor.

Project Goals

Our collaborators at the Atomic Weapons Establishment (AWE) have proven the capabilities of a complete PAS that uses a macroscale PASS system. It was our goal to miniaturize the PASS system and turn it into an all-optical system to allow for its use in confined spaces that prohibit electrical devices. This goal demanded the study of all the system components, selection of an appropriate optical readout system, and the design and integration of the optical sensor to the PASS system. A stretch goal was to fabricate a completed PASS system prototype.

Relevance to LLNL Mission

Future surveillance of the nuclear weapons stockpile demands specialized sensors for systems monitoring. This need includes broad-specie gas monitoring. A variety of commercial gas monitoring tools are available but none of these tools come close to meeting the stringent requirements for stockpile implementation. Specifically, material, size, power, safety, and security requirements eliminate the use of commercial devices. For this reason, novel instrumentation must be developed. This effort is part of an ongoing LLNL Microsensors Program that creates these novel sensing systems.

FY2008 Accomplishments and Results

During the year, the demand for a miniature, all-optical PASS system evolved from a problem statement to an array of working prototypes. The following sections present chamber design, sensor design, fiber coupling design, and system integration.

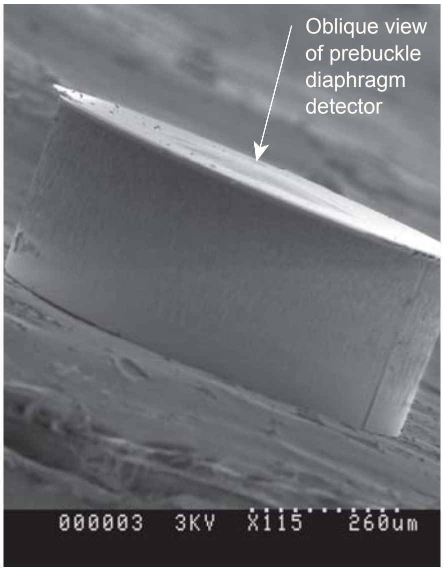

Figure 2. Electron micrograph of a MOMS diaphragm sensor.

Chamber Design. The PAS system depends on the measurement of pressure pulses if a gas of interest is present. The sensitivity of this measurement depends on the magnitude of pressure fluctuation around ambient. Although an open-air system is possible, the magnitude is enhanced by an enclosure that constrains the gas volume. Modeling work performed by AWE suggests a cylindrical acoustic chamber with no significant openings provides excellent pressure response. Modular cylindrical prototypes were designed and fabricated to allow system characterization under varied chamber dimensions. Several chamber lengths and diameters were created.

Sensor Design. A sensor design that shows excellent sensitivity and durability is desired. The material choice must meet the stringent constraints of weapon systems and survive very long deployments. A variety of optical films were created in the LLNL microfabrication facility. These include combinations of silicon nitride, silicon oxide, and metallic coatings. Ultimately, a circular diaphragm was created that includes a multilayer material stack for stress-tuning (Figs. 1 and 2). Optical measurements show that an excellent optical return is achieved with a pre-buckled diaphragm. The buckled diaphragm is designed to give enhanced sensitivity by reducing the diaphragm stiffness.

Choice of a specialized optical interferometer readout system allows for very robust diaphragm movement detection. Fiber alignment and positioning of the readout system is not critical, making the overall PASS system very robust. The power and sensing systems were designed to be insensitive to position variation, enhancing the system's long-term survivability and simplicity.

Fiber Coupling Design. For this study, both single and dual fiber designs were considered but only the dual fiber design was pursued to simplify initial testing and to help isolate any difficulties that may occur in testing. For PAS operation, laser power is coupled to the acoustic chamber in either time or modulation-frequency division multiplexing via the power fiber. A single fiber carries the stimulating laser light to the acoustic chamber. The interferometric readout system also uses a single fiber to detect diaphragm motion. This fiber is coupled to the opposite end of the acoustic chamber (Fig. 3). Both coupling ferrules are modular and similar in form to allow efficient testing of varied diaphragm sensors.

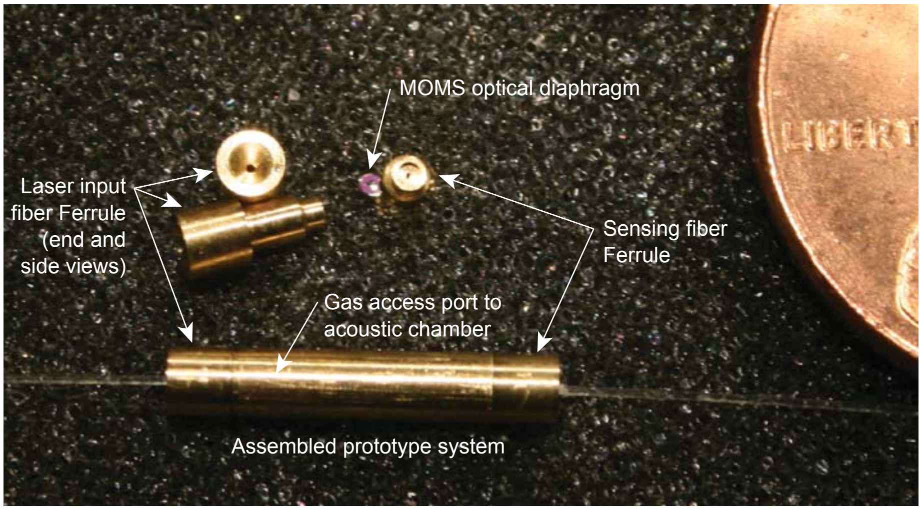

Figure 3. Components of the PASS system and a complete PASS prototype.

Related References

1. Parkes, A. M., K. A Keen, and E. D. McNaghten, "Trace Gas Detection Using a Novel Cantilever-Based Photoacoustic Spectrometer with Multiplexed Optical Fiber-Coupled Diode Lasers and Fiber-Amplification," *Fibre Optic Sensors and Applications V, Proc. SPIE, E. Udd, Ed.*, **67701C**, 2007.

2. Lindley, R. E., A. M. Parkes, K. A. Keen, E. D. McNaghten, and A. J. Orr-Ewing, "A Sensitivity Comparison of Three Photoacoustic Cells Containing a Single Microphone, a Differential Dual Microphone or a Cantilever Pressure Sensor," *Applied Phys. B., Lasers and Optics*, 2006.

Project Summary

This one-year feasibility study proved the design and fabrication of a novel, miniature PASS system can be achieved. The system was conceived, preliminary studies performed, and ultimately, several prototypes were built that will be tested by collaborators at AWE. Follow-on work is anticipated to advance the technology once the results are obtained from the initial testing and quantification of the system performance.

Cadmium-Zinc-Telluride Sandwich Detectors for Gamma Radiation

Rebecca J. Nikolić
(925) 423-7389
nikolic1@llnl.gov

Detectors to sense nuclear and radioactive weapons concealed in transit through borders, airports, and seaports are crucial for countering terrorism and proliferation of weapons of mass destruction. Currently, germanium (Ge) detectors offer the best performance in detecting gamma rays; however, they must be operated at cryogenic temperatures. A room-temperature detector is greatly preferred because of cost and ease of use, but the only available alternative is based on cadmium zinc telluride (CZT) technology, which offers inferior performance.

Here we propose a pathway for CZT gamma-detectors to achieve the desired energy resolution of better than 1%. We will use a multilayered structure which we call a “sandwich detector,” to allow signal collection while simultaneously rejecting noise. By applying energy bandgap engineering to this discipline, we believe detector performance can be improved.

Project Goals

With this project, we expect to demonstrate a gamma detector with better than 1% energy resolution that will operate at room temperature. To achieve this goal, we will design a novel structure using bandgap engineering concepts that will result in a 90% reduction in leakage current relative to a resistive device. We also will provide leadership to the detector community by providing a technical roadmap for how to demonstrate 0.5% energy resolution within five years.

Relevance to LLNL Mission

The solution to the radiation-detector materials problem is expected to have significant impact on efforts to develop detectors that are compact, efficient, inexpensive, and operate at ambient temperature for the detection of special nuclear materials as well as radiological dispersal devices. The multidisciplinary nature of this work and the relevance to national and homeland security

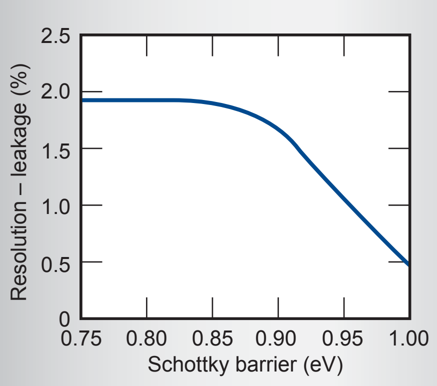

Figure 1. Calculated data showing the relationship between resolution and Schottky barrier height. With a hole barrier height of > 1 eV, we predict the component of resolution stemming from leakage will be 0.5%.

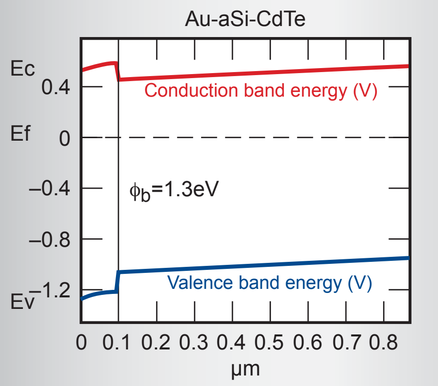

Figure 2. Silvaco simulation showing energy band diagram of an amorphous Si CdTe detector resulting in a large Schottky barrier height of 1.3 eV.

align well with LLNL capabilities and missions.

FY2008 Accomplishments and Results

In FY08, we accomplished the following as illustrated in Figs. 1 to 4:

1. We determined the relationship between resolution, dark current, and Schottky barriers.
2. We prepared amorphous material films including electron beam evaporated Ge and chemical vapor deposition of hydrogenated silicon (Si), characterized by current-voltage methods for resistivity, Rutherford backscattering for hydrogen content (for hydrogenated Si) and substrate curvature measurements for stress evaluation.
3. These techniques were used to fabricate low-leakage gamma detectors using an amorphous layer between the metal contact and the CdTe.
4. We demonstrated an effective resistivity of > 10^{11} Ω-cm at 100 V in material (resistivity of 10^9 Ω-cm) that is considered too conductive for high performance CdTe gamma detectors.

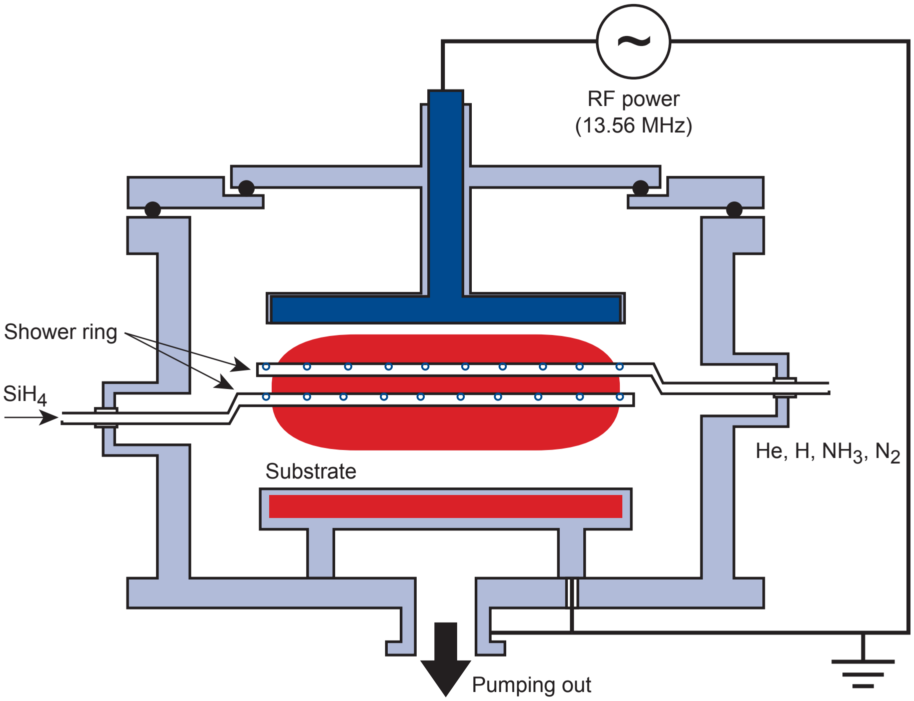

Figure 3. Schematic of the plasma-enhanced chemical vapor deposition tool used for the hydrogenated amorphous Si deposition using SiH_4.

FY2009 Proposed Work

In FY2009, we propose to 1) benchmark our models with experimentally gathered data from FY2008 and refine models to account for any discrepancy; 2) design and fabricate CZT detectors with amorphous layers and carry out both electrical and radiation characterization; 3) use these structures to characterize the interface and energy barrier between the amorphous material and single-crystalline CZT; and 4) demonstrate an effective resistivity of > 10^{11} Ω-cm (>200 V) in material that is considered too conductive for typical CZT gamma detectors with resistivity of 10^9 Ω-cm.

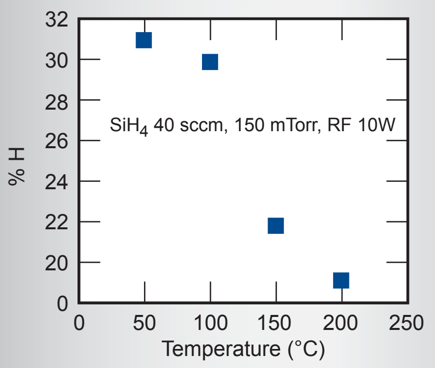

Figure 4. Hydrogen content determined by RBS of our hydrogenated amorphous Si films.

Fabrication of High Resolution CZT Detectors

Rebecca J. Nikolić
(925) 423-7389
nikolic1@llnl.gov

Summary of detector parameters using both 1000- and 3000-Å barriers.

Epi-growth		
Composition	Thickness	Doping
$Hg_{0.7}Cd_{0.3}Te$	1000 & 3000 Å	Undoped
Wafer		
n - type, growth on 211 orientation, 10^{-9} cm		

It is an important national security need to be able to ubiquitously deploy high-resolution (preferably room temperature) gamma detectors in the field to provide unambiguous identification of special nuclear materials (SNM) as well as other potential threats.

The energy resolution for semiconductor-based gamma detectors is defined as the full width at half maximum (FWHM) of a peak divided by the energy of the peak. The ideal characteristic would be an impulse function. This, however, is not the case in practice and the detected signals can be challenging to resolve and interpret. At present, the only commercially available room-temperature (E_g = 1.6 eV) alternative to cryogenically-cooled germanium (Ge) detectors is based on Cadmium Zinc Telluride (CdZnTe), which has a resolution of about 10 times worse than Ge-based gamma detectors. The cooling requirement of Ge is an encumbrance and a room temperature detector is greatly preferred. It is critical to have very-high-resolution gamma detectors for unambiguous identification of SNM, so as to avoid false alarms. Only the cryogenically-cooled Ge material is able to resolve the SNM signatures with high certainty. Much improvement in CdZnTe is necessary.

There are two approaches that can be taken to improve the resolution of CZT. The first approach is by increasing the resistivity of the CdZnTe material, which will reduce the current through the device. The second approach is to change the physical layer configuration of the device. In this work we will grow lattice-matched materials on CdZnTe

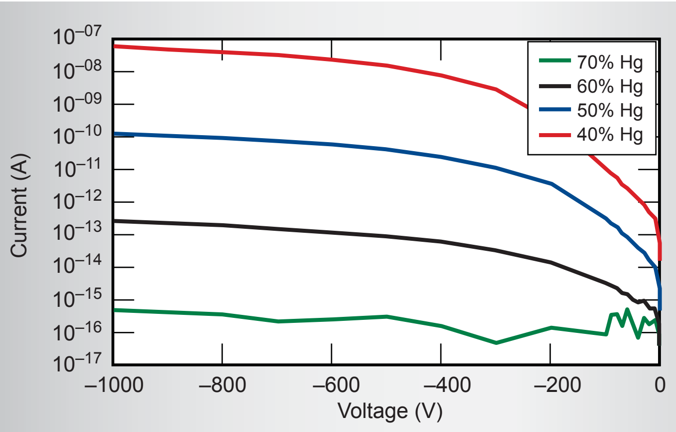

Figure 1. Silvaco simulations of voltage vs. current for various Hg compositions for the $Hg_xCd_{1-x}Te$ blocking layer. The simulations show that a dramatic decrease in leakage current through the device can be achieved with 70% Hg composition.

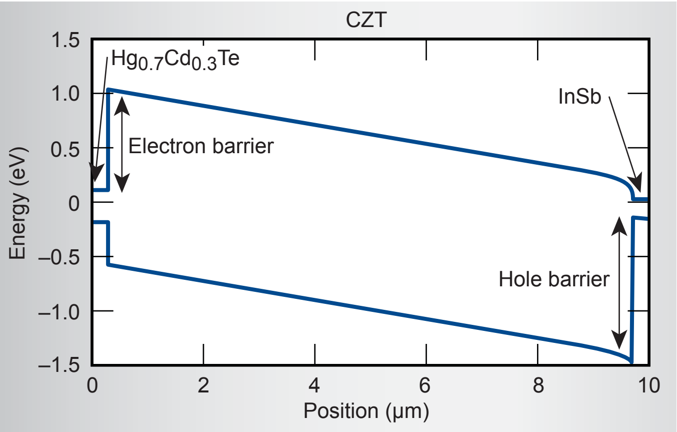

Figure 2. Silvaco simulation of HgCdTe/CZT/InSb radiation detector.

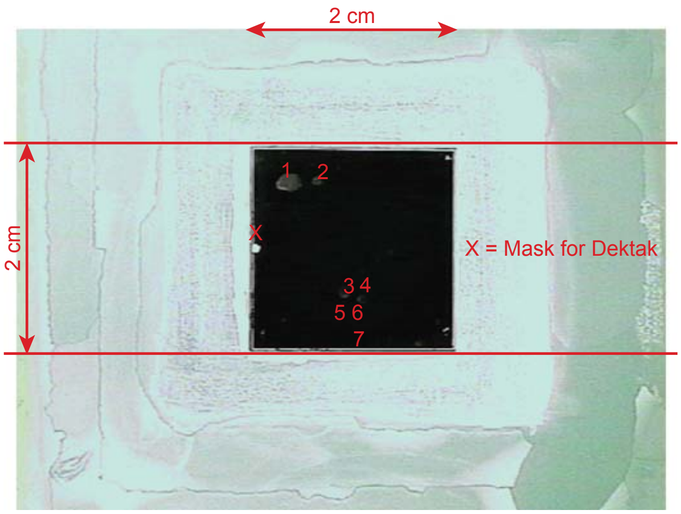

Figure 3. Wafer photograph after growth.

Defects	Defect type	Nomarski
1–6	Polishing scratches	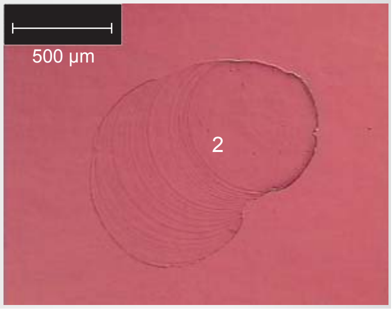
7	Point defects	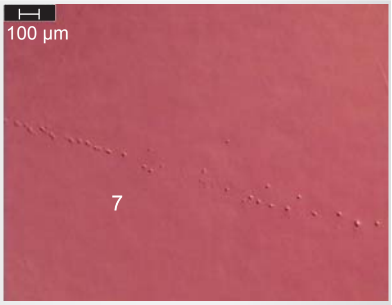
Defects are mainly large polishing scratches similar to other wafers (around the edges of the wafer).		

Figure 4. Defect identification for wafer shown in Fig. 3.

detectors to block the leakage current within the device. For this project the focus is on the electron barrier mercury cadmium telluride (HgCdTe); however, a hole barrier (InSb) can also be used.

Project Goals

We will create layer structures of lattice-matched HgCdTe on CdZnTe wafers. Parameters will include the CdZnTe wafer orientation and resistivity as well as the HgCdTe composition for lattice matching to the CdZnTe wafer, and HgCdTe thickness, doping type, and concentration. This will be implemented with the Silvaco simulation code. Wafers will be grown at Teledyne.

Relevance to LLNL Mission

The detection of radioactive and nuclear materials in the field is an important component of the LLNL mission both from a counterterrorism as well as nonproliferation perspective. The proposed work aligns well with the internal Science and Technology roadmap that supports this mission.

FY2008 Accomplishments and Results

Our accomplishments included the following:

1. Silvaco simulations were carried out to evaluate various Hg compositions and downselect to a low leakage current structure. The parameters included CdZnTe wafer orientation and resistivity as well as the HgCdTe composition for lattice matching to the CdZnTe wafer, and HgCdTe thickness and doping. The completed configuration is shown in the table.
2. The wafers were grown by molecular beam epitaxy (MBE) at Teledyne. The wafers have a small number of polishing scratches and defects which will be correlated to the device performance.

FY2009 Proposed Work

The next step of the project will focus on testing and characterizing the performance of the device and demonstrating significant reductions in leakage current as a result of the new architecture.

Flow Programmed Mesoscale Assembly of Nanoengineered Materials and Net Shape Components

Klint A. Rose
(925) 423-1926
rose38@llnl.gov

In a continuing effort from FY2007, we demonstrated the ability of our mesoscale assembly system to synthesize porous polymer layers with varying density profiles and packing structures. The system is currently capable of integrating highly dissimilar materials and producing features with critical dimensions in the submicron range. This system enables nm-scale precision synthesis of mm- to cm-scale materials and parts in a simple, low-cost system.

We perform this synthesis by computer-controlled electrophoretic deposition in a miniature aqueous deposition cell interfaced to computer-controlled automated fluidics. Nanoparticle solutions are available in a wide and ever-growing variety of material compositions, morphologies, and surface chemistry states. We introduce mixtures of various precursor solutions into the deposition cell, and deposit nm- to µm-scale layers by the pulsed-field electrophoretic deposition of particles onto substrates. We use post-deposition sintering to achieve densification of these films.

The high degree of control and wide range of heterogeneous materials made accessible by this approach brings powerful, low-cost capabilities to the fabrication of density- and composition-varying layers. The highly conformal nature of the deposition allows the fabrication of near-net shape high precision parts. The lack of need for vacuum conditions allows high-speed and low-cost nanomaterial synthesis in a simple benchtop system.

The system is available for follow-on work to capitalize on the broader capabilities it makes accessible, including the programmed synthesis of parts incorporating dissimilar and custom materials, the *in-situ* fabrication of hemispherical and other net-shape parts, and

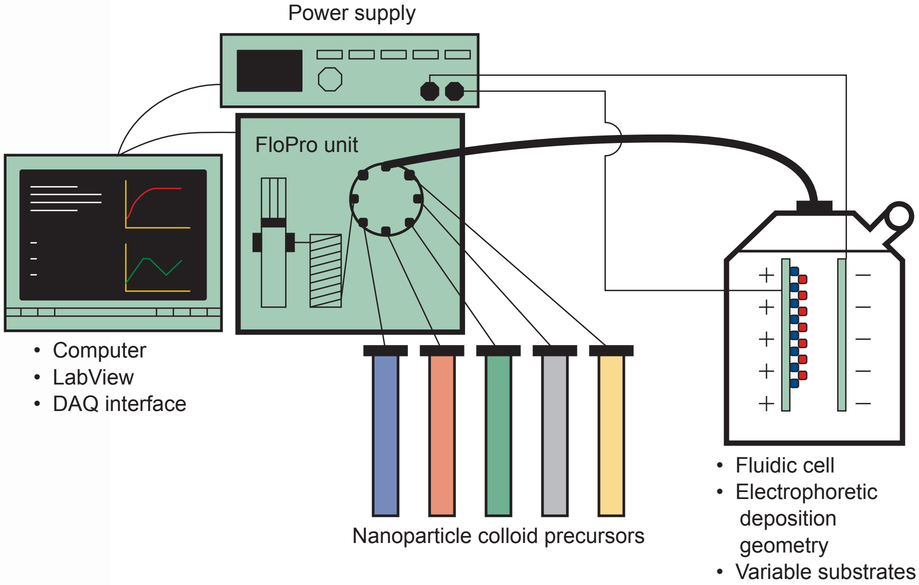

Figure 1. Schematic of the mesoscale assembly system. A FloPro unit provides automated valving and pumping to move particle solutions through the deposition cell. The power supply provides either constant voltage or constant current across the particle-laden fluid. The fluidics and the power supply are controlled via LabView software for full automation.

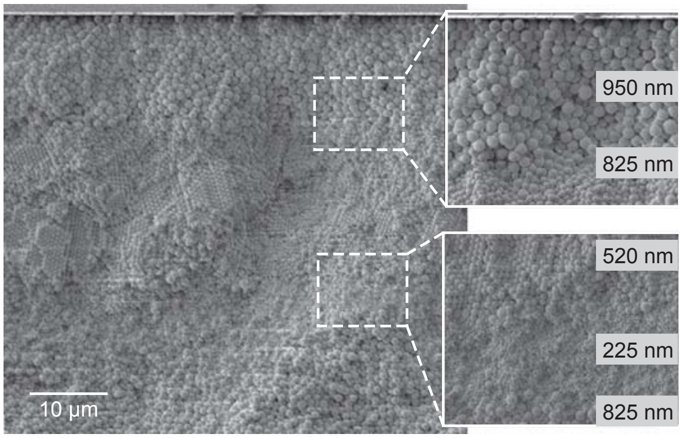

Figure 2. Example of a five-layer film deposited using polystyrene particles as the precursor material. The particles range in size from 225 to 950 nm in diameter. The total film thickness for this example is approximately 100 µm.

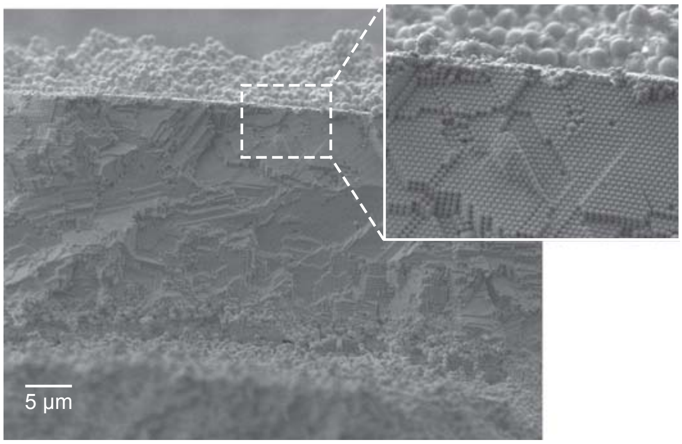

Figure 3. Example of the ordered packing structure achievable with the appropriate deposition parameters. The particles are 525-nm-diameter polystyrene.

ultimately the electronically-controlled assembly of nanostructured composite and functional materials.

Project Goals

The goals in the second year of this project were to: 1) optimize the control scheme for operating the deposition system based on basic transport models; and 2) demonstrate the synthesis of porous polymer layers with pre-defined, smoothly varying density profiles.

Relevance to LLNL Mission

This project was part of a new, integrated, mutually supporting, and dynamic multi-project portfolio in novel nanomaterial synthesis capabilities for mesoscale manufacturing. This portfolio is directed to LLNL application areas in target materials and structures, sensor materials, and biodetection devices. The short-term payoff is the creation of new nanoscale target structures. The proposed technology is ideal for combining novel nanomaterial components such as engineered nanoparticles, carbon nanotubes, and others into complex materials and structures. Future applications of this approach could include transparent ceramic optics for new high-powered lasers, ceramic armor, and new structures for radiation and IR detectors.

FY2008 Accomplishments and Results

We have accomplished the second year goals of this project using the prototype system assembled in FY2007 (Fig. 1). Specific results and accomplishments include the following.

1. fabricated four- and five-layer polystyrene films of different particle sizes with sharp transitions between each layer (Fig. 2);
2. demonstrated the ability to deposit polystyrene particle layers with ordered packing structures (Fig. 3);
3. demonstrated the deposition and drying of a relatively thick (> 375 µm) multilayer polymer film with smooth transitions between regions of different density (Fig. 4); and
4. deposited polydisperse 200-nm YAG particles to create a 6-mm-thick part which sintered translucent. Total deposition time was 5 min.

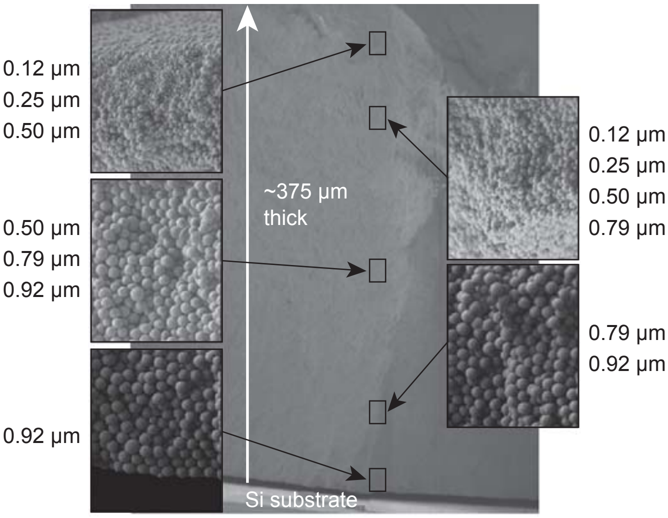

Figure 4. Cross-section of a multilayer polystyrene film with smooth transitions between each region. The smooth transitions reduce film stresses between the layers and eliminate cracking and peeling.

High-Resolution Projection Micro-Stereo-lithography (PμSL) for Advanced Target Fabrication

Christopher M. Spadaccini
(925) 423-3185
spadaccini2@llnl.gov

Our objective is to advance the state of the art in 3-D target fabrication by using Projection Micro-Stereolithography (PμSL), first developed at the University of California, Los Angeles (UCLA) and the University of Illinois, Urbana-Champaign (UIUC). PμSL is a low-cost, high-throughput, microscale, stereolithography technique that uses a Digital Micromirror Device (DMD^{TM} Texas Instruments) or a Liquid Crystal on Silicon (LCoS) chip as a dynamically reconfigurable digital photomask.

PμSL is capable of fabricating complex 3-D microstructures in a bottom-up, layer-by-layer fashion. A CAD model is first sliced into a series of closely spaced horizontal planes. These 2-D slices are digitized in the form of a bitmap image and transmitted to the DMD. A UV lamp illuminates the DMD, which acts as a dynamically reconfigurable photomask and transmits the image through a reduction lens into a bath of photosensitive resin. The resin that is exposed to the UV light is then cured and anchored to a platform and z-axis motion stage. The stage is lowered a small increment and the next 2-D slice is projected into the resin and cured on top of the previously exposed structure.

Figure 1 shows a schematic of this process. This layered fabrication continues until the 3-D part is complete (Fig. 2).

The process has already been shown at UIUC to have the capability to rapidly generate complex 3-D geometries. Applying this concept to target fabrication problems and advancing PμSL capability with respect to these issues constitutes the primary focus of the research. PμSL performance, such as resolution, materials, geometries, and substrates, will be greatly improved by the following research directions:

1. the study of meta-materials to enhance the system resolution to below the diffraction limit of the UV light enabling a 3-D, nanoscale, direct write fabrication system;
2. the use of multiple light beams to generate 3-D holographic interference patterns;
3. the use of laminar flow microfluidic systems to more optimally deliver

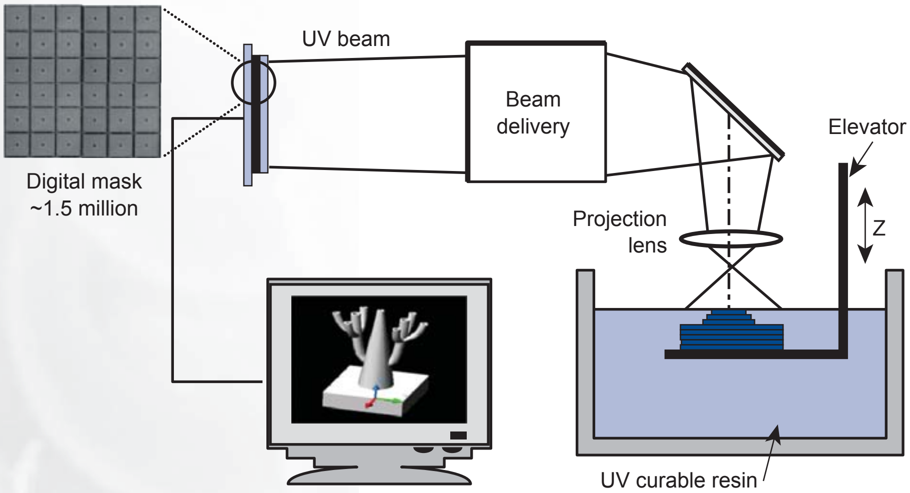

Figure 1. Schematic of baseline PμSL system currently at UIUC.

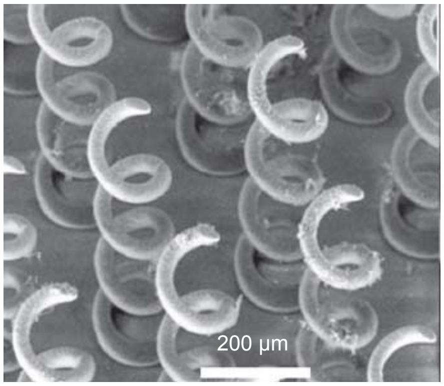

Figure 2. SEM image of PμSL fabricated coils.

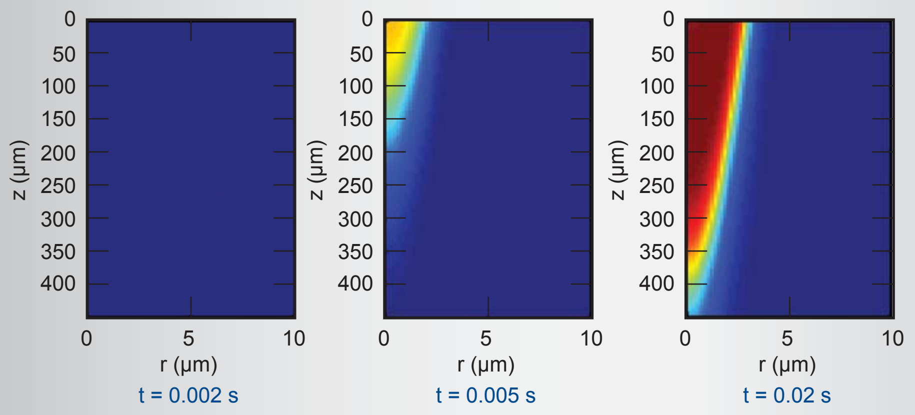

t = 0.002 s

t = 0.005 s

t = 0.02 s

Figure 3. Results from COMSOL model: depth profiles of polymerized resin with a light intensity of 260 kW/m^2 for three times.

and distribute photosensitive resins enabling fabrication with multiple materials; and

4. the development of a coupled optical-chemical-fluidic model resulting in an empirically validated design tool.

Project Goals

The project goals for FY2008 include the following:

Establishing a baseline PμSL capability at LLNL. A PμSL system will be constructed based on the existing system at UIUC. This system will be capable of fabricating fully 3-D parts out of polymer resin with feature sizes below 10 μm.

Improving resolution using meta-materials. Imaging and lithography using conventional optical components is restricted by the diffraction limit of light. Subwavelength information is carried by evanescent waves, which decay exponentially. Meta-materials and plasmonic engineering may be used to retain and even to protect these evanescent wave fields. Our collaborators at UIUC are working in this area to identify a path toward improved resolution using these techniques.

Establishing a baseline coupled optical-chemical-fluidic model. Two fundamental factors limiting the spatial resolution of PμSL systems are the optical resolution of the projected image and the physical-chemical characteristics of the resin. A numerical model will be established and implemented to reveal the fundamental limiting phenomenon.

Relevance to LLNL Mission

Target fabrication for LLNL's NIF and other stockpile stewardship physics experiments has been a critical factor in limiting the scope of tests that can be conducted. Research efforts across LLNL have focused on developing new fabrication techniques that can generate meso- to micro-scale targets with micro- to nanoscale precision. Although much progress has been made, several key target features have been difficult to achieve. High-resolution PμSL has the potential to directly impact all of these limitations and may also have great benefit to the newly emerging LIFE program at LLNL, which has its own set of target fabrication challenges. An ancillary impact of this work is to enable a host of new MicroElectroMechanical Systems (MEMS) devices never before achieved, due to the rapid, high-resolution, fully 3-D nature of the technique.

FY2008 Accomplishments and Results

Accomplishments in FY2008 began with the construction of a baseline PμSL system at LLNL. We have built a functioning system using an LCoS chip as the digital masking element and a UV LED array as the light source. The system is controlled via a LabView graphical interface.

Additionally, the use of meta-materials to improve resolution of a PμSL system at UIUC is underway.

Finally, the modeling effort at LLNL has resulted in a baseline optical-chemical model, which can predict the depth and profile of photo-polymerization. The model has been implemented in COMSOL Multiphysics. Figure 3 shows the depth and shape of the polymerizing medium for several times after exposure to UV light at an intensity of 260 kW/m^2.

Related References

1. Cox, A., C. Xia, and N. Fang, "Micro-Stereolithography: A Review," *ICOMM*, No. 55, 2006.

2. Sun, C., N. Fang, D. M. Wu, and X. Zhang, "Projection Micro-Stereolithography Using Digital Micro-Mirror Dynamic Mask," *Sensors and Actuators: A Physical*, **121**, pp. 113–120, 2005.

FY2009 Proposed Work

Expected achievements and goals for FY2009 include:

1. fabrication of first components from the baseline LLNL PμSL system and optimization of the system;

2. fabrication of the first nanoscale features;

3. validation of the baseline optical-chemical model via comparison with fabricated parts;

4. inclusion of fluid motion into the optical-chemical model; and

5. design for multiple light beams to enable holographic lithography.

Microfabricated Technologies for Target Fabrication

Robin Miles
(925) 422-8872
miles7@llnl.gov

Atomic layer deposition (ALD) is the newest form of chemical vapor deposition technique, capable of achieving layer thickness control to atomic monolayer resolutions and conformal coating in deep complex structures. This technique has been used to make novel structures such as nano-film capacitors, nano-FETS and tunable nano-magnetic structures.

Figure 1. Atomic layer deposition tool installed in LLNL's Microfabrication Facility.

Project Goals

The goal of this project was to become familiar with the operation of the tool, to make the appropriate fixtures to use the tool on a number of substrates of interest, and to characterize the tool for use with various deposited layers.

Relevance to LLNL Mission

LLNL has purchased an ALD tool primarily for coating foams for physics/fusion targets. The ALD system shown in Fig. 1 is installed in LLNL's Microfabrication Facility cleanroom.

FY2008 Accomplishments and Results

Many materials in target fabrication, in particular the low-density foams used in the current capsule configurations, can be fabricated using an ALD system. ALD is a newer deposition technique wherein high-aspect-ratio features can be conformally coated to very precise thicknesses. ALD works by using a two-step deposition process. First, a vapor-phase precursor is introduced that reacts only with the substrate surface. Because only an exposed surface can be coated in this step, a monolayer is applied to the substrate and over a period of time the gas penetrates into the crevices of the structure, applying this monolayer uniformly over complex structures.

A second vapor-phase precursor is introduced that reacts only with the deposited layer of the first precursor to create a new layer of the desired substrate material, which is now able to again react with the first precursor gas. The precursor gases are alternately introduced into the reaction chamber and with each cycle an additional atomic layer is deposited. The high vapor pressure of the gases allows for the penetration into high-aspect-ratio features. The number of cycles determines the deposition thickness.

The tool can be used in both dynamic and static modes. In dynamic mode, the precursors are introduced into moving streams of carrier gas, which sweeps through the chamber. This is the most common mode of operation. In static mode, the chamber exit is closed for a period of time to allow for more time for the precursor to penetrate into the pores of the materials such as deep holes and foams.

Many of the targets used in physics experiments require low-densities of specific materials. One mechanism for producing these materials is to coat foam materials. Foam structures such as silica aerogel are complex porous materials. The ALD precursor gases can penetrate into the lattice of the foams and apply an ultra-thin layer to the foam ligaments. In this way, it is possible to create any number of low-density metal foams such as copper, tungsten or platinum foams.

Users were trained in the use of the tool in both static and dynamic modes. A sample holder was made to hold smaller than wafer size parts such as foams. A series of test articles were made to test conformal characteristics of the coatings. Test results for alumina depositions on silicon wafers show high uniformity across a 150-mm-diameter wafer. A graph of the deposition thickness versus cycles (Fig. 2) shows a deposition rate of about 0.11 nm/cycle for alumina with uniformity across a 150-mm wafer of less than 0.5 nm in a 450-nm-thick film (Fig. 3).

Related References

1. Klootwijk, J. H., *et al., IEEE Electron Device Letters*, **28**, pp. 740–742, 2008.
2. Winkelmann, C. B., *et al., Nano-Letters*, **7**, pp. 1454–1458, 2007.
3. Bachmann, J., *et al., J. American Chemical Society*, **129**, pp. 9554–9555, 2007.

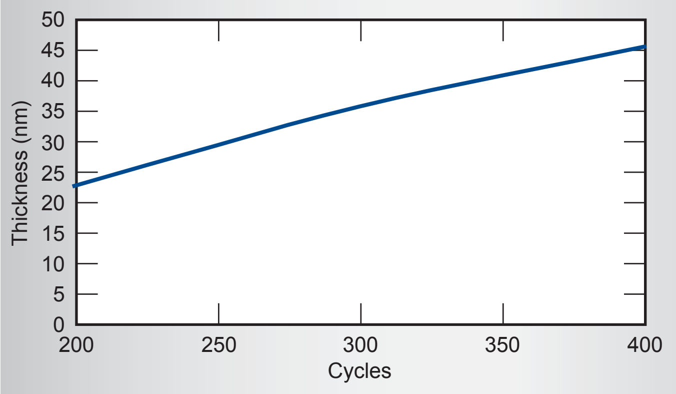

Figure 2. Graph showing layers of alumina deposited per cycle.

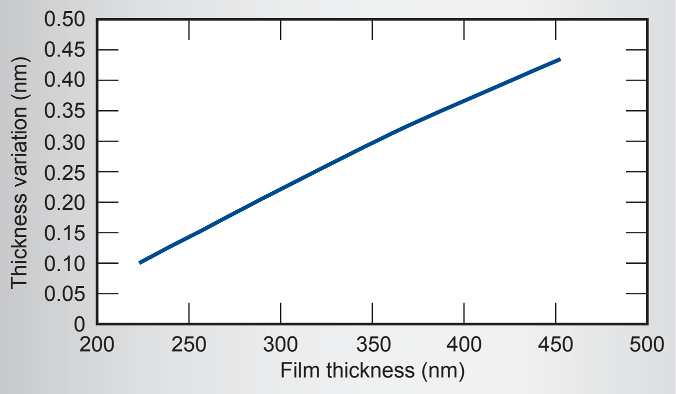

Figure 3. Graph showing uniformity of depositions on a 150-mm wafer.

Compact High-Intensity Neutron Source Driven by Pyroelectric Crystals

Vincent Tang
(925) 422-0126
tang23@llnl.gov

A promising technique for identification of unknown threats containing explosives or nuclear material is active interrogation via neutron bombardment and detection of induced gammas or scattered neutrons. A compact, lightweight (<10 lbs), palm-sized, pulse-able neutron source or "neutron flare" requiring little electrical power could provide unique capabilities for active interrogation of these threats in the field. Pyroelectric crystals offer a means of achieving such a source by allowing a traditional neutron tube's ~100- to 200-kV power supply, ion source, and accelerator structure to be integrated on a scale an order of magnitude smaller than that of conventional technology. Figure 1 shows a schematic of the first proof-of-principle Crystal Driven Neutron Source (CDNS) experiment, illustrating the pyrofusion principle with a "coupled" ion source and acceleration approach.

Project Goals

The objective is to establish the scientific basis for a >10^6 D-T equivalent n/s palm-size, pulse-able neutron source driven by pyroelectric crystals using an independent nano-ion source. A primary goal is to achieve the "reverse" configuration in Fig. 2 after extending the coupled configuration. By decoupling the ion source from the pyroelectric crystal providing the acceleration voltage, the neutron source can be pulsed at frequencies and rates required for some interrogation applications, and the accelerating voltages tailored for either the D-D or D-T neutron producing reactions.

To achieve this, we seek a comprehensive understanding and development of pyroelectric HV sources, pyrofusion, and the development of novel nano-ion sources based on arrays of carbon nanotubes or gated nanotips. These new compact, high-yield, low-power ion sources would also have wide application for accelerator technology in general. A successful integrated demonstration with neutron production would complete the scientific basis needed for the development of the palm-size "neutron flare."

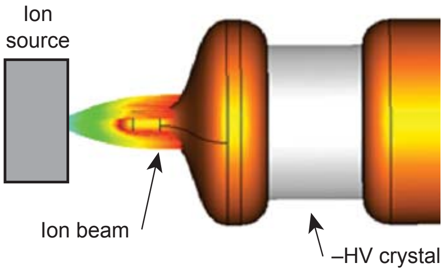

Figure 2. The LLNL CDNS concept. The incorporation of a user-controlled ion source provides pulsing capability, and can significantly increase neutron intensity. In contrast to Fig. 1, the crystal in this case is biased negatively.

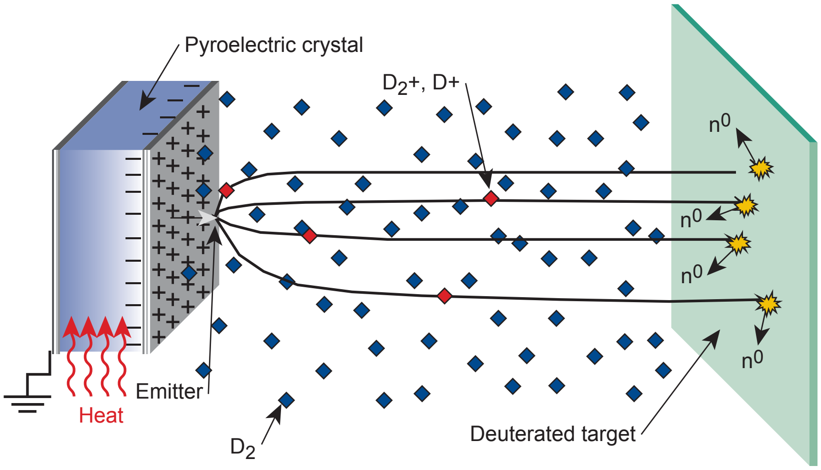

Figure 1. Illustration of pyrofusion effect. Voltages of ~100 kV are produced in ~cm-thick $LiTaO_3$ crystals, which results in intense electric fields at the emitter apex. These fields ionize the surrounding deuterium, creating an ~100-kV deuteron beam, which produces neutrons from the D-D reaction in the deuterated target.

Relevance to LLNL Mission

This technology will have a significant impact for applications in homeland security, the military, and intelligence gathering needs. This project supports LLNL's national security mission by investigating a technique that would enable a new concept of operations, such as the possibility of a remote, autonomous neutron probe for covert interrogation.

FY2008 Accomplishments and Results

During FY2008 significant progress was made on pyrofusion and pyroelectric HV supplies and on developing the required nano-ion sources for the reverse configuration. Additionally, the viability of the reverse configuration was demonstrated for the first time.

First, the record neutron yields achieved with the LLNL CDNS in

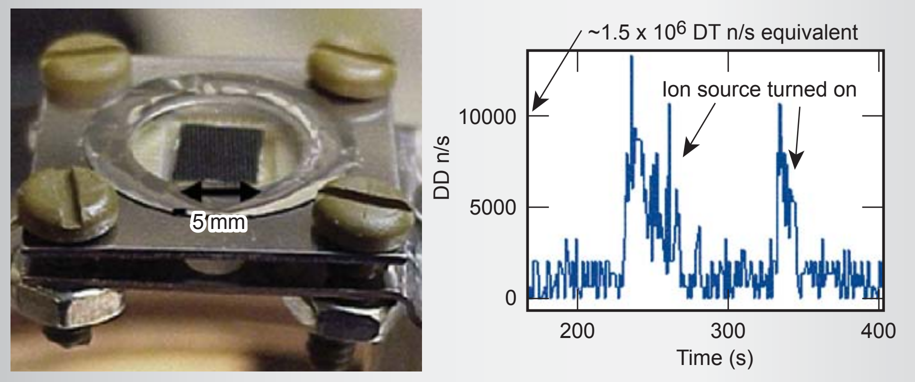

Figure 4. Novel nanotube ion source used to produce >10^6 D-T equivalent n/s with conventional negative 80-kV supply.

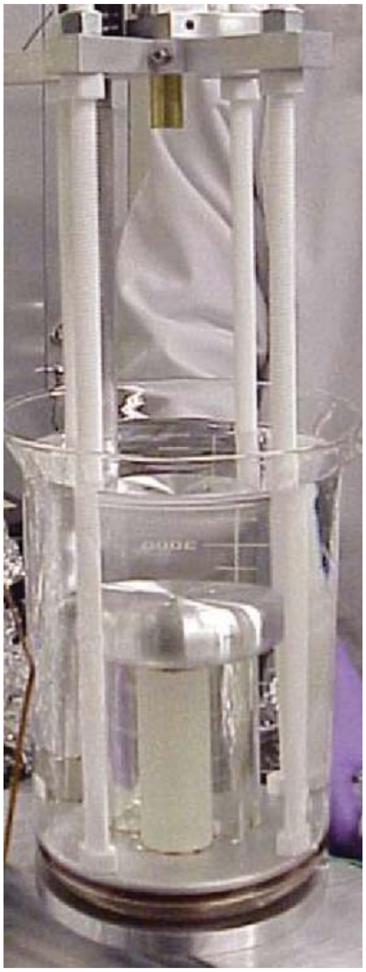

Figure 3. Dielectric fluid quench experiments. Different crystal configurations were tested, including the multi-crystal layout shown.

coupled configuration were published. For the reverse configuration, we identified and overcame supply challenges associated with field emission current created by the high negative voltage. We investigated setups using dielectric fluids for both voltage insulation and rapid thermal cycling in quench experiments (Fig. 3). The work resulted in ~10 x higher pyroelectric current in palm-size setups holding negative voltages of ~300 kV, and the demonstration of the first electron accelerator powered by liquid-driven crystals.

The limitation of this approach was also identified, consisting of leakage currents from electrohydrodynamic flows and larger thermal power requirements than desired. On the vacuum side, we tested various target terminals for holding negative HV, and successfully coated a crystal with deuterated polystyrene for an all dielectric negative HV crystal target that held voltages of ~—100 kV. By coupling this crystal with an available spark ion source we demonstrated experimentally user-controlled pulse neutrons with peak rates >10^{10} D-D n/s via the reverse configuration.

Concerning potentially more efficient ion sources, we developed a nanotube ion source and were the first to test a nanotube device for neutron production (Fig. 4), culminating in >10^6 D-T equivalent average n/s using a conventional –80-kV test stand. However, the D^+/D_2^+ fraction needs to be improved to minimize parasitic losses that are important to charge-limited crystals.

Finally, we designed and constructed a novel gated nanotip structure, (Fig. 5), which is ready for testing.

Related References

1. Tang, V., *et al.*, “Crystal Driven Neutron Source: A New Paradigm for Miniature Neutron Sources,” *20th Conference on the Application of Accelerators in Research and Industry*, 2008.
2. Naranjo, Gimzewski, and Putterman, *Nature*, **434**, pp. 1115–1117, 2005.
3. Tang, V., *et al.*, “Neutron Production from Feedback Controlled Thermal Cycling of a Pyroelectric Crystal,” *Review of Scientific Instruments*, **78**, 123504, 2007.
4. Tang, V., *et al.*, “Experimental Investigation and Simulations of Liquid Driven Pyroelectric Voltage Sources for Compact Accelerators,” *20th Conference on the Application of Accelerators in Research and Industry*, 2008.
5. Tang, V., *et al.*, “Nano-Structure Ion Sources for Neutron Production,” *20th Conference on the Application of Accelerators in Research and Industry*, 2008.

FY2009 Proposed Work

In FY2009, we will continue to study dielectric targets for additional voltage stand-off capability, and continue improvements to our nanotube source. We will also test the gated nanotip arrays constructed in FY2008. Integrated system testing will continue and is expected to result in >10^6 D-T equivalent average n/s by the end of the year.

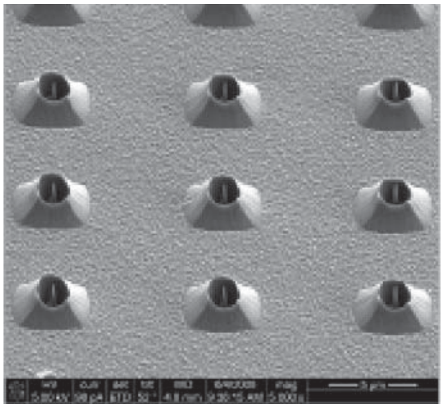

Figure 5. Gated nanotip array ion source.

Study of Transport Behavior and Conversion Efficiency in Pillar Structured Neutron Detectors

Rebecca J. Nikolić
(925) 423-7389
nikolic1@llnl.gov

A radiation detection device that can be easily fielded and offers high detection efficiency is vital to national security efforts. In this project, we will demonstrate technology that could lead to a solid-state device with over 70% thermal neutron detection efficiency.

By applying microtechnology and microfabrication methods to neutron detection, we expect to make revolutionary improvements in device efficiency and field usability. We will take advantage of recent advancements in material science, charged carrier transport, and neutron-to-alpha conversion dynamics to fabricate semiconductor pillars in a 3-D matrix in which the neutron-to-alpha conversion material has adequate density to capture the full neutron flux.

Project Goals

With this project, we intend to develop and demonstrate a proof-of-principle device, and we will devise a roadmap for scaling the device to optimal efficiency. This is significant because current technology suffers from poor efficiency and adaptability to field use, high voltage, sensitivity to microphonics, a large device footprint, and high pressure, resulting in significant complications in air transport and deployments. The advances we propose in micro- and nanofabrication methods are applicable to many other fields, including biochemical detection, communications, and computations.

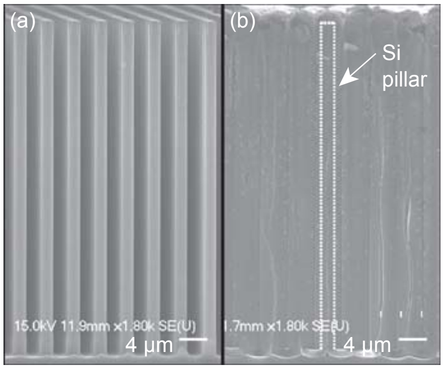

Figure 1. SEM photos of 50-μm-tall Si pillars with a 2-μm diameter and 2-μm spacing: (a) before ^{10}B CVD, and (b) after ^{10}B CVD with ~98-99% fill factor.

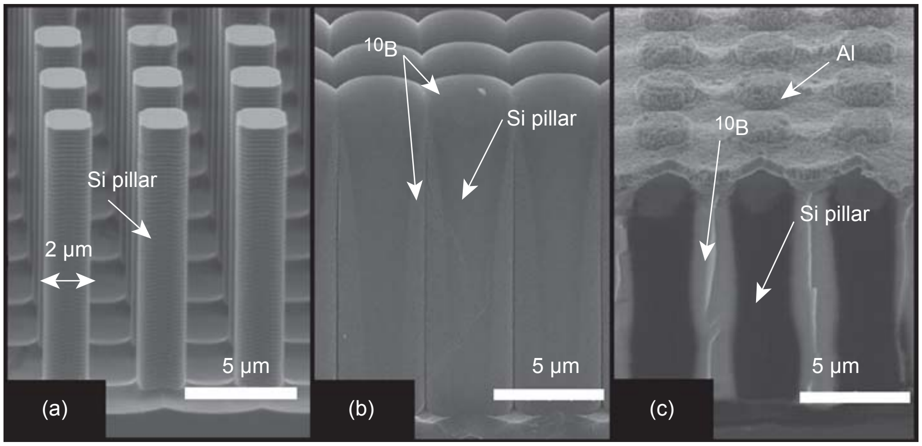

Figure 2. SEM images of 12-μm silicon pillars structured thermal neutron detector: (a) as fabricated by etching, (b) after boron deposition, and (c) after etch-back of excess boron and aluminum evaporation.

Relevance to LLNL Mission

Our project supports the Laboratory's national security mission by advancing technology for detection of special nuclear materials and radiological dispersal devices. If our demonstration device meets the requirements for high efficiency and demonstrates suitability for field use, it would pave the way to manufacturing field-ready devices in partnership with an industrial collaborator.

FY2008 Accomplishments and Results

Our primary milestones reached in FY2008 and illustrated in Figs. 1 through 4, included 1) methods to etch high-aspect-ratio features with 2-µm feature size (pillar diameter and spacing) with a height up to 50 µm and deposition of boron materials in these features with a high fill factor; 2) fabrication and characterization of 12-µm-tall pillar detector with a 7.3% thermal neutron detection efficiency; and 3) simulation of the pillar detector that includes both nuclear physics and semiconductor device physics for efficiency predictions based on geometry and discriminator setting. In addition, we continued to publish papers for both conferences and journals.

Related References

1. Conway, A. M., T. F. Wang, N. Deo, and C. L. Cheung, "Numerical Simulations of Pillar Structured Solid State Thermal Neutron Detector Efficiency and Gamma Discrimination," *Special Conference Issue of the IEEE Transactions on Nuclear Science (TNS)*, 2009.
2. Nikolic, R. J., A. M. Conway, C. E. Reinhardt, R. T. Graff, T. F. Wang, N. Deo, and C. L. Cheung, "Pillar Structured Thermal Neutron Detector with 6:1 Aspect Ratio," *Applied Physics Letters*, **93**, 13, p. 133502, September 2008.
3. Deo, N., J. R. Brewer, C. E. Reinhardt, R. J. Nikolic and C. L. Cheung, "Conformal Filling of Silicon Micro-Pillar Platform with ^{10}Boron," *Journal of Vacuum Science and Technology B*, July/August 2008.
4. Conway, A. M., R. J. Nikolic, and T. F. Wang, "Numerical Simulations of Carrier Transport in Pillar Structured Solid State Thermal Neutron Detector," *International Semiconductor Device Research Symposium ISDRS 2007*, College Park, Maryland, December 12–14, 2007.
5. Nikolic, R. J., A. M. Conway, T. Graff, C. E. Reinhardt, T. F. Wang, N. Deo, and C. L. Cheung, "Fabrication of Pillar-Structured Thermal Neutron Detectors," *IEEE Nuclear Science Symposium*, Honolulu, Hawaii, October 2007.

FY2009 Proposed Work

For FY2009, we plan to determine fundamental scalability limitations of conformal coating of CVD boron; study the scalability limitations of the pillar detector; benchmark simulated efficiencies with experimental data with varying pillar height; update physics-based pillar detector model to account for losses; and publish findings.

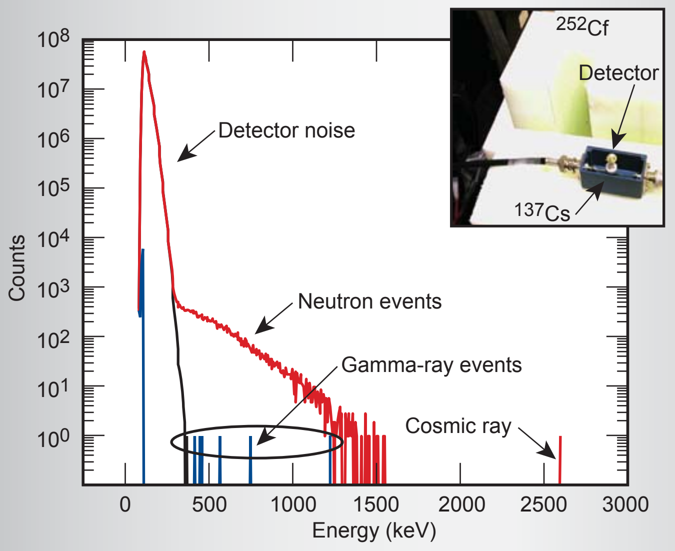

Figure 3. Neutron detection spectrum and gamma detection spectrum of the pillar structured thermal neutron detector with 12-µm silicon pillars structures. The inset shows the test configuration.

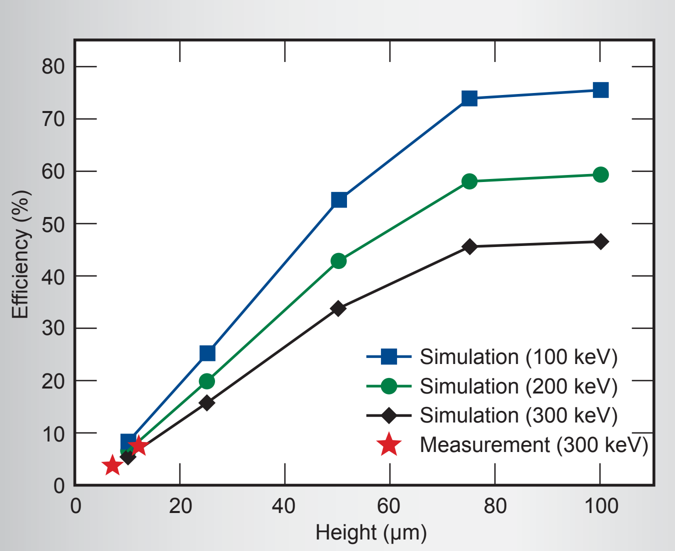

Figure 4. Comparison of simulated detection efficiency at various discriminator values overlaid with the measured detection efficiency for pillar array of 2-µm diameter and 2-µm spacing. At a discriminator threshold of 300 keV there is good agreement (10% error) between simulation and measurement.

Validation of 3-D Commercial Codes for Microfluidic Systems

Klint A. Rose
(925) 423-1926
rose38@llnl.gov

The fabrication and testing of microfabricated structures is very expensive and time consuming. Using model-driven methods, we can reduce the number of iterations and cover the large configuration space of microfabricated structures in an effective and affordable manner. Specifically, we validate the modeling tools against microfluidic structures focused at performing front-end sample preparation for biological assays.

Project Goals

Our goal is to implement a general, multiphysics simulation capability for use as a predictive tool for microfluidic systems.

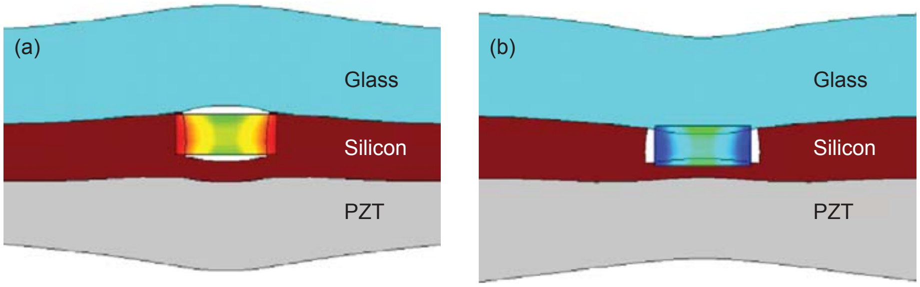

Figure 1. Example of the pressure fields generated in a fluid volume (fixed rectangular center) by a glass-silicon-PZT stack: (a) high pressures (red) generated at the edges of the fluid volume as the sidewalls compress inward; (b) low pressures (blue) generated at fluid volume edges as the sidewalls expand outward.

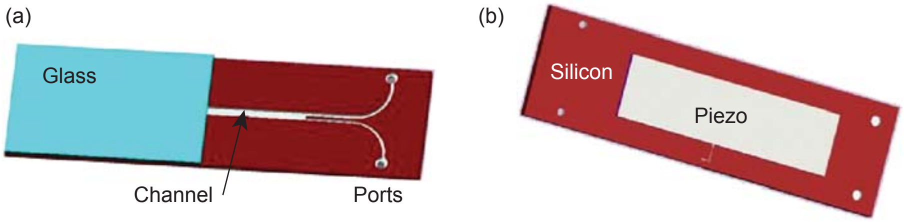

Figure 2. CAD drawing of the microfluidic chip used to validate the simulation: (a) front view of chip showing the glass top and bifurcated separation channel etched into the silicon base; (b) bottom view of the chip showing the PZT.

Relevance to LLNL Mission

The rapid identification of emerging viruses is critical to national security and financial health. Of the 80 emerging pathogens identified since 1980, 59 have been viruses. A common failure mode in biological detection systems is the high false negative rate for viruses because of their large mutation rate, small size, and lack of adequate automated sample preparation instrumentation. Microfluidic technology is ideally suited to improve sample preparation and aid in virus discovery. However, improved modeling tools are required to accelerate the understanding of microfluidic systems when applied to high-throughput front-end sample preparation systems.

FY2008 Accomplishments and Results

We describe a modeling approach used to capture the particle motion within an acoustic focusing microfluidic device. Our approach combines finite element models (FEM) for the acoustic forces with analytical models for the fluid motion and using these force fields to calculate the particle motion in a Brownian dynamics simulation.

Acoustic focusing is an effective technique to manipulate relatively large (> 2 μm) particles and has been used for a variety of applications including sorting blood cells, concentrating cells for optical detection, and measuring particle zeta potentials.

By focusing large contaminants into a single plane or node within the microchannel, we can separate a complex input sample into waste and purified streams and direct each to separate outputs. The location and width of the focused particle band depends on the channel geometry, material properties, and acoustic transducer operating conditions. The transducer generates pressure fields within the microchannel (Fig. 1) creating acoustic radiation forces whose direction and magnitude depend on the relative compressibility and density of the particle and the fluid. Currently, models predicting net particle motion within acoustically driven devices rely on simplified 1-D models for the acoustic forces. FEM simulations have been used to analyze the 2-D force field in a microfluidic device, but this analysis provides only qualitative information regarding the likely particle locations.

In our approach, we solve for the hydrodynamic flow field using analytical solutions based on the geometry of the microchannel and solve for the 2-D acoustic force field within the channel using a commercial FEM code (ATILA FEA). We incorporate the force fields into a Brownian dynamics simulation based on the Langevin equation. This simulation includes random displacements due to Brownian motion and calculates spatial and temporal concentration distributions for any species within the device.

To validate the model we experimentally measured the degree of focusing (full width half maximum) for microspheres with diameters ranging from 1 to 5 µm. We used a microfluidic chip, shown in Fig. 2, with channels etched into a silicon wafer and a piezo-electric transducer (PZT) glued to the backside at a frequency of 1.46 MHz and an input voltage from 0 to 9.6 V. The 2-D force field we predicted for these conditions (Fig. 3) suggests a single node in the lower center region of the channel.

Experimental and simulated results for the width of the focused particle band, shown in Fig. 4, compare favorably across particle sizes and driving voltages when the simulated values are scaled by a factor of 40. This result demonstrates our ability to qualitatively capture the acoustic focusing force magnitudes and directions versus the input flow rates and random particle motion.

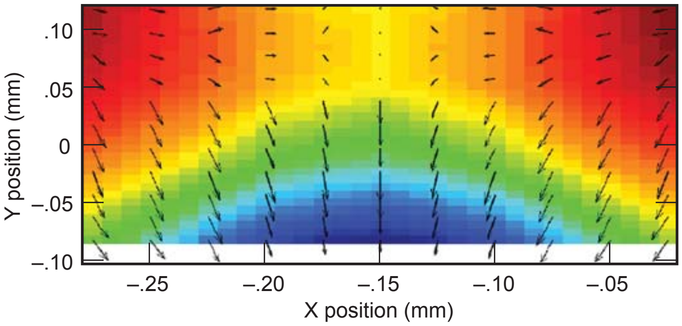

Figure 3. Simulated result for the acoustic radiation force field in the microfluidic chip cross-section when the PZT is driven at 1.46 MHz. The map indicates the high (red) to low (blue) pressure field. Arrows show the direction of the acoustic forces.

Related References

1. Kapishnikov, S., V. Kantsler, and V. Steinberg, "Continuous Particle Size Separation and Size Sorting Using Ultrasound in a Microchannel," *Journal of Statistical Mechanics*, P01012, 2006.
2. Zhou, C., P. Pivarnik, A. G. Rand, and S. V. Letcher, "Acoustic Standing-Wave Enhancement of a Fiber-Optic Salmonella Biosensor," *Biosensors & Bioelectronics*, **13**, pp. 495–500, 1998.
3. Hunter, R. J., and R. W. O'Brien, "Electroacoustic Characterization of Colloids with Unusual Particle Properties," *Colloids and Surfaces A: Physicochemical and Engineering Aspects*, **126**, pp. 123–128, 1997.
4. Nyborg, W. L., "Radiation Pressure on a Small Rigid Sphere," *Journal of the Acoustical Society of America*, **42**, 5, p. 947, 1967.
5. Martyn H., Y. Shen, and J. J. Hawkes, "Modeling of Layered Resonators for Ultrasonic Separation," *Ultrasonics*, **40**, pp. 385–392, 2002.

FY2009 Proposed Work

Our future work will aim to eliminate the need for a scaling factor by modeling the full 3-D force field and including losses due to material interfaces.

Using the methodology described here, we can rapidly iterate over a variety of input parameters including geometry, acoustic driving voltage and frequency, and particle properties to predict the spatial and temporal particle concentration distributions within a microfluidic device and achieve an optimized system configuration.

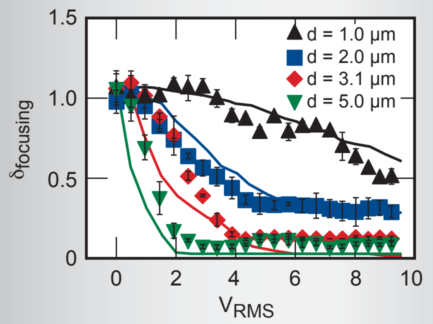

Figure 4. Comparison of experimental and theoretical measurements. The solid lines show the theoretical force field predicted from the simulations; the symbols indicate the experimental values.

Engineering Systems for Knowledge & Inference

Ultra-Scale Tracking in Low-Resolution Image Sequences

Carmen Carrano
(925) 422-9918
carrano2@llnl.gov

Vehicle tracking is a key technology for exploiting persistent surveillance. The technology to track thousands of vehicles over large, cluttered regions has the potential to provide the government with a fundamentally new intelligence source.

Project Goals

The project goal is to provide an advanced vehicle tracking capability for large (> 1 km x 1 km), long (> a few minutes), low resolution (~0.5 m/pixel), and low frame rate (~2 Hz) persistent surveillance image sequences, as well as a means to evaluate the performance of the capability. This capability was tested and documented on several relevant datasets. Other useful products include track visualization, track-file export capabilities (*e.g.*, to KML (Google Earth) and to a spatial database for further exploitation) and rapid generation of vehicle tracking ground-truth from large datasets.

Relevance to LLNL Mission

Prior to this year, LLNL did not have a capability to generate large-scale vehicle tracking information from remotely sensed video. Programs that directly benefit from this capability include NNSA NA-22 nonproliferation programs (*e.g.*, ICue), DoD-related programs (*e.g.*, Persistics), and other USG programs (*e.g.*, STED).

This project also directly advances the Engineering Systems for Knowledge and Inference (ESKI) Roadmap. The application areas of "detection and monitoring of WMD proliferation" and "sensor fusion for pattern discovery and inference" include traffic monitoring over regions that range in size from facilities to cities to countries, which then feed into multisource event prediction, pattern discovery, and activity models. It is difficult, if not impossible, to find the anomalous behavior of a vehicle without tracking a large number of vehicles to learn the normal patterns of behavior.

FY2008 Accomplishments and Results

We began this project with existing basic experimental interface definition language (IDL) tracking codes and significantly extended our capabilities to handle large and long datasets. We can now track all vehicles in a dataset with 4000 x 4000 pixels (at 0.5 m/pixel) by 1000 frames, possessing over 1500 movers/frame in roughly 45 min. At the start of the project, tracking on such a dataset was not feasible, and over halfway through the project, this would have taken many days to complete. For a shorter dataset with fewer objects, such as a set with 4000 x 4000 pixels by 200 frames with ~100 to 200 movers, it takes only a few minutes to complete the tracking. Our current method relies on the mover map, path dynamics, and image features to perform tracking. The benefit of using image features in addition to the mover map is that we can track vehicles not only when they move, but also when they stop. The algorithm performs very well when the vehicles are sufficiently separated and the obscurations are small enough such that the vehicles keep a constant speed and direction under the obscuration.

We have also created IDL tools for the visualization of a single track of interest or multiple tracks in large datasets. The tracks can optionally be exported to kml or xml for further visualization or exploitation. An example of tracks detected in downtown San Diego overlaid on Google Earth is shown in the figure.

Related References

1. Collins, R. T., *et al.*, “A System for Video Surveillance and Monitoring,” *VSAM Final Report*, Carnegie Mellon University, 2000. http://www.cs.cmu.edu/~vsam/research.html

2. Lipton, A. J., H. Fujiyoshi, and R. S. Patil, “Moving Target Classification and Tracking from Real-Time Video,” *WACV ’98. Proceedings, 4th IEEE workshop on Applications of Computer Vision*, pp. 8–14, 1998.

3. Bell, W., P. Felzenszwalb, and D. Huttenlocher, “Detection and Long Term Tracking of Moving Objects in Aerial Video,” *Technical Report, Computer Science*, Cornell, March 1999. http://www.cs.cornell.edu/vision/wbell/identtracker/

4. Baldini, G., *et al.*, “A simple and Robust Method for Moving Target Tracking,” SPPRA, 2002.

FY2009 Proposed Work

Most clearly evident in the figure is the complexity of data at this scale. Since we would like to reliably and accurately evaluate how well the tracker performed, this leads us to the proposed FY2009 work of implementing a computer-aided track generation tool with minimal human intervention to establish ground-truth tracks. Using this ground-truthing tool we will be able to carry out repeatable experiments to assess performance of the tracker. It also facilitates important programmatic work to perform tracking assessment studies.

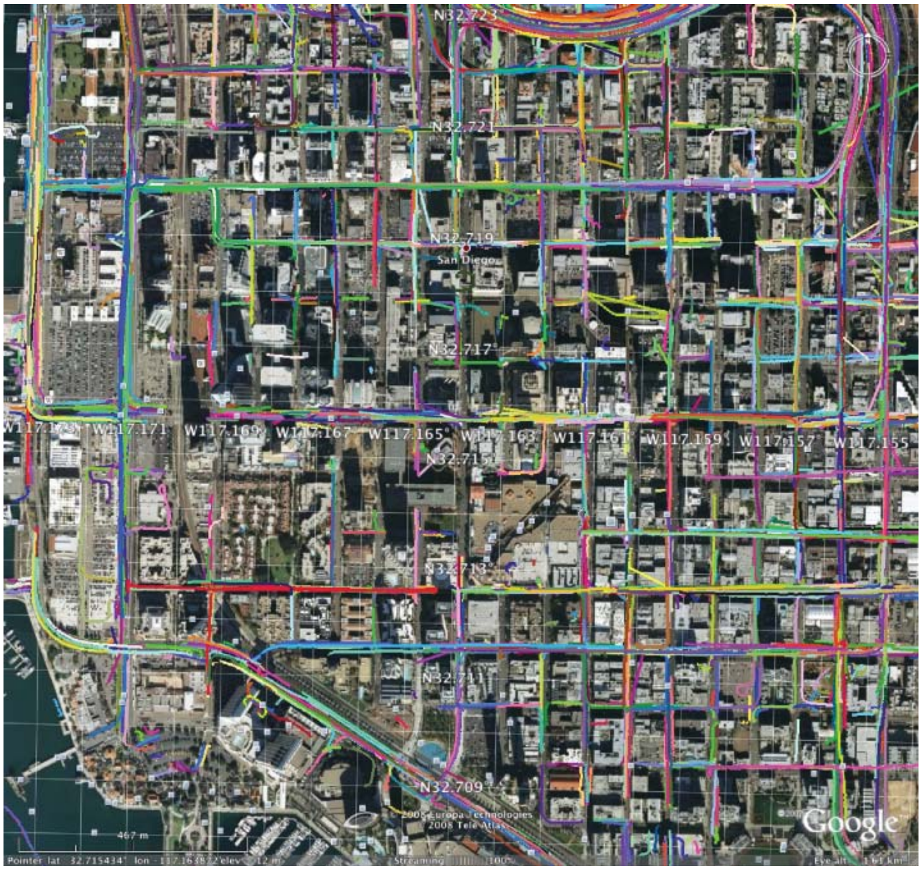

Detected tracks from 200 frames (100 s) of 2-Hz video overlaid on Google Earth.

Automatic Learning of Probabilistic Causal Models

Brenda M. Ng
(925) 422-4553
ng30@llnl.gov

Probabilistic causal models (PCMs) represent non-deterministic cause-and-effect relationships between stochastic entities. These models are crucial for causal reasoning, which ultimately drives informed decision-making, allowing us to achieve situational understanding about complex processes and potential threats that are central to LLNL's mission. Good examples are how one might account for the uncertainties and variability in the preparations for NIF ignition experiments or decide which countermeasure is the most effective against an epidemic. Through PCMs, we can infer these types of mission-critical intelligence. PCMs offer a more informative model than semantic graphs (our current technology), which merely provide associative information between entities and lack the infrastructure necessary for efficient reasoning under uncertainty. Automatic learning of PCMs can reveal hidden patterns and entities, thus providing template models (*e.g.*, Bayesian networks (BNs)) for processes lacking well-defined physics and/or expert domain knowledge.

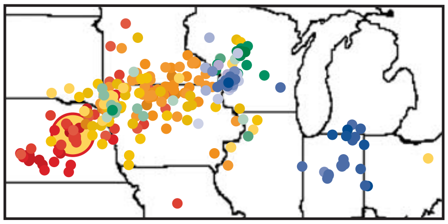

Figure 1. Map of simulated outbreak scenario. The infection source originated from a farm in Nebraska. The colored points denote the locations of infected farms. Red represents the earlier generations; blue represents the later generations. The first generation is defined as the set of farms infected by the source; the second generation consists of the farms infected by the first generation, and so on.

Project Goals

This effort focused on the automated learning of BNs as a means for uncovering causal information from observed data. The goal was to implement a toolbox of state-of-the-art algorithms for learning BNs, which encapsulate independence assumptions and stochastic dynamics among process variables.

Relevance to LLNL Mission

This work is highly relevant to furthering LLNL's missions related to Inference and Adversarial Modeling. The toolbox can 1) enhance pattern discovery, risk analysis, and predictive reasoning in any application related to modeling and decision-making under uncertainty, where the dynamics of agents are poorly understood, as in ignition experiments for NIF and disease propagation for the Biodefense Knowledge Center (BKC); 2) reduce time/labor and mitigate inconsistencies, uncertainties, and oversights associated with building models manually; and 3) be the launching pad for enhanced reasoning tools that integrate Bayesian modeling with general classes of computational expertise (*e.g.*, game-theoretic or agent-based) to improve optimal decision-making. Our results could be extended to decision-theoretic tools for a variety of applications including 1) predicting disease spread and assessing risk of nonintervention in an epidemic scenario; and 2) improving process modeling and experiments under uncertainty.

FY2008 Accomplishments and Results

A BN is a directed acyclic graph (DAG) that encodes a joint probability distribution over a set of random variables, in a factored manner that makes explicit use of the conditional independencies between variables. Given data from an unknown process, the goal is to perform BN learning on the data to estimate a model of the underlying process. Focusing on BN technology, our accomplishments include 1) a survey report of advanced machine learning methods; 2) implementations of learning methods; and 3) demonstrations on available programmatic data.

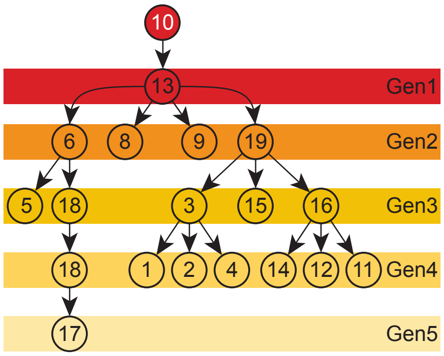

Figure 2. Trace tree of a particular outbreak scenario. Traces (*e.g.*, generation information) offer valuable information about the propagation of the disease outbreak.

BN learning involves uncovering the graphical structure, as well as the parameters that quantify probabilistic influences between variables. Structural learning is generally hard, because the number of possible structures (*i.e.*, DAGs) grows super-exponentially in the number of attributes. Evaluating all structures is intractable by traditional means.

Our toolbox implements two state-of-the-art algorithms. Both assume pre-specification of the number of variables and the cardinality of possible states. The first computes probabilities for all potential edges simultaneously, faster than any previous Markov Chain Monte Carlo (MCMC)-based samplers, and is applicable for edge discovery in networks. The second speeds up MCMC sampling of DAG structures, by applying dynamic programming for updating the proposal distribution to judiciously

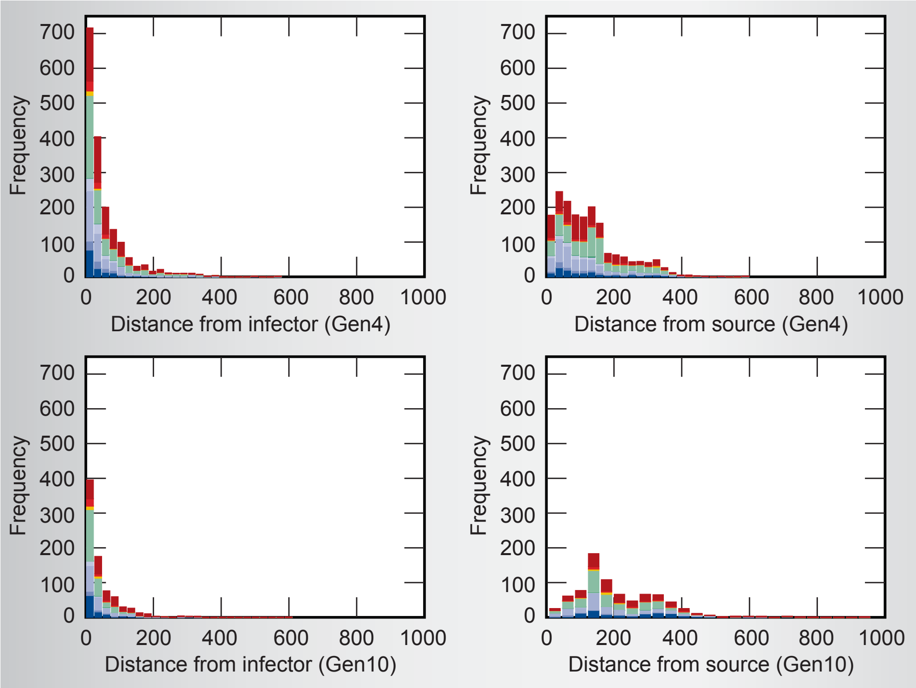

Figure 3. Stacked histograms comparing two generations' frequency counts in terms of distances from the infector (*i.e.*, the infecting farm from the previous generation) and the source (*i.e.*, the farm from which the outbreak originated). The constituent colors on each bar reflect the different farm types that make up the generation. From an earlier to a later generation, the outbreak spreads to similar farm types but is gradually moving away from the source.

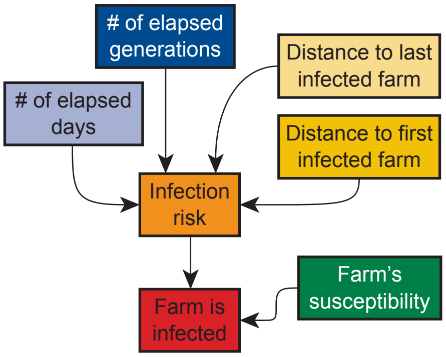

Figure 4. Bayesian network constructed from the MESA data. Using this, we want to assess whether a farm is infected as a function of the observable variables in the graph.

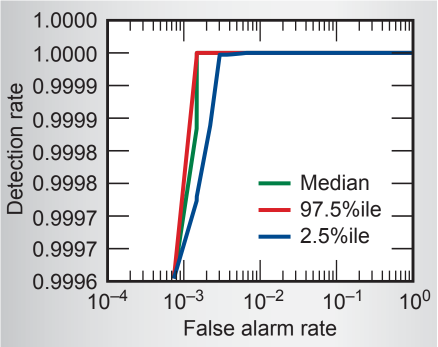

Figure 5. Receiver-operator characteristics (ROC) curves derived from five-fold cross-validation experiments. The ROC curve shows the tradeoff between the true positive rate (*i.e.*, the fraction of correctly identified infected farms) and the false positive rate (*i.e.*, the fraction of non-infected farms incorrectly identified as infected). The ROC curves show near-optimal performance with high detection rates and low false alarm rates.

guide the exploration through the space of DAGs.

The implemented algorithms were applied to simulated data sets from two sources: 1) energetics/diagnostics data from NIF; and 2) epidemiological data from BKC's Multiscale Epidemiological/Economic Simulation and Analysis (MESA) project.

We present findings here only for the MESA data. The data was derived from 401 independent simulations (resulting in 15667 infected farms) of a hypothetical, non-intentional foot-and-mouth disease outbreak. Figure 1 shows the extent of the outbreak from one simulated scenario. Each simulation contains the outbreak history that specifies the infection source, which farm(s) were infected next as time progressed, along with the farms' spatial locations and types. For each simulation, we performed tracing (Fig. 2) and derived generations linking the infected farms. In characterizing the data (Fig. 3), we have found that trace information, along with farm types and distances, are key attributes in detecting disease propagation. Putting this together, we constructed a BN (Fig. 4) consisting of these and other variables. Our results are summarized in Fig. 5.

Related References

1. Koivisto, M., "Advances in Exact Bayesian Structure Discovery in Bayesian Networks," *Proc. 22nd Conference on Uncertainty in Artificial Intelligence*, 2006.
2. Wood, F., T. L. Griffiths, and Z. Ghahramani, "A Non-Parametric Bayesian Method for Inferring Hidden Causes," *Proc. 22nd Conference on Uncertainty in Artificial Intelligence*, 2006.
3. Mansinghka, V., C. Kemp, J. Tenenbaum, and T. Griffiths, "Structured Priors for Structure Learning," *Proc. 22nd Conference on Uncertainty in Artificial Intelligence*, 2006.
4. Eaton, D., and K. Murphy, "Bayesian Structure Learning Using Dynamic Programming and MCMC," *Proc. 23rd Conference on Uncertainty in Artificial Intelligence*, 2007.
5. Fox, E. B., E. B. Sudderth, M. I. Jordan, and A. S. Willsky, "An HDP-HMM for Systems with State Persistence," *Proc. 25th International Conference on Machine Learning*, 2008.

FY2009 Proposed Work

FY2009 focus is on nonparametric modeling methods (*e.g.*, structured priors, infinite-state Hidden Markov Models, and hidden variable discovery), which will enable the discovery of newly active states and/or entities involved in a process. This work will produce powerful tools for generating more flexible and realistic models, thus enhancing complex system modeling, inference, and decision-making.

Enhanced Event Extraction from Text via Error-Driven Aggregation Methodologies

Tracy D. Lemmond
(925) 422-0219
lemmond1@llnl.gov

Knowledge discovery systems are designed to construct massive data repositories via text and information extraction methodologies, and then infer knowledge from the ingested data, in effect allowing analysts to "connect the dots." The extraction of complex relational information (events) and related entities such as people or organizations generally forms the basis for data ingestion. However, these systems are particularly vulnerable to errors introduced during the ingestion process, frequently resulting in misleading downstream inference and unreliable ensuing analysis. Though current state-of-the-art event extraction tools achieve insufficient accuracy rates for practical use, not all extractors are prone to the same types of error. This suggests that substantial improvements may be achieved via appropriate combinations of existing extraction tools, provided their behavior can be accurately characterized and quantified.

Our research is addressing this problem via the aggregation of existing extraction tools based upon a general inferential framework that exploits their individual strengths and mitigates their most egregious weaknesses.

Project Goals

The primary objective of this effort is to develop a significantly improved event extraction system that will enable 1) greater insight into the effects of extraction errors on downstream analysis; 2) more accurate automatic information extraction; 3) better estimates of uncertainty in extracted data; 4) effective use of significant investments by the Natural Language Processing community; and 5) rapid incorporation of future advancements in event extraction technologies. The system will use as its foundation an end-to-end analysis of the error processes of individual extractors that will yield insights into their synergistic and conflicting behaviors. These analyses will be leveraged to configure a collection of base extractors, via a general inferential framework, into an aggregate meta-extractor with a substantially improved extraction performance.

Relevance to LLNL Mission

Nonproliferation, counterterrorism, and other national security missions rely principally upon the acquisition of knowledge, most of which is buried in exabytes of unstructured text documents too vast to be manually processed. Knowledge discovery systems are under development by LLNL and by its customers to automatically extract critical information from these sources. In order for extracted data to provide an effective foundation for knowledge discovery, however, extraction error rates must be driven down. Probabilistic aggregation is a promising and innovative approach to accomplishing this goal. This effort directly supports the Engineering Systems for Knowledge and Inference (ESKI) focus area and the Threat Prevention and Response Technologies theme in the LLNL Science and Technology Plan with an emphasis on knowledge discovery, advanced analytics, and architectures for national security.

Successful completion of this research will provide a highly-valued and unprecedented capability both to existing LLNL programs, such as IOAP and CAPS, and to critical customers such as the IC, DHS and DoD, enabling them to develop significantly improved inference and decision-making capabilities.

FY2008 Accomplishments and Results

Our FY2008 efforts concentrated on two primary thrusts: 1) a preliminary approach to probabilistic aggregation of *entity* extractors; and 2) a formal end-to-end analysis of the impact of *event* extraction error processes on queries and downstream inference.

In information extraction, one can conceive of an entity as the simplest, most degenerate event. Hence, entity extractor aggregation forms a practical foundation for developing an aggregation methodology over event space. In our first effort to construct an entity meta-extractor, we defined seven distinct and disjoint error types and developed an approach to probabilistic aggregation that was applied to three open-source extractors: Stanford's Named Entity Recognizer (SNER), GATE, and LingPipe. Our initial naïve approach achieved a more than 15% error reduction over our best individual extractor (SNER) (see figure). These preliminary results present strong evidence that a more sophisticated probabilistic framework can yield significant gains in overall extraction performance.

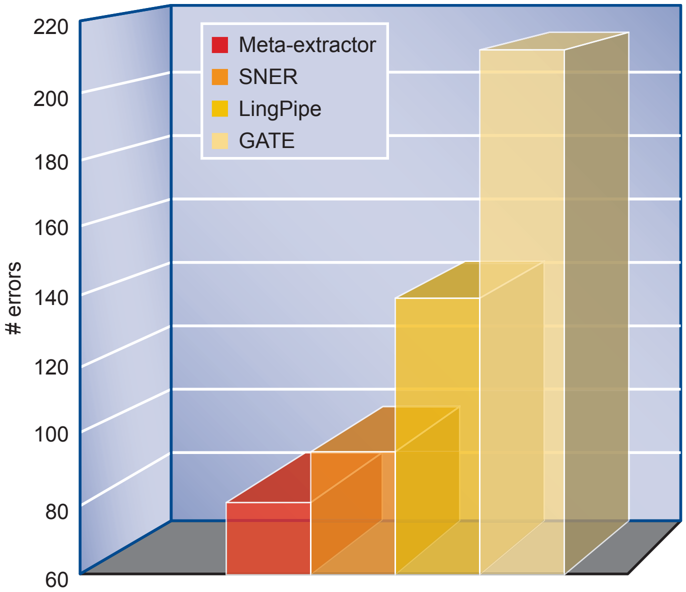

Entity aggregation performance. The performance of the entity meta-extractor is shown in red, compared with the performance of its component extractors. The number of errors produced by the meta-extractor is greatly reduced.

In a parallel effort, we performed an end-to-end analysis of the impact of event extraction error processes on queries and downstream inference. We defined and modeled five event extraction errors that occur relatively often in practical information extraction applications. These errors include 1) event detection failure; 2) failure to detect entities involved in an event; 3) misidentified entities; 4) pronoun resolution failure; and 5) false entity detection.

Formally designed statistical experiments were performed to analyze the effects of these errors on queries issued against several real data sets. Our analyses revealed behaviors that led to a number of critical insights with respect to the impact of these errors on downstream inference. As an example, we discovered that the misidentification of entities is typically more devastating to a query response than any other error we modeled (with entity detection failure a close second), though for fused data, the effects of pronoun resolution failure can be nearly as severe. The results of these error analyses will ultimately be valuable in limiting the computational complexity of the event aggregation framework.

We have designed and begun development of an operational system that will unify these methodologies into a single meta-extraction framework.

Related References

1. Chen, M., Q. Shao, and J. Ibrahim, Monte Carlo Methods in Bayesian Computation, Springer, 2000.
2. Hettmansperger, T. P., "Non-parametric Inference for Ordered Alternatives in a Randomized Block Design," *Psychometrika*, **40**, 1, pp. 53–62, 1975.
3. Milliken, G.A., and D. E. Johnson, Analysis of Messy Data, Volume I: Designed Experiments, Chapman and Hall, 1992.
4. Montgomery, D. C., Design and Analysis of Experiments, John Wiley and Sons, Inc., 1991.

FY2009 Proposed Work

In FY2009, we will enhance the entity aggregation methodology with increasingly more sophisticated probabilistic techniques to help define the requirements for the more complex event aggregation framework. We will also begin extending these approaches to the aggregation of real event extractors, augmented by the error analyses performed in FY2008. Development of an operational system will proceed concurrently.

Robust Ensemble Classifier Methods for Detection Problems with Unequal and Evolving Error Costs

Barry Y. Chen
(925) 423-9429
chen52@llnl.gov

Successful analysis in real-world detection applications often hinges upon the automatic collection of massive amounts of data over time. However, the pace of automatic data collection far exceeds our manual processing and analysis capabilities, making automated pattern detection in streaming data critical.

Machine learning classifiers capable of detecting patterns in datasets have been developed to address this need, but none can simultaneously address the many challenging characteristics of real-world detection problems. In particular, the costs associated with false alarms and missed detections are frequently unequal, extreme (demanding near-zero false alarm or miss rates), or changing over time. Moreover, the underlying data distribution modeled by the classifiers may also evolve over time, resulting in progressively degraded classification performance.

We are addressing these deficiencies via the development of new dynamic ensemble classifier algorithms that leverage diverse cost-sensitive base-classifiers.

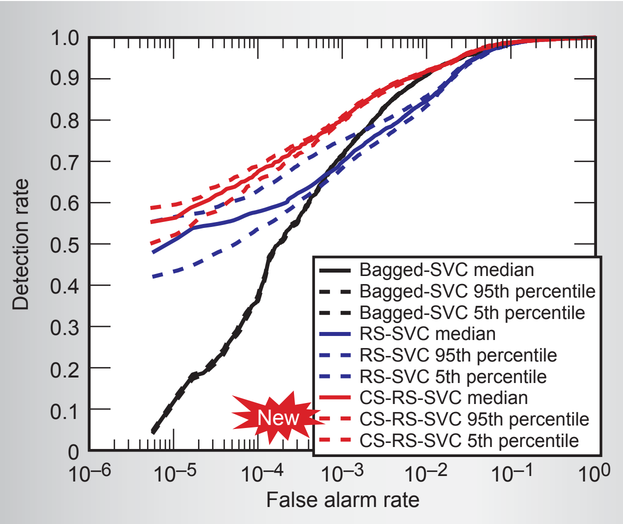

Figure 1. Median and 90% empirical confidence interval ROC curves for Support Vector Classifier-based ensembles.

Project Goals

The ultimate goal of this two-year effort focuses on the understanding and development of new ensemble learning algorithms that can effectively address the considerable challenges presented by detection problems of national significance. The developed methodologies will yield significantly improved performance at near-zero false alarm (or missed detection) rates and be able to adapt to changing costs and data distributions in a dynamic environment. Moreover, this research will lead to greater insight into the factors that interact to govern classification performance, including ensemble size, feature dimensionality, and data sampling.

Relevance to LLNL Mission

This research directly supports the Engineering Systems for Knowledge and Inference (ESKI) focus area and the Threat Prevention and Response Technologies theme in the LLNL Science and Technology Plan with an emphasis on knowledge discovery, advanced analytics, and architectures for national security. Our research explicitly addresses needs in the counterterrorism, nonproliferation, and national security missions for a broad range of customers, including the IC, DHS, DOE, DoD, and NNSA.

FY2008 Accomplishments and Results

The development of new ensemble classifier algorithms involves the optimization of performance metrics such as receiver operating characteristic (ROC) curves with respect to a variety of ensemble design factors. In FY2008, we completed a comprehensive study of these factors and their impact on classifier performance. Our development of classification algorithms leveraged a Hidden Signal Detection application in which false alarms are deemed extremely costly. These efforts ultimately led to the development of several groundbreaking ensemble classifiers, two peer-reviewed publications, and one provisional patent.

Built from many cost-sensitive Support Vector Classifiers (SVCs), our novel Cost-Sensitive Random Subspace Support Vector Classifier (CS-RS-SVC) ensemble significantly outperforms existing SVC ensembles built from non-cost-sensitive SVCs. It achieves a 55.3% detection rate on Hidden Signal Detection at 5.5x10^{-6} false alarm rate. This is a 15.5% relative improvement over an approach built using conventional SVCs (RS-SVC) and about three times better compared to a standard Bagged-SVC ensemble (Fig. 1).

We also significantly enhanced the state-of-the-art Random Forest (RF) classifier by developing variants in which node decisions are no longer constrained to be axis-aligned or linear, resulting in more fluid decision boundaries that better separate the classes (Fig. 2). This new classifier, called the Discriminant Random Forest (DRF), is 40% more

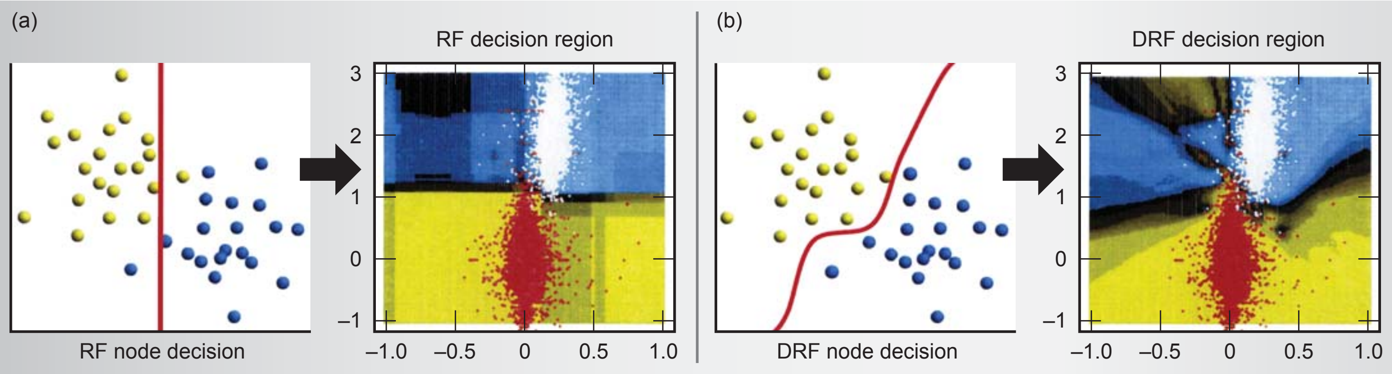

Figure 2. The Random Forest's (RF) axis-aligned linear decision boundaries in tree nodes give rise to "stair-step" decision regions (a), while the Discriminant Random Forest's (DRF) flexible node boundaries result in fluid, better-fitting decision regions (b).

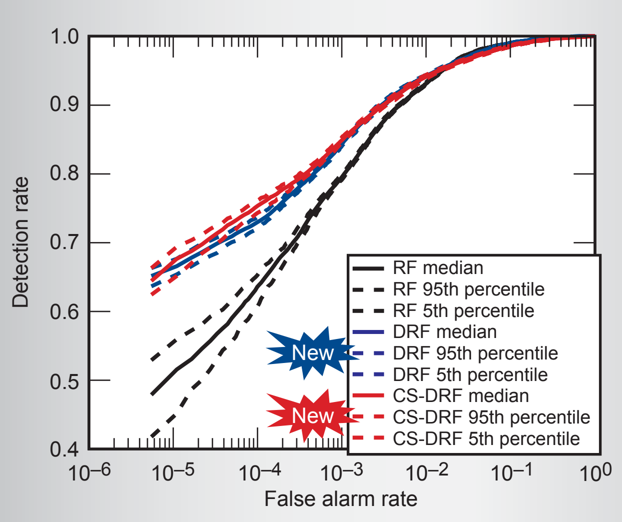

Figure 3. Median and 90% empirical confidence interval ROC curves for Random Forest-based ensembles.

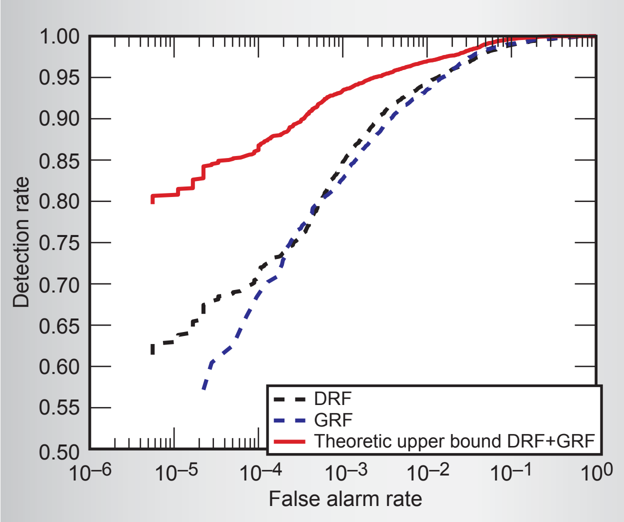

Figure 4. Two different Random Forest variants (DRF and GRF) are combined using an oracle, resulting in a theoretic upper bound on the performance of their combination.

compact, over six and a half times faster, and attains 36.2% higher detection rates at 5.5x10^{-6} false alarm rate than the conventional RF on the Hidden Signal Detection problem (65.1% versus 47.8%) (Fig 3). We also created a cost-sensitive extension to the DRF, the CS-DRF, which further improves DRF detection performance, particularly in the false alarm rate region around 10^{-4}.

Additionally, this research made substantial contributions to other LLNL detection applications, including Radiation Threat Detection (RadThreat) and Standoff High Explosives Detection (SHED). For RadThreat, our classifiers outperformed currently fielded approaches, even on heavily shielded sources. In SHED, our classifiers achieved significantly faster and higher detection rates at lower false alarm rates than human experts on the same data set.

Related References

1. Breiman, L., "Random Forests," *Machine Learning*, **45**, 1, pp. 5–32, 2001.
2. Davenport, M. A., R. G. Baraniuk, and C. D. Scott, "Controlling False Alarms with Support Vector Machines," *Proceedings of International Conference on Acoustics, Speech, and Signal Processing*, 2006.
3. Ho, T. K., "The Random Subspace Method for Constructing Decision Forests," *IEEE Transactions on Pattern Analysis and Machine Intelligence*, **20**, 8, pp. 832–844, 1998.
4. Lemmond, T. D., A. O. Hatch, B. Y. Chen, D. A. Knapp, L. J. Hiller, M. J. Mugge, and W. G. Hanley, "Discriminant Random Forests," *Proceedings of 2008 International Conference on Data Mining*, 2008.
5. Valentini, G., and T. G. Dietterich, "Bias-Variance Analysis of Support Vector Machines for the Development of SVM-Based Ensemble Methods," *Journal of Machine Learning Research*, **5**, pp. 725–775, 2004.

FY2009 Proposed Work

In FY2009, we will 1) further enhance detection performance by extending our homogeneous ensembles to ensembles of heterogeneous base classifiers, exploiting the game-changing potential of combining different ensemble classifiers (Fig. 4); 2) extend the DRF methodology to allow more flexible node decisions; 3) generalize the current binary classifiers to handle multi-class situations; and 4) develop adaptive extensions of our learning approaches to address changing costs and changing data distributions.

Evaluating Deterrence Measures in Adversary Modeling

Carol A. Meyers
(925) 422-1252
meyers14@llnl.gov

Deterrence is a state of mind that is best defined as "the prevention of action by fear of the consequences." This state is typically brought about by the existence of a credible threat of unacceptable counteraction. The phenomenon of deterrence is not often addressed in studies of adversary modeling, primarily because it can be difficult to quantify its effects. This is at least in part because historically, deterrence has been studied within three broad areas (see table), each of which has developed a different motivation and methodology for capturing its results.

Our work integrates across the different areas in which deterrence has been studied to present a unified framework of methods for quantitatively evaluating the effects of deterrence. The end result is a toolbox of three different approaches, which we have implemented within the Modeling the Adversary for Responsive Strategy (MARS) project, an existing LLNL adversary modeling effort.

Project Goals

This project provides a toolbox of methods for quantifying deterrence. Specifically, we focus on three different kinds of deterrent effects: 1) actions that cause the adversary to shift to a different attack; 2) actions that cause the adversary to shift to not attacking; and 3) actions that cause an increased probability of interdiction of the adversary during an attack. Each of these topics corresponds to one area of the toolbox. Ultimately, we intend for these toolbox methods to be used in future studies of adversary modeling.

Relevance to LLNL Mission

In recent years, LLNL has invested effort in developing expertise in methods of adversary modeling, including probabilistic risk analysis, agent-based modeling, social networks, and Bayesian inference techniques. This work extends capabilities in these areas and increases proficiency for other applications, such as the assessment of critical infrastructure. It aligns with the adversary modeling roadmap within the Engineering Systems for Knowledge and Inference (ESKI) focus area and the Threat Prevention and Response Technologies theme in the LLNL Science &Technology plan.

FY2008 Accomplishments and Results

The first area of the toolbox concerns actions that cause the adversary to shift to a different attack. For this topic, we synthesized a decision-making model from the literature and built it into the MARS effort. The cornerstone of this model is a parameter, β, that shifts between the extremes of the adversary choosing randomly and always choosing according to its maximum multi-attribute utility. Running this model, we discov-

Areas in which deterrence has been studied.

Area	Timeframe	Goal of deterrence
Crime fighting	1800s to present	Manipulation of actors through harsh punishments
Negotiations between hostile nations	1940s to present (peak during Cold War)	Manipulation of actors through threats
Counterterrorism	1970s to present (peak after 9/11)	Manipulation of actors through obstacles to action

ered a counterintuitive finding, which is that occasionally countermeasures can cause more damage than they prevent. This happens when a countermeasure is placed on a less damaging target, and the adversary responds by shifting to a more damaging target (Fig. 1).

The second toolbox area addresses actions that cause the adversary to shift to not attacking. One difficulty we found with this topic is that it can be very hard to quantify the utility of not attacking. We addressed this issue by adding a non-attack option to MARS, and varying the utility associated with that option via sensitivity analyses. We noted that the addition of non-attacks can cause certain countermeasures to perform better, which happens when the addition of the countermeasure significantly decreases the overall probability of attack.

The third toolbox area deals with actions that cause an increased probability of interdiction of the adversary. Here we used an existing agent-based model of an adversary attack on a subway station, created as part of the LLNL Vulnerability Reduction effort. In this model, the adversary enters a station and attempts to detonate an explosive charge, while patrol units simultaneously attempt to interdict the adversary (Fig. 2). We showed how the agent-based model can be used in conjunction with MARS to generate a quantitative assessment of conops countermeasures, such as the number of patrols posted on each platform and whether security cameras are used.

Related References

1. Anthony, R., "A Calibrated Model of the Psychology of Deterrence," *Bulletin on Narcotics*, **56**, pp. 49–64, 2004.
2. Ehrlich, I., "The Deterrent Effect of Capital Punishment: A Question of Life and Death," *The American Economic Review*, **65**, pp. 397–417, 1975.
3. Huth, P., and B. Russett, "Deterrence Failure and Crisis Escalation," *International Studies Quarterly*, **32**, pp. 29–45, 1988.
4. Jacobson, S., T. Karnani, and J. Kobza, "Assessing the Impact of Deterrence on Aviation Checked Baggage Screening Strategies," *International Journal of Risk Assessment and Management*, **5**, pp. 1–15, 2005.

FY2009 Proposed Work

Our goal is to expand upon all of the areas in the toolbox, particularly the agent-based modeling component. We plan on adding Bayesian learning techniques to the patrol decision-making processes, as well as using such models to evaluate the deterrent effects of decoy countermeasures.

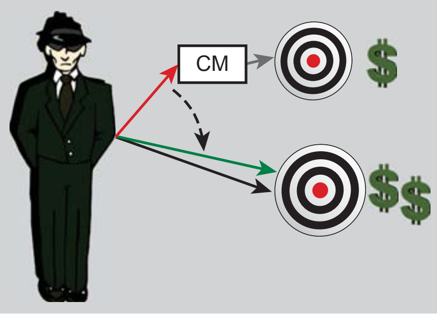

Figure 1. Illustration of model result: when a countermeasure is placed on a less damaging target, the adversary can respond by shifting to a more damaging target.

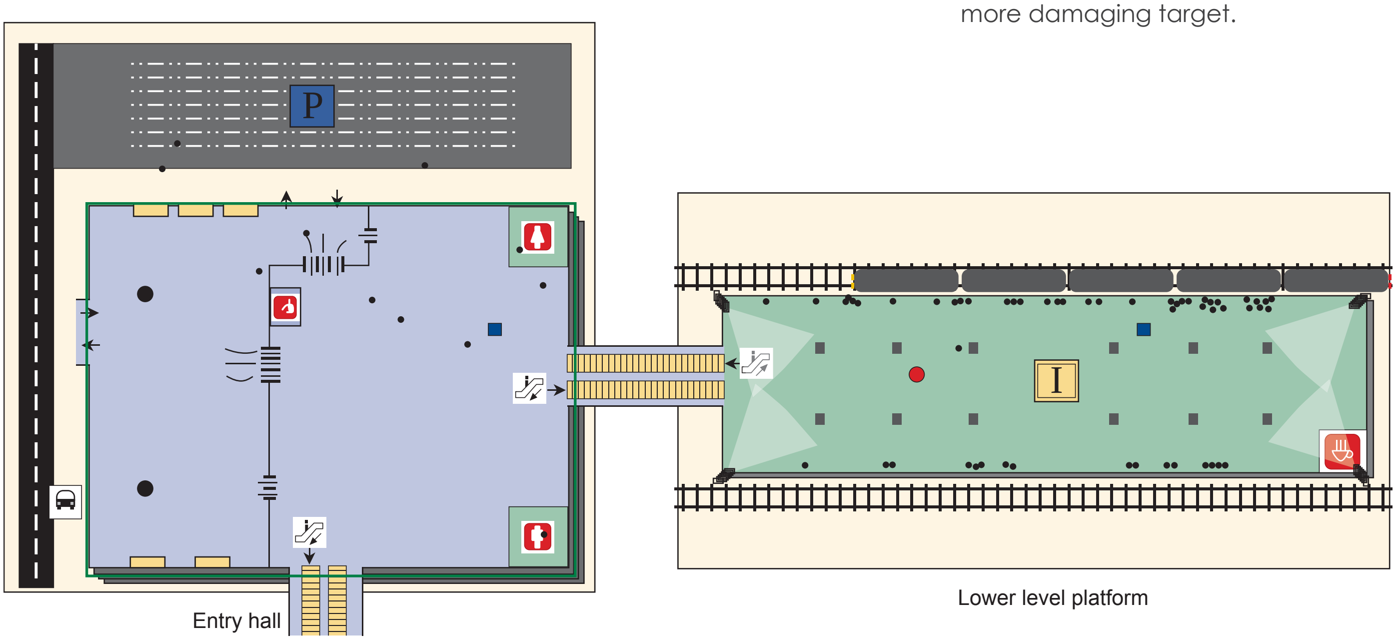

Entry hall

Lower level platform

Figure 2. The agent-based model. The patrols are blue; the adversary is red; and the pedestrians are black.

Insider Threat Scenarios and Signatures

Deborah W. May
(925) 422-1448
may14@llnl.gov

Current cyber and information security methods rely on static signature-based approaches to detect and block undesirable network traffic. This is typically done at the perimeter of an intranet or subnet. This approach is extremely limited, especially in a world where malware and adversaries modify their techniques frequently to evade signature-based detection, and perform their malicious functions *within* intranets and on hosts, all distributed across time and IP-space.

To remove some of these limitations, the community is moving toward behavioral signatures that evolve over time. Additionally, rather than addressing network security at a single point, such as the firewall, there is increasing interest in distributing security throughout the network space, providing the ability to collect and correlate data from multiple points, thus enabling behavioral signature detection.

Figure 1. Server sink flow types by hour of the week.

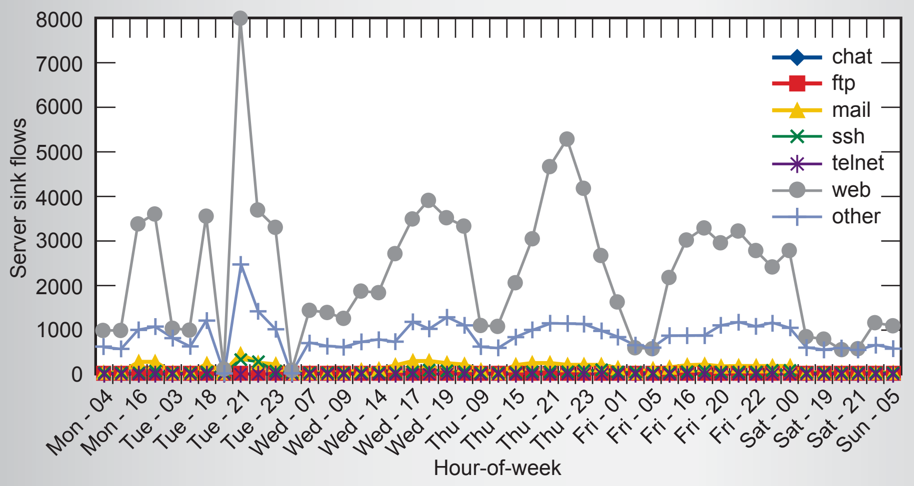

Project Goals

To further our understanding of behavioral signature evolution, we set out to contribute to one of network security's greatest challenges: the insider threat problem. This problem calls for distributed behavioral signature detection even more than outside attacks do, because the insider generally will not have to bypass a firewall or rely on tools that are sophisticated or noisy on the network since they already have some level of access.

Our intent is to describe the behavior of a threatening insider from the viewpoint of computer network traffic, first as visible at a major access point, and then, as seen across multiple sensors. We apply both adversary modeling and pathway analysis to create our model.

To determine if the insider behavior signature is detectable is another challenge. It is easier for insiders to cloak their actions in what appears to be normal and benign traffic. Understanding what portions of a signature can be used to effectively identify malicious behavior while keeping false-positives low is another goal of this project.

Relevance to LLNL Mission

Cyber security in general, and next-generation approaches that push forward the technology base in particular, are emerging as a major focus of LLNL. In addition to potentially improving the security posture of LLNL and the DOE complex, this work contributes to a new national initiative to transform cyber security to more effectively address the sophisticated threats of today and tomorrow. The specific problem we address in this project, and the approaches we chose to pursue, draw upon several LLNL core competencies including threat and vulnerability modeling, distributed computing, and network security.

FY2008 Accomplishments and Results

This project resulted in two overarching "lessons learned."

First, pathway analysis is not particularly effective for computing environments. This is largely because of the sheer number of paths from the outside of a network to an attractive target. We were able to address this by effectively collapsing multiple paths based on equivalent security posture characteristics. However, unlike the physical world where pathways are fairly static, the networked world presents new and changing pathways all the time. This dynamism makes cyber security difficult and pathway analysis results age-off too quickly to be effective.

Second, attempting to detect an insider behavior signature at a single point in time and network space is not feasible. Our studies show that some behavior signatures match up to 80% of firewall traffic in an open-science computing environment.

However, there may be hope. Adding just one more detection point, and correlating the two, reduced the hit rate significantly. We hypothesize that this reduction rate would continue, possibly exponentially, as additional detection points are added. Many factors would have to be considered, such as the ability to do precise time and actor correlation, and the utility of the data being correlated. Also, our project addressed only static behavior signatures; more sophisticated methods of building and detecting dynamic signatures are areas of research that would greatly enhance these approaches to cyber security and the insider threat problem.

In addition to these lessons learned, we made numerous recommendations to the security staff for the network analyzed, to enhance security posture and improve potential for detection of malicious activity.

Figures 1 through 3 are representative of our results.

Related Reference

Wright, C., *et al.*, "On Inferring Application Protocol Behaviors in Encrypted Network Traffic," *Journal of Machine Learning Research*, **7**, pp. 2745–2769, December 2006.

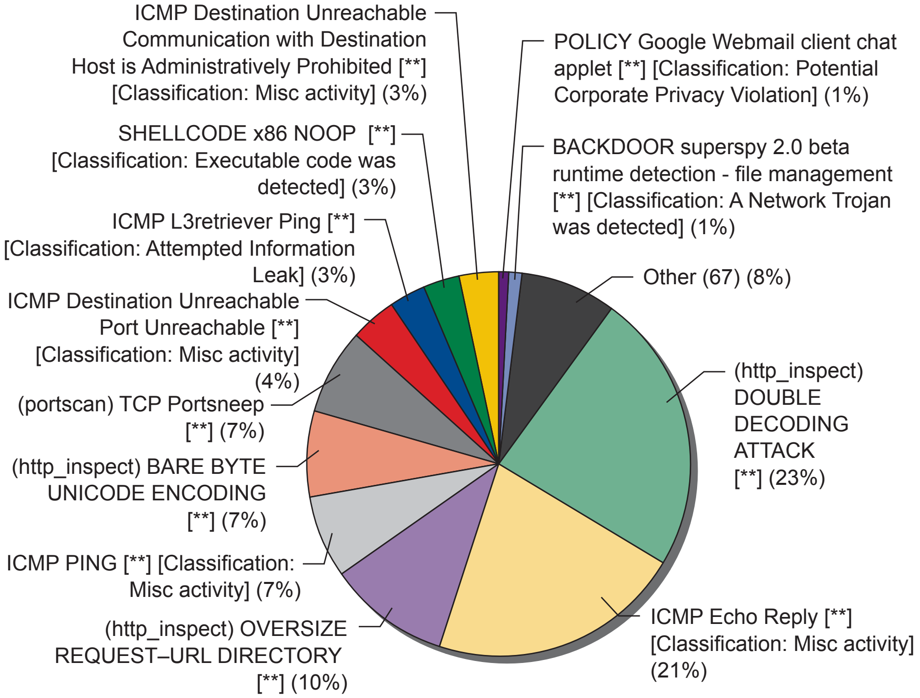

Figure 2. Pie chart depicting SNORT rule alert types at the firewall. (SNORT is a rule-based intrusion detection/prevention system and is the *de facto* standard tool.)

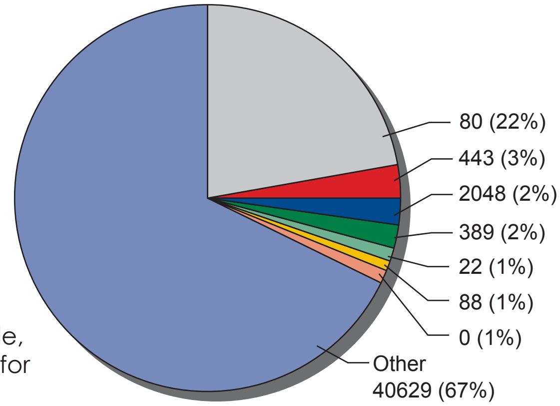

Figure 3. Pie chart depicting the destination port of incoming network traffic. Port 80, for example, is the standard port used for web traffic.

Proliferation Resistance and Physical Protection of Current Nuclear Fuel Cycles

Thomas A. Edmunds
(925) 423-8982
edmunds2@llnl.gov

Fifty years of worldwide operation of nuclear power plants has generated a large inventory of nuclear materials that must be managed responsibly. The proliferation resistance of spent fuel from past and current operations must be characterized in order to provide perspective on emerging and proposed nuclear fuel cycles. By emerging, we refer to the trend towards higher fuel burnups in existing light (LWR) and heavy water reactor fuel cycles. We also place high-temperature gas reactors and their associated tristructural isotropic coated particles (TRISO) fuel into the class of emerging nuclear fuel cycles. New nuclear fuel cycles include proposed uranium extraction (UREX) fuel cycles in which actinides in spent nuclear fuel are not separated from the plutonium in order to reduce the utility of the material for weapons use.

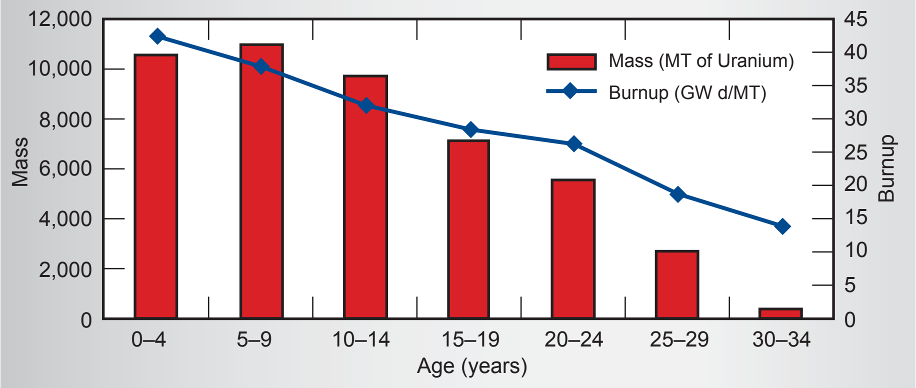

Figure 1. Characteristics of spent fuel in U.S. inventories. This figure shows that older spent fuel has lower burnup (irradiation time in a reactor). This low-burnup fuel scores lower with regard to all three proliferation resistance metrics: a lower radiation barrier, more attractive plutonium isotopics for weapons use, and lower heat generation rates.

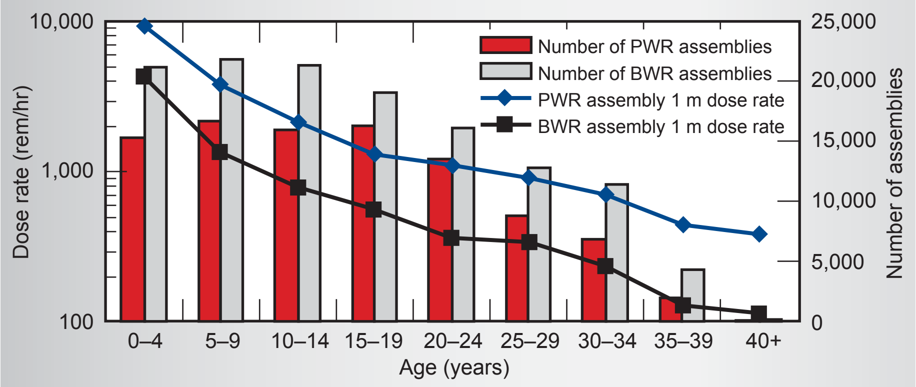

Figure 2. 2010 U.S. spent fuel assemblies and dose rates at one meter. This projection of average spent fuel properties for given vintages shows that many spent fuel assemblies will no longer have dose rates in excess of 100 rem/hr by 2010. (This is the dose rate needed to be "self-protecting" by the International Atomic Energy Administration definition.)

We measure proliferation resistance in terms of three fundamental metrics: radiation field, plutonium isotopic composition, and heat generation rates. We develop quantitative estimates of these metrics for a number of different fuel cycle materials. We also identify process operations in nuclear fuel cycles that may be a source of proliferation or theft risk.

Project Goals

The goal of this project is to establish proliferation resistance benchmarks that can be used to assess the relative benefits of proposed nuclear fuel cycles. Characterizing existing commercial LWR fuel cycle materials and processes with regard to quantitative proliferation resistance metrics provides a reasonable benchmark. Characterizing the near-term evolution of commercial nuclear fuel cycles provides a measure of proliferation resistance goals that can be achieved within a short period of time without major structural changes in the industry.

Relevance to LLNL Mission

Nuclear nonproliferation and global climate monitoring have been longstanding missions at LLNL. Advising key government decision-makers regarding the impacts of energy policy decisions on the risks of nonproliferation and impacts on global carbon emissions requires a thorough understanding of current and proposed commercial nuclear fuel cycles.

FY2008 Accomplishments and Results

We developed estimates of spent fuel properties for a number of different nuclear fuel cycles. As indicated in Fig. 1, there is a trend towards higher burnup fuel in commercial LWRs. This higher burnup provides improved proliferation resistance. We implemented code and estimated dose rates from spent fuel derived from a number of different fuel cycles and reactor operating conditions (principally fuel burnup levels). Dose rate estimates are shown in Fig. 2 for spent fuel from LWR fuel cycles and in Fig. 3 for higher burnup TRISO fuel used in a pebble bed modular reactor (PBMR). We also conducted literature surveys and ran models to estimate the plutonium isotopic composition of spent fuel. Finally, we estimated heat generation rates from spent fuel.

We identified potential improvements in proliferation resistance. First, if the current regulatory limit of 5% enrichment of LWR fuel is increased, higher burnups might be possible that would increase proliferation resistance of the plutonium in spent fuel. However, higher enriched uranium fuel would be less proliferation resistant because the effort to further enrich the fuel to weapons grade uranium would be reduced. As shown in Fig. 4, we quantified the decrease in signatures of these operations when higher enriched uranium feedstocks are used. The second structural change would be a switch to high-temperature gas reactor fuel cycle and TRISO fuel. The higher burnups achievable with this technology and the inherent difficulty of chemical separation of plutonium from the fuel matrix offer improved proliferation resistance.

Finally, we evaluated the process steps in different fuel cycles to identify opportunities for proliferant nations and sub-national groups to acquire material and fabricate weapons. We examined physical processes and inspection regimes in order to identify points in the fuel cycle that may pose a risk.

Related References

1. Albright, D., F. Berkhout, and W. Walker, Plutonium and Highly Enriched Uranium 1996, Oxford University Press, New York, 1997.
2. Bathke, C. G., *et al.*, "An Assessment of the Proliferation Resistance of Materials in Advanced Nuclear Fuel Cycles," *8th International Conference on Facility Operations – Safeguards Interface*, 2008.
3. Butler, J., A. Chebeskov, J. Dyer, T. Edmunds, V. Oussanov, and J. Jia, "The Adoption of Multi-Attribute Utility Theory for the Evaluation of Plutonium Disposition Options in the United States and Russia," *Interfaces*, **35**, 1, January 2005.
4. International Atomic Energy Agency, "Guidance and Considerations for the Implementation of INFCIRC/225/Rev.4, The Physical Protection of Nuclear Material and Nuclear Facilities," *IAEA-TECDOC-967 (Rev. 1)*, May 2000.
5. Slabber, J., "PBMR Nuclear Material Safeguards," *2nd International Topical Meeting on High Temperature Reactor Technology*, Beijing, China, September 22–24, 2004.

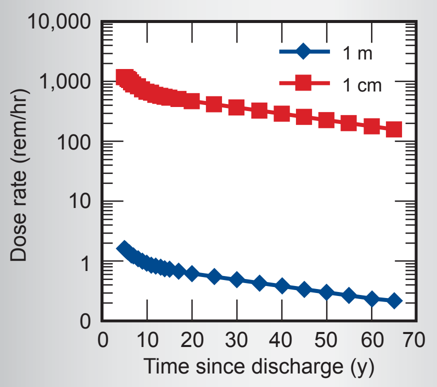

Figure 3. PBMR fuel sphere dose rates for 133 GWd/MT. This figure shows the dose rate for a 6-cm-diameter sphere of TRISO fuel used in a PBMR. This high-temperature reactor technology achieves high burnup levels that improve proliferation resistance. The high dose rate at 1 cm precludes handling spent fuel for protracted periods. Each sphere can contain up to 9 g of uranium or plutonium.

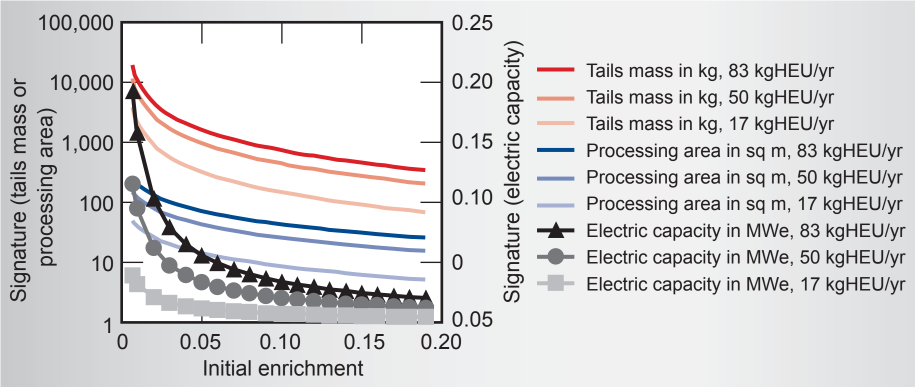

Figure 4. Clandestine enrichment plant signatures. Higher burnup fuel would require higher initial enrichments. This figure shows how signatures of enrichment from commercial to weapons grade uranium would decrease. Signatures decrease by a factor of two when initial enrichment is increased from the current NRC limit of 5% to just below 20%.

Software Module for Statistical Analysis in Climate-Related Impact

Gardar Johannesson
(925) 422-3901
johannesson1@llnl.gov

Projected climate change will impact all aspects of everyday life and has the potential to alter the world as we know it. To carry out studies of the potential impact of climate change requires working with massive output data from global climate models (GCMs). These models are inherently uncertain about their future climate projections; they operate on various spatial and temporal scales; and their output is not in general directly suited for use in local/regional climate impact studies.

The starting point of a regional climate impact study is to spatially downscale one or more GCM projections. This can be done by either a finer-resolution regional climate model (bounded by the output from a given GCM) or a statistical model (trained using historical data). In either case, additional uncertainty is introduced in downscaling a given GCM projection.

The aim of this effort is to create statistical methods and tools to assist with local/regional climate impact studies, in particular in terms of quantifying climate-change uncertainty. This involves gathering relevant data from multiple GCMs, both for past and future climate, along with various observation-based datasets for the region of interest. The data-acquiring step is then followed by a statistical analysis of the projected climate change, both at the spatial scale of the GCMs and on statistically downscaled projections.

Project Goals

The goals of this effort are to 1) set up a web-access to a static (already established) database of downscaled results from multiple GCMs; 2) build software tools to gather and process climate data from multiple online databases; and 3) implement statistical analysis tools for both large- and fine-scale analysis of the regionalized climate data.

Relevance to LLNL Mission

Climate change has been identified as a major national and global security threat, as highlighted in a recent report by the National Intelligence Council. This is reflected in LLNL's Science and Technology Plan, which identifies regional climate-change prediction, mitigation, and adaptation as one of its primary thrust areas.

FY2008 Accomplishments and Results

A static database of downscaled temperature and precipitation projections from multiple GCMs is now hosted at LLNL Green Data Oasis with a public web-access interface: http://gdo-dcp.ucllnl.org/downscaled_cmip3_projections/dcpInterface.html.

The downscaled projections cover North America at a one-eighth degree (~ 12 km) spatial resolution and 1-month temporal resolution, which might be sufficient in some cases, but quite often finer-resolution data is required, along with a quantification of uncertainty in the projected changes.

A Python module was created under this effort to gather and postprocess climate-related data. This module leverages the Climate Data Analysis Tools (CDAT) developed by the Program for Climate Model Diagnosis and Intercomparison (PCMDI) at LLNL to extract and postprocess GCM data from the archive at PCMDI. It also fetches large-scale reanalysis data (NCEP2 data) and local weather station data from the online Climate Data Library of the International Research Institution (IRI) of Climate and Society. Hence, given a region of interest such as the Livermore Valley, the Python module is used to build a local database of 1) GCM variables of interest for past and future climate relevant to that region of interest; 2) large-scale observational-based data; and 3) local weather station data. This typically yields 1 to 2 Gb of data (Fig. 1).

A library of statistical analysis tools was developed in the R statistical

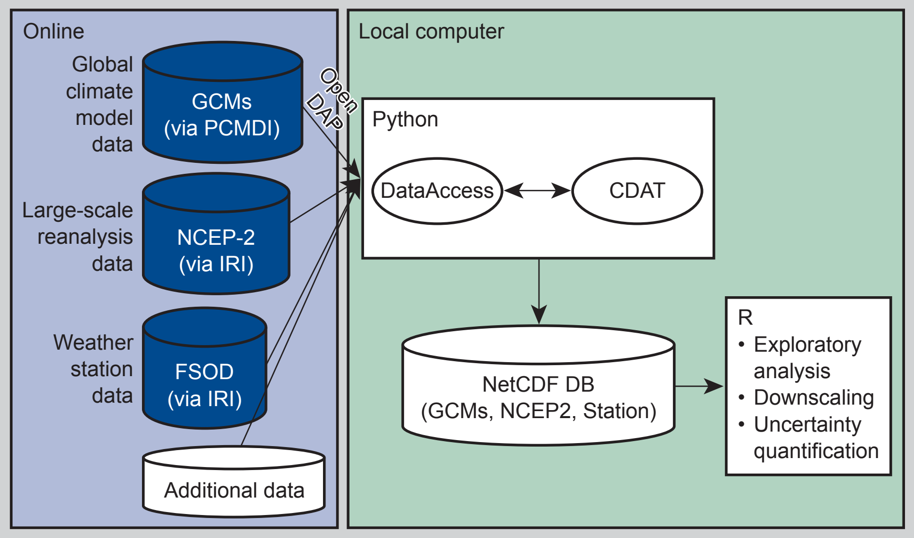

Figure 1. The Python climate-data access (DataAccess) module. The module runs on a local computer and is used to build a local regional climate database by extracting the relevant data from online sources. The local climate database is then analyzed using a library of tools written in the R statistical language.

computing language to interact with the regionalized climate database and carry out exploratory data analysis, statistical downscaling of future GCM projections, and uncertainty quantification.

An example of an application of these tools is given in Figs. 2, 3 and 4 for two weather stations located at the Ross and the Diablo Dams in the North Cascade of the state of Washington, an important hydroelectricity region that might be severely impacted by climate change. The location of the dams, approximately 3.5 mi apart, is shown in Fig. 2. Figure 3 summarizes changes in daily average temperature at the GCM grid-scale, while Fig. 4 summarizes changes in daily maximum temperature at the two sites using statistical downscaling. Similar analysis can be carried out for other climate variables of interest, such as precipitation, at the same sites.

Project Summary

This project produced an initial version of a Python module to gather and process climate-related data for a regional impact study. It also yielded a suite of statistical tools in R to carry out analysis of the resulting data. The analysis tools are being refined and extended under LLNL's current Climate Initiative.

Related References

1. Christensen, J. H., *et al.*, "Regional Climate Projections," Climate Change 2007: The Physical Science Basis. Contribution of Working Group I to the Fourth Assessment Report of the Intergovernmental Panel on Climate Change, Cambridge University Press, 2007.
2. Collins and Knight, Eds., *Phil. Trans. of the Royal Soc. Series A, Theme Issue Ensembles and Probabilities: A New Era in the Prediction of Climate Change*, **365**, pp. 1957–2191, 2007.
3. Hastie, T., R. Tibshirani, and J. Friedman, The Elements of Statistical Learning: Data Mining, Inference, and Prediction, Springer-Verlag, 2003.

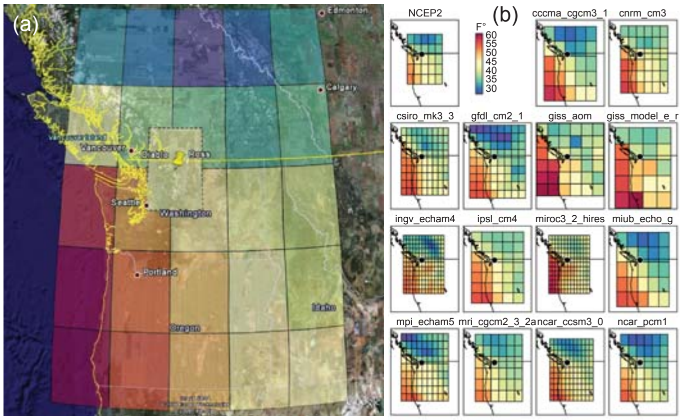

Figure 2. (a) Location of the Diablo and the Ross dams in Washington (yellow pin). The map is overlaid by a 5-x-5 grid showing the 1980 to 2000 average temperature as given by the large-scale NCEP2 reanalysis data. (b) Smaller maps contrast the spatial resolution of the NCEP2 data (upper-left panel) to that of 14 different GCMs in the PCMDI archive.

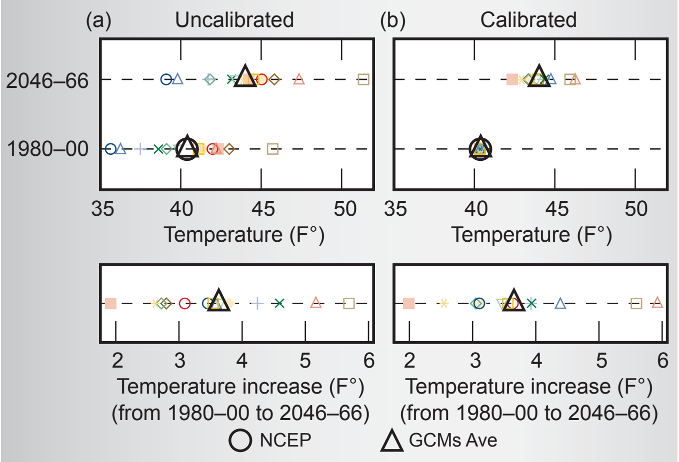

Figure 3. Changes in the average daily temperature between 1980 and 2000 and 2046 and 2066 as projected by 14 GCMs in a single NCEP2-size grid-cell centered on the sites of interest (Fig. 2a). The difference between the uncalibrated plots in (a) and the calibrated plots in (b) is that the data from each GCM is calibrated (shifted and scaled) to yield the same mean and variance as the NCEP2 data for 1980 to 2000. This results in a visible difference in the uncertainty in the projected temperature range (the two top plots), but less so in the temperature increase (the two bottom plots).

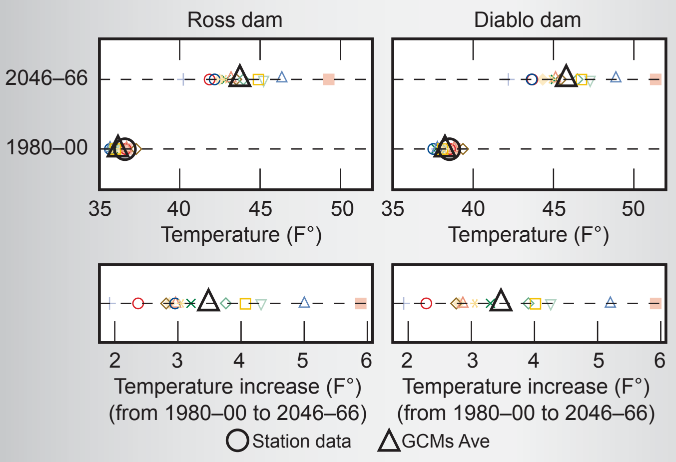

Figure 4. Changes in the daily maximum temperature from 1980 to 2000 and from 2046 to 2066 at the two sites of interest as projected by 13 GCMs. The GCMs data is statistically downscaled using Multivariate Adaptive Regression Splines (MARS) to the two sites using daily temperature and mean sea level data in a 3-x-3 NCEP2-sized grid, where the center grid-point covers the two sites.

Energy Manipulation

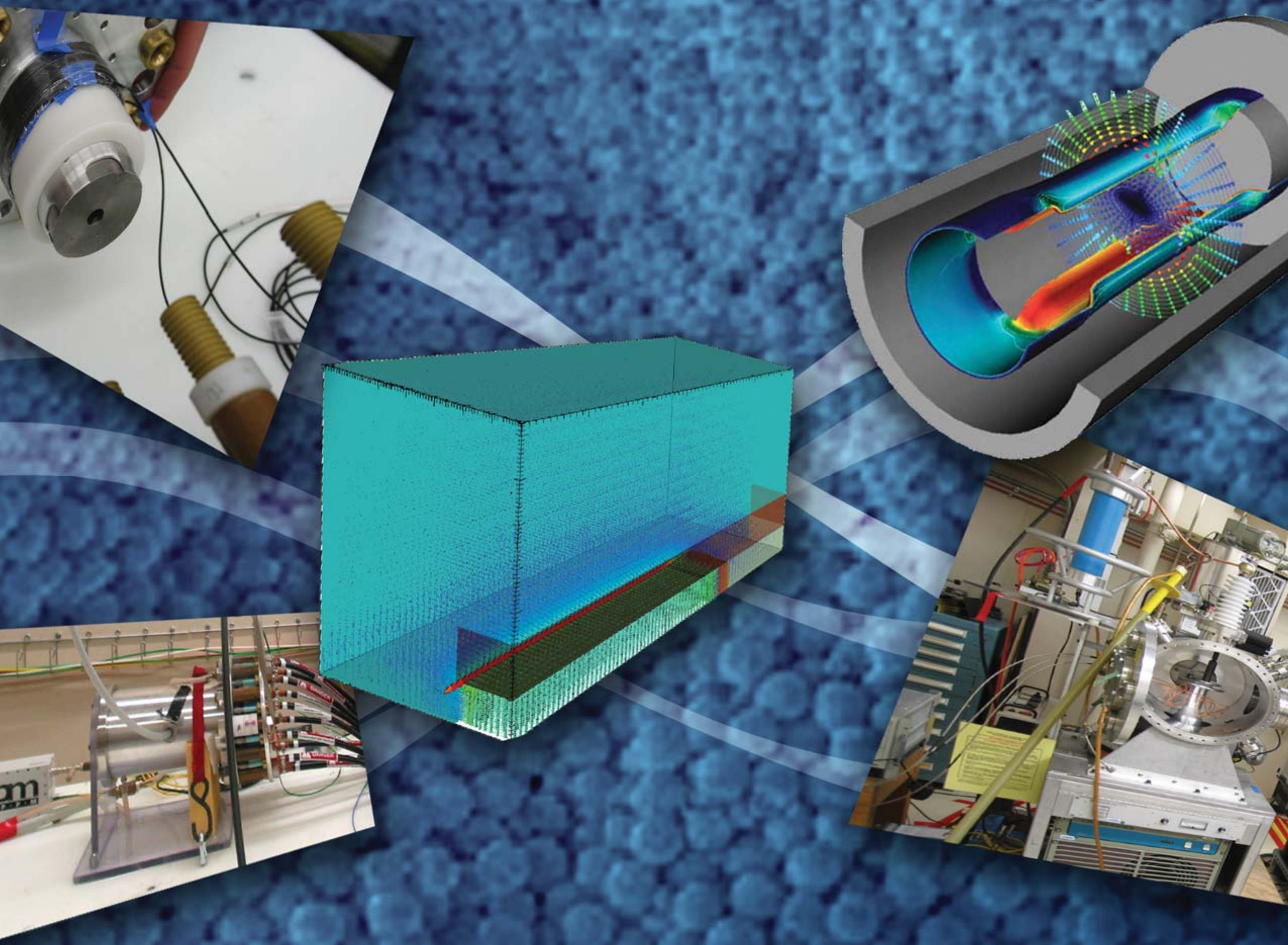

Ultrahigh-Velocity Railgun

Jerome M. Solberg
(925) 422-5971
solberg2@llnl.gov

Since early experiments, in the mid 1970s, railguns have held promise as a controllable means to launch gram-sized (or larger) projectiles at ultrahigh velocities, (UHV), greater than 10 km/s. Though other means exist to launch projectiles at such speeds, they suffer from lack of controllability and extremely high rates of acceleration, both of which severely limit their utility. Railguns are essentially simple devices, nothing more than one-turn coils where a portion of the coil, the armature, can slide relative to the other two portions, the rails. The magnetic pressure exerted on the armature accelerates it down the rails.

In a UHV railgun the sliding velocities and current densities are such that the portion of the armature in contact with the rail almost immediately melts and transitions to a plasma. Hence the standard UHV railgun dispenses with a solid armature altogether, in favor of a mass of conductive plasma, pushing on the launch package at high pressure.

Experiments at LLNL and elsewhere found that the standard plasma armature railgun experienced a drastic drop in efficiency as the velocity approached 6 km/s, resulting in an effective velocity limit at approximately this value. There are numerous theories as to why such a limit exists, but the preponderance of researchers believe that at high enough speeds one or more alternate paths or short-circuits develop behind the armature, depriving it of current, and hence reducing the propulsive force. This phenomenon is known as “restrike.” Understanding what leads to restrike, and determining what can be done to minimize or eliminate it, are generally considered the key to improving railgun performance.

Project Goals

The project goal is to develop a simulation capability, starting with the LLNL code ALE3D, which can adequately simulate UHV railguns, and therefore investigate the phenomena of restrike and possible remediation techniques. In concert with the development of the simulation tools, experimental techniques are to be developed as a means towards understanding the relevance and accuracy of the simulation results.

Relevance to LLNL Mission

Accurate equation-of-state (EOS) data is key to ensure confidence in weapon simulations. Current theoretical

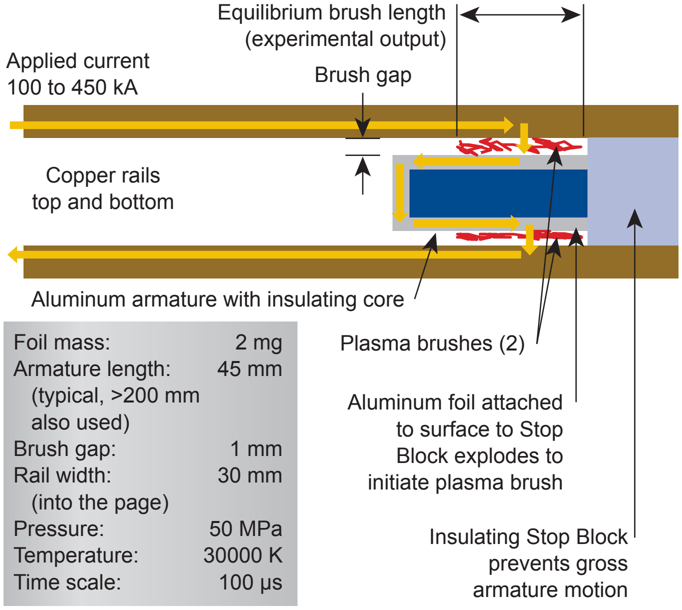

Foil mass:	2 mg
Armature length: (typical, >200 mm also used)	45 mm
Brush gap:	1 mm
Rail width: (into the page)	30 mm
Pressure:	50 MPa
Temperature:	30000 K
Time scale:	100 μs

Figure 1. Illustration of the Fixed Hybrid Armature experimental apparatus.

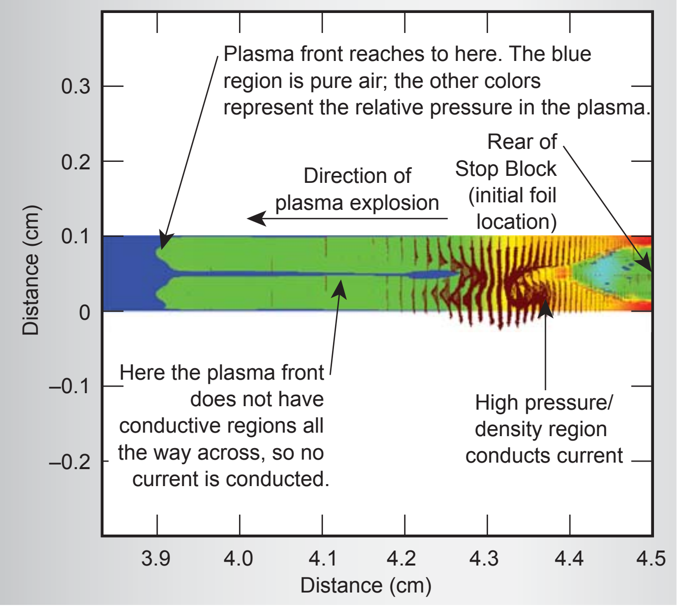

Figure 2. Exploding Foil creating railgun plasma at t = 2.5 μs, simulated by ALE3D.

models are not adequate in all regimes; experiments are needed to confirm the combination of empirical and theoretical models used. At very high strain rates and temperatures, laser implosion such as provided by NIF is an adequate technology. At lower strain rates and temperatures, two-stage gas guns such as JASPER are an excellent experimental tool. However, in the mid-range there does not exist an adequate experimental tool. A railgun could fill this gap. Additional applications for railguns, which dovetail with LLNL's support for DoD interests, include kinetic energy weapons, launch-to-space, and the testing of space components against asteroid impacts.

FY2008 Accomplishments and Results

In FY2008 we concentrated on using and refining the basic simulation techniques developed in FY2007. Much of the work was focused on simulating the Fixed Hybrid Armature Experiment (Fig. 1), which develops a plasma with typical railgun characteristics, but in a setting with no gross motion of the armature (the "projectile" is mechanically prevented from forward motion).

In addition, work was begun on the simulation of moving railguns in concert with similar developments supporting a program for a high-velocity (> 2 km/s) railgun for long-range fire support.

Figures 2 through 5 illustrate our results.

Related References

1. Rashleigh, S. C., and R. A. Marshall, "Electromagnetic Acceleration of Macroparticles to High Velocity," *Journal of Applied Physics*, **49**, 4, pp. 2540–2542, 1978.

2. Hawke, R. S., *et al.*, "Summary of EM Launcher Experiments Performed at LLNL," *IEEE Trans. on Magnetics*, **22**, 6, pp. 1510–1515, 1986.

3. Parker, J. V., "Why Plasma Armature Railguns Don't Work (And What Can Be Done About It)," *IEEE Trans. on Magnetics*, **25**, 1, pp. 418–424, 1989.

4. Boynton, G. C., and M. A. Huerta, "Secondary Arcs in 2-D MHD Numerical Simulations of EML Plasma Armatures," *IEEE Trans. on Magnetics*, **31**, 1, pp 564–569, 1995.

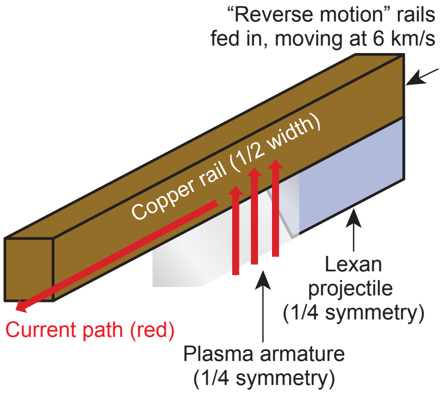

Figure 3. Diagram showing general simulation technique for moving railguns.

FY2009 Proposed Work

In 2009 the work on simulating moving railguns will continue, with the goal of simulating incipient restrike in actual plasma and hybrid (combination of solid and plasma armature) railguns. This work will culminate in the simulation of various design ideas we have, aimed at reducing or eliminating restrike, and hence extending the performance envelope of railguns to the UHV region.

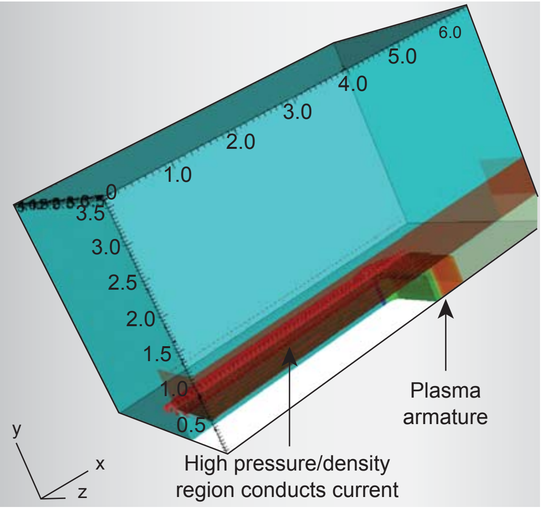

Figure 4. Plasma Railgun at 6 km/s, current distribution, simulated by ALE3D. This represents early time history before significant plasma loss.

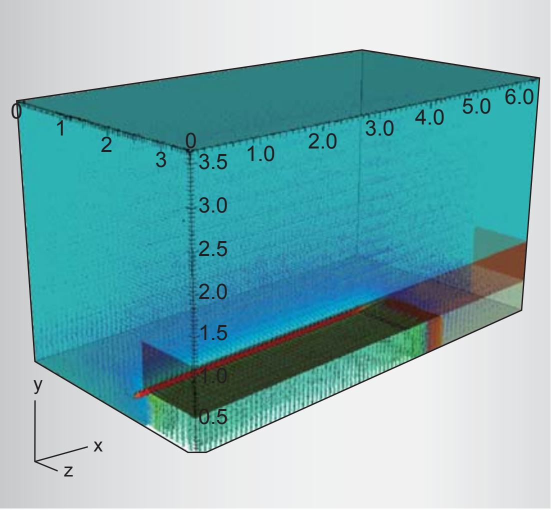

Figure 5. Plasma railgun at 6 km/s, magnetic field distribution, simulated by ALE3D.

Pulse Power Systems and Diagnostics for the Fixed Hybrid Armature Railgun

Todd J. Clancy
(925) 422-8571
clancy5@llnl.gov

Plasma physics within the confines of railgun science is not well understood. Since plasma *re-strike* is primarily responsible for limiting ultra-high velocities (UHV) and equation of state (EOS) studies, there is a great need to predict and control this behavior.

For this purpose, we have rebuilt and explored a Fixed Hybrid Armature (FHA) railgun. In these experiments, plasma brushes are formed from exploding aluminum foils, which then provide a current path through the armature. Since the armature is fixed in place, a pseudo-steady-state is achieved and diagnostic investigation of the plasma is confined to a small region (Fig. 1).

We have implemented a suite of diagnostics, including two arrays of Bdots (B-field sensors) used to measure the magnetic fields produced by the plasma currents as a function of position (Fig 2). Plasma position is also measured by the use of a fiber optic photo emission array. Total current is measured by a single Faraday rotation diagnostic and Rogowski coils positioned on the upper rail of the FHA railgun and on each module of the capacitor bank. Plasma pressure is obtained by both a piezoelectric quartz sensor and a fiber optic Bragg grating sensor. Voltage measurements are performed across the plasma brushes, from rail to rail, and also on the modules of the capacitor bank.

Eleven experiments over a range of total currents from 164 kA to 475 kA have been performed. Experimental data has been provided to the UHV railgun project and applied to the validation of a new plasma model in ALE3D, a multiphysics computational platform.

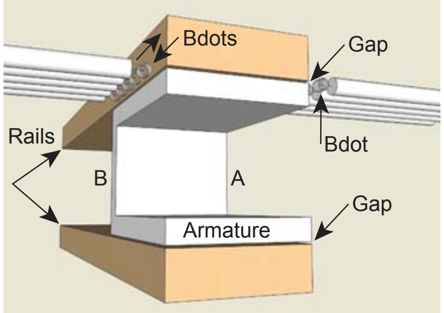

Figure 1. Depiction of the Fixed Hybrid Armature railgun. The armature is floating, thus a small gap (~1 mm) exists between it and the rails. This gap contains conducting plasma that changes parameters such as location, density, and temperature over the length of the experiment. Two arrays of five Bdots are installed on each side of the top of the armature and are oriented to be sensitive to the magnetic field of the current through the plasma.

Project Goals

The primary goal of this project was to provide diagnostic data with sufficient

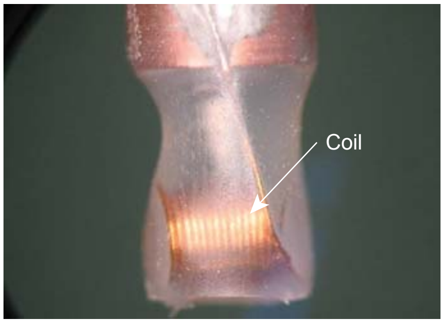

Figure 2. The Bdot sensors are heat-shrink encapsulated 15-turn loop antennas with 0.077-in.-diameter turns of 0.006-in.-thick wire. The loops are wrapped around a mandrel and soldered to semi-rigid coaxial cable, then imbedded in the insulating walls of the FHA railgun.

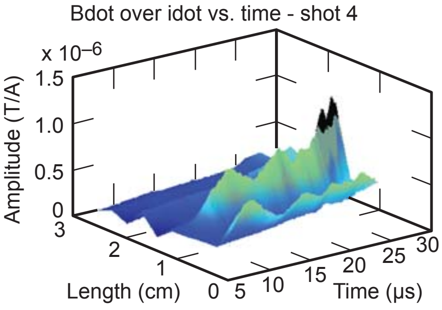

Figure 3. Bdot sensor data divided by total current gradient (idot) as measured by the Rogowski diagnostic positioned on the rail. Plasma generated magnetic field distribution varies in strength and position over time.

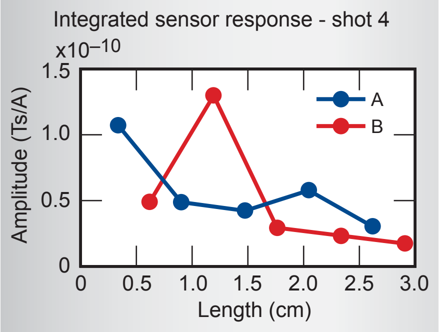

Figure 4. The integral of Bdot over idot response with respect to time, generates a total magnetic field contribution within the time window of interest. Clearly, side B of the FHA railgun received a larger contribution of signal than side A.

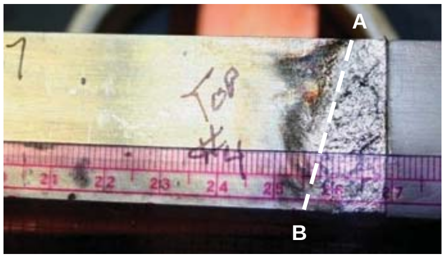

Figure 5. A post-mortem photograph of the armature reveals a skewing in the ablation of the aluminum armature. This skewing is predicted by the integrated response of the Bdot data shown in Figure 4.

resolution and relevance to validate a plasma model in ALE3D that is applicable in the railgun regime. To achieve this, we assembled the FHA railgun and configured a test bed for the application of high-energy pulsed power and sensitive diagnostics.

Relevance to LLNL Mission

This project directly addresses immediate needs in the LLNL's Engineering Energy Manipulation Focus Area Roadmap. These include the creation of a railgun test bed and high-energy diagnostic systems. Also addressed is the investigation of the feasibility of UHV railguns. These goals directly impact many pulsed power programs at LLNL and support the commitment to UHV and EOS research and shock physics.

ALE3D is a 3-D multiphysics computational platform. With the addition of a plasma model, this code has a wide range of application, including the understanding of high-energy pulsed-compression generators.

FY2008 Accomplishments and Results

By leveraging legacy hardware from the early 1990s, we assembled the FHA railgun test facility. The first experimental shot was performed in FY2007, successfully delivering 290 kA to the FHA railgun. In FY2008, we continued these experiments for a total of eleven shots over a range of total currents from 164 kA to 475 kA.

Diagnostic fidelity improved in FY2008 by fine tuning of the recording parameters for the Bdot array and Rogowski coils. Work on the fiber optic emission array and pressure sensor diagnostic continued and we achieved successful recordings over a few of the experiments. We also added voltage measurements to the breach end of the FHA railgun, as well as to the top and bottom plasma brushes.

A vast amount of measurement data has been generated, processed, and analyzed. A typical example of the Bdot time history data is given in Fig. 3, which shows how the plasma-generated magnetic field varies over time and space. The total contribution of this field over time is shown in Fig. 4. Here, the data suggests a distinct imbalance is between each side of the armature. This imbalance is confirmed in post-mortem photographs of the armature shown in Fig. 5.

The raw and processed data from all of the diagnostics are currently being applied to the validation of a new plasma model in ALE3D.

Related References

1. Drobyshevski, E. M., *et al.*, "Physics of Solid Armature Launch Transition into Arc Mode," *IEEE Transactions on Magnetics*, **37**, 1, pp. 62–66, 2001.
2. Hawke, R. S., *et al.*, "Summary of EM Launcher Experiments Performed at LLNL," *IEEE Transactions on Magnetics*, **22**, 6, pp. 1510–1515, 1986.
3. Hawke, R. S., *et al.*, "Plasma Armature Formation in High Pressure, High-Velocity Hydrogen, Starfire: Hypervelocity Rail Gun Development of High Pressure Research," *IEEE Transactions on Magnetics*, **25**, 1, p. 219, 1989.

FY2009 Proposed Work

The FHA railgun and capacitor bank provide a test bed for the continuation of experimental investigations concerning railgun plasmas. Additional experiments are planned for the testing of advanced non-ablating materials and for continued work on fiber optic sensors.

ALE3D/EM Validation Experiments

Laura K. Tully
(925) 424-2235
tully2@llnl.gov

The configuration of high-performance magnetic flux compression generators and electromagnetic launchers depends on detailed knowledge of the effects generated by interacting electromagnetics, solid mechanics, and thermal phenomena. To provide this information, a coupled 3-D electro-thermal-mechanical (ETM) simulation code has been created that self-consistently solves equations of electromagnetics (primarily magnetostatics and diffusion), heat transfer (primarily conduction), and nonlinear mechanics (primarily elastic-plastic deformation and contact with friction).

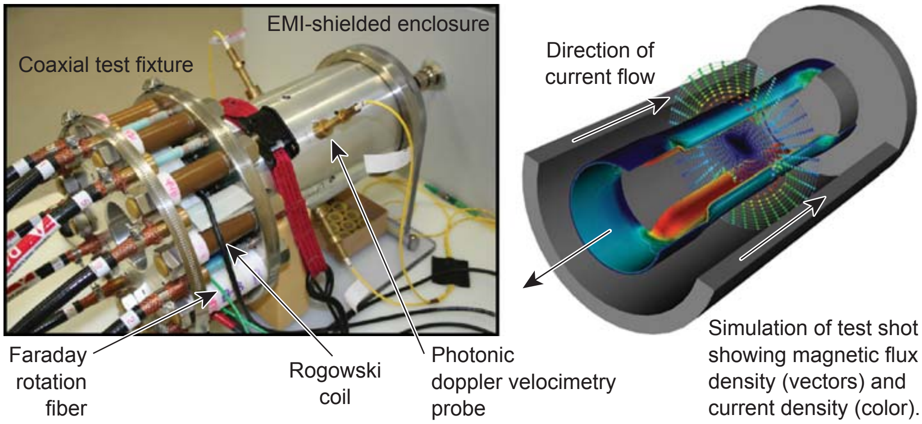

Figure 1. Coaxial validation experiment. The test stand uses a shorted transmission line and diverse diagnostics with results of a dynamic simulation from ALE3D/EM to provide a time history of the magnetic flux density, current density, and resulting mechanical deformation in the test fixture.

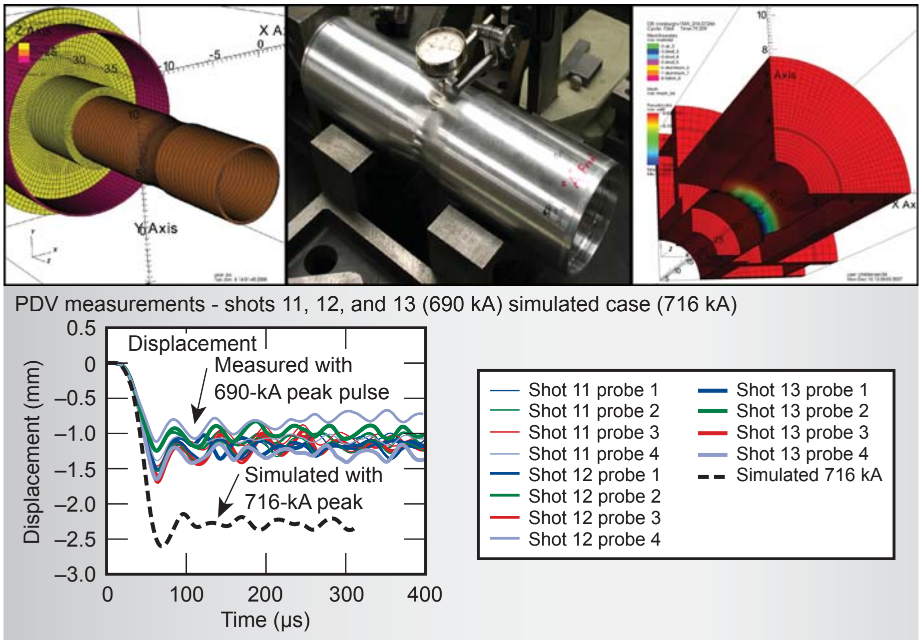

Figure 2. Early simulations and tests using the coaxial test fixture and a quadrant-symmetric simulation to model the formation of deformations and to initiate the study of instabilities that might be triggered by structural abnormalities.

ALE3D, a heavily used Arbitrary-Lagrangian-Eulerian hydrodynamics code with a large user community in the DOE complex, has recently been extended (ALE3D/EM) with an electromagnetics simulation capability to enable the simulation and optimization of ETM systems. In a similar vein, Diablo, a relatively new ASC-class parallel coupled multi-mechanics code built from LLNL-produced finite element (FEM) codes, has also been extended to include coupled EM effects.

We now have the foundation of a premier engineering tool for the simulation of the interacting electromagnetic, structural and thermal effects in high performance pulse power systems. Such systems are found in the overall power flow structures between flux compression generators and high-energy-density experiments as well as in electromagnetic launchers such as railguns. To round out this claim, we have started a validation campaign for the code.

Project Goals

The generation of high-quality data for validating simulation codes has been the challenging goal of this project. We chose to embark on a set of experiments that generate high-quality data for testing the accuracy of the modeling tools to be used for describing the details of the physical operation of the system. Concurrently, the experiments have been meant to provide the motivation and environment for the creation, testing, and qualification of experimental diagnostics.

A validation experiment was devised and a coaxial test fixture was used to provide high-quality experimental data from a controlled environment undergoing large magnetically induced deformations. These experimental data are particularly useful for the validation of coupling between **J** x **B** or Lorentz electromagnetic forces and structural momentum equations in ALE3D and Diablo.

The fixture permits injecting up to 1 MA current into a shorted coaxial transmission line from a 10-kV, 225-kJ capacitor bank. Such a current applies electromagnetic forces that crush the aluminum center conductor (Fig. 1). Our goal was to test the code against experiments using center conductor test cylinders of varying wall thicknesses, a nominal 6-in. working length, and 3-in. nominal diameter with a number of variations, including cylinders with slots or other imperfections, for the study of both 2-D and 3-D effects. This would enable validation in the presence of kink and buckling instabilities, and electrical contacts.

The fixture is such that the cylinders can be instrumented with strain gauges and thermocouples connected to signal conditioners and digitizers within an EMI-protected enclosure. The test fixture also allows for Photonic Doppler Velocimetry (PDV) measurements of the radial motion and displacements of the tube at four locations. Digital high-speed video is used to capture the rapid movement of the wall from a viewpoint within the center conductor of the structure. Accurate measurements of strain, temperature, displacement, and current have been recorded.

Relevance to LLNL Mission

These experiments provide a set of well-characterized data for the validation of engineering simulation codes for systems involving relevant, coupled electromagnetic, mechanics, and thermal effects. The validated codes are necessary for enabling LLNL to reliably create high performance systems and hardware. For example ALE3D/EM, when validated, promises to become the premier engineering tool for this purpose with widespread applications in explosive pulse power systems and electromagnetic launchers such as rail guns.

FY2008 Accomplishments and Results

FY2008 accomplishments have included the computer-supported creation of hardware for coaxial validation test apparatus, simulation of test shots in the coaxial test fixture, and the implementation and verification of advanced diagnostics for data acquisition. A successful experimental campaign included three “radial groove” axisymmetric shots (Fig. 2) and six “axial slots and radial groove” non-axisymmetric shots (Fig. 3). The high-quality data return was enhanced by Faraday Rotation and Rogowski Coil measurements for magnetic flux and current density; Photonic Doppler Velocimetry for localized structural displacement; and a high-speed video capture capability to record structural deformation on a more global scale at extended time.

Related Reference

Tully, L. K., D. A. Goerz, R. D. Speer, and T. J. Ferriera, “Modular High Current Test Facility at LLNL,” *IEEE Inter. Power Modulator Conf.*, May 2008.

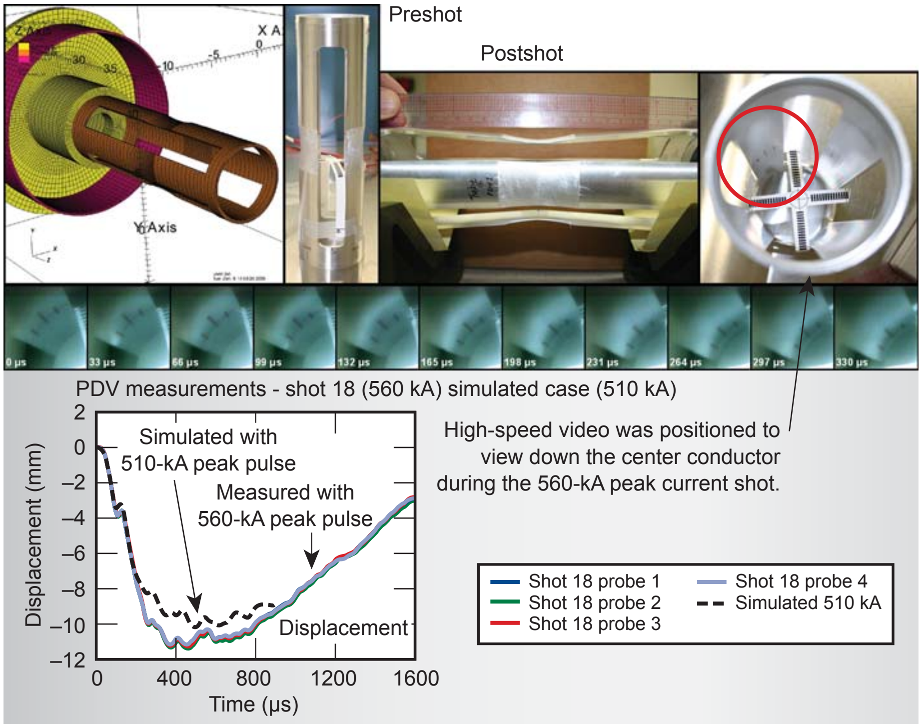

Figure 3. Sample results. A non-axisymmetric center conductor in the coaxial test fixture enables extension of the validation in the presence of instabilities in somewhat complicated structures. The full suite of diagnostics captures deformation of the center conductor with high-speed video capturing the dynamics of a large portion of the surface and the PDV system capturing, in high resolution, the displacement of a point on the surface.

FY2009 Proposed Work

In FY2009, we will investigate key areas especially pertinent to code validation. In particular, we will study the buckling and kinking instabilities that will challenge the full 3-D, high-spatial-resolution capability in ALE3D/EM. Using the high-speed video capability, we will be able to capture the formation of the modal buckling phenomenon with a microsecond-order frame-by-frame sequence over long time periods and therefore enable an extensive electromagnetic-structural-thermal code validation.

Magnetic Insulation in a Sulfur Hexaflouride (SF_6) Filled Power Flow Channel

Timothy L. Houck
(925) 423-7905
houck1@llnl.gov

Magnetic insulation is often used in pulse power generation and transmission systems to suppress the potentially deleterious effects of field emission due to high-electric-field stresses. The suppression is realized by applying a magnetic field orthogonal to the electric field that is extracting the electrons (field emission) from a surface. The resulting Lorentz force due to the magnetic field can cause a cycloidal motion of the electrons which can suppress the breakdown so long as the Larmor radius (the radius of the circular motion of a charged particle in the presence of a uniform magnetic field) is less than the electrode spacing. Of course, the magnetic field can be produced by the current flowing through the transmission system and/or by externally applied fields.

Often gas must be introduced in the region between the electrodes with the attendant introduction of complexity due to electron collisions with gas molecules. The collisions can be either elastic or inelastic. Further, the seemingly simple elastic collisions are complicated by the direction of the electron after the collision since the electron can gain (lose) energy by bouncing toward (away from) the anode.

Since breakdown is such an important factor in limiting pulse power system performance, it is imperative that the mechanism and mitigating methods be understood and that the database supporting the mitigating techniques is well-populated. Ionization and electrical breakdown of gases in crossed electric and magnetic fields are moderately explored areas limited to low gas pressure, low electrical/magnetic fields, and weak or non-electronegative gases primarily of interest in gas switch technology. High-power devices such as explosively-driven magnetic flux compressors operate at electrical stress, magnetic fields, and insulating (strongly electronegative) gas pressures nearly two orders of magnitude greater than published research.

The most applicable data available for SF_6 was taken at pressures of 22 torr, electrical fields less than 10 kV/cm and magnetic fields less than 1.3 T. However, present magnetic flux compressors may operate at a gas pressure of 760 torr (1 atm), electrical fields greater than 100 kV/cm, and magnetic fields approaching 100 T.

Figure 1 illustrates the knowledge base uncertainty that exists in the operating range of interest for LLNL's flux compression generators. It includes results of statistical analysis (Monte Carlo) of the motion of a large number of electrons and their collision products (secondary electrons, ions, and photons); the results of the Effective Reduced Electric Field (EREF) theory, which involves scaling with the gas pressure (number density); the extrapolation of earlier limited data; and five data points collected in this effort at atmospheric pressure. Unfortunately, the generation of experimental data in the laboratory has been limited by the inability to generate sufficiently high magnetic fields to demonstrate a measurable effect at atmospheric pressure.

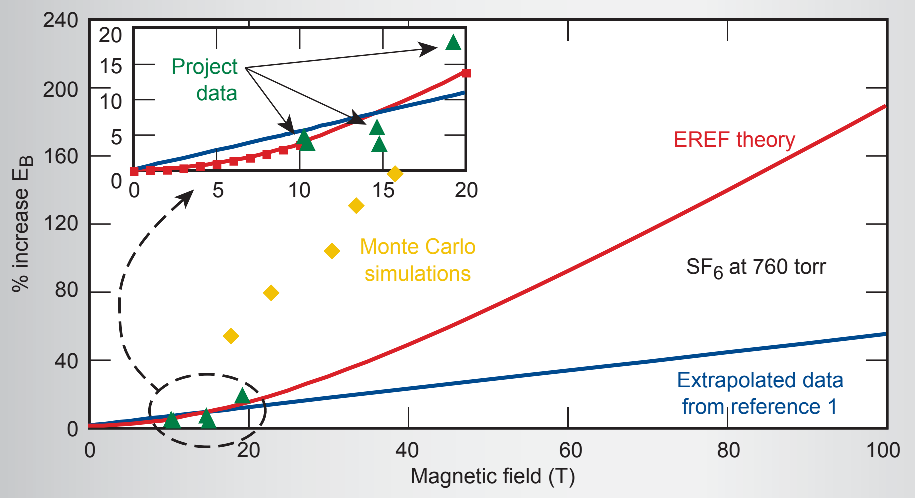

Figure 1. Increase in the electric field required for breakdown in SF_6 as predicted by extrapolation of data from earlier experiments (<1.2 T and 22 torr), the EREF theory, and Monte Carlo simulation. The inset graph shows our project data at 760 torr. The operating region of interest for magnetic flux compression includes fields near 100 T and pressures near 760 torr, well beyond our database.

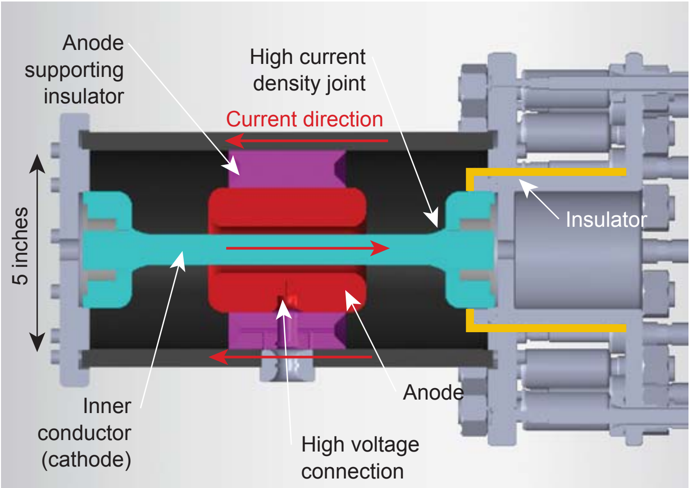

Figure 2. The coaxial load. The current is provided to the load through 12 cables, flows onto the outer conductor, and returns through the High Current Density Joint. A voltage applied to the anode with its neutral at the inner conductor generates the electric field.

Project Goals

The primary goal of the project was to populate a portion of the database by acquiring data for breakdown in SF_6 at atmospheric pressure with crossed electric and magnetic fields up to 20 T on the cathode surface. The experiments were executed in the LLNL HV Pulsed Power Laboratory using a 100-kV HV pulser, a 1-MA high-current (HC) pulser, and a coaxial load (Fig. 2).

There were two major challenges to producing the large magnetic field. The first challenge was generating a sufficiently large current to avoid the need for an extremely small cathode radius and problematic non-uniform fields. The second challenge was that the load had to withstand the tremendous magnetic pressure on conducting surfaces, pressure = $B_\theta^2/(2\mu m)$ or 23,000 psi for 20 T.

A secondary goal was studying very-high-current-density joints. While the current from the HC pulser is introduced to the coaxial load through 12 cables, the total current is carried on the inner conductor and passes through a single joint at the end flange.

Relevance to LLNL Mission

The LLNL mission in high-energy-density physics and weapons science motivates substantial requirements for the delivery of gargantuan pulses of electrical energy to assorted loads. A critical issue in extending the performance of envisioned pulse power devices and generators is the suppression of electrical breakdown or flashover that can exist at the extraordinarily high field stress levels that are being created. Another is the behavior of HC joints in near-yield conditions. The results of this project will indicate how far we can take the next generation of pulse power systems, and will also provide supporting evidence for validating models and theories applicable to these regimes.

FY2008 Accomplishments and Results

The experiment (Fig. 3) was executed during FY2008. Shots were done at currents (magnetic fields) between 500 kA (10 T) and 1 MA (20 T). Increases in the required electric field stress for breakdown in SF_6 varied from 4% at 500 kA to 18% at 1 MA. These measurements (Fig. 2) support the more conservative extrapolation of data and theory over computer simulation, but indicate the need for more data in the range of interest.

Two different HC-density joints were also tested. A simple butt-joint with a diameter of 1 cm failed on a 650-kA pulse (< 200 kA/cm). A flared-end joint with a contact diameter of ~3 cm survived multiple 750-kA pulses and a 1-MA pulse (>160 kA/cm). For this we used the magnetic pressure to force the joint together during the pulse and the contact resistance for the joint actually decreased after the initial 750-kA pulse.

Related Reference

1. Dincer, M. S., and A. Gokmen, "Electrical Field Breakdown of SF_6 in Crossed Magnetic Fields," *J. Phys. D: Appl. Phys.*, **25**, pp. 942–944, 1992.
2. Raju, G. R. G., and M. S. Dincer, "Monte Carlo Calculation of the Ionization and Attachment Coefficients in SF_6 in E x B Fields," *Proc. IEEE*, **73**, 939, 1985.
3. Heylen, A. E. D., "Electrical Ionization and Breakdown of Gases in a Crossed Magnetic Field," *Proc. IEEE, Pt. A*, **127**, 4, May 1980.
4. Faehl, R. J., *et al.*, "Results of a 100-Megaampere Liner Implosion Experiment," *IEEE Trans. Plasma Sci.*, **32**, 5, pp. 1972–1985, October 2004.

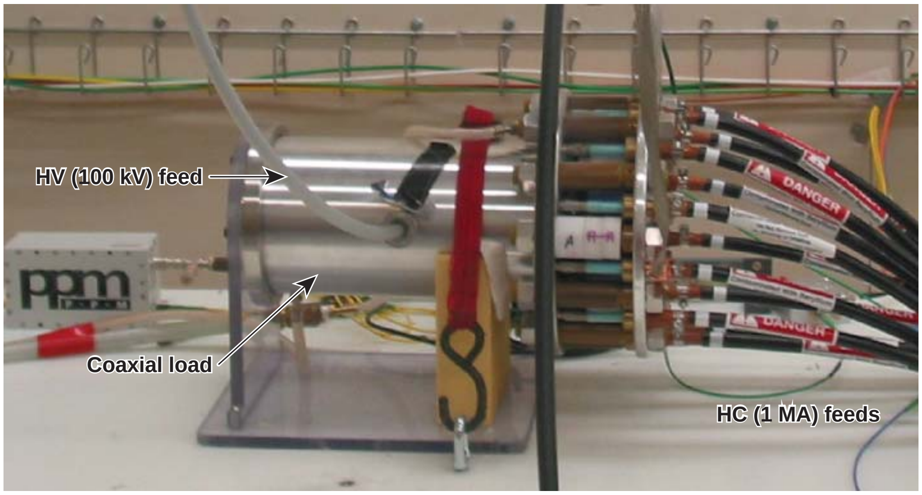

Figure 3. Photograph of the experimental configuration described in Fig. 2.

Evaluation of Spark Gap Technologies for High Current, High Charge Transfer Switches

Brent McHale
(925) 422-8730
mchale3@llnl.gov

High energy pulsed power applications often require closing switches capable of handling hundreds of kiloamps of current and transferring hundreds of coulombs per shot. These systems, such as EM launchers and large laser amplifiers, have long relied on a rather limited variety of switching technologies capable of satisfying the necessary current and charge transfer requirements. Triggered spark gaps of varying types have largely remained the standard solution in pulsed power switching, but electrode erosion is a predictable problem due to the nature of the switch's operation.

Spark gaps produce a localized high temperature plasma as the conduction path between the electrodes, and exposure to this plasma inevitably leads to electrode erosion. Erosion can occur by several related mechanisms, but the effect of each is essentially the same. Material is lost from the electrode, degrading its original shape, and that material then gets deposited on the surfaces of insulators within the switch. Both phenomena can lead to decreased switching performance, unreliable triggering and decreased lifetime resulting in added cost for maintenance and replacement.

It is possible to mitigate the effects of electrode erosion and extend the effective lifetime of a switch, but the ideal solution would minimize or eliminate the issue altogether. There are switch geometries in production that use the Lorentz force to move the arc along an electrode in order to distribute the energy over a larger area, reducing the localized effects of single point arcing as seen in a standard spark gap.

Project Goals

The goal of this project was to conduct a trade study and literature search to evaluate commercially available switching technologies with a focus on moving arc switches and potential improvements to existing switches that would result in higher reliability and lower overall cost. Innovative solutions in the form of switch geometries and electrode materials were a particular focus. Future goals would include testing a specific switch on an in-house test stand and applying those results to improved switches for pulsed power and power conditioning systems.

Relevance to LLNL Mission

A robust, high-energy switch with lower total cost would be a highly useful addition to the pool of technologies currently used at LLNL in pulsed power and power conditioning applications. The project emphasis is on highlighting switch technologies that have the potential to achieve higher reliability and lower operating costs as compared to a traditional spark gap. Numerous efforts in National Security, Defense Technologies, Laser Systems, and Energy Manipulation that involve pulsed power and power conditioning systems will benefit from a lower cost, low maintenance, and highly reliable switch.

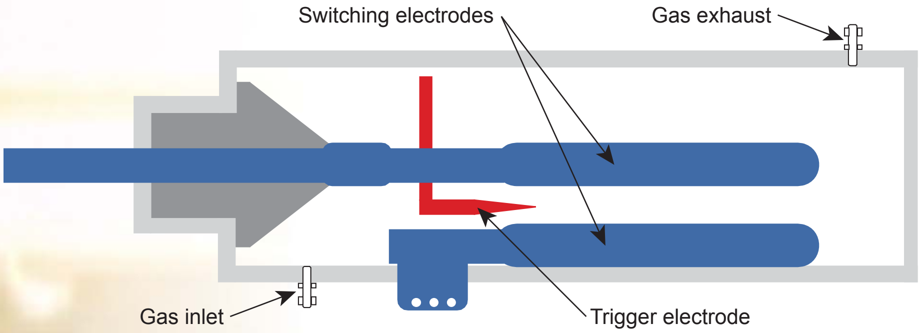

Figure 1. Basic geometry and features of a linear moving arc gap.

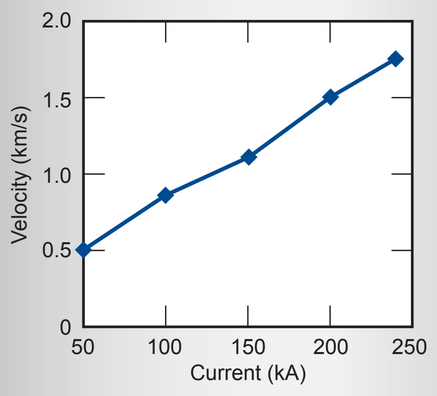

Figure 2. Projected average arc velocity vs. peak current for linear arc gap.

FY2008 Accomplishments and Results

In examining the currently available approaches to high-energy switching, the most promise was seen in moving arc switches. A linear moving arc gap switch (Figs. 1 to 3) was selected for the LMJ (Laser Mégajoule Project, a French effort similar to NIF) to satisfy their high charge transfer requirements, and it has demonstrated excellent reliability and a lifetime in excess of 22,000 shots without maintenance. Similarly, rotary arc gaps have also been used reliably in high energy switching applications, but commercially available units tend to have very high triggering requirements and necessitate a high-pressure gas system.

The geometry of the moving arc switch can be adapted to almost any switching requirements. Based on voltage hold-off, charge transfer requirements, and peak current, a moving arc switch could be tailored to any application provided the required linear length did not make it impractical. Should the linear length be constrained, a rotary arc gap would be a possible alternative.

In examining experimental results for various electrode materials, we found that copper was the best choice for nearly all applications. Other materials such as tungsten, tantalum, graphite, and hybrid material matrixes were the focus of several experiments, and in the vast majority of cases they did not offer substantial gains in electrode longevity when compared to copper. In addition, these materials were found to be more expensive and harder to work with than copper.

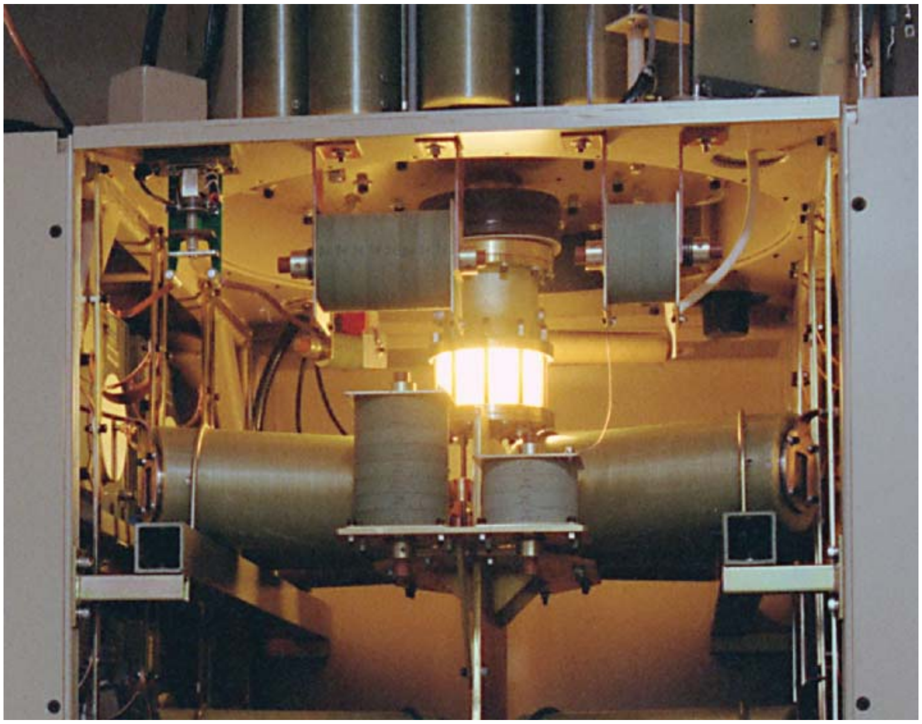

Figure 3. 500-kA Spark gap switch being discharged in one of the NIF power conditioning modules. There are 192 such modules in NIF. This high-current switch will require refurbishment approximately every 1,500 to 2,000 shots over an estimated NIF lifetime of 20,000 shots.

Related References

1. Kovalchuk, B. M., A. A. Kim, A. V. Kharlov, E. V. Kumpyak, N. V. Tsoy, V. V. Vizir, and V. B. Zorin, “Three-Electrode Gas Switches with Electrodynamic Acceleration of a Discharge Channel,” *Review of Scientific Instruments*, **79**, 2008.
2. Mexmain, J. M., D. Rubin de Cervens, J. P. Marret, V. Roos, P. Eyl, P. Père, B. Cassany, S. Sierra, P. Mathieu, J. Fauvel, P. Bènin, G. Callu, C. Vincent, and P. Michalczyk, “Pulsed Power Conditioning System for the Megajoule Laser,” *IEEE Transactions*, **0-07803-7915-2**, 03, 2003.
3. Savage, M. E., W. W. Simpson, R. A. Sharpe, and F. D. Reynolds, “Switch Evaluation Test System for the National Ignition Facility,” *IEEE Transactions*, **0-7803-4214-3**, 97, 1997.
4. Savage, M. E., “Final Results from the High-Current, High-Action Closing Switch Test Program at Sandia National Laboratories,” *IEEE Transactions*, **0-7803-5498-2**, 99, 1999.
5. Spinks, H. C., and A. E. Guile, “The Movement of High-Current Arcs in Transverse External and Self-Magnetic Fields in Air at Atmospheric Pressure,” *University of Leeds/Ministry of Aviation Aeronautical Research Council C.P.*, **777**, 1965.

FY2009 Proposed Work

Given the results of the literature search and the current state of the art, future work would focus on increasing in-house expertise on linear arc gap implementation. This would ideally be achieved through on-site experimentation on a test stand, which would also provide experimental data for electromagnetic and electromechanical computer code validation.

Pulsed Magnetic Field Measurements Using Faraday Rotation Diagnostics

Brent McHale
(925) 422-8730
mchale3@llnl.gov

It is often necessary to measure extremely large pulsed electric currents when conducting pulsed power, explosively driven pulsed power, or controlled fusion experiments. There are a limited number of diagnostics that can be used to accurately measure currents at these levels. The most common are inductive field sensors that are susceptible to undesirable field coupling, and electromagnetic interference (EMI).

Faraday Rotation Diagnostics (FRD) relies instead on magneto-optical phenomena: the plane of polarization of light passing through magnetized media is rotated as it passes through the media. The degree of rotation is directly proportional to the magnetic field strength and the distance over which the magneto-optical interaction occur. By using optical fiber that is wrapped an integer number of times around current-carrying conductors, symmetry in Ampere's law is exploited, and the induced optical rotation can be related directly to the current flowing through the conductor.

A FRD of this type has been installed in the LLNL Pulsed Power Laboratory and used on a number of high interest experiments, including the Fixed Hybrid Armature (FHA) experiment, the ALE3D Coaxial Load Validation experiment, and the Magnetically Insulated Sulfur-Hexafluoride Transmission Line (MIST) experiment.

Project Goals

The goal of this project is to acquire local expertise in FRDs, and to assess and identify potential improvements to the diagnostic. This year, we had several technical milestones for diagnostic improvement, including migration to a lower wavelength of operation for improved diagnostic sensitivity, improved bulk-optics polarization analysis hardware, and demonstration of proof-of-concept of an all-fiber polarization analysis scheme.

Relevance to LLNL Mission

FRD sensors have excellent linearity and bandwidth characteristics, and are optically isolated and largely immune to EMI. These qualities make FRDs particularly well suited for application in

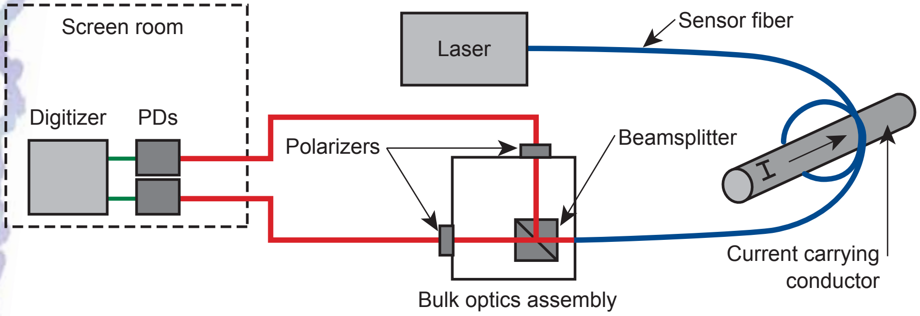

Figure 1. Block diagram of FRD system.

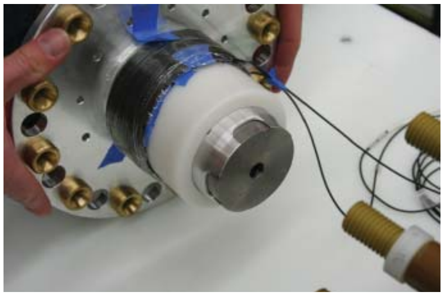

Figure 2. FRD sensor fiber installed on the ALE3D coaxial load test bed.

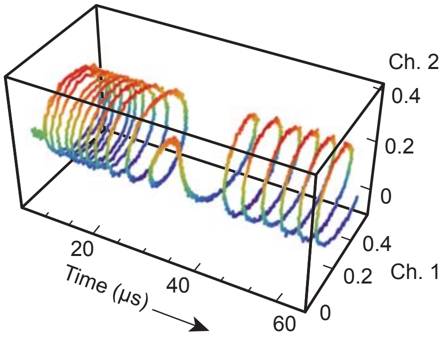

Figure 3. Raw FRD data from an FHA experiment. The pitch and handedness of the helix determines the sign and the rate of change of current. Peak current occurs at the reversal in helix direction near the middle of the figure.

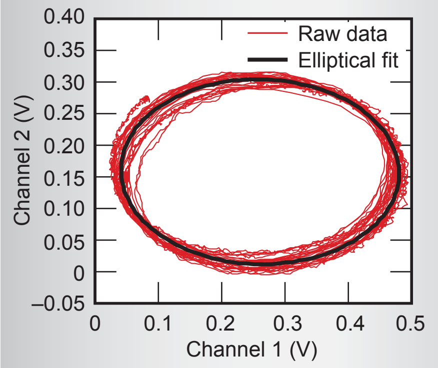

Figure 4. Projection of the helix in Fig. 3 onto *x-y* plane, and least-squares fit ellipse. Helix data is transformed using conic parameters of fit, and rotation deduced from fit. The resulting current waveform is shown in Fig. 5.

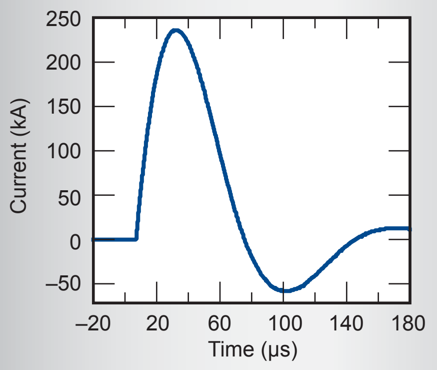

Figure 5. Current waveform computed from applying conic parameters in Fig. 4 elliptical fit to helical data in Fig. 3.

experiments that involve large quantities of guided or radiated electromagnetic energy. Since failure modes of FRDs differ from those of conventional inductive field sensors, FRDs offer a level of data redundancy for high-value single-shot experiments that is not easily achievable otherwise. Numerous programs at LLNL stand to benefit from this expertise, including explosive pulsed power for high-energy-density physics experiments, EM launcher experiments for military applications, and operations at NIF.

FY2008 Accomplishments and Results

A graphical depiction of the FRD implemented at LLNL is shown in Fig. 1. A 635-nm diode laser launches a few mW of linearly polarized light at a FRD sensor fiber, which is a twisted single-mode fiber installed in the experimental test bed (Fig. 2). The magnetic field in the vicinity of the sensor fiber induces Faraday rotation of the linearly polarized light. The rotating signal is coupled into a bulk optics assembly that splits the beam via a non-polarizing beam splitter and passes each beam through polarizers that are at a known relative angle. Both signals are then coupled through multi-mode fiber onto photodetectors and a digitizer in the screen room.

We have implemented the FRD on twenty-one shots across three experimental test beds with 100% data return. We have created a novel method of analyzing the data that is accurate and expeditious. A typical set of raw data is shown in Fig. 3; the helix shown is projected against the x-y axes where elliptical fit parameters are determined (Fig. 4). The elliptical fit parameters are applied to the helical data and rotation and current are computed. The results are shown in Fig. 5.

We have successfully migrated to a 635-nm system and have a proof-of-concept for an all-fiber polarization analysis scheme.

Related References

1. Rose, A. H., S. M. Etzel, and C. M. Wang, “Verdet Constant Dispersion in Annealed Optical Fiber Current Sensors,” *J. Lightwave Technology*, **15**, pp. 803–807, May 1997.
2. Day, G. W., and A. H. Rose, “Faraday Effect Sensors: The State of the Art,” *Proc. SPIE*, **985**, pp. 138–150, September 1988.
3. Bland, S. N., D. J. Ampleford, S. C. Bott, A. Guite, G. N. Hall, S. M. Hardy, S. V. Lebedev, P. Shardlow, A. Harvey-Thompson, F. Suzuki, and K. H. Kwek, “Use of Faraday Probing to Estimate Current Distribution in Wire Array Z Pinches,” *Rev. Sci. Instrum.*, **77**, 10E315, 2006.

FY2009 Proposed Work

The primary focus of FY2009 will be to migrate from fiber-based sensors to highly sensitive glass probes that will provide magnetic field measurements at a point rather than integrated around a loop. We will continue to acquire expertise in ancillary aspects of FRD implementation such as sensor fabrication, modeling, and data analysis that permits improvement of the precision and accuracy of the diagnostic.

UV-Induced Insulator Flashover

Jay B. Javedani
(925) 422-8569
javedani1@llnl.gov

In high-energy pulsed power systems, an insulator's main function is to provide an interface between regions of insulating fluid/gas and vacuum that separate electrodes at different high-voltage potentials. It is known that the vacuum surface of the insulator will flashover when illuminated to a critical dose of ultraviolet (UV) radiation, depending on the insulator material, insulator cone angle, applied voltage, and insulator's residual charge. Surface flashover refers to the cascade of electrons across the insulator's surface leading to the immediate collapse of voltage between the electrodes.

The UV radiation may be generated by ohmic heating of metal surfaces, coronas in high electrical field regions, or plasmas from explosive emission. As the power of the pulsed power system is increased, so is the UV fluence. An accurate knowledge of the UV fluence (energy per unit area) required for flashover is critical for producing the next generation of high-power flow systems.

Figure 1. Photograph of experimental setup.

Project Goals

The objective of this project was to conclude the measurement of UV fluence required for flashover of four candidate insulator materials and cone angles. The data gathered not only validated some of the measurements reported in the 1980s, but also extended the knowledge base to present parameters. These results are useful to electrically stressed, UV-radiated systems in many pulsed power applications.

Relevance to LLNL Mission

For many systems the delivery of pulsed power into a vacuum region is the most critical factor impacting performance and reliability. The applicability of our investigation in UV flashover performance addresses issues related to power flow channels for flux compression generators. As such, the results have a significant impact on LLNL's national security mission.

FY2008 Accomplishments and Results

A test bed comprised of an excimer laser (KrF, 248 nm), vacuum chamber (10^{-6} torr), and dc high-voltage (< 60 kV) power supply was established in FY2007. Fast capacitive probes (D-dot), the specialized diagnostic for this work, were embedded in the anode electrode underneath the insulator to give the time of arrival of flashover. A photograph of the test bed is provided in Fig. 1.

Testing included four types of 1.0-cm-thick insulator materials: 1) high-density polyethylene (HDPE), 2) a crossed linked polystyrene

Figure 2. Photograph of insulators (clear HDPE, milky Rexolite).

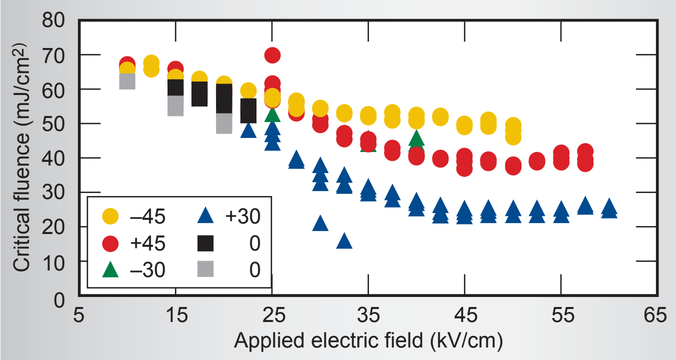

Figure 3. HDPE critical fluence results for different angles.

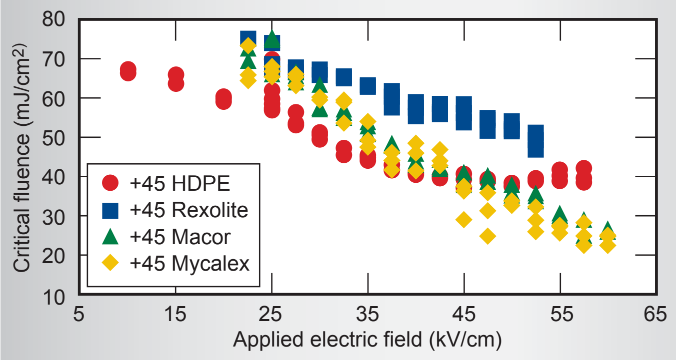

Figure 4. Critical fluence results for different insulator materials, all at +45°.

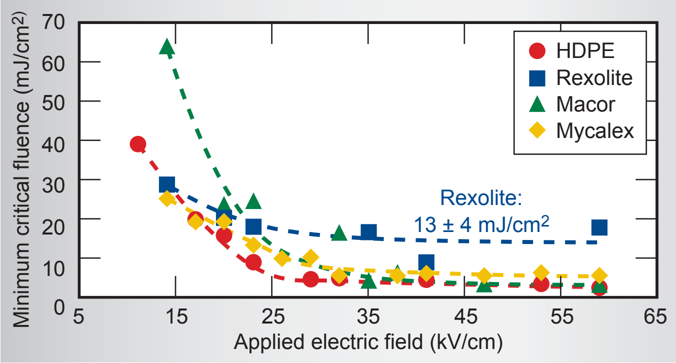

Figure 5. Minimum critical fluence results, all at +45°.

Rexolite® 1400, 3) a silicate-based machinable ceramic Macor,$^{\text{TM}}$ and 4) a fluorine-glass-based machinable ceramic Mycalex. The materials were extensively tested with insulator angles of 0, ±30, and ±45 degrees. Figure 2 is a photograph of some of the tested insulators.

The insulator was illuminated to a laser pulse while holding a dc charge (up to 60 kV). The nominal laser energy that impinged on the surface of the insulator was ~70 mJ/cm^2 (FWHM 30 nm, 2 MW/cm^2). More than 2000 data points were recorded, for different configurations of materials and angles. For each data point, the amount of UV dose for breakdown, *i.e.*, critical UV energy density, was measured by integrating the laser output power waveform all the way to the arrival time of flashover indicated by the fast D-dot probes (> 4 GHz bandwidth). Figure 3 shows the angle dependence of UV critical energy density for HDPE. Figure 4 shows the material dependence of UV critical energy density for all the tested materials.

A new effect was observed related to the UV power level on flashover that had not been previously reported. It appears that UV pulses with intensity greater than the minimum UV fluence need more than the established minimum energy/fluence to induce surface flashover. In other words, the energy/fluence required for flashover is also a function of the intensity of the UV pulse. This effect would bias the data toward higher minimum flashover fluence and lead to an incorrect interpretation of the data. Figure 5 shows the minimum critical UV energy needed for flashover. Among the four considered materials, Rexolite® 1400 showed the best UV hold off properties for surface flashover with the newly established minimum critical energy of 13 ±4 mJ.

Related References

1. Enloe, C. L., and R. E. Reinovsky, "Ultra-Violet Induced Insulator Flashover as a Function of Material Properties," *Proc. 4th IEEE Pulsed Power Conf*, **I**, Albuquerque, New Mexico, pp. 679–682, June 1983.

2. Enloe, C. L., and R. M. Gilgenbach, "Microscopic and Macroscopic Material Property Effects on Ultraviolet-Laser-Induced Flashover of Angled Insulators in Vacuum," *IEEE Trans. Plasma Sci.*, **16**, 3, pp. 379–389, June 1988.

3. Javedani, J. B., T. L. Houck, B. T. Kelly, D. A. Lahowe, M. D. Shirk, and D. A. Goerz, "UV Induced Insulator Flashover," *Power Modulator Conference*, Las Vegas, Nevada, April 2008.

Author Index

Barton, Nathan R. 2
Beer, N. Reginald 46
Bernier, Joel V. 4
Bond, Tiziana 54
Brown, Charles G., Jr. 18
Candy, James V. 30
Carrano, Carmen 76
Chambers, David H. 6
Chen, Barry Y. 82
Clancy, Todd J. 96
Corey, Bob 20
Dombroski, Matthew J. 16
Dzenitis, John M. 50
Edmunds, Thomas A. 88
Florando, Jeffrey N. 8
Heebner, John E. 36, 38
Houck, Timothy L. 100
Javedani, Jay B. 106
Johannesson, Gardar 90
Killingsworth, Nicholas J. 42
King, Michael J. 10
Kotovsky, Jack 56
Kroll, Jeremy J. 32
Lemmond, Tracy D. 80
Lin, Jerry I. 22
May, Deborah W. 86
McCarrick, James F. 14
McHale, Brent 102, 104
Meyers, Carol A. 84
Miles, Robin 66
Ng, Brenda M. 78
Nikolić, Rebecca J. 58, 60, 70
Noble, Chad R. 12
Puso, Michael A. 24
Rose, Klint A. 48, 62, 72
Seugling, Richard M. 34
Solberg, Jerome M. 94
Spadaccini, Christopher M. 64
Tang, Vincent 68
Tully, Laura K. 98
Vernon, Stephen P. 40
Weisgraber, Todd H. 52
White, Daniel A. 26

Manuscript Date April 2009
Distribution Category UC-42

This report has been reproduced directly from the best copy available.

Available from
National Technical Information Service
5285 Port Royal Road
Springfield, VA 22161

Or online at *www-eng.llnl.gov/pubs.html*

This work was performed under the auspices of the U.S. Department of Energy by Lawrence Livermore National Laboratory under Contract DE-AC52-07NA27344.
ENG-08-0065

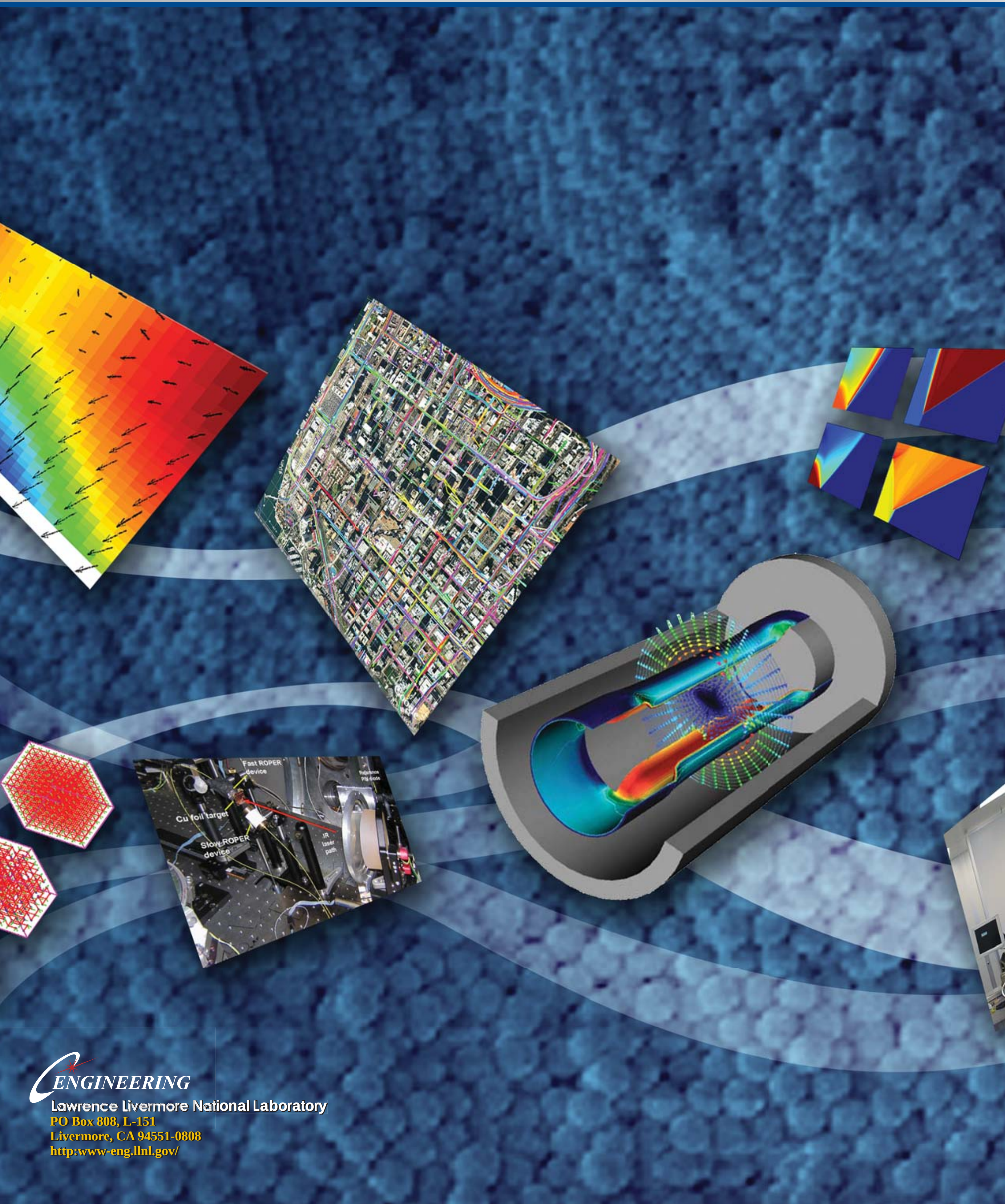

ENGINEERING
Lawrence Livermore National Laboratory
PO Box 808, L-151
Livermore, CA 94551-0808
http:www-eng.llnl.gov/